HAL
open science

Modeling the transport properties of molecular ions of krypton and xenon for the optimization of cold plasma generators using rare gases

Cyril van de Steen

▶ **To cite this version:**

Cyril van de Steen. Modeling the transport properties of molecular ions of krypton and xenon for the optimization of cold plasma generators using rare gases. Quantum Gases [cond-mat.quant-gas]. Université Paul Sabatier - Toulouse III, 2018. English. NNT : 2018TOU30264 . tel-02379733

HAL Id: tel-02379733

https://theses.hal.science/tel-02379733v1

Submitted on 25 Nov 2019

HAL is a multi-disciplinary open access archive for the deposit and dissemination of scientific research documents, whether they are published or not. The documents may come from teaching and research institutions in France or abroad, or from public or private research centers.

L'archive ouverte pluridisciplinaire **HAL**, est destinée au dépôt et à la diffusion de documents scientifiques de niveau recherche, publiés ou non, émanant des établissements d'enseignement et de recherche français ou étrangers, des laboratoires publics ou privés.

THÈSE

En vue de l'obtention du

DOCTORAT DE L'UNIVERSITÉ DE TOULOUSE

Délivré par l'Université Toulouse 3 - Paul Sabatier

Cotutelle internationale : IT4Innovations National Supercomputing Center à la VSB – Technical University of Ostrava

Présentée et soutenue par

Cyril VAN DE STEEN

Le 11 décembre 2018

Modélisation des propriétés de transport des ions moléculaires de krypton et xénon pour l'optimisation des générateurs de plasma froids utilisant les gaz rares

Ecole doctorale : **GEET – Génie Electrique Electronique et Télécommunications : du système au nanosystème**

Spécialité : **Ingénierie des Plasmas**

Unité de recherche :
LAPLACE - Laboratoire PLAsma et Conversion d'Energie - CNRS-UPS-INPT

Thèse dirigée par
Malika BENHENNI & René KALUS

Jury

Mme Nelly BONIFACI	*Chargé de recherche au CNRS – G2ELab, Grenoble*	Rapporteur
M. Ahmed RHALLABI,	*Professeur à l'Université de Nantes – IMN*	Rapporteur
M. Ioan SCHNEIDER	*Professeur à l'Université du Havre – LOMC*	Examinateur
M. Mohammed YOUSFI	*Directeur de recherche au CNRS – LAPLACE, Toulouse*	Président
Mme Malika BENHENNI	*Maître de conférences au LAPLACE, Toulouse*	Co-directrice de thèse
M. René KALUS	*Associate Professor at IT4I – VSB-TU Ostrava*	Co-directeur de thèse
M. Florent Xavier GADEA	*Directeur de recherche au CNRS – LCPQ, Toulouse*	Invité
M. Bruno LEPETIT	*Chargé de recherche au CNRS – LCAR, Toulouse*	Invité

Titre

Modélisation des propriétés de transport des ions moléculaires de krypton et xénon pour l'optimisation des générateurs de plasma froids utilisant les gaz rares.

Résumé

L'utilisation de plasmas froids à base de gaz rares (Rg) dans des applications biomédicales ainsi que dans la propulsion spatiale est en nette évolution. Pour optimiser ces réacteurs plasmas, une compréhension fine des processus ayant lieu dans ces réacteurs est nécessaire. Ce travail de thèse a pour objectif de fournir les données manquantes dans la littérature (coefficients de transport et réaction) en passant par des données mésoscopiques (sections efficaces) obtenues à partir de données microscopiques (potentiels d'interaction) pour le xénon et krypton dans leur gaz parent. Seul des plasmas froids composés d'un seul type d'atome sont considérés. Comme le krypton et le xénon sont des gaz rares, et ont donc, à l'état de neutralité peu/pas d'interaction entre eux. Par conséquent, seules les collisions ion – atome seront considérées. Du fait des faibles énergies des ions dans le plasma froid, seul les 6 premiers états excités du couple Rg_2^+ seront pris en compte. Ces 6 états seront classés en deux groupes, $^2P_{1/2}$ et $^2P_{3/2}$. Lors de ce travail, deux potentiels d'interaction différents disponibles dans la littérature sont utilisés et comparés pour les systèmes collisionnels Kr^+/Kr et Xe^+/Xe dans le calcul des sections efficaces. Pour les collisions impliquant des dimères ioniques (Kr_2^+/Kr et Xe_2^+/Xe), les potentiels d'interaction sont calculés à partir du modèle DIM (*Diatomics In Molecules*) qui est une combinaison des potentiels atomiques d'interaction neutre – neutre et ion – neutre.

Les sections efficaces, requises pour obtenir les données mésoscopiques manquantes, sont calculées à partir de trois méthodes différentes. La première méthode est la méthode quantique qui permet, par une résolution de l'équation de Schrödinger, d'obtenir de manière exacte les sections efficaces à partir des potentiels d'interaction. Cette méthode exacte, étant grande consommatrice de temps de calcul, est utilisée en tant que référence pour valider les deux autres méthodes approchées. La seconde méthode, nommée semi-classique, est basée sur la même expression que la section efficace quantique mais utilise un déphasage approché (approximation JWKB), induit par le potentiel d'interaction, entre l'onde diffusée et l'onde incidente. Cette méthode a l'avantage d'être plus rapide que la méthode quantique tout en ayant des résultats très proches. La dernière méthode est la méthode hybride qui consiste à traiter les atomes par une méthode classique et les électrons par le formalisme quantique. Cette méthode est la seule des méthodes approchées qui permet de traiter les collisions entre dimère et atome en prenant en compte la vibration et la rotation du dimère.

Lors de collision dimère – atome, une fragmentation du dimère peut avoir lieu et donc la section efficace de dissociation du dimère, apparaissant à partir d'un seuil d'énergie, a été prise en compte dans les calculs Monte Carlo. Les coefficients de diffusion ainsi que la mobilité des ions dans leurs gaz parents sont calculés à partir des sections efficaces avec un code Monte-Carlo. Les mobilités ainsi calculées sont comparées aux mesures expérimentales disponibles dans la littérature. Dans le cas des dimère, la rotation et la vibration dans la molécule doivent être prises en compte. Tous les résultats montrés sont réalisés sur l'état fondamental du dimère.

Les mobilités ainsi calculées par les méthodes disponibles donnent des résultats proches des valeurs expérimentales, nous permettant de conforter nos autres coefficients de transport et réaction.

Mots clés

Modélisation physico-chimique, donnée de base, ion atomique (Kr^+ et Xe^+) et diatomique (Kr_2^+ et Xe_2^+), interaction ion – neutre, potentiel d'interaction, section efficace de collision et dissociation, méthode quantique, méthode semi-classique (JWKB) méthode hybride, simulation Monte Carlo, coefficients de transport, taux de réaction

Title

Modeling the transport properties of molecular ions of krypton and xenon for the optimization of cold plasma generators using rare gases.

Abstract

The use of cold plasmas based on rare gases (Rg) in biomedical applications as well as in space propulsion is clearly evolving. To optimize these plasma reactors, a fine understanding of the processes taking place in these reactors is necessary. This thesis aims to provide the missing data in the literature (transport coefficients and reaction rates) through mesoscopic data (cross-sections) obtained from microscopic data (interaction potentials) for xenon and krypton in their parent gas. Only cold plasmas composed of a single type of atom are considered. As krypton and xenon are rare gases, and so have, in the neutral state little / no interaction between them. Therefore, only ion – atom collisions will be considered. Due to the low ion energies in the cold plasma, only the first 6 excited states of the Rg_2^+ pair will be taken into account. These 6 states will be classified in two groups, $^2P_{1/2}$ and $^2P_{3/2}$. In this work, two different interaction potentials available in the literature are used and compared for the Kr^+/Kr and Xe^+/Xe collision systems in the calculation of cross-sections. For collisions involving ionic dimers (Kr_2^+/Kr and Xe_2^+/Xe), the interaction potentials are calculated from the DIM model (*Diatomics In Molecules*) which is a combination of the atomic potentials of neutral – neutral and ionic – neutral interactions.

The cross-sections required to obtain the missing mesoscopic data are calculated from three different methods. The first method is the quantum method which allows, by a resolution of the Schrödinger equation, to obtain exactly the cross-sections from the interaction potentials. This exact method, which consumes a lot of computation time, is used as a reference to validate the two other approximate methods. The second method, called semi-classical, is based on the same expression as the quantum cross section but uses an approximate phase shift (JWKB approximation), induced by the interaction potential, between the scattered wave and the incident wave. This method has the advantage of being faster than the quantum method while having very close results. The last method is the hybrid method, consisting of treating atoms by a classical method and electrons by quantum formalism. This method is the only one of the approximate methods which makes it possible to treat the collisions between dimer and atom taking into account the vibration and the rotation of the dimer.

In a dimer – atom collision, fragmentation of the dimer may occur and thus the dissociation cross-section of the dimer, appearing from an energy threshold, has been taken into account in the Monte Carlo calculations. The diffusion coefficients as well as the mobility of the ions in their parent gases are calculated from the cross-sections with a Monte Carlo code. The mobilities thus calculated are compared with the experimental measurements available in the literature. For dimer calculations, rotation and vibration in the molecule must be taken into account. All the results shown are made on the ground state of the dimer.

The mobilities thus calculated by the available methods give results close to the experimental values, allowing us to reinforce our other coefficients of transport and reaction.

Keywords

Physicochemical modeling, basic data, atomic ion (Kr^+ and Xe^+) and diatomic (Kr_2^+ and Xe_2^+), ion-neutral interaction, interaction potential, collision cross section and dissociation, quantum method, semi-classical method (JWKB), hybrid method, Monte Carlo simulation, transport coefficients, reaction rate

2017

Cyril Van de Steen, Malika Benhenni and René Kalus. *Mobility of Kr^+ ions in Kr for cold plasma modelling.* **ICPIG XXXIII**

Cyril Van de Steen, René Kalus and Malika Benhenni. *Mobility of Xe^+ ions in Xe for cold plasma modelling.* **ISPC23**

2018

Cyril Van de Steen, Malika Benhenni, René Kalus, Bruno Lepetit, Florent Xavier Gadéa and Mohammed Yousfi. *Quantum and semi-classical collision cross-sections and transport data for a Kr^+/Kr system.* **Plasma Sources Science and Technology**, Volume 27, Number 6, page 065005

Cyril Van de Steen, Malika Benhenni, René Kalus, Bruno Lepetit, Florent Xavier Gadéa and Mohammed Yousfi. *Calculations with experimental validations of cross-sections and transport coefficients of Xe^+ colliding with Xe*. **Journal of Physics B: Atomic, Molecular and Optical Physics**, Volume 51, Number 18, page 185204

Cyril Van de Steen, Malika Benhenni, René Kalus, Rajko Ćosić, Silvie Illésová, Florent Xavier Gadéa and Mohammed Yousfi. *Cross-sections, transport coefficients and dissociation rate constants for Kr_2^+ molecular ion interacting with Kr.* **Plasma Sources Science and Technology**, https://doi.org/10.1088/1361-6595/aaebe0

Cyril Van de Steen, Rajko Ćosić, René Kalus, Malika Benhenni. *Mobility of Xe_2^+ ions in Xe for cold plasma modelling*. **GEM XX**

Cyril Van de Steen, Malika Benhenni, Rajko Ćosić, René Kalus. *Mobility of Kr_2^+ ions in Kr for cold plasma modelling.* **ESCAMPIG XXIV**

Acknowledgements

This work of research was done in two different laboratories, universities and countries. Since one of these laboratories is in France, I will do my thanks to related people in French in the following of this text. It will be easier for me to express my fillings in my native language and I'm sure it will be easier for them to understand it also.

Firstly I would like to thank all members of my 2 juries (French and Czech) who were not directly involved in my daily work. I'm grateful to Mrs Bonifaci, Mrs Paidarová, M. Rhallabi and M. Janecek for being the reviewers of my thesis and the time they spent reading it carefully. I would also like to thank M. Schneider, M. Kozubek, M. Lampart, M. Ciprian and M. Alexa for the time they spent for the attention they spent on my thesis and thesis defense.

Outside of the Jury members I would also like to thank all the people met in Czech Republic. I would like to give a warm thanks to Mr. René Kalus from IT4Innovations in VSB University for his help. He not only helped me with my work and provided me with advice on the work but also for common life in a foreign country. He is probably one of the best thesis directors a Ph.D. student can have. I would like also to thanks IT4Innovations and Vysoká Škola Báňská - Technická Univerzita Ostrava for the chance they give me to make PhD studies and, also, for all the translations they did in English so that I could understand. I would also like to thank the Moldyn group (René, Alex, Rajko, Stanislav, Martin and Martin) and the other PhD students of IT4I (Simona, Michal and Michal) for their help and effort to make all meeting/ discussions in English so that I could understand. In summary *dekuji moc* to all the people met in Czech Republic for their tolerance and acceptance of a foreign student.

Concernant la partie de la thèse réalisée en France, Je tiens à exprimer ma profonde gratitude à Madame Malika Benhenni de l'Université Paul Sabatier pour son aide, soutien et conseils lors de ma thèse dans le groupe P.R.H.E. (Plasma réactifs Hors-Équilibre) au sein du Laplace (Laboratoire de Plasma et Conversion d'Énergie). Un grand merci

aussi à Messieurs Mohammed Yousfi, Bruno Lepetit et Florent-Xavier Gadéa pour leur aide et conseils durant ma présence en France. Un merci aussi au Laplace pour son accueil ainsi qu'au groupe P.R.H.E. en général pour leur bonne humeur ainsi que leur compréhension progressive de belgicismes.Une pensée aussi à Mofel Nerbaoui pour son courage et sa patience. Un merci à mes camarades de l'ADeL (Andréa, Simo et François) pour les moments de décompressions créés pour les Laplaciens. Un merci aussi aux Doctoriants (Chaimae, Inthu, Nico et tous les autres) qui ont permis une mise en perspective de la thèse ainsi que des sorties des plus enrichissantes. Une pensée aussi aux petits stagiaires qui sont devenus doctorants maintenant (Julien et Maxime) ainsi qu'aux autres doctorants Laplaciens du bâtiment d'en face (Philou et Marjorie principalement). De vifs remerciements ensuite pour deux camarades de thèse avec qui j'ai vécu des moments de pression et de détente. À savoir Farah Fawaz et Docteur Julie Chauvin. Merci à vous deux pour tous ces moments passés ensembles. Je tiens également à remercier M. Dufour qui m'a envoyé l'offre de thèse afin de me permettre de pouvoir continuer dans la recherche. Un merci aussi au secrétaire du jury de master qui, de par son discours peu encourageant sur mes capacités scientifiques lors de ma soutenance de master, m'a donné l'envie de continuer. Une pensée est bien sur dirigée à mes anciens camarades de promo au sein de mon parcours universitaires à l'ULB, les premiers noms qui me viennent en tête sont Mawie, Adrien, Jordane, Jonathan, Arnaud et pleins d'autres dont je ne pourrais écrire ici tous leurs noms. Enfin un énorme merci à ma famille sans qui je n'aurais pas pu faire cette thèse loin d'eux. Merci pour leur soutien inconditionnel durant toute la durée de ses trois ans de thèse.

List of Used Abbreviations and Symbols

k_B	–	Boltzmann constant
E	–	Energy
T	–	Temperature
r	–	Distance
E	–	Electric field
N	–	Gas density
E/N	–	Reduced electric field
K_0N	–	Reduced mobility
eV	–	Electronvolt
eD_T	–	Transverse diffusion coefficient
eD_L	–	Longitudinal diffusion coefficient
$\sigma^{(INT)}$	–	Integral Cross-Section (ICS)
$\sigma^{(MT)}$	–	Momentum Transfer Cross-Section (MTCS)
k_m	–	Wave vector of state m. $k = \mu\upsilon_m/\hbar$
μ	–	Reduce mass
υ	–	Velocity of the atom
$\hbar$	–	Reduced Planck constant (Planck constant divided by 2π)
$\hat{\mathrm{H}}$	–	Hamiltonian
l	–	Angular momentum number
$\langle\Phi\|X\|\Phi\rangle$	–	Bra-Ket notation, $\int \Phi^* X \Phi$
${}^{X}\mathrm{Rg}_{Y}^{Z}$	–	Rare-gas (krypton and xenon in this thesis) with X number of proton + number of neutron, Z is the charge and Y is the number of atom in the molecule

Contents

1 Overview of actual context **5**

1.1 General informations on plasmas 5

1.1.1 Different low temperature plasma sources 8

1.1.2 Dielectric Barrier Discharge (DBD) at atmospheric pressure 8

1.1.3 Corona discharges 9

1.1.4 Direct Current (DC) plasma 10

1.1.5 Radio Frequency (RF) plasma 11

1.2 Potential applications of non-thermal rare-gas plasma generators 12

1.2.1 Biomedical 12

1.2.2 Excilamps 14

1.2.3 Plasma propulsion for Spacecraft 15

1.3 Thesis objectives 16

1.3.1 Plasma modeling 17

2 Theory **21**

2.1 Interaction potentials 21

2.1.1 Ion - Atom potential 21

2.1.2 Dimer - Atom potential 26

2.2 Cross-section 28

2.2.1 Quantum method 34

2.2.2 Semi-classical method 43

2.2.3 Hybrid method 45

2.2.4 Inverse method 54

2.3 Ions transport coefficients: Monte Carlo Method 55

3 Ionic Atom - Neutral Atom Collisions 61

3.1 Krypton 61

3.1.1 Interaction potentials 62

3.1.2 Experimental data reported in literature 65

3.1.3 Cross-sections 67

3.1.4 Mobility and diffusion coefficient 75

3.1.5 Discussions 79

3.2 Xenon 84

3.2.1 Interaction potentials 84

3.2.2 Experimental data reported in literature 85

3.2.3 Cross-sections 86

3.2.4 Mobility and diffusion coefficient 92

3.3 Conclusions 96

4 Ionic Dimer - Neutral Atom Collisions 99

4.1 Selection of initial conditions 99

4.2 Krypton 103

4.2.1 Experimental data reported in literature 104

4.2.2 Neutral potentials 104

4.2.3 Cross-sections 106

4.2.4 Mobilities 114

4.2.5 Diffusion coefficients 121

4.2.6 Dissociation rate constants 123

4.3 Xenon 125

4.3.1 Experimental data reported in literature 125

4.3.2 Neutral potentials 127

4.3.3 Cross-sections 128

4.3.4 Mobilities 133

4.3.5 Diffusion coefficients 140

4.3.6 Dissociation rate constants 141

4.4 Conclusions 142

5 Conclusions and Perspectives **145**

Appendices **149**

A Tables of transport coefficients for $\mathrm{Kr}^+/\mathrm{Kr}$ collisions 149

B Tables of transport coefficients for $\mathrm{Xe}^+/\mathrm{Xe}$ collisions 155

C Tables of transport coefficients and dissociation rate constant for $\mathrm{Kr}_2^+/\mathrm{Kr}$ collisions 161

D Tables of transport coefficients and dissociation rate constant for $\mathrm{Xe}_2^+/\mathrm{Xe}$ collisions 187

Bibliography **213**

General Introduction

This work subscribes in the continuity of research which started 7 years ago on rare-gases helium (He), argon (Ar) and neon (Ne) atomic and molecular ions in collision with their parent gases which involves 3 different laboratories (LAboratoire Plasma et Conversion d'Energie) LAPLACE at Toulouse, (Institut de Recherches Sur les Agrégats, Molécules et Collisions) IRSAMC at Toulouse and IT4Innovations at Ostrava. The present thesis work is performed in two different laboratories, IT4Innovations at Vysoká Škola Báňská - Technická Univerzita Ostrava (Czech Republic) under the supervision of Mr Kalus René and the LAPLACE at Université of Toulouse III (France) under the supervision of Mrs Benhenni Malika in the research group PRHE (Plasmas Réactifs Hors Equilibre). In this thesis, we are focused on krypton (Kr) and xenon (Xe) rare-gases in collision with their respective parent gas at ambient temperature and atmospheric pressure.

The first chapter presents the context of this thesis, i.e. to complete the missing basic data such as transport coefficients (mobility and diffusion) and constant rate of monoatomic and dimer ions of krypton (Kr^+ and Kr_2^+) and xenon (Xe^+ and Xe_2^+). These data are needed as input in chemical hydrodynamic model of low temperature plasmas generated at atmospheric pressure used for applications such as biomedical, spacecraft propulsion and dielectric barrier discharges excimer lamps. Indeed, the ion transport coefficients are rather incompletely reported in the literature where the only available basic data are the measured mobility on a limited reduced electric field range and no measurements are available both on monoatomic and dimer ions diffusion coefficient and dimer ion dissociation. Moreover, ion mobility data were measured by several authors and show a clear disparity especially in the very low field range probably due to the presence of impurities in their signal. Furthermore, calculations reported by Barata [1] (as reported in reference [2]) show disagreement with experimental data. This

chapter reports on the different setups of cold plasma generators found in the literature. The different potential applications of krypton and xenon cold plasma generators such as biomedical, excimer lamp or spacecraft propulsion are presented in this chapter. It also describes the electro-kinetic model which allows to determine the different active species densities and the electric field needed for targeted potential applications.

The second chapter describes the ion - atom potentials used for collision cross-section calculations. Two sets of interaction potentials for ion-atom collisions (Kr^+- Kr and Xe^+- Xe) available in the literature are compared, and the methodology DIM (*Diatomics In Molecule*) used to generate the interaction potential for the ionic dimer - neutral atom collision (Kr_2^+- Kr and Xe_2^+- Xe) is described as well. Moreover, this chapter details the basis of the three considered methods namely quantum, semi-classical, and hybrid method that uses quantum formalism for the electronic cortege while a classical treatment is applied to nuclei. The semi-classical method uses an approximate phase shift induced by the interaction potential between the scattered and the incident wave functions. This method has the advantage of being faster than the quantum method while providing quasi identical cross-sections. It is used in this thesis specially to verify the hypothesis of assuming in the calculations, an artificial krypton or xenon isotope with average mass, instead of the real masses of the different natural isotopes in order to save computational time. The hybrid method is the only one which allows to treat the collisions between dimer ions and neutral atoms. An inverse method, based on a spherical potential with adjustable parameters, is also described in this chapter. This method is very useful when no interaction potential is available and, is used to extend the mobility data to electric fields where they are missing, and to provide diffusion coefficient not available in literature. Monte Carlo method which uses probabilities associated to the different calculated elastic and inelastic collision cross-sections to simulate the ion transport under the action of a uniform electric field, is also described in this chapter. This method allows to calculate, from these elastic and inelastic cross-sections, the transport coefficients (mobility

and diffusion) and constant rate over a large reduced electric field range.

The third chapter is dedicated to the monoatomic (Kr^+ and Xe^+) ions in collision with their respective parent gases. This chapter reports the calculated momentum transfer collision cross-section by using two different potentials ionic atom - neutral atom collisions available in the literature. Then, the calculated mobilities with Monte Carlo code from these collision cross-sections are compared to measured ion mobilities in order to select the best potential that will be used for dimer - atom collisions. Moreover, the ion transverse and longitudinal diffusion coefficients are also calculated and reported over a large reduced electric field range (5 Td to 3000 Td).

Chapter 4 concerns the ion basic data in the dimer ion - neutral atom collisions Kr_2^+- Kr and Xe_2^+- Xe. In this case, fragmentation of dimer ion takes place with a characteristic threshold energy, so the dimer dissociation cross-section is also calculated and reported along with the momentum transfer collision cross-section by using hybrid method. The vibration and rotation of the dimer are also taken into account to enhance the agreement between calculated and measured dimer ion mobilities. The influence on the dimer mobility of the neutral - neutral potential in the DIM model is also discussed in this chapter.

Finally, a general conclusion summarizing the different chapter conclusions is given at the end of this thesis.

Chapter 1

Overview of actual context

1.1 General informations on plasmas

The term "plasma" was used by Irving Langmuir in 1928 to designate ionized gases [3]. Many technologies of everyday life now incorporate these plasmas, which are therefore more widely known to the general public. This is the case for example with plasma television screens, neon lamps, fluorescent tubes and one can also mention commercially available plasma balls, this showing its a democratization [4]. Plasma processes have been widely used in industry for almost a century. They are present in the field of polymers (engraving, surface functionalization), microelectronics to mention a few and have more recently entered the world of biology, medicine and space propulsion.

Plasma is commonly referred to as the "fourth state of matter" after solid, liquid and gaseous states. Quite rare in the natural state of our planet, it represents 99% of the known universe matter, the stars, the solar wind, the ionosphere of the earth are plasma examples [4]. In the natural state, lightning and the northern lights (Aurora Borealis) such as shown in figure 1.1 are phenomena that are often observed.

Beyond this very global definition, a plasma is defined from the point of view of physics as a partially or totally ionized gas. An ionized gas is thus composed of electrons and ions, but also of molecules and excited atoms (that is to say in a

Figure 1.1: Aurora Borealis in Greenland [5]

higher energy level than that of the ground state). Neutral and ions often called heavy particles in the plasma, can also be excited for short time (10^{-6} to 10^{-8}s) before emitting photon during their desexcitation. This emission of photon is mostly responsible of the light emitted by a plasma and is, also, a signature of the plasma. An ionized plasma may be called plasma if, and only if, the plasma is electrically neutral, this means that the negative and positive charges inside the plasma have to counterbalance each other. This propriety is verified at distance, around an ionized particle, higher than the Debye radius. To ionize an atom or a molecule, it must be given enough energy for an electron to leave its electronic layer and becomes a free electron. This energy can be provided thermally, electrically, magnetically, radiatively, chemically or mechanically. It is therefore possible to generate plasmas in the laboratory through these various sources of energy. An essential parameter for defining a plasma and for "classifying" it, is therefore its degree of ionization α, which represents the ratio of the electron density (n_e) to

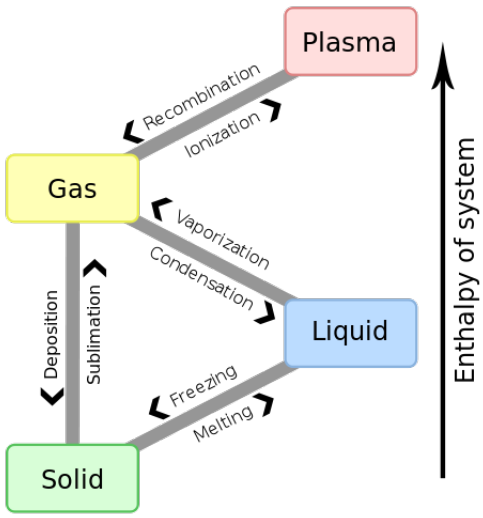

Figure 1.2: All possibilities of states modification

the total density of electrons and neutral species (N):

$$\alpha = \frac{n_e}{n_e + N}. \tag{1.1}$$

When the degree of ionization is close to or equal to 1, the plasma is totally ionized, and it is called "hot plasma". These plasmas are said to have the thermodynamic equilibrium and the temperature of the charged species is of the order of one million kelvin. They are present especially in the field of nuclear fusion (tokamaks [4]) and the sun is another perfect example. Furthermore, the plasmas generated by electric arcs due to gas breakdown leads to ionization and dissociation of most of the molecules species and can reach several thousands of kelvin (20000 to 30000 K). They are also considered at thermal or quasi-thermal equilibrium. When the degree of ionization is low (between 10^{-4} and 10^{-7}), the plasma is weakly ionized, and it is called "non-equilibrium or non thermal plasma" because it is out of thermodynamic and chemical equilibrium. Indeed, when an electric field is applied between two electrodes to generate a plasma, the free electrons which first receive this electrical energy via an electric force $\vec{F} = q\vec{E}$ then, transfer only a part to the heavy particles. If time or energy is not sufficient, electrons can-

not balance their temperature with other particles, which explains the differences in temperature between electrons (T_e) and other particles (ions T_i and neutral T_0) in a weakly ionized plasma. Thus, in the weakly ionized plasmas presented in this work, we have

$$T_e > T_i > T_0. \tag{1.2}$$

In fact T_e can reach several eV energy in order to be able to ionize, excite and dissociate the carrier gas. However, the electron density is too low to heat the weakly ionized plasma which has a mean temperature close to ambient one. This is why the low temperature or cold plasmas are used for instance in biomedical applications, because of their average temperature close to the ambient temperature [3, 6].

1.1.1 Different low temperature plasma sources

There are multiple electrical discharge sources to generate low temperature plasmas with different parameters that can be modulated, such as temperature and electron density, ions and neutrals, the density of excited atoms or molecules and the intensity of photon sources (UV). Electrical discharges producing these plasmas can be grouped in different categories and often, different groups are associated in a single setup in order to take advantage of each group specificity.

1.1.2 Dielectric Barrier Discharge (DBD) at atmospheric pressure

The use of a dielectric covering one the electrode (or both electrodes for the case of a double dielectric barrier) makes it possible to avoid the passage to the electric arc which could damage the plasma generator system and the samples to be treated. But the presence of a DBD implies the formation of an electric field of direction opposite to the applied electric field, because when the positive (or negative) streamer reaches the cathode (or the anode respectively), the charges are deposited on the surface of the dielectric. If this induced electric field becomes equal to the applied electric field, the plasma goes out. It is therefore preferable

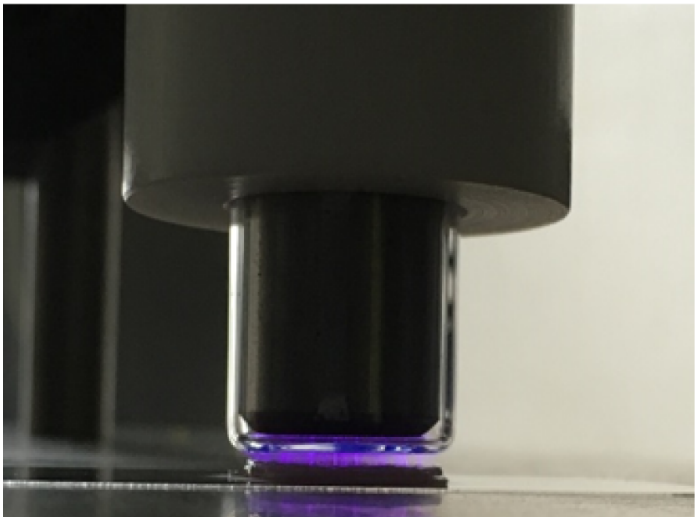

Figure 1.3: Example of a DBD reactor [7]

to supply the reactor with a alternative or pulsed regime (kHz frequency) so that the electrodes can be discharged between each pulse. In addition, the short duration of the pulses limits the increase of the electric field [4]. The combined use of these dielectric barriers and an adequate power supply regime thus allows to generate "filaments", which will not evolve in an electric arc [8–10].

1.1.3 Corona discharges

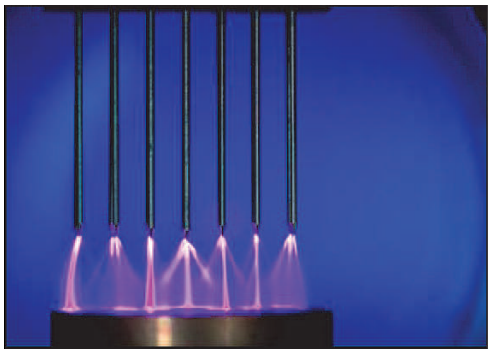

Figure 1.4: Example of a Corona reactor [7]

The corona effect is a partial discharge without arcing the background gas enclosed between two asymmetric electrodes where a strong electric field pre-

vails. Several configurations exist such as the foreground, the wire-cylinder and the wire-plane. If the electrode having the smallest curvature radius is supplied with a DC (Direct Current) voltage positive relative to the other electrode, it is a positive corona discharge. Conversely, we speak of negative corona discharge. This distinction is important because the phenomena induced during the discharge will differ significantly by their nature that the amount of chemical species formed (the negative discharge produces for example much more ozone than the positive one) [6]. To be able to increase the voltage (and produce more chemical species without generating an arc and damage the electrodes), the electrodes can be powered with alternating voltage and frequency of a few kHz or using a pulse voltage generator. The pulse duration is then chosen so that the inter-electrode voltage returns to zero before the occurrence of an electric arc.

1.1.4 Direct Current (DC) plasma

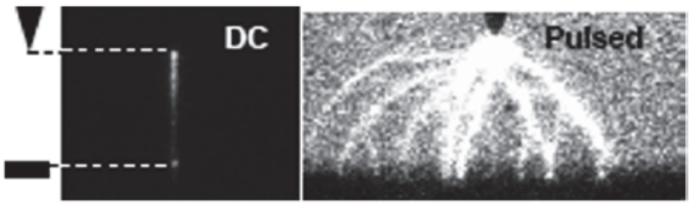

Figure 1.5: Example of a DC and pulsed corona discharge in a positive point-to-plane geometry [7]

Semiconductor fabrication techniques, micro-discharge structures have been used to generate DC plasmas [11, 12]. Hollow cathode discharges with cathode dimensions less than one millimeter have also been widely used [13]. Micro-discharges generate non-thermal high-pressure plasmas having cathode dimensions in the micrometer range, which allows an increase in pressure while maintaining a relatively low applied voltage. DC frequencies (50/60 Hz) have also been used to produce cold plasmas. In this case, resistive barrier discharges are used where a uniformly distributed resistive film is used to cover the electrodes

[14]. Here, the discharge current is limited by the resistive layer, which acts as a ballast, and does not allow the discharge to pass to an arc.

1.1.5 Radio Frequency (RF) plasma

Figure 1.6: Example of a RF generator [15]

Radio Frequency sources have also been used to generate cold plasmas with devices similar to DBDs and with devices whose electrodes are bare metal [16]. With bare metal electrodes, the arc is a problem and both the temperature of the electrodes must be controlled (usually by water cooling) and the gas flow adjusted to a certain level to minimize the risk of formation of the electrodes arcs. RF driven devices require impedance matching between the power source and the plasma to optimize the deposited power into the plasma and to minimize the reflected power.

1.1.5.1 Plasma jets

Non-thermal atmospheric pressure plasma jets are playing an increasingly important role in various biomedical applications because of their practical ability to provide spatially unbound plasmas [18]. They are generated under a wide range of controlled frequencies and with various electrode geometries and dif-

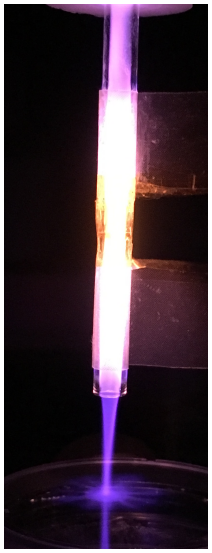

Figure 1.7: Example of a plasma jet reactor [17]

ferent gases. The used carried gas are generally composed by rare-gases (He or Ar or Ne) mixed with other rare-gases (Kr or Xe) or molecular gases as for instance N_2, O_2 or H_2O. The plasma jet is very convenient for in vivo treatment where it can be dangerous to put living tissues inside the inter electrode due to the applied high voltage. Main configuration (as visible in figure 1.7) of plasma used in PRHE group is composed of two electrodes fixed around a quartz tube providing a DBD set up in order to avoid arc formation. In the quartz tube a flux of gas is controlled, by playing on the nature of the gas, the flow of the gas, the inter-electrode distance, the frequency of electric signal and the voltage creation of different active plasma is possible.

1.2 Potential applications of non-thermal rare-gas plasma generators

1.2.1 Biomedical

In the biomedical field, thermal discharges are used for the ablation of tissues in surgery, or for the cauterization of tissues. Non-thermal discharges are used for

instance for sterilization, decontamination or treatment of pathological tissues. The non-thermal plasmas at atmospheric pressure have shown a high potential for biomedical applications [19]. The plasma generators and studies dedicated to biomedical applications use mainly helium as carrier gas. But more recently, neon and krypton are also studied in different laboratories. Indeed, recent measurements reported by Li *et al.* [20] show that plasma jets have a very different behavior when krypton is used as carrier gas as compared to helium, argon or neon. To better understand such differences, it is necessary to better know more particularly ion transport and reaction rate in all these carrier rare-gases. The basic data on He, Ne and Ar gases have already been reported in previous work [21–25].

Figure 1.8: Plasma jet propagating inside a flexible tube of about 1m length before to be launched in the ambient air. Such device can be used, for instance, for endoscopic plasma treatment : Example of direct plasma application [26]

Non-thermal plasma at atmospheric pressure using rare-gas are a promising device in plasma medicine. Several beneficial aspects of these cold plasma have been proved these last 10 years such as inactivation of bacteria or malignant cell in cancer therapy, chronic wound healing and blood coagulation. Plasma in biomedicine can be classified in two groups, direct or indirect, depending on their application. Because in cold plasma, the ions and the neutrals remain relatively cold, the plasma does not cause any thermal damage which allow to use these direct non-thermal plasmas for the treatment of materials that are sensitive to heat as well as cells and tissues. These cold plasmas generate many active species such as charged particles (ions and electrons), radicals, UV radiation that

can interact with the living cells, the plasma generated electric field can also participate to the bacteria inactivation. For indirect contact, active species produced by cold plasma may also interact with medium in order to be used more easily. Indeed recent research are performed on Plasma Activated Medium (PAM) to treat cancer with injection of this PAM directly in contact with cancer cells, even if this one is located inside the body [7, 27, 28]. Another example of the indirect plasma is Plasma Activated Water (PAW) which is used to improve plant growth [29]. However, the active mechanisms in such applications are not well known and deep understanding of these mechanisms is necessary in order to quantify the different active species and electric field that are involved in the observed effect of these applications.

1.2.2 Excilamps

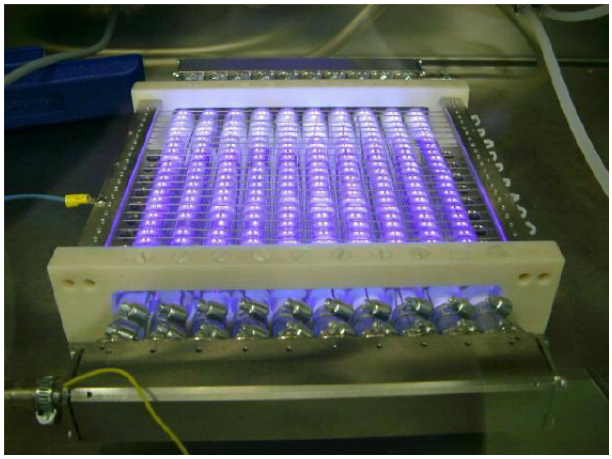

Figure 1.9: Example of excilamps [30]

Excilamps are dielectric barrier discharge lamps using excitations of excimer which refers to the bound excited upper state of a molecule that breaks apart and a photon is emitted. Excimer lamps are almost monochromatic light sources that can operate over a wide range of wavelengths in the ultraviolet (UV) and vacuum ultraviolet (VUV) spectral ranges. Radiation wavelength is dependent on the gas composing the lamp. For the two gases considered in this thesis (kryp-

ton and xenon), emitted wavelengths are in the UV-C region (respectively 148 [31] and 172 nm [32] for the peak maximum) with a Lorentzian photon emission distribution. UV spectrum emission is important for bio-decontamination of water or of surface [33–35]. These excilamps represent useful sources emitting narrow band UV-radiation that initiate oxidation and mineralization of organic substrates contained in water or air contaminants. Also, this kind of lamps are used in the treatment of skin diseases such as psoriasis or vitiligo with the advantage of treating exclusively the affected skin [36]. Krypton and xenon are usually used in mixtures, for example KrCl [37] or XeBr [38] excilamps emitting UV-C, at respectively 222 and 282 nm, wavelength being very efficient for bacteria inactivation in infected water [39].

1.2.3 Plasma propulsion for Spacecraft

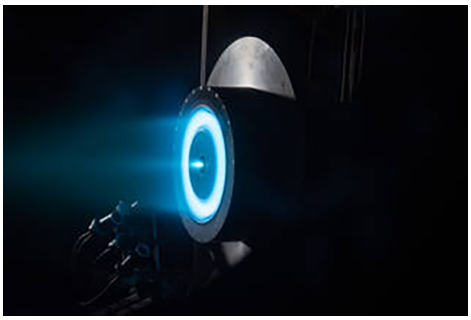

Figure 1.10: Example of spacecraft used in NASA's Asteroid Redirect Mission [40]

Another application of these rare-gases is spacecraft propulsion [41] in satellite repositioning. In fact xenon is used as the usual propellant gas due to the small value of its first ionization potential, high mass, absence of toxicity and favorable thermodynamic properties. Even if the power delivered by this kind of propulsion is low compared to chemical propulsion, its main advantage consists of a perfectly controlled power delivery, sun power electricity and gain of mass. Effectively, only the carrier gas is needed and replaces fuel and oxidant. Actually, the delivered power by this plasma reactor is only used in space, i.e. satellite repositioning, but it is insufficient for shuttle takeoff [42–44]. Moreover,

Propellant	Mass (amu)	E_i (eV)	Melting/ Boiling point (K)	Cost
He	4.0	24.6	1 / 4	Low
Ar	39.9	15.8	84 / 87	Low
Kr	83.9	14.0	116 / 120	High
Xe	131.3	12.1	161 / 164	Very High

Table 1.1: Partial table of reference [44] with E_i referring to the first ionization energy

krypton can be used as an alternative to xenon in spacecraft propulsion because of its lower cost than xenon. Some research have been reported by Liu *et al.* [45], where they concluded that an efficient use of krypton in Hall-thruster requires modifications of the currently used thruster designed for xenon.

1.3 Thesis objectives

Ion transport coefficients, reaction rate constants and cross-sections have been calculated in the past for lighter rare-gas such as helium, neon and argon [21–25] but there are not enough data for ions in krypton and xenon. So the aim of this thesis work is to complete with basic data on ionic atom - neutral atom and ionic dimer - neutral atom collisions occurring in homogeneous krypton or xenon gas.

To produce accurate macro plasma modeling, lot of mesoscopic data are required. Diffusion coefficient, mobility, drift velocity, dissociation constant of ions and electrons in the carrier gas are crucial. However, all this data for ions are very sparse in the literature. They mostly cover narrow range of reduced electric field. The aim of this thesis is therefore to obtain, using different interaction potentials, cross-sections that allow calculations of transport coefficients and rate constants, that will be compared to the existing experimental one, in order to complete the missing data in the literature.

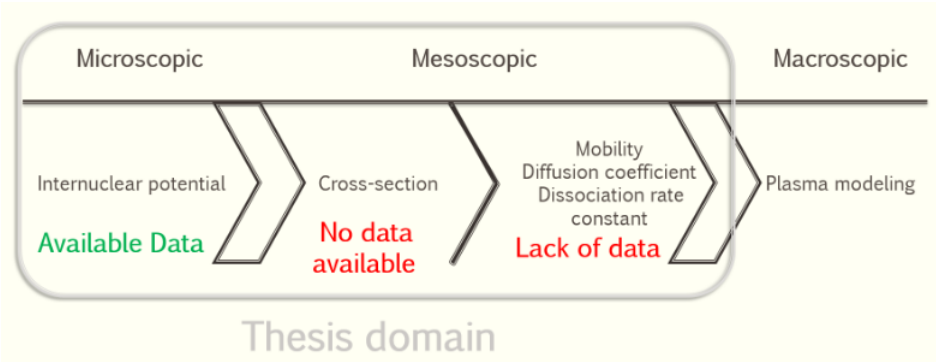

Figure 1.11: Organigram of thesis domain

1.3.1 Plasma modeling

Experiments on plasma are generally expensive and complex to set up. Modeling allows to test a lot of configurations, in shorter time, without performing any experiment provided that the model and their input data are validated. Figure 1.12 displays an experimental plasma jet set up along with the ion density in this plasma jet is calculated from plasma modeling.

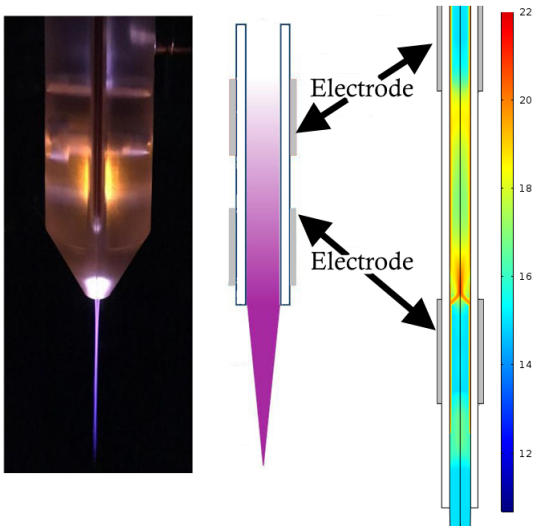

Figure 1.12: Example of plasma modeling of a plasma jet

The model used in PRHE group is based on fluid model of order 1, using:

- a system of equations of density conservations of charged species of the plasma,
- the drift-diffusion approximation to take into account the momentum transfer,
- Poisson's equation in order to obtain the electric field of space charges,
- local field hypothesis assuming an energetic equilibrium of the species charged with the electric field.

For example, if only two species are considered (electron "e" and positive ions "p") with two main reactions (ionization "i" and recombination "r") the equations of this fluid model are written as:

$$\frac{\partial n_e}{\partial t} + \vec{\nabla}.n_e\vec{v}_e(E/N) = k_i(E/N)Nn_e - k_r(E/N)n_pn_e \tag{1.3}$$

$$\frac{\partial n_p}{\partial t} + \vec{\nabla}.n_p\vec{v}_p(E/N) = k_i(E/N)Nn_e - k_r(E/N)n_pn_e \tag{1.4}$$

$$n_e\vec{v}_e(E/N) = K_{0,e}(E/N)\vec{E} - D_e(E/N)\vec{\nabla}n_e \tag{1.5}$$

$$n_p\vec{v}_p(E/N) = K_{0,p}(E/N)\vec{E} - D_p(E/N)\vec{\nabla}n_p \tag{1.6}$$

$$\vec{E} = -\vec{\nabla}V \tag{1.7}$$

$$\Delta V = -\frac{\rho}{\varepsilon_0} = \frac{q_en_e + q_pn_p}{\varepsilon_0} \tag{1.8}$$

where n, $\vec{v}$, K_0, D and k are respectively the density, the average speed, the reduced mobility, the diffusion coefficient and the reaction constant ($_i$ for ionization and $_r$ for recombination reactions). Equations 1.3 and 1.4 are respectively the density conservation equations of electrons and ions while equations 1.5 and 1.6 are

the drift-diffusion approximations used to obtain the transport flux of equations 1.3 and 1.4. Equations 1.7 and 1.8 allow us to calculate the value of the electric field $\vec{E}$ and last equation depicts the electric potential (V) depending of the space charge (ρ) and the vacuum permittivity (ε_0). Approximation of equilibrium with the field allows us to pretabulate all values (reduced mobility, diffusion coefficient, and reaction rate) as function of the reduced electric field (E/N) (N being the gas density).

All these equations can be discretized in 1, 2 and 3 dimensions and are strongly coupled. Indeed, modifying one term in any equation will lead to modifications in all the other equations. For example, a variation of ions or electron concentration lead to variation of potential, that will modify electric field $\vec{E}$ (trough respectively equations 1.7 and 1.8). This variation will be redirected towards transport equations (1.5 and 1.6) and density conservation equations (1.3 and 1.4) since transport coefficients and rate constants (K_0, D, k_r, k_i) are strongly dependent on reduced electric field (E/N).

Chapter 2

Theory

In this chapter we will explain all the theory needed to understand further chapters. First a definition of internuclear potential between two atoms will be introduced. An extension to three atoms using *Diatomics In Molecules (DIM)* methodology will also be evoked. Then definition of cross-sections and three methods used here to obtain them will be described. Finally a Monte Carlo method used to obtained mesoscopic results, such as transport coefficients, will be explained.

2.1 Interaction potentials

2.1.1 Ion - Atom potential

Potential energy "$V(r)$" is a function depending on the distance (r) between two atoms or molecules. By convention, at long distance, energy between particles is set equal to 0. The potential energy is a combination of two parts, one repulsive at short distances (V_{short}) and another attractive at long distances (V_{long}).

Generally, long distance potential, V_{long}, is composed of multiple parts.

$$V_{\text{long}} = V_{\text{pol}} + V_{\text{dis}} + V_{\text{ele}}, \tag{2.1}$$

where V_{pol} is a potential due to the interaction of the ionic charges with multipole moments induced by the ion in the neutral atom. In addition, the electronic dis-

persion produces mutually coupled correlated electric multipole moments. The interaction between these multipoles gives V_{dis}. V_{ele} is the electrostatic potential due to interactions between the charge of an ion and the permanent multipole moment of the neutral [46]. For rare-gas ions (Rg_n^+) this last interaction is equal to 0. Effectively, no permanent moments are present for Rg atoms.

Pauli exclusion principle gives the repulsive part of the potential at short distances where electronic clouds overlap between two atoms,

$$V_{\mathrm{short}} = Ae^{-ar}, \tag{2.2}$$

where A and a are parameters depending on the nature of the two atoms and r is the distance between the atoms. This equation depicts just one of several analytic representation of the repulsive wall (Born-Mayer), there are also others.

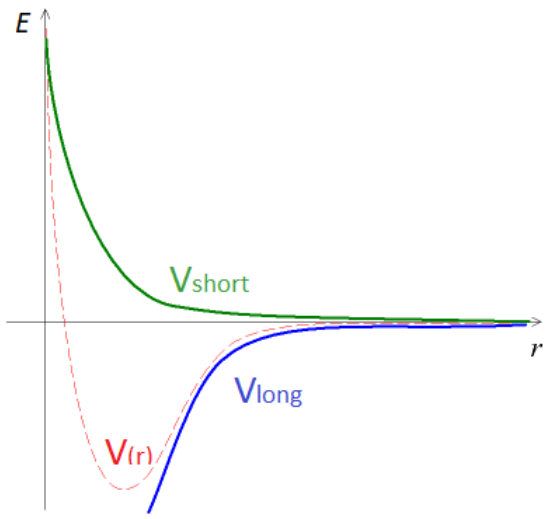

Figure 2.1: Schematic representation of the potential composed of short and long distance contributions.

Potential energy is the sum of this two components ($V(r) = V_{\mathrm{long}} + V_{\mathrm{short}}$) as visible in figure 2.1. However, in some case, V_{long} is damped at short distance using an appropriate damping function. Atomic ion - neutral atom potentials are obtained by the solution of Schrödinger equation. Thanks to Born Oppenheimer approximation, nuclear and electronic motion can be separated. Potentials are

calculated for fixed atoms and therefore nuclear Schrödinger equations can be neglected. Numerical method to resolve Schrödinger equations provide *ab initio* potential energy values.

For rare-gas with p orbitals fully filled as the last ones (like krypton and xenon), multiple interaction potentials can appear depending on the molecular orbitals. Molecular orbitals depend on the way atom orbitals are combined. Combination of two P_Z orbitals leads to a molecular orbital called σ, while P_X and P_y atomic orbitals provide molecular orbitals called π. σ and π denote, namely, the projection of electrons angular momentum on the bond axis. Each of this configuration can be in a *gerade* or *ungerade* state. This terms denote the symmetry of the bond. Effectively, if a rotation of the orbitals about the line joining the two nuclei followed by a rotation of the orbitals on the line perpendicular to the previous rotation leads to a remained sign of the lobes the orbital is be called *gerade* otherwise the orbital will be called *ungerade*. We have 6 different states corresponding to 4 different energies levels (π are degenerate states) as visible in figure 2.2. This hold for spin-orbit free interaction potentials.

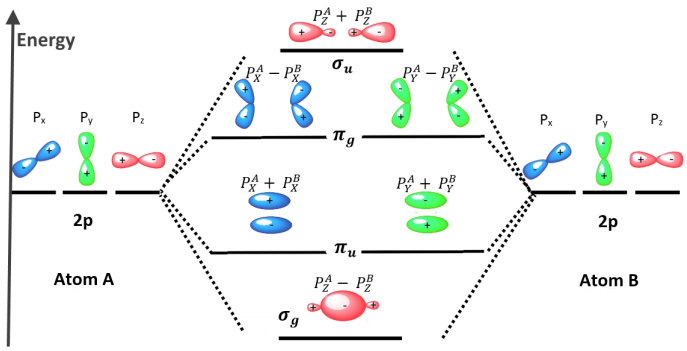

Figure 2.2: Molecular states for a dimer with p orbitals being the highest occupied orbitals in atoms of which the dimer is composed

This 4 different energy levels can be represented with 4 different curves depending on the distance as adiabatic interaction potentials (see section 3.1.1, figure 3.1a for example).

By having a hole on one of this 4 energy levels, representing a missing electron for the ionic atom, the resulting energies will change. σ_g energy state will become

highly repulsive curve Σ_g^+, π_u become repulsive curve Π_u, π_g become mostly repulsive curve Π_g and σ_u energy state will become mostly attractive curve Σ_u^+. Example of this behavior can be seen in figure 3.1a.

Atomic ion - neutral atom potentials used in this thesis are all documented in literature. Sometimes, only *ab initio* values are given and sometimes there is an analytical curve describing the potential. For discrete *ab initio* values, a cubic spline curve was used to obtain potential values for all the distances required.

Orbital movement of electron produces intern magnetic field that can interact with the magnetic moment associated to the spin of the electron. This weak interaction is called Spin-Orbit Coupling (SOC). When SOC is considered, the 4 previously discussed curves are perturbed and the inclusion of the SOC provides 6 different doubly degenerate energy levels. Previous same energy level are now better separated and can be observed separably. Example of such interaction potentials with the SOC included can be seen in section 3.1.1 (figure 3.2a) or in section 3.2.1 (figure 3.15a).

To transform spin free curves to SOC curves, an already known and successfully tested scheme is used. This scheme is known as a Cohen-Schneider scheme [47]. Using this scheme, the $\Omega = 1/2$ potentials are obtained by diagonalizing a 2 by 2 matrix,

$$\begin{pmatrix} V_\Sigma(R) & -\frac{a}{\sqrt{2}} \\ -\frac{a}{\sqrt{2}} & V_\Pi(R) + \frac{a}{2} \end{pmatrix} \tag{2.3}$$

either for u and g symmetry, while the $\Omega = 3/2$ spin-orbit potentials are simply $V_\Pi(R) - a/2$, a being 2/3 of the E($^2P_{3/2}$) - E($^2P_{1/2}$) fine structure splitting in atomic ion.

The lowest excited state of the Kr^+ ion (4s4p^6) lies more than 13 eV above the ground-state (4s^{2}4p^5) [48] and a similar asymptotic separation can be expected between the lowest Kr_2^+ states (asymptotically correlating to 4s^{2}4p^5) and higher excited states. For ionized xenon, the difference between the first excited state (5s5p^6) and ground-state(5s^{2}5p^5) is 11 eV [48]. Separation between Xe_2^+ and Xe^+ is expected to have the same behavior as for krypton. As will be discussed later

	$^2P_{3/2}$	$^2P_{1/2}$
$\Omega = 1/2$	$I(1/2)_u$	$II(1/2)_u$
	$I(1/2)_g$	$II(1/2)_g$
$\Omega = 3/2$	$I(3/2)_g$	
	$I(3/2)_u$	

Table 2.1: Tabulate representation of state and subspace for Rg_2^+ interaction.

(see section 3.1.4), collision energies of Rg^+ with the carrier gas atoms are typically several electronvolts. For example, for Kr^+ it is always below 13 eV for reduced electric field going to 2000 Td. For 3000 Td, at most 1% of collisions will appear beyond this region. For xenon even at 3000 Td (highest reduced electric field used for this thesis) none ion arrived (center-of-mass) energy above 11 eV (see section 3.2.4). As a consequence, only the six lowest electronic states of the Rg^+/Rg collision complex (correlating respectively to $4s^24p^5$ and $5s^25p^5$ Kr^+ and Xe^+ atomic ions) [49] are effectively involved if the SOC is considered, namely, $I(1/2)_{u,g}$, $I(3/2)_{u,g}$, and $II(1/2)_{u,g}$. Concerning ionic dimer - neutral atom collision, in this thesis, only one electronic state, $I(1/2)_u$, will be considered for the dimer interactions. Effectively, the difference between $I(1/2)_u$ and $I(3/2)_g$ being approximatively 1.5 eV, only future calculations will be done in the future to provide cross-section and transport coefficient for this more excited states.

With p orbitals, azimuthal number (l) is equal to 1 and s (spin number) equal to 1/2. The total orbital angular momentum (j) is delimited between $|l - s|$ and $|l + s|$. In the case of rare-gas atomic ions, respectively, 1/2 or 3/2. Using orbital angular momentum, the 6 curves can be distributed in two different section $^2P_{3/2}$ for $j = 3/2$ containing $I(1/2)_{u,g}$ and $I(3/2)_{u,g}$; and $^2P_{1/2}$ for $j = 1/2$ containing $II(1/2)_{u,g}$. Another way to distinguished among these 6 curves is to consider diatomic angular momentum projection subspaces (Ω), in other words the sum of the projection of total orbital momentum on the z axis and the projection of the total spin angular momentum on the z axis. $I(1/2)_{u,g}$ and $II(1/2)_{u,g}$ are represented by subspace corresponding to $\Omega = 1/2$ and $I(3/2)_{u,g}$ by subspace $\Omega = 3/2$ (see Table 2.1).

2.1.2 Dimer - Atom potential

When 3 atoms are involved, total interatomic potentials are calculated using *Diatomics In Molecules* (DIM) methodology [50]. It consists in writing the electronic Hamiltonian as a sum of contribution of diatomic and atomic contributions:

$$\hat{\mathrm{H}} = \sum_{a=1}^{n-1} \sum_{b=a+1}^{n} \hat{\mathrm{H}}_{ab} - (n-2) \sum_{a=1}^{n} \hat{\mathrm{H}}_{a}, \tag{2.4}$$

where n denotes the number of atoms, and then is expanded against an appropriately chosen basis set enabling to construct the resulting matrices exclusively from diatomic and atomic energies. These energies are obtained from independent sources (either experiments or calculations) and it is well known that if highly accurate input energies are used, the DIM approach leads, despite its approximate nature, to a highly accurate estimate of the electronic Hamiltonian matrix.

For singly ionized complexes of rare-gases [49, 51], such basis set consists of a set of valence-bond Slater determinants representing states with the positive charge localized on a specific atom in a specific spin-orbital,

$$\Phi_{kls_z} = |\mathrm{Rg}\cdots\mathrm{Rg}^{+}_{kls_z}\cdots\mathrm{Rg}|, \tag{2.5}$$

where Rg denotes the electronic configuration of a ground-state rare-gas atom and Rg^{+} stands for the electronic configuration of kth atom, $k = 1, \ldots, n$, from which an electron has been removed from spin-orbital specified by angular momentum $l = \mathrm{p}_x, \mathrm{p}_y, \mathrm{p}_z$, and spin projection $s_z = \pm 1/2$. Note that the basis set is approximately orthogonal and diabatic.

The Hamiltonian matrix resulting from an expansion of $\hat{\mathrm{H}}$ against the basis set of equation 2.80 can be built up from four lowest potential energy curves of Rg_2^{+}, corresponding to the electronic ground-state ($^2\Sigma_{\mathrm{u}}^{+}$) and three lowest excited states ($^2\Pi_{\mathrm{g}}$, $^2\Pi_{\mathrm{u}}$, and $^2\Sigma_{\mathrm{g}}^{+}$), and the ground-state potential ($^1\Sigma_{\mathrm{g}}^{+}$) of the neutral dimer, Rg_2. The atomic contributions to the electronic Hamiltonian matrix can be nullified by identifying the zero of the total potential energy to a dissociate state

consisting of $n-1$ neutral atoms and an atomic ion, all of them at infinite separations. Following our study on $\mathrm{Kr}^+/\mathrm{Kr}$ collisions [52] (see also subchapter 3.1, we have used two sets of ionic diatomic potentials in the present thesis, one obtained from *ab initio* calculations [53] (hereafter denoted as "Model A") and the other based on state-of-the-art spectroscopic experiments combined with *ab initio* calculations [54] (Model B). If not stated otherwise, the neutral potential is taken from semiempirical modeling [55], but recent *ab initio* calculations [56, 57] will also be considered to analyze the effect of differences between different neutral potentials in the DIM modeling of the three-particle $\mathrm{Kr}_2^+/\mathrm{Kr}$ collision complex.

For heavy rare-gases, relativistic electronic effects are important. While scalar relativistic contributions are usually taken into account in *ab initio* calculations by using relativistic effective core potentials [58], the leading vector effect, the spin-orbit coupling, has to be included at the DIM level. An approximate method based on a semiempirical *atoms-in-molecule* Model [47] was proposed for the ionic complexes of rare-gases in reference [49]. Despite of the approximations employed, it provides a highly accurate description of the spin-orbit coupling in ionic rare-gas complexes. For example, a thorough comparison of rovibronic spectra calculated for Kr_2^+ with available experiments [53, 54] shows an excellent agreement. The only external input to this method is the value of the fine-structure energy splitting between $^2\mathrm{P}_{1/2}$ and $^2\mathrm{P}_{3/2}$ states of the atomic rare-gas ion. In this work, an accurate experimental value, $\Delta E_{\mathrm{SOC}} = 5370.1\,\mathrm{cm}^{-1}$, reported for Kr^+ in reference [59] has been used.

Note also that the electronic space resulting from the DIM Model used in this thesis is fully sufficient for the present calculation. As discussed in detail in the previous subsection(see also section 2 of reference [52]), going above the electronic states asymptotically correlating to $4s^24p^5$ atomic ion (i.e., above the states considered in the present DIM model) will require excitation energies of about 13 eV and higher [48]. However, as follows from the present calculation (see section 4.2.6), even up to rather high electric fields, the mean $\mathrm{Kr}_2^+/\mathrm{Kr}$ collision energy is well below this excitation limit (e.g., $\bar{\mathrm{E}}_{\mathrm{coll}} \approx 4.5\,\mathrm{eV}$ for $E/N = 1000\,\mathrm{Td}$). Only for

the highest electric fields considered here (E/N = 2000 Td and E/N = 3000 Td), the collision energy ($\bar{\mathrm{E}}_{\mathrm{coll}} \approx 10.7$ eV and $\bar{\mathrm{E}}_{\mathrm{coll}} \approx 16.3$ eV, respectively) may be sufficiently high for the higher electronic states (asymptotically correlating to the 4s4p^6 configuration of the Kr^+ ion) to enter the play.

2.2 Cross-section

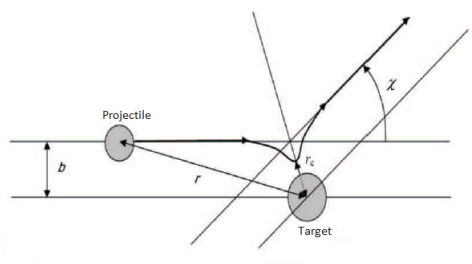

Figure 2.3: Particle scattering under the influence of target potential.

For illustration, let us place two particles in a plane (z, y) where one of these particles is immobile (the target) from initial position [0,0] and the other moves (the projectile) with position [z,y]. Direction of the projectile movement will be parallel to the z axis. Due to the interaction between the projectile and target, the projectile will be scattered by an angle χ, this scattering angle will depend on the impact parameter b (the initial value of projectile y coordinate) and the energy of the system. b can alternatively defined as the closest distance of projectile approach to the target if there was no interaction potential between both particles. In the case of non-zero interaction between the two particles, the closest distance between them achieved during a particular collision will be different, we denote it as r_c in figure 2.3.

From a classical point of view, differential cross-section (σ_{d}) can be seen as the number of impacting particles scattered per unit of time into a solid angle (dΞ, for axially symmetric scattering $\mathrm{d}\Xi = 2\pi \sin\chi \mathrm{d}\chi$) and divided by the flux of particles. There is more than one way for a projectile to be scattered in the solid angle dΞ.

To compare with experimental results, averaging on randomly distributed initial conditions is required. By using a flux of particle (j), $\Delta N(\chi, \chi + \Delta\chi)$ being the number of projectile scattered between χ and $\chi + \Delta\chi$ per second,

$$\sigma_{\mathrm{d}}(\chi) = \frac{1}{j} \lim_{\Delta\chi \to 0} \frac{\Delta N(\chi, \chi + \Delta\chi)}{2\pi \sin\chi \Delta\chi}, \tag{2.6}$$

a corollary equation can be set depending on impact parameters,

$$\mathrm{d}\sigma_{\mathrm{d}}(\chi) = \sum_i \frac{b_i}{\sin\chi(\frac{\mathrm{d}\chi}{\mathrm{d}b})_i}. \tag{2.7}$$

This equation has one important singularity. When χ goes to 0, the differential cross-section tends to infinity. Since calculations have to be done on all impact parameters which contribute to the differential cross-section into angle χ, for low scattering angle approaching zero, b diverges to infinity. Effectively, the farther is the target, the less the interaction potential has effect and the less the projectile is deflected.

Integral and momentum transfer cross-sections (respectively ICS "$\sigma^{(\mathrm{INT})}(\mathrm{E})$" and MTCS "$\sigma^{(\mathrm{MT})}(\mathrm{E})$") are obtained by integration of differential cross-sections over all scattering angles.

$$\sigma^{(\mathrm{INT})}(\mathrm{E}) = \int_0^{\pi} \sigma_{\mathrm{d}}(\mathrm{E}, \chi) 2\pi \sin\chi \mathrm{d}\chi, \tag{2.8}$$

$$\sigma^{(\mathrm{MT})}(\mathrm{E}) = \int_0^{\pi} (1 - \cos\chi) \sigma_{\mathrm{d}}(\mathrm{E}, \chi) 2\pi \sin\chi \mathrm{d}\chi. \tag{2.9}$$

MTCS is preferred to ICS, in this thesis, for multiple reasons. The principal one is that in the hybrid method, only MTCS can be calculated since ICS is infinite due to the non-integrable singularity of σ_{d} for χ approaching zero. The hybrid method, explained later in this chapter (see i.e. section 2.2.3), treats nuclei classically and applies a quantum formalism on electrons and allows us to obtain cross-sections for atom - atom or molecule - atom collisions. MTCS has also the advantage of decreasing the dependence on high impact parameters values for

low scattering angle since the factor $(1-\cos\chi)$ is close to 0 for this case. MTCSs are used in Monte Carlo code to produce accurate results if we assume an isotropic scattering for the deflection angle calculation after every calculation. Momentum transfer approximation is often used to save computational efforts and previous calculation (see reference [22]) demonstrates that it leads to acceptable accuracy calculations.

For atomic ion - neutral atom collisions considered in this thesis, multiple channels are open for the scattering of the particles (see also figure 2.4 for a graphical summary): Elastic, process (1) in figure 2.4,

$$\begin{aligned} \mathrm{Rg}^+(^2P_{3/2}) + \mathrm{Rg} \rightarrow \mathrm{Rg}^+(^2P_{3/2}) + \mathrm{Rg}, \\ \mathrm{Rg}^+(^2P_{1/2}) + \mathrm{Rg} \rightarrow \mathrm{Rg}^+(^2P_{1/2}) + \mathrm{Rg}, \end{aligned} \tag{2.10}$$

Elastic, charge transfer, process (2) in figure 2.4,

$$\begin{aligned} \mathrm{Rg}^+(^2P_{3/2}) + \mathrm{Rg} \rightarrow \mathrm{Rg} + \mathrm{Rg}^+(^2P_{3/2}), \\ \mathrm{Rg}^+(^2P_{1/2}) + \mathrm{Rg} \rightarrow \mathrm{Rg} + \mathrm{Rg}^+(^2P_{1/2}), \end{aligned} \tag{2.11}$$

non-elastic, spin change collisions, either without the charge transfer, process (3) in figure 2.4,

$$\begin{aligned} \mathrm{Rg}^+(^2P_{3/2}) + \mathrm{Rg} \rightarrow \mathrm{Rg}^+(^2P_{1/2}) + \mathrm{Rg}, \\ \mathrm{Rg}^+(^2P_{1/2}) + \mathrm{Rg} \rightarrow \mathrm{Rg}^+(^2P_{3/2}) + \mathrm{Rg}, \end{aligned} \tag{2.12}$$

or with the charge transfer, process (4) in figure 2.4,

$$\begin{aligned} \mathrm{Rg}^+(^2P_{3/2}) + \mathrm{Rg} \rightarrow \mathrm{Rg} + \mathrm{Rg}^+(^2P_{1/2}), \\ \mathrm{Rg}^+(^2P_{1/2}) + \mathrm{Rg} \rightarrow \mathrm{Rg} + \mathrm{Rg}^+(^2P_{3/2}), \end{aligned} \tag{2.13}$$

non elastic, angular momentum change collision, either without the charge transfer, process (5) in figure 2.4,

$$\begin{aligned} \mathrm{Rg}^+(^2P_{3/2}, \Omega = 1/2) + \mathrm{Rg} \rightarrow \mathrm{Rg}^+(^2P_{3/2}, \Omega = 3/2) + \mathrm{Rg}, \\ \mathrm{Rg}^+(^2P_{3/2}, \Omega = 3/2) + \mathrm{Rg} \rightarrow \mathrm{Rg}^+(^2P_{3/2}, \Omega = 1/2) + \mathrm{Rg}, \end{aligned} \tag{2.14}$$

or with the charge transfer, process (6) in figure 2.4,

$$\begin{aligned} \mathrm{Rg}^+(^2P_{3/2}, \Omega = 1/2) + \mathrm{Rg} \rightarrow \mathrm{Rg} + \mathrm{Rg}^+(^2P_{3/2}, \Omega = 3/2), \\ \mathrm{Rg}^+(^2P_{3/2}, \Omega = 3/2) + \mathrm{Rg} \rightarrow \mathrm{Rg} + \mathrm{Rg}^+(^2P_{3/2}, \Omega = 1/2). \end{aligned} \tag{2.15}$$

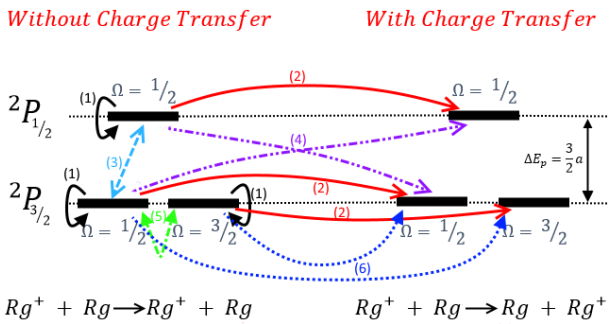

Figure 2.4: Schematic representation of possible transitions in a Rare-gas (Rg) ion during a collision with its neutral parent

Three different methods were used to calculate the differential cross-sections. Explanation of all methods is given in the three next sub-chapters.

Depending on the method used, some channels will not be allowed in the code. Semi-classical method allows only elastic (equation 2.10) and resonant charge transfer (equation 2.11) collisions. Quantum method will allow spin change processes (equations 2.12 and 2.13) but neglects changes in the projection of the total angular momentum along the internuclear axis (equations 2.14 and 2.15). Hybrid method will consider all the processes given in figure 2.4 including angular momentum change collisions (equations 2.14 and 2.15).

For ionic dimer - neutral atom collisions, multiple collisions channels are pos-

sibles, for example in non reactive scattering,

$$\begin{aligned}
&\mathrm{Rg}_2^+(\mathrm{I}(1/2)_\mathrm{u}) + \mathrm{Rg} \rightarrow \mathrm{Rg}_2^+(\mathrm{I}(1/2)_\mathrm{u}) + \mathrm{Rg},\\
&\mathrm{Rg}_2^+(\mathrm{I}(1/2)_\mathrm{u}) + \mathrm{Rg} \rightarrow \mathrm{Rg}_2^+(\mathrm{I}(3/2)_\mathrm{g}) + \mathrm{Rg},\\
&\mathrm{Rg}_2^+(\mathrm{I}(1/2)_\mathrm{u}) + \mathrm{Rg} \rightarrow \mathrm{Rg}_2^+(\mathrm{I}(3/2)_\mathrm{u}) + \mathrm{Rg},\\
&\mathrm{Rg}_2^+(\mathrm{I}(1/2)_\mathrm{u}) + \mathrm{Rg} \rightarrow \mathrm{Rg}_2^+(\mathrm{I}(1/2)_\mathrm{g}) + \mathrm{Rg},\\
&\mathrm{Rg}_2^+(\mathrm{I}(1/2)_\mathrm{u}) + \mathrm{Rg} \rightarrow \mathrm{Rg}_2^+(\mathrm{II}(1/2)_\mathrm{u}) + \mathrm{Rg},\\
&\mathrm{Rg}_2^+(\mathrm{I}(1/2)_\mathrm{u}) + \mathrm{Rg} \rightarrow \mathrm{Rg}_2^+(\mathrm{II}(1/2)_\mathrm{g}) + \mathrm{Rg},
\end{aligned} \tag{2.16}$$

$$\begin{aligned}
&\mathrm{Rg}_2^+(\mathrm{I}(3/2)_\mathrm{g}) + \mathrm{Rg} \rightarrow \mathrm{Rg}_2^+(\mathrm{I}(1/2)_\mathrm{u}) + \mathrm{Rg},\\
&\mathrm{Rg}_2^+(\mathrm{I}(3/2)_\mathrm{g}) + \mathrm{Rg} \rightarrow \mathrm{Rg}_2^+(\mathrm{I}(3/2)_\mathrm{g}) + \mathrm{Rg},\\
&\mathrm{Rg}_2^+(\mathrm{I}(3/2)_\mathrm{g}) + \mathrm{Rg} \rightarrow \mathrm{Rg}_2^+(\mathrm{I}(3/2)_\mathrm{u}) + \mathrm{Rg},\\
&\mathrm{Rg}_2^+(\mathrm{I}(3/2)_\mathrm{g}) + \mathrm{Rg} \rightarrow \mathrm{Rg}_2^+(\mathrm{I}(1/2)_\mathrm{g}) + \mathrm{Rg},\\
&\mathrm{Rg}_2^+(\mathrm{I}(3/2)_\mathrm{g}) + \mathrm{Rg} \rightarrow \mathrm{Rg}_2^+(\mathrm{II}(1/2)_\mathrm{u}) + \mathrm{Rg},\\
&\mathrm{Rg}_2^+(\mathrm{I}(3/2)_\mathrm{g}) + \mathrm{Rg} \rightarrow \mathrm{Rg}_2^+(\mathrm{II}(1/2)_\mathrm{g}) + \mathrm{Rg},
\end{aligned} \tag{2.17}$$

$$\begin{aligned}
&\mathrm{Rg}_2^+(\mathrm{I}(3/2)_\mathrm{u}) + \mathrm{Rg} \rightarrow \mathrm{Rg}_2^+(\mathrm{I}(1/2)_\mathrm{u}) + \mathrm{Rg},\\
&\mathrm{Rg}_2^+(\mathrm{I}(3/2)_\mathrm{u}) + \mathrm{Rg} \rightarrow \mathrm{Rg}_2^+(\mathrm{I}(3/2)_\mathrm{g}) + \mathrm{Rg},\\
&\mathrm{Rg}_2^+(\mathrm{I}(3/2)_\mathrm{u}) + \mathrm{Rg} \rightarrow \mathrm{Rg}_2^+(\mathrm{I}(3/2)_\mathrm{u}) + \mathrm{Rg},\\
&\mathrm{Rg}_2^+(\mathrm{I}(3/2)_\mathrm{u}) + \mathrm{Rg} \rightarrow \mathrm{Rg}_2^+(\mathrm{I}(1/2)_\mathrm{g}) + \mathrm{Rg},\\
&\mathrm{Rg}_2^+(\mathrm{I}(3/2)_\mathrm{u}) + \mathrm{Rg} \rightarrow \mathrm{Rg}_2^+(\mathrm{II}(1/2)_\mathrm{u}) + \mathrm{Rg},\\
&\mathrm{Rg}_2^+(\mathrm{I}(3/2)_\mathrm{u}) + \mathrm{Rg} \rightarrow \mathrm{Rg}_2^+(\mathrm{II}(1/2)_\mathrm{g}) + \mathrm{Rg},
\end{aligned} \tag{2.18}$$

$$\begin{aligned}
&\mathrm{Rg}_2^+(\mathrm{I}(1/2)_\mathrm{g}) + \mathrm{Rg} \rightarrow \mathrm{Rg}_2^+(\mathrm{I}(1/2)_\mathrm{u}) + \mathrm{Rg},\\
&\mathrm{Rg}_2^+(\mathrm{I}(1/2)_\mathrm{g}) + \mathrm{Rg} \rightarrow \mathrm{Rg}_2^+(\mathrm{I}(3/2)_\mathrm{g}) + \mathrm{Rg},\\
&\mathrm{Rg}_2^+(\mathrm{I}(1/2)_\mathrm{g}) + \mathrm{Rg} \rightarrow \mathrm{Rg}_2^+(\mathrm{I}(3/2)_\mathrm{u}) + \mathrm{Rg},\\
&\mathrm{Rg}_2^+(\mathrm{I}(1/2)_\mathrm{g}) + \mathrm{Rg} \rightarrow \mathrm{Rg}_2^+(\mathrm{I}(1/2)_\mathrm{g}) + \mathrm{Rg},\\
&\mathrm{Rg}_2^+(\mathrm{I}(1/2)_\mathrm{g}) + \mathrm{Rg} \rightarrow \mathrm{Rg}_2^+(\mathrm{II}(1/2)_\mathrm{u}) + \mathrm{Rg},\\
&\mathrm{Rg}_2^+(\mathrm{I}(1/2)_\mathrm{g}) + \mathrm{Rg} \rightarrow \mathrm{Rg}_2^+(\mathrm{II}(1/2)_\mathrm{g}) + \mathrm{Rg},
\end{aligned} \tag{2.19}$$

$$\begin{aligned}
&\mathrm{Rg}_2^+(\mathrm{II}(1/2)_\mathrm{u}) + \mathrm{Rg} \rightarrow \mathrm{Rg}_2^+(\mathrm{I}(1/2)_\mathrm{u}) + \mathrm{Rg},\\
&\mathrm{Rg}_2^+(\mathrm{II}(1/2)_\mathrm{u}) + \mathrm{Rg} \rightarrow \mathrm{Rg}_2^+(\mathrm{I}(3/2)_\mathrm{g}) + \mathrm{Rg},\\
&\mathrm{Rg}_2^+(\mathrm{II}(1/2)_\mathrm{u}) + \mathrm{Rg} \rightarrow \mathrm{Rg}_2^+(\mathrm{I}(3/2)_\mathrm{u}) + \mathrm{Rg},\\
&\mathrm{Rg}_2^+(\mathrm{II}(1/2)_\mathrm{u}) + \mathrm{Rg} \rightarrow \mathrm{Rg}_2^+(\mathrm{I}(1/2)_\mathrm{g}) + \mathrm{Rg},\\
&\mathrm{Rg}_2^+(\mathrm{II}(1/2)_\mathrm{u}) + \mathrm{Rg} \rightarrow \mathrm{Rg}_2^+(\mathrm{II}(1/2)_\mathrm{u}) + \mathrm{Rg},\\
&\mathrm{Rg}_2^+(\mathrm{II}(1/2)_\mathrm{u}) + \mathrm{Rg} \rightarrow \mathrm{Rg}_2^+(\mathrm{II}(1/2)_\mathrm{g}) + \mathrm{Rg},
\end{aligned} \tag{2.20}$$

$$\begin{aligned}
&\mathrm{Rg}_2^+(\mathrm{II}(1/2)_\mathrm{g}) + \mathrm{Rg} \rightarrow \mathrm{Rg}_2^+(\mathrm{I}(1/2)_\mathrm{u}) + \mathrm{Rg},\\
&\mathrm{Rg}_2^+(\mathrm{II}(1/2)_\mathrm{g}) + \mathrm{Rg} \rightarrow \mathrm{Rg}_2^+(\mathrm{I}(3/2)_\mathrm{g}) + \mathrm{Rg},\\
&\mathrm{Rg}_2^+(\mathrm{II}(1/2)_\mathrm{g}) + \mathrm{Rg} \rightarrow \mathrm{Rg}_2^+(\mathrm{I}(3/2)_\mathrm{u}) + \mathrm{Rg},\\
&\mathrm{Rg}_2^+(\mathrm{II}(1/2)_\mathrm{g}) + \mathrm{Rg} \rightarrow \mathrm{Rg}_2^+(\mathrm{I}(1/2)_\mathrm{g}) + \mathrm{Rg},\\
&\mathrm{Rg}_2^+(\mathrm{II}(1/2)_\mathrm{g}) + \mathrm{Rg} \rightarrow \mathrm{Rg}_2^+(\mathrm{II}(1/2)_\mathrm{u}) + \mathrm{Rg},\\
&\mathrm{Rg}_2^+(\mathrm{II}(1/2)_\mathrm{g}) + \mathrm{Rg} \rightarrow \mathrm{Rg}_2^+(\mathrm{II}(1/2)_\mathrm{g}) + \mathrm{Rg}.
\end{aligned} \tag{2.21}$$

Or for dissociation of the ionic dimer, here only a general example is shown, different initial electronic states can be inserted,

$$\begin{aligned}
&\mathrm{Rg}_2^+ + \mathrm{Rg} \rightarrow \mathrm{Rg}^+ + \mathrm{Rg} + \mathrm{Rg},\\
&\mathrm{Rg}_2^+ + \mathrm{Rg} \rightarrow \mathrm{Rg}^+ + \mathrm{Rg}_2.
\end{aligned} \tag{2.22}$$

For this thesis only two different channels are considered, where the initial dimer is on the electronically ground-state $\mathrm{I}(1/2)_\mathrm{u}$ and final Rg^+ electronic state is $^2\mathrm{P}_{3/2}$. The first one is the Non-Reactive Scattering (NRS),

$$\mathrm{Rg}_2^+ + \mathrm{Rg} \rightarrow \mathrm{Rg}_2^+ + \mathrm{Rg}, \tag{2.23}$$

the second one is the Collision Induced Dissociation (CID),

$$\mathrm{Rg}_2^+ + \mathrm{Rg} \rightarrow \mathrm{Rg}^+ + \mathrm{Rg} + \mathrm{Rg}. \tag{2.24}$$

It is important to note that charge transfer channel in not distinguished from the non charge transfer channel in the CID process.

2.2.1 Quantum method

This is the most accurate method used in this work. This method requires also the longest calculation time. Another issue with this method is that it is easy to use for atom - atom collisions, while the computational complexity increases for dimer - atom collisions. This is why this method will only be used, as benchmark, for atom - atom collisions in this work.

If non-interacting particles are considered, their relative motion can be represented with a plane wave in quantum mechanics thanks to wave-particle duality. Due to the uncertainty principle valid in quantum physics, a well defined linear momentum, like in this case, induces that the plane wave is totally delocalized in space. The wave function for such an interactionless collision ($\psi_0(\vec{r}, k)$) is usually written as,

$$\psi_0(\vec{r}, \mathrm{E}) = \sqrt{\frac{k\mu}{2\pi h^2}} e^{ik\vec{r}}, \tag{2.25}$$

where k is the wavenumber, E is the energy of the system and μ is the reduced mass of colliding atoms.

$$k = \frac{\mu \nu_r}{\hbar}, \tag{2.26}$$

with ν_r is the velocity. The projectile will move along the z axis, considering the target is localized in the origin [0,0]. With a spherically symmetrized interaction potential, the azimuthal angle (ϕ) will play no role during collisions. After a collision, the projectile will be scattered with a scattering amplitude ($f(\mathrm{E}, \chi)$). At long distances from the collision point, the wave function can be written as

$$\psi(\vec{r}, \mathrm{E}) = \sqrt{\left(\frac{k\mu}{2\pi h^2}\right)} \left\{ e^{ikz} + f(\mathrm{E}, \chi) \frac{e^{ikr}}{r} \right\}. \tag{2.27}$$

By applying the momentum operator $-i\hbar\vec{\nabla}$ on the incident wave we see that it has a momentum magnitude along the z axis of $k\hbar$ and consequently the incident flux of atoms for the plane wave (e^{ikz}) is $\frac{k\hbar}{\mu} * |e^{ikz}|^2 = \frac{k\hbar}{\mu}$. Flux of atoms passing through a small area of $r^2 \sin\chi \mathrm{d}\chi \mathrm{d}\phi$ from the scattered wave $f_{mn}(\varepsilon, \chi)\frac{e^{ik\vec{r}}}{\vec{r}}$ is $\frac{k\hbar}{\mu} \mid f_{mn}(\mathrm{E}, \chi) \mid^2 \sin\chi \mathrm{d}\chi \mathrm{d}\phi$.

Differential cross-section is defined as the flux of scattered atoms through a given solid angle ($\mathrm{d}\Xi = \sin\chi \mathrm{d}\chi \mathrm{d}\phi$) divided by the incident flux. The differential cross-section can be rewritten as

$$\sigma_{\mathrm{d}}(\mathrm{E},\chi)\mathrm{d}\Xi = \frac{\frac{k\hbar}{\mu}\,|f(\mathrm{E},\chi)\,|^2 \sin\chi \mathrm{d}\chi \mathrm{d}\phi}{\frac{k\hbar}{\mu}}. \tag{2.28}$$

After simplifications and having taken into account that the final wavenumber (k_n) can be different from the initial wavenumber (k_m) the differential cross-section can be transformed as,

$$\sigma_{\mathrm{d}}(\mathrm{E},\chi) = \frac{k_n}{k_m}\,|f_{mn}(\mathrm{E},\chi)\,|^2\,. \tag{2.29}$$

For simplification in the rest of the chapter k will be written in place of $\sqrt{k_n k_m}$.

To resolve the scattering wave function we need to use the time independent Schrödinger equation. Let's start with a general form of the Schrödinger equation,

$$\hat{\mathrm{H}}\Psi(\vec{r}_1,\vec{r}_2,\vec{r}_3,...,\vec{r}_{N_e};\vec{r}) = \mathrm{E}\Psi(\vec{r}_1,\vec{r}_2,\vec{r}_3,...,\vec{r}_{N_e};\vec{r}), \tag{2.30}$$

where $\Psi(\vec{r}_1,\vec{r}_2,\vec{r}_3,...,\vec{r}_{N_e};\vec{r})$ is the total wave function, depending on the electrons positions ($\vec{r}_x$) and the nuclear position ($\vec{r}$), and E is the total energy of the system ($\mathrm{E} = \frac{\hbar^2}{2\mu}k^2$). Hamiltonian of the system ($\hat{\mathrm{H}}$) consists of two parts (nuclear and electronic),

$$\hat{\mathrm{H}} = \hat{\mathrm{T}}_{\mathrm{nucl}} + \hat{\mathrm{H}}_{\mathrm{elec}}. \tag{2.31}$$

$\hat{\mathrm{T}}_{\mathrm{nucl}}$ is the kinetic energy related to nuclei, $\hat{\mathrm{H}}_{\mathrm{elec}}$ is the sum of the kinetic energy of the electrons and the Coulomb energy of electrons and nuclei.

By expanding the total wave function of the system, ($\Psi(\vec{r}_1,\vec{r}_2,\vec{r}_3,...,\vec{r}_{N_e};\vec{r})$), and the electronic Hamiltonian in the adiabatic wave functions basis,

$$\hat{\mathrm{H}}_{\mathrm{elec}}\Phi_n(\vec{r}_1,\vec{r}_2,\vec{r}_3,...,\vec{r}_{N_e};\vec{r}) = \epsilon_n(\vec{r})\Phi_n(\vec{r}_1,\vec{r}_2,\vec{r}_3,...,\vec{r}_{N_e};\vec{r}), \tag{2.32}$$

$$\Psi(\vec{r}_1, \vec{r}_2, \vec{r}_3, ..., \vec{r}_{N_e}; \vec{r}) = \sum_{n=1}^{N_b} \psi_n(\vec{r}) \Phi_n(\vec{r}_1, \vec{r}_2, \vec{r}_3, ..., \vec{r}_{N_e}; \vec{r}), \tag{2.33}$$

where ϵ_n are the eigenvalues of the electronic Hamiltonian and $\psi_n(\vec{r})$ is a function depending only on the nuclear positions. By knowing that wave functions $\phi_n(\vec{r}_1, \vec{r}_2, \vec{r}_3, ..., \vec{r}_{N_e}; \vec{r})$ are orthonormal, inserting equations 2.31 - 2.33 into equation 2.30, multiplying by $\psi_{n'}$ and by integrating on the different $\vec{r}_i$ associated to the electrons, we obtain, using bra-ket notation,

$$\left\langle \Phi_n \middle| \hat{\mathrm{T}}_{\mathrm{nucl}} \middle| \sum_{n'} \psi_{n'}(\vec{r}) \Phi_{n'} \right\rangle + \epsilon_n(\vec{r}) \psi_n(\vec{r}) = \mathrm{E} \psi_n(\vec{r}), \tag{2.34}$$

where bra-kets denote, as usual, integration over electronic coordinates. This can be reduced, after a development on N_b equations with N_b unknowns, by neglecting the couplings. This approximation supposes that the system is fully described with one potential energy curve (surface). ϵ_n will be thus replaced by a unique potential $V(\vec{r})$.

$$-\frac{\hbar^2}{2\mu} \nabla^2 \psi(\vec{r}) + V(\vec{r}) \psi(\vec{r}) = \mathrm{E} \psi(\vec{r}), \tag{2.35}$$

This equation only depends on nuclear positions and not on electronic positions and by expressing the Laplacien operator (∇^2) of equation 2.35 in spherical polar coordinates,

$$-\frac{\hbar^2}{2\mu} \left\{ \frac{1}{r^2} \frac{\partial}{\partial r} \left(r^2 \frac{\partial \psi(\vec{r})}{\partial r} \right) + \frac{1}{r^2} \left[\frac{1}{\sin \chi} \frac{\partial}{\partial \chi} \left(\sin \chi \frac{\partial \psi(\vec{r})}{\partial \chi} \right) + \frac{1}{\sin^2 \chi} \frac{\partial^2 \psi(\vec{r})}{\partial \phi} \right] \right\} + V(\vec{r}) \psi(\vec{r}) = \mathrm{E} \psi(\vec{r}). \tag{2.36}$$

By multiplying this equation by r^2, the Hamiltonian operator becomes a sum of angular and radial parts. The angular part is then represented by eigenfunctions of the orbital angular momentum operator,

$$-\hbar^2 \left[\frac{1}{\sin \chi} \frac{\partial}{\partial \chi} \left(\sin \chi \frac{\partial}{\partial \chi} \right) + \frac{1}{\sin^2 \chi} \frac{\partial^2}{\partial \phi} \right] \mathrm{Y}_{lm}(\chi, \phi) = l(l+1) \hbar^2 \mathrm{Y}_{lm}(\chi, \phi), \tag{2.37}$$

where $\mathrm{Y}_{lm}(\chi, \phi)$ are the spherical harmonics. If extra factor $(1/r)$ is introduced in

the radial wave function,

$$\psi_{lm}(\vec{r}) = \frac{1}{r} g(r) \mathrm{Y}_{lm}(\chi, \phi), \tag{2.38}$$

we obtain by substituting equation 2.38 in equation 2.36,

$$\frac{\hbar^2}{2\mu}\left[-\frac{\mathrm{d}^2}{\mathrm{d}r^2} + \frac{l(l+1)}{r^2}\right] g(r) + V(r)g(r) = \mathrm{E}g(r), \tag{2.39}$$

or alternatively

$$-\frac{\hbar^2}{2\mu}\frac{\mathrm{d}^2}{\mathrm{d}r^2} g(r) + \left[V(r) + \frac{\hbar^2}{2\mu}\frac{l(l+1)}{r^2}\right] g(r) = \mathrm{E}g(r). \tag{2.40}$$

where the term in the bracket is called the effective potential(V_{eff}). At long distances ($r \to \infty$), V_{eff} tends to 0 and equation 2.39 has an asymptotic solution,

$$g(r) = A\frac{i^{l+1}e^{-i\delta_l}}{2}\left\{e^{ikr} + (-1)^{l+1}e^{-i(kr+2\delta_l)}\right\}, \tag{2.41}$$

where $k = \frac{\sqrt{2\mu \mathrm{E}}}{\hbar}$ and δ_l is the phase shift representing the difference in phase compared to the solution obtained in the absence of potential.

Equation 2.39 has two linearly independent solutions called spherical Riccati-Bessel functions ($\hat{j}_l(kr)$ and $\hat{n}_l(kr)$) at large distance when V is negligible with respect to the centrifugal force potential,

$$\begin{aligned} \hat{j}_l(kr) &= krj_l(kr) \to \sin\left(kr - \tfrac{l\pi}{2}\right), \\ \hat{n}_l(kr) &= krn_l(kr) \to -\cos\left(kr - \tfrac{l\pi}{2}\right). \end{aligned} \tag{2.42}$$

If the impacting plane wave spreading in the positive direction of z axis is expanded against regular spherical Bessel functions,

$$e^{ikx} = \sum_{l=0}^{\infty}(2l+1)i^l j_l(kr)P_l(\cos\chi), \tag{2.43}$$

where $P_l(\cos\chi)$ are the Legendre Polynomials, one obtains by using equation 2.42

and equation 2.43 in equation 2.27,

$$\psi(\vec{r},\mathrm{E}) = \sqrt{\frac{k\mu}{2\pi h^2}}\left\{\sum_{l=0}^{\infty}(2l+1)\left(\frac{1}{kr}\right)\frac{(-1)^{l+1}}{2i}\left[e^{-ikr}+(-1)^{-(l+1)}e^{ikr}\right]P_l(\cos\chi)+f(\chi)\frac{e^{ikr}}{r}\right\}. \tag{2.44}$$

Expanding the scattering amplitude in terms of Legendre polynomials,

$$f(\chi) = \sum_{l=0}^{\infty} f_l P_l(\cos\chi), \tag{2.45}$$

and inserting this expansion in equation 2.44 leads to,

$$\psi(\vec{r},\mathrm{E}) = \sqrt{\frac{k\mu}{2\pi h^2}}\frac{1}{2ikr}\left\{\sum_{l=0}^{\infty}\left[(2l+1)(-1)^{l+1}e^{-ikr}+((2l+1)+2ikf_l)e^{ikr}\right]P_l(\cos\chi)\right\}. \tag{2.46}$$

Since the incoming and outgoing radial waves must have equal amplitudes because of the particle numbers conservation laws, comparing equation 2.41 and equation 2.46

$$(-1)^{-(l+1)}e^{i(2\delta_l)} = \frac{(2l+1)+2ikf_l}{(2l+1)(-1)^{l+1}}, \tag{2.47}$$

allows us to calculate f_l and, by inserting it to equation 2.45, to write

$$f(\chi) = \frac{1}{2ik}\sum_l (2l+1)(e^{i2\delta_l}-1)\mathrm{P}_l(\cos\chi). \tag{2.48}$$

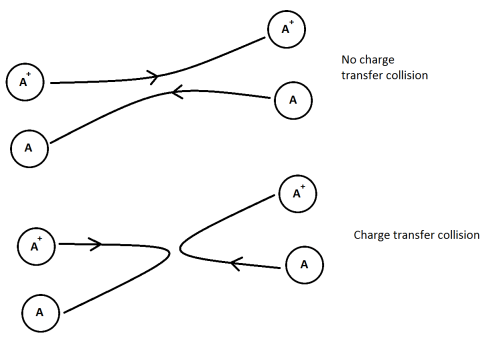

Figure 2.5: Schematic representation of the possibility to have a charge transfer during a collision.

For identical particles, interchange can appear and has to be taken into account. In this case, the position vector changes its sign. As a consequence a symmetrized wave function must be used for identical particles. However, since symmetrized function is dependent on the fermionic or bosonic behavior of the nuclei, S_n parameter (nuclear spin) will be used,

$$\psi_{sym}(\vec{r}, \mathrm{E}) = \frac{1}{\sqrt{2}}[\psi(\vec{r}, \mathrm{E}) + (-1)^{2S_n+1}\psi(-\vec{r}, \mathrm{E})], \tag{2.49}$$

where the $1/\sqrt{2}$ factor is included to preserve the normalization of the symmetrized wave function. With consideration that a collision with No Charge Transfer (NCT) with a scattering angle χ is not distinguishable from a collision with Charge Transfer (CT) with scattering angle of $\pi - \chi$, we can consider only elastic cases with π and $\pi - \chi$ scattering angles. One gets at long distances

$$\psi(\vec{r}, \mathrm{E}) = \frac{1}{\sqrt{2}}\sqrt{\frac{k\mu}{2\pi h^2}}\left\{\left[e^{ikx} + (-1)^{2S_n+1}e^{-ikx}\right] + [f(\chi) + f(\pi - \chi)]\frac{e^{ikr}}{r}\right\}. \tag{2.50}$$

Like in equation 2.45, the CT scattering amplitude can be expressed as

$$f(\pi - \chi) = \sum_l f_l \mathrm{P}_l(\cos(\pi - \chi)) = \sum_l (-1)^{2S_n+1}(-1)^l f_l \mathrm{P}_l(-\cos(\chi)), \tag{2.51}$$

which further leads to

$$f(\chi) + f(\pi - \chi) = \frac{1}{2ik}\sum_{l=0,2,4,\ldots}(2l+1)(e^{i2\delta_l} - 1)\mathrm{P}_l(\cos\chi), \tag{2.52}$$

for bosonic case and

$$f(\chi) - f(\pi - \chi) = \frac{1}{2ik}\sum_{l=1,3,5,\ldots}(2l+1)(e^{i2\delta_l} - 1)\mathrm{P}_l(\cos\chi), \tag{2.53}$$

for fermionic case. For bosonic case, if both elastic and inelastic collisions are

considered, T and S matrices will be used to simplify notation,

$$\begin{aligned} S^l &= e^{2i\delta_l}, \\ T^l &= 1 - S^l. \end{aligned} \tag{2.54}$$

equation 2.52 will thus be transformed to

$$f(\chi) + f(\pi - \chi) = -\frac{1}{2ik} \sum_{l=0,2,4,\ldots} (2l+1) T^l P_l(\cos\chi), \tag{2.55}$$

or, if we write the full formula, after taking into account different initial and final wave vectors,

$$f_{mn}(\chi) + f_{mn}(\pi - \chi) = -\frac{1}{2ik_m {k_n}^{1/2}} \sum_{l=0,2,4,\ldots} (2l+1) T^l_{mn} \mathrm{P}_l(\cos\chi), \tag{2.56}$$

If fermionic case was considered, equation 2.56 is

$$f_{mn}(\chi) - f_{mn}(\pi - \chi) = -\frac{1}{2ik_m {k_n}^{1/2}} \sum_{l=1,3,5,\ldots} (2l+1) T^l_{mn} \mathrm{P}_l(\cos\chi), \tag{2.57}$$

A simplification in the code was done by considering angular momentum transfer as improbable. Therefore we use the fact that transitions between $\Omega = 1/2$ and $\Omega = 3/2$ states are not allowed. Calculation are thus split in two independent groups depending on the value of Ω. This allows us to block-diagonalize the transition matrix to a 4 by 4 matrix for the $\Omega = 1/2$ subspace and a 2 by 2 matrix for the $\Omega = 3/2$ subspace.

Transition matrix elements are then obtained by

$$\mathrm{T}^l_{y,mn}(E) = U^t_{SO_y} [U^t_{AD_y} T^l_x(\mathrm{E}) U_{AD_y}] U_{SO_y}, \tag{2.58}$$

where y represents $\Omega = 1/2$ or $\Omega = 3/2$. To increase readability, let's denote T^l_x the transition matrix in the adiabatic base with respect to electrostatic interactions. U_{AD} is the matrix to transform a matrix from an adiabatic to a diabatic base. U_{SO} is the matrix to transform a matrix from an adiabatic to a diabatic base related to

the spin-orbit.

$$\mathrm{U}_{\mathrm{AD}_{\Omega_{1/2}}} = \begin{pmatrix} \sqrt{1/2} & 0 & -\sqrt{1/2} & 0 \\ 0 & \sqrt{1/2} & 0 & -\sqrt{1/2} \\ \sqrt{1/2} & 0 & \sqrt{1/2} & 0 \\ 0 & \sqrt{1/2} & 0 & \sqrt{1/2} \end{pmatrix}, \tag{2.59}$$

$$\mathrm{U}_{\mathrm{SO}_{\Omega_{1/2}}} = \begin{pmatrix} \sqrt{2/3} & \sqrt{1/3} & 0 & 0 \\ \sqrt{1/3} & -\sqrt{2/3} & 0 & 0 \\ 0 & 0 & \sqrt{2/3} & \sqrt{1/3} \\ 0 & 0 & \sqrt{1/3} & -\sqrt{2/3} \end{pmatrix}, \tag{2.60}$$

$$\mathrm{U}_{\mathrm{AD}_{\Omega_{3/2}}} = \begin{pmatrix} \sqrt{1/2} & -\sqrt{1/2} \\ \sqrt{1/2} & \sqrt{1/2} \end{pmatrix}, \tag{2.61}$$

and

$$\mathrm{U}_{\mathrm{SO}_{\Omega_{3/2}}} = \begin{pmatrix} 1 & 0 \\ 0 & 1 \end{pmatrix}. \tag{2.62}$$

To obtain the transition matrix, equation 2.40,

$$\frac{\mathrm{d}^2 g(r)}{\mathrm{d}r^2} = -\frac{2\mu}{\hbar^2}[\mathrm{E} - V_{\mathrm{eff}}(r)]g(r), \tag{2.63}$$

where V_{eff} is the effective potential, $V_{\mathrm{eff}} = V(r) + \frac{\hbar^2 l(l+1)}{2\mu r^2}$, is to be solved numerically. For further simplification lets denote $W_i = \frac{-2\mu}{\hbar^2}[\mathrm{E} - V_{\mathrm{eff}}(r_i)]$ and $g_i = g(r_i)$ where r_i equidistantly spaced points with a step of O going from r_0 to r_n. Equation 2.63 becomes thus,

$$\frac{\mathrm{d}^2 g(r_i)}{\mathrm{d}r^2} = W_i g(r_i), \tag{2.64}$$

Using a Taylor expansion of g around r_i,

$$g_{i+1} = g_i + O g_i^{(1)} + \frac{O^2}{2} g_i^{(2)} + \frac{O^3}{6} g_i^{(3)} + \frac{O^4}{24} g_i^{(4)} + \ldots, \tag{2.65}$$

where $g_i^{(x)}$ is the x-th derivation of the wave function g at r_i. We get, after adding

the series for g_{i+1} and g_{i-1},

$$g_{i+1} + g_{i-1} = 2g_i + O^2 g_i^{(2)} + \frac{O^4}{12} g_i^{(4)} + C(O^6). \tag{2.66}$$

We can now extract the value of the second derivative (used in equation 2.64),

$$g_i^{(2)} = \frac{g_{(i+1)} + g_{(i-1)} - 2g_i}{O^2} - \frac{O^2}{12} g_i^{(4)} + C(O^4). \tag{2.67}$$

To evaluate the 4th derivative term, equation 2.64 is multiplied by a factor $1 + \frac{O^2}{12}\frac{\partial^2}{\partial r^2}$. After simple algebra, this lead to

$$g_i^{(2)} - W_i g_i + \frac{O^2}{12} g_i^{(4)} - \frac{O^2}{12}\frac{\mathrm{d}^2}{\mathrm{d}r^2}[W_i g_i] = 0, \tag{2.68}$$

and, after replacing of $(g_i^{(2)} + O^2 g_i^{(4)}/12)$ by an expression following from equation 2.67, to

$$g_{(i+1)} + g_{(i-1)} - 2g_i O^2 W_i g_i - \frac{O^4}{12}\frac{\mathrm{d}^2}{\mathrm{d}r^2}[W_i g_i] + C(O^6) = 0. \tag{2.69}$$

Evaluation of $\frac{\mathrm{d}^2}{\mathrm{d}r^2}[W_i g_i]$ by using a finite difference formula provides us

$$\frac{\mathrm{d}^2}{\mathrm{d}r^2}[W_i g_i] = \frac{W_{(i+1)} g_{(i+1)} + W_{(i-1)} g_{(i-1)} - 2W_i g_i}{O^2}, \tag{2.70}$$

which finally leads to

$$g_{(i+1)} = \frac{\left(2 - \frac{5}{6}O^2 W_i\right) g_i - \left(1 - \frac{1}{12}O^2 W_{(i-1)}\right) g_{(i-1)}}{1 + \frac{1}{12}O^2 W_{(i+1)}}. \tag{2.71}$$

To obtain the wave function $g(r)$ and, in the same time, the phase shift, we need to know the two boundary values g_0 and g_n. g_0 approaches 0 since the wave function vanishes as r goes to 0 due to the forbidden region. Only g_n has to be chosen. Arbitrarily chosen value of g_n will change the norm of the wave function, $g(r)$, but not the phase shift, because the latter depends on W_i and thus on the interaction potential.

To avoid calculation up to impracticably large values of l, calculations were

stopped once a properly chosen parameter of convergence was reached. The parameter is the value of the norm of the T matrix. After a few tests, its optimal value (for coherent results and good time consuming policy) was set at $1\text{x}10^{-4}$. Calculations were thus stopped if the norm of the T matrix was below this value for two consecutive angular momentum numbers. This led to for example, to 4880 angular momentum values for $\mathrm{E_{coll}}$ = 1 eV (of center-of-mass collision kinetic energy) to almost 115000 angular momentum value for $\mathrm{E_{coll}}$ = 100 eV. All of the formalism used can be found in [60–62]

2.2.2 Semi-classical method

In the semi-classical method, it is important to mention that for equation 2.56 k_m has to be equal to k_n otherwise this give zero results because only elastic collisions are treated and allowed by this method. Compared to the quantum method, this means that the overall calculation can be split in three parts (I(1/2), I(3/2), and II(1/2)). Each one, based on the quantum method with two channels considered (u and g).

The semi-classical method is an approximate method where the phase shift of scattered wave (see equation 2.41) is calculated using the Jeffreys-Wentzel-Kramers-Brillouin (JWKB) approximation for each interaction energy potential curve

$$\delta_l^{\mathrm{E}} \approx \delta(\mathrm{E}, b) = k \int_{r_c}^{\infty} \left[1 - \left(\frac{b}{r}\right)^2 - \frac{V(r)}{\mathrm{E}} \right]^{1/2} \mathrm{d}r - k \int_{b}^{\infty} \left[1 - \left(\frac{b}{r}\right)^2 \right] \mathrm{d}r, \tag{2.72}$$

where l is the angular momentum quantum number, b = (l +1/2)/k, r_c is the distance of closest approach between both nuclei calculated for a given potential curve, r is the distance between atomic ion and atomic neutral and $V(r)$ is the potential energy. The distance of the closest approach is obtained by taking the largest positive value of r for which the bracket in the first integral on the r.h.s. of equation 2.72 is equal to zero.

Using this approximation allows us to save a lot of computational time because we don't need to use, i.e., the costly Numerov algorithm (like in quantum method) to obtain the phase shift. Scattering amplitude can then be calculated through independent calculations, like in the quantum method, by using equation 2.48 with the transition matrix

$$\mathrm{T}^{\mathrm{l}} = \begin{pmatrix} -2\mathrm{i}e^{i\delta_l^{\mathrm{E,u}}} \sin\delta_l^{\mathrm{E,u}} & 0 \\ 0 & -2\mathrm{i}e^{i\delta_l^{\mathrm{E,g}}} \sin\delta_l^{\mathrm{E,g}} \end{pmatrix}. \tag{2.73}$$

As mentioned in reference [63], the scattering amplitude can thus be calculated independently for g and u symmetry,

$$f^{\mathrm{x}}(\mathrm{E},\chi) = \frac{1}{2ik}\sum_l (2l+1)\left(\mathrm{e}^{2\mathrm{i}\delta_{\mathrm{l}}^{\mathrm{E,x}}} - 1\right)\mathrm{P}_l(\cos\chi), \tag{2.74}$$

where $x = g$ or $x = u$. Once phase shifts and scattering amplitudes (u and g) are obtained using equations 2.72 and 2.74, respectively, they are used depending on the collision type (distinguishable atoms, elastic scattering, charge transfer calculation), to obtain differential cross-sections. The cross-sections are calculated for pairs of *gerade* and *ungerade* potentials and symmetrized properly. As discussed in detail in reference [63], the differential cross-sections can be expressed, for a particular *gerade-ungerade* pair, as:

$$\sigma_{\mathrm{d}}(\mathrm{E},\chi) = \frac{1}{4}\left|f^{\mathrm{g}}(\mathrm{E},\chi) + f^{\mathrm{u}}(\mathrm{E},\chi)\right|^2, \tag{2.75}$$

for elastic scattering (without charge transfer) of two distinguishable nuclei,

$$\sigma_{\mathrm{d}}(\mathrm{E},\chi) = \frac{1}{4}\left|f^{\mathrm{g}}(\mathrm{E},\pi-\chi) - f^{\mathrm{u}}(\mathrm{E},\pi-\chi)\right|^2, \tag{2.76}$$

for (non-resonant) charge-transfer scattering of two distinguishable nuclei, and

$$\begin{aligned}\sigma_{\mathrm{d}}(\mathrm{E},\chi) = {} & \tfrac{X}{4}\left|f^{\mathrm{g}}(\mathrm{E},\chi) + f^{\mathrm{u}}(\mathrm{E},\chi) + f^{\mathrm{g}}(\mathrm{E},\pi-\chi) - f^{\mathrm{u}}(\mathrm{E},\pi-\chi)\right|^2 \\ & + \tfrac{1-X}{4}\left|f^{\mathrm{g}}(\mathrm{E},\chi) + f^{\mathrm{u}}(\mathrm{E},\chi) - f^{\mathrm{g}}(\mathrm{E},\pi-\chi) + f^{\mathrm{u}}(\mathrm{E},\pi-\chi)\right|^2,\end{aligned} \tag{2.77}$$

for the scattering of two identical nuclei (including resonant charge transfer). Parameter X in the last equation depends on the spin (S) of the two identical nuclei, $X = (S+1)/(2S+1)$ for isotopes with integral spin and $X = S/(2S+1)$ for the isotope with half-integral spin.

Transitions between different pairs $u-g$ states are neglected because their frequency is very small and they are thus often neglected in literature, especially for heavy atoms. Moreover, they are calculated in the quantum method and their negligibility will be verified in chapter 3. The same convergence tests, to stop the calculation, were done as for quantum method.

2.2.3 Hybrid method

The hybrid method uses a different approach. Firstly, the Born-Oppenheimer approximation (electronic cloud immediately follows nuclei moves) is considered. Atomic nuclei are, in addition, treated classically by integrating Newton's equations of motion. The hybrid method combines thus a classical treatment of heavy atomic nuclei and a full quantum treatment of light electrons. For the latter, all the relevant electronic states as well as transitions between them should be considered. The primary output of the hybrid method consists of bunches of classical trajectories from which scattering data like differential, integral, and momentum transfer cross-sections of relevant collision processes are calculated using standard tools of the classical scattering theory. The main task of the hybrid method, when dealing with a scattering problem, is thus a calculation of sufficiently large bunches of trajectories started from appropriately sampled initial conditions (which should realistically represent conditions of typical experimental setups). As a consequence, two basic ingredients are needed: a sufficiently accurate and computationally cheap dynamical method for propagating collision trajectories and a realistic scheme for sampling the initial conditions of the collision system.

The methodology employed in this work has already been used and tested in previous calculations for helium [21], neon [23] and argon [25, 64].

In most of the present calculations (atom-ion two-particle collisions), Ehrenfest's, mean-field scheme [65, 66] is used to evolve the collision complex in time. Hereafter, the method will be denoted by acronym MF (Mean-Field). Within the MF scheme, classical equations of motions are solved for atomic nuclei,

$$\dot{q}_j = \frac{p_j}{m_j}, \quad \dot{p}_j = \langle\Psi| - \frac{\partial \hat{\mathrm{H}}_{\mathrm{elec}}}{\partial q_j}|\Psi\rangle, \tag{2.78}$$

moving under the action of averaged forces exerted on them by electrons which are, on the other hand, treated quantum mechanically with the time depending Schrödinger equation,

$$i\hbar\frac{\partial\Psi}{\partial t} = \hat{\mathrm{H}}_{\mathrm{elec}}\Psi. \tag{2.79}$$

Here, m_α, q_α and p_α are nuclear masses, coordinates and momenta, respectively, $\hat{\mathrm{H}}_{\mathrm{elec}}$ is the electronic Hamiltonian, Ψ represents the time dependent electronic wave function, and brackets in equation 2.78 are used to indicate integration over electronic coordinates. The lower index, j, is used to distinguish between nuclear degrees of freedom and they range, for an N-particle system between $j = 1$ and $j = 3N$, where N is the number of particles in the collision system (in this work, $j = 1, \ldots, 6$ for atom-ion collisions and $j = 1, \ldots, 9$ atom-diatom collisions).

The electronic Hamiltonian has been represented by a 12×12 (for Rg_2^+) and 18×18 (for Rg_3^+) matrix using an (approximately) diabatic basis set of electronic wave functions,

$$\Phi_{1ls_z} = |\mathrm{Rg}^+_{Kls_z}\mathrm{Rg}| \text{ and } \Phi_{2ls_z} = |\mathrm{Rg}\,\mathrm{Rg}^+_{Kls_z}|, \tag{2.80}$$

where, Φ_{Kls_z} ($K = 1, 2$) corresponds to the Rg_2^+ complex with the positive charge localized in the ls_z spin-orbital ($l = \mathrm{p}_x, \mathrm{p}_y, \mathrm{p}_z$ and $s_z = \pm 1/2$) of atom K. Computationally cheap, but still sufficiently accurate representation of the Hamiltonian is needed for a realistic and practicable dynamical calculation. For this, a methodology based on the *Diatomics In Molecules* (DIM) approach [50] as described in references [49, 51] has been used. The spin-orbit coupling , which cannot be neglected

for heavy "krypton and xenon" has been included using the *atoms-in-molecules* approach [47] following the scheme proposed in reference [49].

Time depending electronic wave function, can be expressed as a sum of (approximately orthogonal and diabatic) valence bond wave functions.

$$|\psi(t)\rangle = \sum_{\alpha} a_{\alpha}|\Phi_{\alpha}(q_i(t))\rangle. \tag{2.81}$$

For ionic systems of rare-gases, small greeks letters indices $\alpha = [K, p_m, s_z]$ with $K = 1, ..., N$, $m = x, y, z$ and $s_z = \pm 1/2$. Electronic Hamiltonian can also be expressed in an expanded form,

$$H = \sum_{\beta,\gamma} H'_{\beta,\gamma}|\Phi_{\beta}\rangle\langle\Phi_{\gamma}|, \tag{2.82}$$

where $H'_{\beta,\gamma} = S_{\beta,\kappa}\langle\Phi_{\kappa}|H_{\text{elec}}\Phi_{\lambda}\rangle S_{\lambda,\gamma}$ and $S_{\alpha,\beta} = \langle\Phi_{\alpha}|\Phi_{\beta}\rangle$ are the overlaps matrix elements. Since wave functions are (approximately) orthogonal and normalized, $S_{\alpha,\beta} \approx \delta_{\alpha,\beta}$. Insertion of this expansions in equation 2.78 enables to determine nuclear trajectories by solving

$$\dot{p}_j = -\sum_{\alpha,\beta} a^{\star}_{\alpha} a_{\beta} \frac{\partial H_{\alpha,\beta}}{\partial q_j} \tag{2.83}$$

Note that simplifications have been done in equation 2.83, by assuming that nonadiabatic coupling coefficients ($\langle\Phi_{\alpha}|\partial\Phi_{\beta}/\partial q_j\rangle$) and overlaps ($S_{\alpha,\beta}$) are equal to 0. However, as was shown previously [49, 51], the valence bond wave used here obey these assumptions with a sufficient accuracy.

As confirmed in previous publications [49] and papers on ionic potentials [53, 54, 67], this intrinsically approximate solution leads to a highly accurate description of the electronic structure of Rg_2^+ (as well as larger complexes) including heavy krypton and xenon. It is noteworthy that the approach adopted in hybrid calculations is very appropriate for dynamical studies since the electronic Hamiltonian can easily be converted to a small Hermitian matrix if the valence-bond basis set of equation 2.80 is introduced [49]. Most importantly, the basis

of equation 2.80 is approximately diabatic, which further simplifies dynamical calculations. It should be also emphasized that the resulting approach provides, despite its approximate nature, a very accurate description of the interactions in ionic rare-gas complexes if accurate diatomic potentials and an accurate value of the spin-orbit coupling constant are used as independent inputs. As already mentioned in section 2.1, high-level potentials of references [67, 68] respectively for Kr_2^+ and Xe_2^+ , but also potential for Kr_2[57] and Xe_2[69] and accurate experimental estimates of the spin-orbit coupling constant available in reference [59] (for Kr or Xe) have been used in the present work.

Another issue which is worth to be mentioned here is the well known fact that the mean-field approach may lead to mixing of adiabatic electronic states and, as a consequence, to unphysical nuclear trajectories if it is combined with the classical treatment of nuclear degrees of freedom. For an ionic rare-gas complex, this usually leads to the production of partially charged fragments after the complex disintegrates. In the case of the Rg^+ ion colliding with a Rg atom, the collision may proceed as follows,

$$Rg^+ + Rg \rightarrow Rg^{q+} + Rg^{(1-q)+}, \tag{2.84}$$

where $0 < q < 1$. This does not represent a serious problem, however, since the electronic states of the Rg^+/Rg complex are basically degenerate at large interatomic separations and the dissociation dynamics is thus not considerably influenced by the distribution of the positive charge between the two colliding atoms. In addition, correct cross-sections can easily be obtained in this case if the partial charge, q, is treated as quantum probability. That means that the process given by equation 2.84 is treated as $Rg^+ + Rg \rightarrow Rg^+ + Rg$ with weight q and as $Rg^+ + Rg \rightarrow Rg + Rg^+$ with weight $(1 - q)$.

It is well known that the mean-field approach may lead to non-physical trajectories resulting from a non-physical mixing of adiabatic electronic states in the electronic wave function (ψ). In the specific case of ionic complexes of rare-gases, it means that fragments carrying fractional charges may be produced which,

eventually, leads to non-physical artifacts if fragments larger than monomers are produced. As shown before [70], this defect is removed if electronic quantum decoherence is included in the mean-field method. A couple of empirical schemes were introduced in reference [70], all consisting of a) periodically proposed quenching of the electronic wave function to a properly selected adiabatic state and b) subsequent adjusting of nuclear velocities so that the total energy of the system (kinetic energy of nuclei plus total electronic energy) is conserved; see reference [70] for details. In addition, the velocity adjustment must be performed, as detailed in reference [21], in a coordinate system in which the simulated system has zero angular and zero linear momentum so that the two parameters are also preserved during the decoherence step. A specific scheme [21], denoted in previous works as MFQ-AMP/SR, has been adopted here. Within this scheme, the Mean-Field method is enhanced via a Quenching algorithm based on the selection of the adiabatic state towards which the current electronic wave function is quenched according to the occupation probabilities of adiabatic states in the current electronic wave function (calculated as squares of its adiabatic AMPlitudes). The subsequent nuclear velocity adjustment is then performed by a simple Scaling (multiplication by a constant) of all velocities in the Rotating (body-fixed) frame. According to previous calculations [21, 23, 25], the period of quenching attempts has been set to $\Delta t_{\mathrm{Q}} = 10\,\mathrm{fs}$.

As discussed in reference [70], these additional electronic quenches approximately model quantum decoherence in Mean-Field calculations and practically remove partial charges from the hybrid method. Like in previous studies, the electronic collapse probability has been calculated from squared moduli of adiabatic amplitudes of the electronic wave function, Ψ, and necessary adjustments of atomic velocities have been performed via a simple multiplicative scaling performed in the collision-complex-fixed frame [21]. Following previously published studies on helium and argon [64], the period of the quenching step has been set to $\Delta t_{\mathrm{Q}} = 10\,\mathrm{fs}$ [21, 23, 25]. In this work, the method including electronic quenches will be denoted as MFQ (Mean-Field with Quenchings). To test this

assumption, additional calculations have been performed in which periodical attempts to collapse current electronic wave function, Ψ, to one of the available adiabatic states have been introduced.

2.2.3.1 Atom - Atom collisions, initial conditions

The initial condition consists for equations 2.78 and 2.79 of the initial positions and velocities (momenta) of colliding nuclei and the initial state of the electronic subsystem. Since the two particle collision can always be restricted to a plane, one of the coordinates (y in this work) and one of the linear momentum components (p_y) can be set to zero. The remaining two coordinates has been set in the $\mathrm{Rg}^+/\mathrm{Rg}$ center-of-mass (CMS) system so that the initial distance of the two atoms measured along the z-axis (collision axis) is equal to 30 Å and so that the impact-parameter has a selected value, b. A series of calculations have been performed with the impact-parameter sampled from b = 0 Å to $b = b_{\mathrm{max}}$ = 30 Å with a step of Δb = 0.1 Å. For krypton, test with b_{max} of 20 Å provide converged results and this b_{max} values was kept to save computational time. Concerning xenon, a b_{max} value of 25 Å was used since it provide also converged results. The initial linear momenta of the two colliding nuclei have been calculated (in the $\mathrm{Rg}^+/\mathrm{Rg}$ CMS system) from predefined collision energy, $\mathrm{E_{coll}}$, and oriented along the collision axis (z-axis).

For ionic atom - neutral atom collisions, the collision complex can be treated, at large distances, as a neutral Rg atom and an Rg^+ ion. The initial electronic state of the complex is thus defined by the initial electronic state of the ion since electronic excitations in the neutral are neglected (see section 3.1.4 and 3.2.4, respectively for $\mathrm{Kr}^+/\mathrm{Kr}$ and $\mathrm{Xe}^+/\mathrm{Xe}$ cases, for confirmation of this assumption). In the experiment, the $^2\mathrm{P}_{3/2}$ and $^2\mathrm{P}_{1/2}$ ions are distinguished from each other and, so, we performed separate calculations for both. Since the $^2\mathrm{P}_{3/2}$ and $^2\mathrm{P}_{1/2}$ states of the Kr^+ ion are degenerate, the initial state of the Kr^+ ion has been, in most of our calculations, represented by a linear combination of the degenerate components. For example, for the $^2\mathrm{P}_{3/2}$ state (J = 3/2) four such components have to be taken

into account corresponding to four different projections of the total electronic angular momentum on the z-axis, $M = \pm 3/2$ and $M = \pm 1/2$. In this way, the $^2\mathrm{P}_{3/2}$ initial state has been set to

$$\Psi_{3/2}\rangle = \sum_{M=-3/2}^{3/2} c_M |J = 3/2, M\rangle, \tag{2.85}$$

where c_M are randomly chosen complex coefficients homogeneously distributed on the surface of the unit complex hypersphere, $\sum_{M=-3/2}^{3/2} |c_M|^2 = 1$. Similarly, the initial electronic state of the $^2\mathrm{P}_{1/2}$ ion has been set to

$$\Psi_{1/2}\rangle = \sum_{M=-1/2}^{1/2} c_M |J = 1/2, M\rangle, \tag{2.86}$$

with isotropically distributed complex random coefficients obeying $|c_{-1/2}|^2 + |c_{+1/2}|^2 = 1$.

To test the validity of the assumption that the coherent mixtures of degenerate components, particularly for the $^2\mathrm{P}_{3/2}$ state (equation 2.85), realistically mimic the experimental conditions, additional calculations have been performed for the $^2\mathrm{P}_{3/2}$ ion discriminating between the $3/2$ and $1/2$ projections. The initial electronic state of the Kr^+ ion has been set in this case either to

$$\Psi_{3/2,3/2}\rangle = c_{-3/2}|J = 3/2, M = -3/2\rangle + c_{+3/2}|J = 3/2, M = +3/2\rangle, \tag{2.87}$$

or to

$$\Psi_{3/2,1/2}\rangle = c_{-1/2}|J = 3/2, M = -1/2\rangle + c_{+1/2}|J = 3/2, M = +1/2\rangle. \tag{2.88}$$

2.2.3.2 Dimer - Atom collision, initial conditions

The initial conditions of equations 2.78 and 2.79 consist of the initial positions and momenta (velocities) of atomic nuclei and the initial electronic state of the Kr_2^+ ion. In the present work, the Kr_2^+ ion is assumed to be, prior to the collision, in its electronic ground-state, so only the way how the nuclear initial con-

ditions have been generated is to be described. The nuclear initial conditions are represented by kinematic initial conditions (initial positions and momenta of the neutral atom and the center-of-mass (CM) of the dimer ion) and internal initial conditions of the colliding dimer (its rotational-vibration state and its orientation in space). All the nuclear degrees of freedom have first been set in a specific space frame schematically depicted in figure 2.6 for krypton case, then a transition to the CM frame of the $\mathrm{Kr}_2^+/\mathrm{Kr}$ collision complex has been performed and, finally, electronic amplitudes of the electronic ground-state of the dimer ion have been calculated in the basis set of equation 2.80 by diagonalizing corresponding electronic Hamiltonian matrix and selecting the eigenvector belonging to the lowest eigenvalue. By doing this, we basically follow the procedure used in previous studies on neon [23] and argon [25].

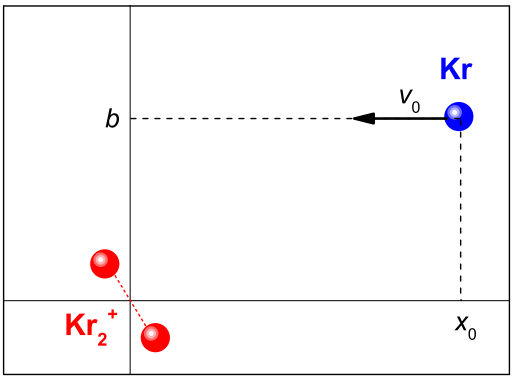

Figure 2.6: Initial conditions for a $\mathrm{Kr}_2^+/\mathrm{Kr}$ collision.

The kinematic initial conditions are schematically shown in figure 2.6. Here, the CM of the dimer ion initially resides at rest in the origin of the selected space frame. The impacting atom starts from initial position $(x_0, b, 0)$ with the initial velocity oriented along the x-axis (collision axis) and calculated from the preset collision energy, $\mathrm{E}_{\mathrm{coll}}$, given in the $\mathrm{Kr}_2^+/\mathrm{Kr}$ center-of-mass system, $v_0 = \sqrt{3E_{\mathrm{coll}}/m}$ (m being the atomic mass). The value of x_0 has been set to $x_0 = 20\,$Åand b has

been taken, step by step, from an interval of $[0, b_{\max}]$, $b_{\max} = 30\,\text{Å}$. The maximum value $b_{\max}$ has been verified to lead to both converged momentum transfer cross-sections of non-reactive (i.e., non-dissociative) $\mathrm{Kr}_2^+/\mathrm{Kr}$ scattering as well as converged Kr_2^+ dissociation cross-section for all the collision energies considered [71]. The impact-parameter b has been sampled with a step of $\Delta b = 0.1\,\text{Å}$, with each value contributing to the calculated differential cross-sections with a weight proportional to b.

The internal initial conditions of the Kr_2^+ ion are given by its rotational-vibrational state [72] and its orientation in space. The rotational-vibrational energies and related wave functions have been calculated by numerically solving the nuclear Schrödinger equation on the electronic ground-state potential energy curve, $\mathrm{I}(1/2)_\mathrm{u}$,

$$-\frac{\hbar^2}{2\mu}\frac{\mathrm{d}^2\chi_{jv}(r)}{\mathrm{d}r^2} + \left[V_{\mathrm{I}(1/2)_\mathrm{u}} + \frac{\hbar^2 j(j+1)}{2\mu r^2}\right]\chi_{jv}(r) = E_{jv}\chi_{jv}(r), \tag{2.89}$$

where j and v are rotational and vibrational quantum numbers, respectively, and $\mu = m/2$ is the effective mass of the Kr_2^+ dimer. A DVR representation of the wave function has been used with a Dirichlet boundary condition imposed, $\chi_{jv}(0) = \chi_{jv}(r_{\max}) = 0$ ($r_{\max} = 30$ a.u.), and with discretization step equal to $\Delta r = 0.02$ a.u. For a particular rotational-vibrational state, the initial distances in the ion dimer have then been sampled from the square of χ_{jv} and the kinetic energy have been calculated from current potential energy and the total rotational-vibrational energy, E_{jv} [73]. Corresponding velocities have then be added to both Kr_2^+ nuclei and oriented anti-parallelly along the dimer bond axis. After the vibrational state of the Kr_2^+ dimer has been set in this way, anti-parallel velocities perpendicular to the dimer bond axis have been added to the dimer nuclei so that the angular momentum corresponding to a specific choice of the rotational quantum number, j, is achieved. Finally, the dimer has been randomly oriented in space. In the present work, we denote a particular rotational-vibrational excitation of the Kr_2^+ dimer by [J=j, ν=v]. For example, [J=0, ν=0] means that the dimer has been prepared, prior to collision, in the rotational-vibrational ground-state with $j = 0$ and $v = 0$.

For each particular choice of the Kr_2^+ rotational-vibrational state (j, v), Kr_2^+/Kr collision energy (E_{coll}), and collision impact-parameter (b), totally 504 trajectories have been integrated for randomly oriented dimers until disintegration, either to $Kr_2^+ + Kr$ or $Kr^+ + Kr + Kr$. A simple distance criterion has been used to detect the particular type of disintegration with the cut-off distance set to 20 Å. This means that about 150 000 trajectories have been used for each collision energy and Kr_2^+ rotational-vibrational excitation to calculate effective collision cross-sections.

2.2.3.3 Numerically integration

For each particular choice of the impact-parameter (b) and collision energy (E_{coll}), totally 504 trajectories have been calculated with randomly chosen electronic states of Kr^+ as described above. The equations of motion have been integrated numerically using a 4th order Runge-Kutta method with minimized discretization error [74]. A semi-analytical algorithm described in reference [75] has been used for the electronic equation of motion, equation 2.79, to avoid needlessly short integration steps otherwise enforced by rapid oscillations emerging in the electronic subsystem. The integration step has been set to $\Delta t = 0.05 - 0.25$ fs, particular value depending on the collision energy (the higher the energy, the shorter the time step). This setting complies with previous calculations on neon [23] and argon [25] and takes into account the larger mass of the krypton or xenon atom.

2.2.4 Inverse method

No experimental measurements of cross-sections are available in the literature for the collisions covered by this thesis. Moreover, experimental mobility measurements reported in the literature do not consider sufficiently large range of reduced electric field and experimental drift coefficients are absent in literature. Therefore, an inverse method was used to obtain pseudo-experimental cross-sections from experimental mobilities. This method was already used in the literature to extrapolate mobility data to electric fields where the mobility drops to zero and is thus difficult to measure [21, 76, 77].

This inverse method is based on using an artificial spherical potential that is iteratively adjusted until calculated mobilities reproduce the experimental ones with a sufficient accuracy. The artificial potential is a spherical potential (V_{core})

$$V_{core}(r) = \frac{n\epsilon_w}{3n-12}\left\{\frac{12}{n}\left(\frac{r_m-a}{r-a}\right)^n - 3\left(\frac{r_m-a}{r-a}\right)^4\right\}, \tag{2.90}$$

where the parameters n, ϵ_w, a and r_m are adjustable. The iterative adjustment of V_{core} parameters proceeds as follows, First cross-sections are obtained from this artificial potential using a simplified semi-classical method (see section 2.2.2) typically equations 2.29, 2.48 and 2.72 are used. Afterward, then mobilities are calculated from these cross-sections. Correlation between experimental and pseudo experimental mobilities are analyzed. Parameters of the artificial potential are changed to improve the agreement between calculated and experimental data and a new set of cross-sections is calculated. Usually, parameters of the V_{core} potential resulting from this iterative procedure are unique. Even if multiple sets of parameters are able to reproduce the mobility plateau at low field, only one of this sets is able to efficiently reproduce the decreasing mobility in the strong field region. From this pseudo experimental cross-sections, new "experimental" mobilities or drift coefficients are obtained for a broader range of the electric field than in the initial reference.

However, for ionic dimer - atom collision, the decreasing mobility region can not be correctly reproduced because inverse method is not able to include collision induced dissociation.

2.3 Ions transport coefficients: Monte Carlo Method

Monte Carlo method is a method based on probabilities and statistics [78]. It is used in multiple field like physics, chemistry, mathematics, technology or finance. A recent common use of this method is the way AI (Artificial Intelligence) calculates the strategy used by a computer to play Go against a human [79]. From

a general point of view, it simulates phenomena with different possibilities by knowing probability of occurrence for each possibility. Random number generation will determine different events at a time. In this thesis, the method is used to simulate the transport of ions in carrier gas under the action of a uniform electric field $\vec{E}$ (conventionally oriented in the z-axis direction). The Monte Carlo method simulates, ion by ion, the motion of a big amount of germinal ions, N_{ion}, on a linear trajectory depending on the intensity and direction of the electric field $\vec{E}$. The electric filed is constant all over the simulation, anode and cathode close space (where the electric field is not constant) are not represented by this method. All these ions will undergo a lot of collisions, elastic and inelastic, against carrier gas particles with a probability depending on the cross-sections. Monte Carlo method will follow each ion separately until its vanishing (dissociation for ionic dimer) or until a spatio-temporal limit is reached (t_{max} or z_{max}). Position ($x_{\text{ion}}(t)$, $y_{\text{ion}}(t)$ and $z_{\text{ion}}(t)$), and velocity of the ion ($v^x_{\text{ion}}(t)$, $v^y_{\text{ion}}(t)$ and $v^z_{\text{ion}}(t)$) are calculated for each ions germ for each time moment during the Monte Carlo calculation. As a result, reduced mobility (K_0), longitudinal (D_L) and transversal (D_T) diffusion coefficients and for dimer dissociation rate constant (k_{diss}) are obtained with this method.

Time occurring between two collisions (t_{flight})is obtained with

$$t_{\text{flight}} = \frac{-log(R_{\text{flight}})}{\nu_{\text{tot}}(t)}, \tag{2.91}$$

where R_{flight} is a random number between 0 and 1, and $\nu_{\text{tot}}(t)$ is the total collision frequency, $\nu_{\text{tot}}(t) = \nu_{\text{ela}} + \nu_{\text{inela}} + \nu_{\text{no}}$, comprising the frequency of elastic, inelastic and none collisions.

$$\nu_{\text{tot}}(t) = N v_r(t) Q_{\text{tot}}. \tag{2.92}$$

Total collision frequency is dependent on the density, the velocity and total cross-section of the gas. The value of $\nu_{\text{tot}}(t)$ for the simulation is calculated on the highest energy achieved. On this energy, none collision are set to 0, and $\nu_{\text{tot}}(t) = \nu_{\text{ela}} + \nu_{\text{inela}}$. This value is kept for the all simulation and since $\nu_{\text{ela}} + \nu_{\text{inela}}$ are decreas-

ing with the decreasing energy and therefore ν_{no} is increasing. None collision was added to have a constant value for the total collision frequency. This total collision frequency is calculated using momentum transfer cross-sections obtained previously. Now that the collision time is known (t_{col}), determination of trajectory and velocity of the ion during its flying time can be obtained from classical mechanics equations,

$$\vec{F} = q\vec{E} = m_{\text{ion}}\frac{\mathrm{d}\vec{v}_{\text{ion}}}{\mathrm{d}t}, \tag{2.93}$$

where $\vec{E}$ is the electric field on z axis, q is the charge of the ion, m_{ion} is the mass of the ion and $\vec{v}_{\text{ion}}$ its velocity. Knowing this we can obtain position and velocity before the collision knowing only values before flying time (t_0). In Cartesian coordinates (x, y, z) we obtain,

$$\begin{aligned} v^x_{\text{ion}}(t_{\text{col}}) &= v^x_{\text{ion}}(t_0), \\ v^y_{\text{ion}}(t_{\text{col}}) &= v^y_{\text{ion}}(t_0), \\ v^z_{\text{ion}}(t_{\text{col}}) &= v^z_{\text{ion}}(t_0) + \tfrac{qE}{m_{\text{ion}}}, \end{aligned} \tag{2.94}$$

and

$$\begin{aligned} x_{\text{ion}}(t_{\text{col}}) &= v^x_{\text{ion}}(t_0)t_{\text{flight}} + x_{\text{ion}}(t_0), \\ y_{\text{ion}}(t_{\text{col}}) &= v^y_{\text{ion}}(t_0)t_{\text{flight}} + y_{\text{ion}}(t_0), \\ z_{\text{ion}}(t_{\text{col}}) &= v^z_{\text{ion}}(t_0)t_{\text{flight}} + z_{\text{ion}}(t_0) + \tfrac{qE}{2m_{\text{ion}}}t^2_{\text{flight}}, \end{aligned} \tag{2.95}$$

where

$$t_{\text{col}} = t_{\text{flight}} + t_0, \tag{2.96}$$

after a collision, t_0 became t_1, then t_2, etc. Limit parameters t_{max} and z_{max} are set so that final values of the Monte Carlo simulation are not influenced by the initial conditions of the ion. Effectively, the Monte Carlo simulation is done on a certain space so that the vicinity influence of the cathode/anode can be neglected. Depending on the collision energy, different collision processes are allowed namely elastic, inelastic and dissociation. Each process has a probability to appear that is equal to its frequency divided by ν_{tot}. The probabilities sum up to unity so that a randomly number drawn between 0 and 1 allows to determine which collision

process appears using a roulette scheme.

After a collision, a new velocity of the ion has to be calculated. Different scenario exist depending on the type of collision. If there is no collision, the velocity remains the same. For an elastic collision, thanks to the conservation of momentum transfer, we can write,

$$m_{\mathrm{ion}}\vec{v}_{\mathrm{ion}} + m_{\mathrm{neu}}\vec{v}_{\mathrm{neu}} = m_{\mathrm{ion}}\vec{v}'_{\mathrm{ion}} + m_{\mathrm{neu}}\vec{v}'_{\mathrm{neu}}, \tag{2.97}$$

where "ion" and "neu" refers respectively to the ion and the neutral considered during the collision. Prime represents values after the collision. Neutral atom velocity is selected randomly from a Maxwellian distribution corresponding to the temperature of the neutral species in the plasma. Using the center-of-masses system (CMS) and relative velocity ($\vec{v}_{\mathrm{r}} = \vec{v}_{\mathrm{ion}} - \vec{v}_{\mathrm{neu}}$) we can write velocity equation as,

$$\begin{aligned}
\vec{v}_{\mathrm{CM}} &= \tfrac{m_{\mathrm{ion}}\vec{v}_{\mathrm{ion}} + m_{\mathrm{c}}\vec{v}_{\mathrm{neu}}}{m_{\mathrm{ion}} + m_{\mathrm{neu}}}, \\
\vec{v}_{\mathrm{ion}} &= \vec{v}_{\mathrm{CM}} + \tfrac{m_{\mathrm{neu}}\vec{v}_{\mathrm{r}}}{m_{\mathrm{ion}} + m_{\mathrm{neu}}}, \\
\vec{v}_{\mathrm{neu}} &= \vec{v}_{\mathrm{CM}} - \tfrac{m_{\mathrm{ion}}\vec{v}_{\mathrm{r}}}{m_{\mathrm{ion}} + m_{\mathrm{neu}}}, \\
\vec{v}'_{\mathrm{ion}} &= \vec{v}_{\mathrm{CM}} + \tfrac{m_{\mathrm{neu}}\vec{v}'_{\mathrm{r}}}{m_{\mathrm{ion}} + m_{\mathrm{neu}}}, \\
\vec{v}'_{\mathrm{neu}} &= \vec{v}_{\mathrm{CM}} - \tfrac{m_{\mathrm{ion}}\vec{v}'_{\mathrm{r}}}{m_{\mathrm{ion}} + m_{\mathrm{neu}}}.
\end{aligned} \tag{2.98}$$

Center-of-mass velocity will remain constant after a collision (easily observable by using equation 2.97 in definition of velocity of the center-of-masses of equation 2.98), furthermore, by conservation of kinetic energy, the modulus of the relative velocity has also to remain constant. The scattering angle after the collision is calculated with,

$$\cos\chi = 1 - 2R_{\chi}, \tag{2.99}$$

where R_{χ} is a random number between 0 and 1. The azimuthal angle is determined as a random value between 0 and 2π. If a charge transfer takes place during the simulated collision, relative velocity will be multiplied by a factor of -1. This variation will not lead to further changes in the next calculations. From all the data collected for all ions during the simulation, positions and velocities will

be used to obtain transport coefficients. Reduced standard mobility $\mathrm{K}_0 N$, longitudinal drift coefficient D_L, transverse drift coefficient D_T, and various reaction rate constants ($k_\mathrm{X} = \langle \nu_\mathrm{X} \rangle / N$ are obtained thanks to,

$$K_0 N = \frac{\langle v_\mathrm{ion}^z \rangle}{E/N} \frac{T_0}{T_\mathrm{gas}} \frac{P_\mathrm{gas}}{P_0}, \tag{2.100}$$

with the following definition of $\langle\ Q\ \rangle$

$$\langle Q \rangle = \frac{1}{n_\mathrm{ion}} \sum_{i=1}^{n_\mathrm{ion}} \frac{1}{n_\mathrm{col}} \sum_{j=1}^{n_\mathrm{col}} Q_{ij}, \tag{2.101}$$

$$D_L = \frac{1}{2} \frac{\mathrm{d}[z(t) - \langle z(t) \rangle]^2}{\mathrm{d}t}, \tag{2.102}$$

$$D_T = \frac{1}{4} \frac{\mathrm{d}[(x(t) - \langle x(t) \rangle)^2 + (y(t) - \langle y(t) \rangle)^2]}{\mathrm{d}t}, \tag{2.103}$$

$$\langle \nu_\mathrm{X} \rangle = \frac{\nu_\mathrm{tot}}{n_\mathrm{ion}} \sum_{i=1}^{n_\mathrm{ion}} \frac{1}{n_\mathrm{X}} \sum_{j=1}^{n_\mathrm{X}} N_{ij}^\mathrm{X}, \tag{2.104}$$

with N_{ij}^X being the number of occurrences of the considered phenomenon (Non Reactive Scattering, dissociation,...) for ion i, N is the density of the gas, T_0 = 273.16 K, T_gas is the temperature of the gas, P_gas is the pressure of the gas, P_0 = 760 Torr, n_ion is the total number of ion germs, n_col is the total number of collisions for ion i, and Q_{ij} is the value of parameter Q for ion i at collision j. This method and code were already used in the past with coherent results (references [21–25])

A simplified scheme of all the interactions treated during the Monte Carlo simulation can be seen in figure 2.7

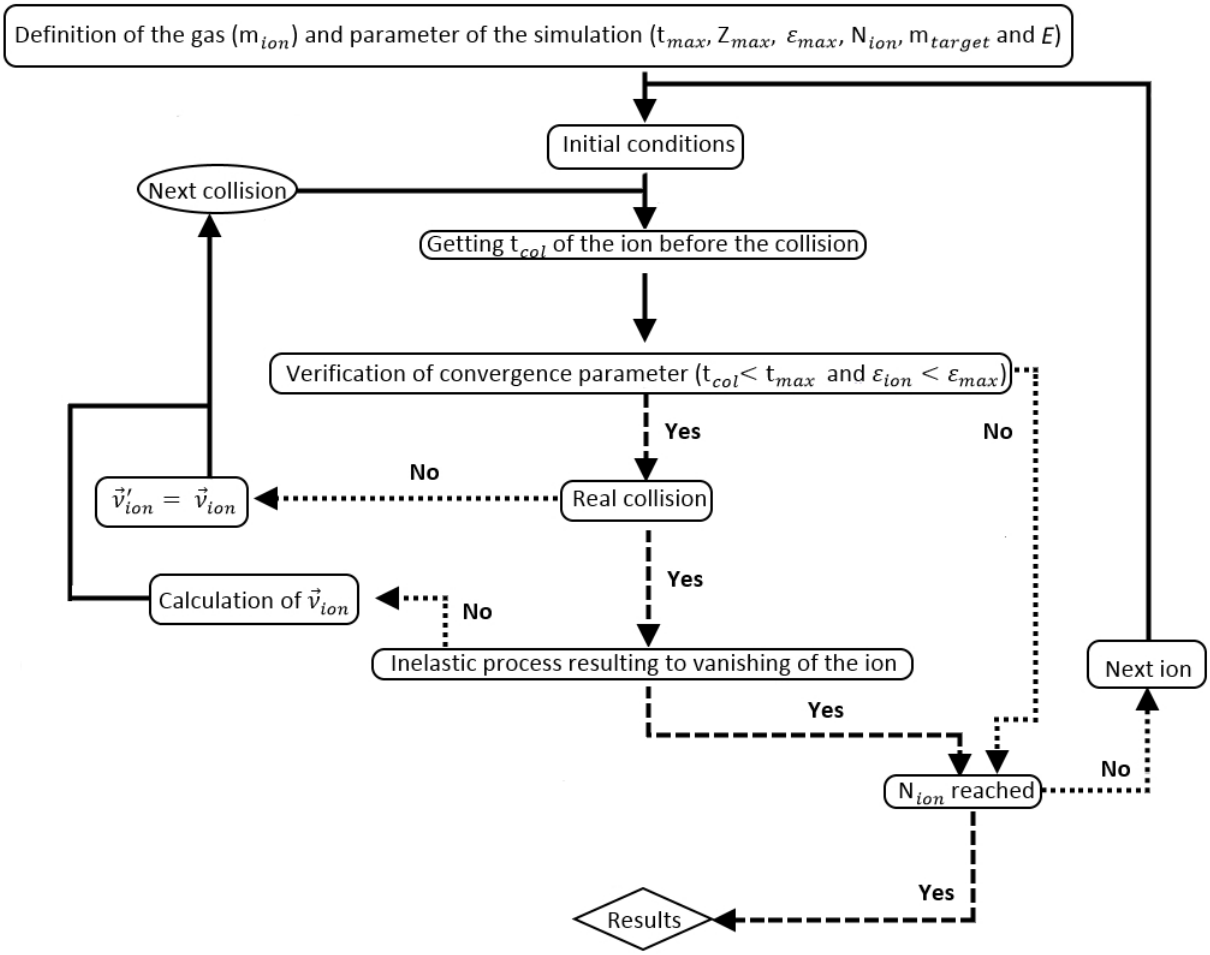

Figure 2.7: Simplified schematic representation of different steps of the Monte Carlo code

Chapter 3

Ionic Atom - Neutral Atom Collisions

This chapter reports on calculations for ionic atom - neutral atom in rare-gas collisions namely $\mathrm{Kr}^+/\mathrm{Kr}$ and $\mathrm{Xe}^+/\mathrm{Xe}$ systems. it will be split in two major sections, each one concerns one type of atom (krypton or xenon). Each section presents a quick description of the used potentials, existing data in literature, comparison of cross-sections obtained via quantum, semi-classical and hybrid and inverse methods. Then mobilities, calculated from these collision cross-sections, are compared to experimental mobilities. Finally, conclusion is given in the last section of this chapter

3.1 Krypton

This work has already been reported in reference [52] and in conference [80]. Neutral krypton in its fundamental state, at ambient temperature and atmospheric pressure, is a noble gas with an electronic configuration of [Ar] $4s^2 3d^{10} 4p^6$. There are 33 known isotopes of krypton with masses ranging from $\simeq 69$ to $\simeq 101$ g.mol^{-1}. In this thesis, only stable isotopes will be taken into account, where stable means here that half-life time is higher than 10^{20} year, there are 6 of them:

Nuclide symbol	Z (number of proton)	N (number of neutron)	isotopic mass	nuclear spin	natural abundance (%)
^{78}Kr	36	42	77.9204	0	0.35
^{80}Kr	36	44	79.9164	0	2.29
^{82}Kr	36	46	81.9135	0	11.59
^{83}Kr	36	47	82.9141	9/2	11.50
^{84}Kr	36	48	83.9115	0	56.99
^{86}Kr	36	50	85.9106	0	17.28

The average atomic mass assigned to krypton is 83.798 g.mol^{-1} [81].

3.1.1 Interaction potentials

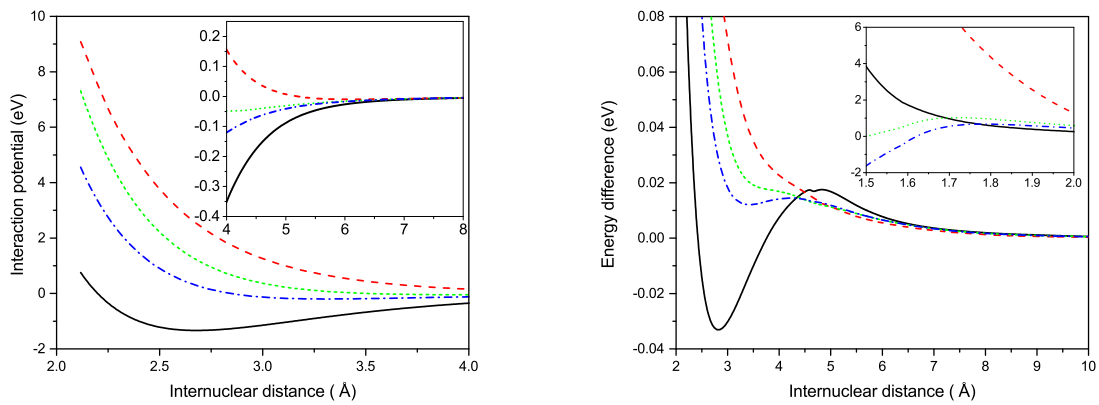

(a) Adiabatic states for Kr^+/Kr internuclear potential (b) Difference between both model used in adiabatic states

Figure 3.1: Figure (a) depicts the interaction potential curves without the inclusion of the Spin-Orbit Coupling interaction for Kr_2^+ using Model A interaction potential [53], figure (b) shows the difference of interaction potential curves when Model B is subtracted from Model A for the four adiabatic states. Full line is Σ_u^+, dashed line is Σ_g^+, dotted line is Π_u and dash dotted line is Π_g

Two *ab initio* potentials for $\mathrm{Kr}^+/\mathrm{Kr}$ interaction were used in this thesis. For both, the 4 spin free potentials ($\Sigma_\mathrm{g}, \Sigma_\mathrm{u}, \Pi_\mathrm{g}, \Pi_\mathrm{u}$) were computed using non-relativistic configuration interaction (CI), *ab initio* approaches involving large basis sets and relativistic core-polarization effective potentials. The Spin-Orbit Coupling is then taken into account following the Cohen-Schneider scheme [47]. The Ω = 1/2 states result from the diagonalization of a simple 2 by 2 matrix:

$$\begin{pmatrix} V_\Sigma(R) & -\frac{a}{\sqrt{2}} \\ -\frac{a}{\sqrt{2}} & V_\Pi(R) + \frac{a}{2} \end{pmatrix} \tag{3.1}$$

either for u and g state symmetries. While for Ω = 3/2 ones, they correspond to the Π potentials, either g or u, shifted by a constant, ($V_\Pi(R)$ -a/2). Asymptotically, Σ and Π potentials are degenerate and the SO coupling splits them in the two atomic fine structure states. The parameter a = 0.4439 eV corresponds to the 2/3 of the atomic splitting. The interaction potential we label A [53] was computed with RHF-RCCSD-T (Restricted Hartree-Fock - spin Restricted Coupled Cluster Single Double - Triplet) level with a large basis set [47] complemented by Gaussians optimized both for equilibrium and separation geometries in order to minimize basis set superposition errors. The potentials we labeled B [54] were computed at the SDCI (Singles and Doubles Configuration Interaction) level [82] extrapolated to full CI (Configuration Interaction) via the Davidson correction [83] using a large ANO (Atomic Natural Orbital) basis set [84, 85]. In potential A, a common set of orbitals, optimized for the neutral dimer, were used for all the states while in potentials B, orbitals have been optimized for each state at RASSCF (Restricted Active Space Self-Consistent Field) level. About the spectroscopic properties, the wells of potentials B are slightly deeper for the lowest state and lightly less deep for the remaining states.

A detailed comparison of potentials Models A and B vibrational spacing were performed for potentials of family I(1/2)$_\mathrm{u}$, I(3/2)$_\mathrm{u}$ and I(3/2)$_\mathrm{g}$. The agreement with experimental measures was quite good as visible in table 1 of reference [53] or table 8 of reference [54]. Only, for the II(1/2)$_\mathrm{g}$ state, for witch experimental

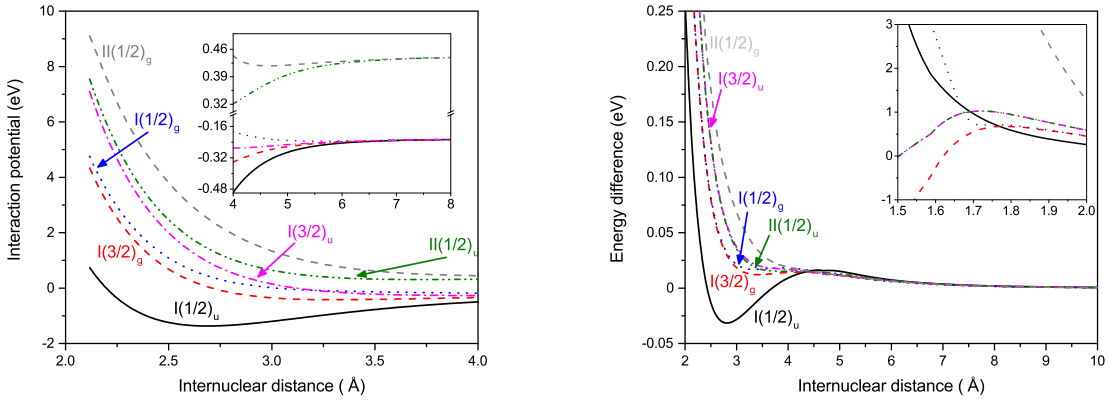

(a) Kr^+/Kr internuclear potential with the inclusion of the Spin-Orbit Coupling

(b) Differences between both models with the inclusion of the Spin-Orbit Coupling

Figure 3.2: Figure (a) depicts the interaction potential curves with the inclusion of the Spin-Orbit Coupling interaction for the six lowest electronic states of Kr_2^+ using Model A interaction potential [53], figure (b) shows the deviation of interaction potential curves of Model B from those of Model A for the six lowest electronic states of Kr_2^+. Full line is $I(1/2)_u$, dashed line is $I(3/2)_g$, short dotted line is $I(1/2)_g$, dash dotted line is $I(3/2)_u$, short dash dotted line is $II(1/2)_u$, short dashed line is $II(1/2)_g$

spectroscopy results [86, 87], show the well depth to be larger than 600 cm^{-1}, much larger than for both potentials A or potentials B. All this indicates that both potentials A and B are rather accurate compared to the established spectroscopy, but may present some deficiencies for the upper states.

Interaction potential calculated from Model A is displayed with and without Spin-Orbit Coupling respectively in figure 3.1a and figure 3.2a. Relative deviations between both interaction potentials is displayed in figure 3.1b without Spin-Orbit Coupling or in figure 3.2b with the Spin-Orbit Coupling. For both figures, Model B interaction potential values were subtracted from corresponding Model A values.

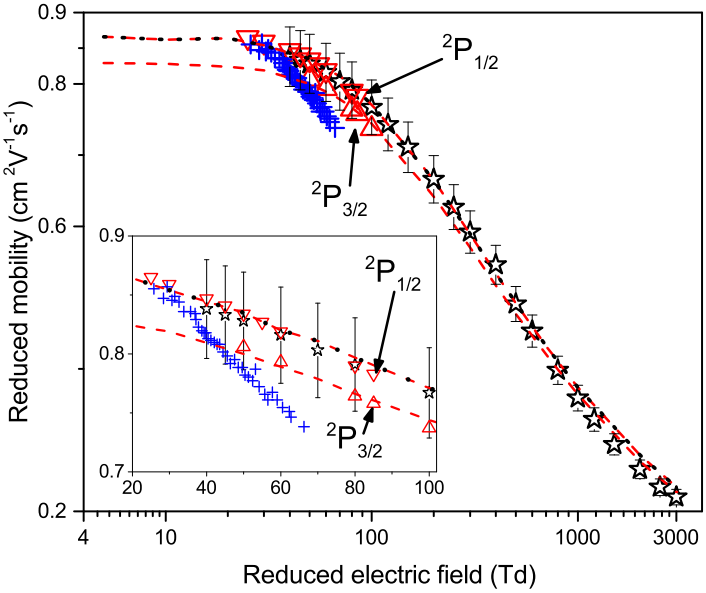

Figure 3.3: Experimental reduced mobility K_0 in $cm^2V^{-1}s^{-1}$ of Kr^+ ions in gaseous Kr. Undistinguished states : + [2]; empty ☆ [88]; $^2P_{1/2}$ state : ▽; $^2P_{3/2}$ state: △ [89]. Dashed curves are mobilities obtained with an inverse method to extrapolate experimental results to lower reduced electric field.

3.1.2 Experimental data reported in literature

Important data for macroscopic modeling of plasmas are mobilities and diffusion coefficients of atomic ions in the carrier gas. Experimental mobilities are available in literature only on a restricted reduced field range and no experimental diffusion coefficients are available in the literature. The present work is devoted to calculations of mobility in a broader reduced electric field range and the calculations will be compared to the measurements available over limited reduced electric field range. Furthermore, theoretical diffusion coefficients will be compared only to the diffusion coefficients obtained via the inverse method since no diffusion measurements are available in literature. Moreover, our calculated diffusion coefficients at low reduced electric field will be compared to the Nernst-

Townsend-Einstein zero field value given by [90]:

$$eD_L/K_0 = eD_T/K_0 = k_B T = 25.3\mathrm{meV}. \tag{3.2}$$

A summary of the most recent experimental data on the Kr^+mobility in Kr is provided in figure 3.3. The measured mobility values can be divided in two groups. Firstly, measurements by Ellis *et al.* [88] and Neves *et al.* [2] do not distinguish between the two fine-structure states ($^2\mathrm{P}_{3/2}$ and $^2\mathrm{P}_{1/2}$) of the Kr^+ ion. Comparing these two sets of values, we can see that the data by Neves *et al.* differ from the data by Ellis *et al.* at intermediate reduced electric fields and show a qualitatively different behavior (a more rapid decrease) with increasing electric field. Since the data reported by Ellis *et al.* represent a critical compilation of experimental results of two independent measurements [91, 92], we consider them as more reliable than Neves *et al.* data. Secondly, more elaborate data sets have been provided by Helm *et al.* [89] (see also [93]) for the $^2\mathrm{P}_{3/2}$ and $^2\mathrm{P}_{1/2}$ states of the Kr^+ ions when they are distinguished. Interestingly, the mobility values reported by Helm lie almost on the Ellis values, the $^2\mathrm{P}_{3/2}$ corresponding mobilities being just slightly below the $^2\mathrm{P}_{1/2}$ ones. This may further justify the more reliability of the not distinguishing fine-structure-state data by Ellis *et al.* then the data reported by Neves *et al.*. Note, however, that the discrimination of the two states of the Kr^+ ion may not have been unbiased in Helm's measurements. More specifically, the differentiation between the two fine-structure states were done, in Helm's work, by fitting curves of Kr^+ drift times containing two peaks. However, since the two peaks are not well separated from each other, a mutual contamination cannot be excluded. $^2\mathrm{P}_{3/2}$ mobilities values are, according to Helm, more accurately extracted from the unresolved double peak than than $^2\mathrm{P}_{1/2}$ ones.

3.1.3 Cross-sections

3.1.3.1 Quantum and semi-classical method

Momentum transfer cross-sections calculated for $\mathrm{Kr}^+/\mathrm{Kr}$ collisions using quantum and semi-classical methods, introduced in section 2.2, are plotted in figure 3.4. We notice from this figure that semi-classical approach, as expected, gives close cross-sections to quantum method for both $^2\mathrm{P}_{1/2}$ and $^2\mathrm{P}_{3/2}$ states. Moreover, relative deviations between semi-classical and quantum cross-sections are shown in figure 3.5a when Model B potential is used. Furthermore, $^2\mathrm{P}_{1/2}$ state cross-sections calculated from model B potential [54] by using quantum or semi-classical methods are in a very good agreement with the one obtained from inverse method based on mobility measurements [88, 89]. On the other hand, for the $^2\mathrm{P}_{3/2}$ state, the momentum transfer cross-section calculated using model B deviates significantly from the cross-sections obtained from the inverse method especially in the low kinetic energy range with a maximum deviation of 25%. Nevertheless, model B provides, for both $^2\mathrm{P}_{1/2}$ and $^2\mathrm{P}_{3/2}$ states, cross-sections in better agreement, with those derived from measurements, than model A.

3.1.3.2 JWKB and isotope hypothesis verification

The use of JWKB approximation is a good hypothesis as shown in figure 3.5a since although the relative deviations between both methods (semi-classical and quantum) seem non negligible (up to 6%), they counterbalance each other. All the calculations presented in this thesis have been performed for an artificial krypton isotope of an averaged mass M_r = $83.798u$. This approximation has been adopted to save computational time since there are 21 different combinations of stable isotopes of krypton which can, in principal, participate in the $\mathrm{Kr}^+/\mathrm{Kr}$ collisions. However, for the cheapest computational method used in this work, the semi-classical method, we have been able to perform calculations on all these possible combinations and to average (using natural abundances of krypton isotopes) the calculated cross-sections. A comparison of these additional data with those

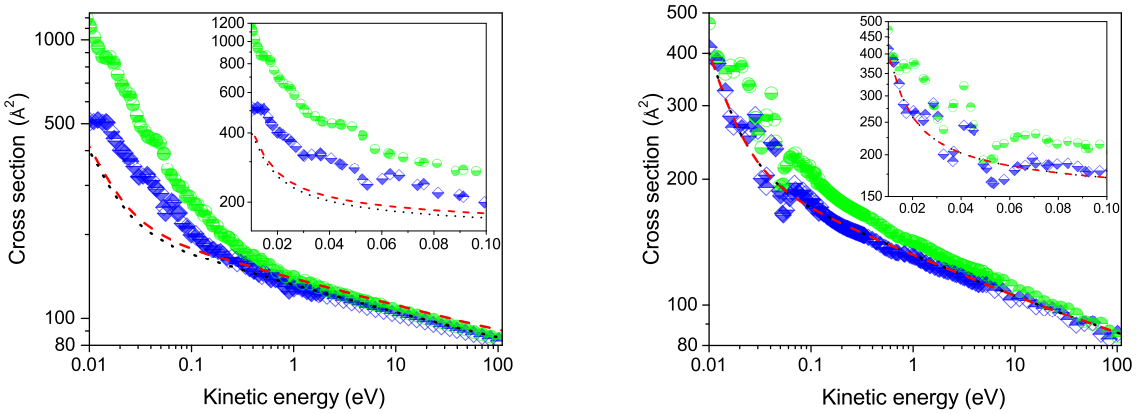

(a) $^2P_{3/2}$ state momentum transfer cross-sections (b) $^2P_{1/2}$ state momentum transfer cross-sections

Figure 3.4: Momentum transfer cross-sections in $Å^2$ of collisions of Kr^+ ions in gaseous Kr obtained from quantum and semi-classical methods. Momentum transfer cross-sections obtained with the inverse method using experimental data without distinction of fine structure states of ions : black dotted curve [88], with distinction of states : red dashed curve [89]. Semi-classical method: upper half fulfilled symbol, quantum method: lower half fulfilled symbol using respectively interaction potentials A and B of references [53]: ◯ and [54]: ⋄.

calculated for the artificial isotope leads to only minor differences as displayed in figure 3.5b. For higher collision energies ($E_{coll} \geq 1.5$ eV), they are completely negligible, in the energy range between $E_{coll} \approx 0.01$ eV and $E_{coll} \approx 1.5$ eV, the differences are always below 2%, and only for energies $E_{coll} \leq 0.006$ eV they grow up to $3 - 5\%$. As a consequence, the use of the artificial "average" isotope of krypton is justified.

The major approximation of the semi-classical method is the non consideration of transition between the two different states. In order to check the validity of such approximation, calculations considering transitions between $^2P_{3/2}$ and $^2P_{1/2}$ states when $\Omega = 1/2$ were performed in the framework of model B by using quantum method.

The evolution of the transition cross-section as a function of kinetic energy is shown in figure 3.6. One can clearly see in this figure that the transition con-

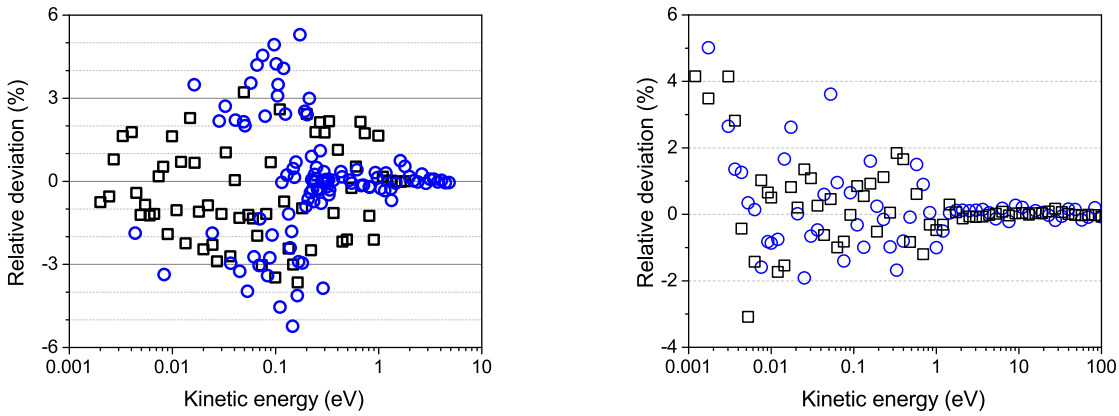

(a) JWKB approximation verification

(b) Isotope hypothesis verification

Figure 3.5: Hypothesis verifications: JWKB approximation (a) and isotropic distribution (b). □ : $^2P_{3/2}$ state; ○ : $^2P_{1/2}$ state.

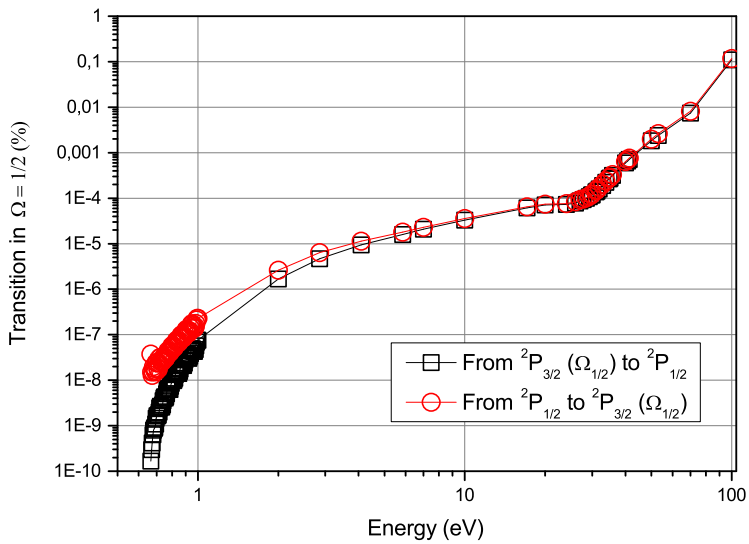

Figure 3.6: Transition cross-section between $\Omega_{1/2}$ states

tributions to the cross-section increase with kinetic energy but they remain low even at very high collision energy (0.1% of E_{coll} = 100 eV), which shows that the

non consideration of transition is semi-classical calculations is therefore a good approximation.

3.1.3.3 Hybrid method

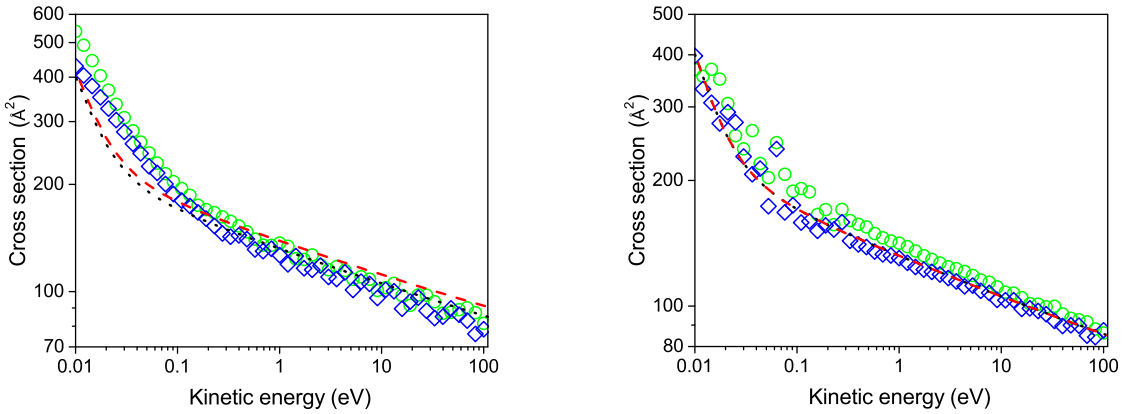

(a) $^2P_{3/2}$ state momentum transfer cross-sections (b) $^2P_{1/2}$ state momentum transfer cross-sections

Figure 3.7: Momentum transfer cross-sections in Å^2 of Kr^+ ions in gaseous Kr for both $^2P_{1/2}$ and $^2P_{3/2}$ states. Cross-sections obtained with the inverse method using experimental data without distinction of states : black dotted curve [88], with distinction of states : red dashed curve [89]. Hybrid method: ◯ and ◇ using respectively interaction potentials of refs [53] and [54].

Momentum transfer cross-sections obtained using hybrid method are shown for $^2P_{1/2}$ and $^2P_{3/2}$ Kr^+ states in figure 3.7. As in the quantum and semi-classical methods, the momentum transfer cross-sections for $^2P_{1/2}$ state obtained using interaction model B, are very close to the ones inferred from mobility measurements [88, 89]. The highest deviation from both states associated cross-sections is observed at small and intermediate kinetic energy ranges. For the $^2P_{3/2}$ state, the momentum transfer cross-section calculated from the hybrid method is in better agreement with inferred cross-section from measured mobility [88, 89] than both quantum or semi-classical methods. Moreover, as for semi-classical or quantum methods, the interaction model B gives better agreement with pseudo experimen-

tal measurements than interaction model A. Since model B gives results in better agreement with experiments, further figures of cross-section in this sub chapter will only show data obtained by using internuclear model B.

3.1.3.4 Quantum decoherence effect in hybrid method

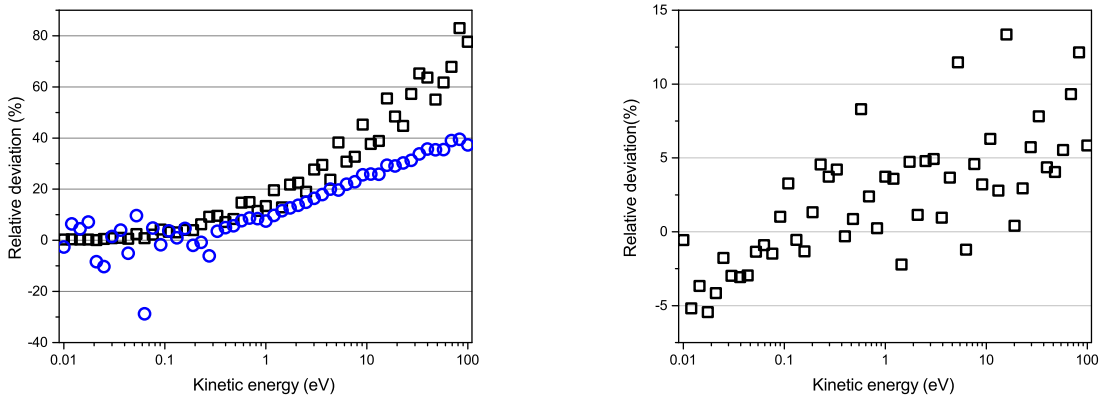

(a) Influence of quenching on cross-section

(b) Influence of subspaces separation in $^2P_{3/2}$ state

Figure 3.8: Verification of hypothesis used in hybrid method: relative deviation between quenching and non quenching cross-sections (a). Relative deviation between cross-sections obtained when the two subspaces are considered separately or simultaneously (b). Symbols : $^2P_{3/2}$ state □ and $^2P_{1/2}$ state ○.

Furthermore, in order to study the effect of quantum decoherence on calculation, we included a periodical quenching of the electronic wave function. Relative deviation (with respect to quenching) between quenching and non quenching cross-sections are plotted in figure 3.8a which shows that the inclusion of quantum decoherence in the calculation affects differently the $^2P_{3/2}$ and $^2P_{1/2}$ states. For low kinetic energy (lower than 1 eV), differences between quenching and non quenching cross-sections are almost negligible for both states. However, for higher energy, the momentum transfer cross-sections rise faster with than without quenching with a higher influence on the $^2P_{3/2}$ state.

Another difference between quantum and hybrid calculation is the different treatment of the two projection subspaces, $\Omega = 3/2$ and $\Omega = 1/2$. In the quantum calculations, the two subspaces are considered separately for Kr^+ initially in the $^2P_{3/2}$ state, and no transitions are allowed between these two subspaces. On the other hand in the hybrid method, transitions between these two subspaces are allowed. To understand the influence of transition, cross-section calculations were done in the $^2P_{3/2}$ state of the ion with either $\Omega = 3/2$ or $\Omega = 1/2$ projections on the collision axis. Figure 3.8b shows the relative deviation between the momentum transfer cross-sections, when the two angular projections are simultaneously considered, and the momentum transfer cross-sections, when the two angular projections are treated separately. One can notice on this figure that the relative deviation between the two cross-sections never exceed 5%.

3.1.3.5 Quantum-hybrid comparison

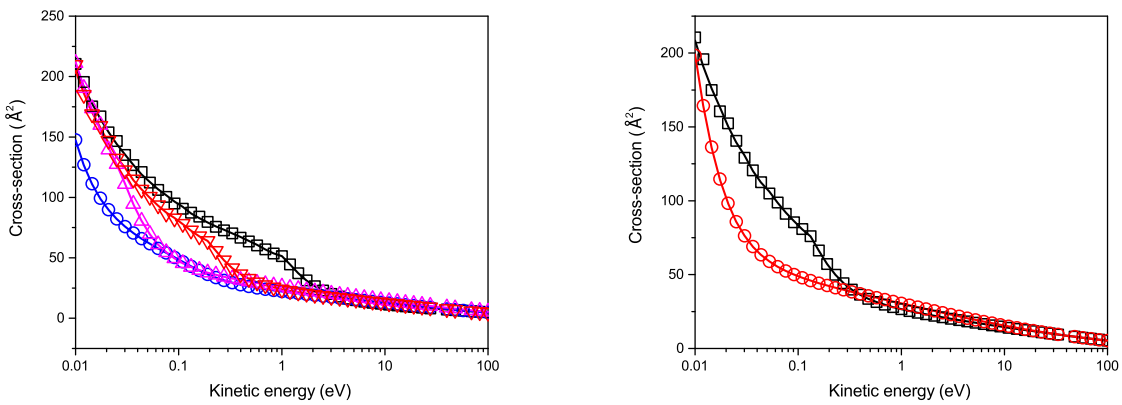

(a) $^2P_{3/2}$ state (b) $^2P_{1/2}$ state

Figure 3.9: Momentum transfer cross-section calculated for single potential curve. Symbols are used for hybrid method values and lines represent quantum values. (a) depicts for $^2P_{3/2}$ state, black curve and □: $I(1/2)_u$, blue curve and ○: $I(1/2)_g$, red curve and ▽: $I(3/2)_g$, magenta curve and △: $I(3/2)_u$. (b) depicts for $^2P_{1/2}$ state: black curve and □, $II(1/2)_u$: red curve and ○: $II(1/2)_g$.

To explain the observed difference between quantum and hybrid results, new calculations of momentum transfer cross-sections have been run by using single potential curve calculations. Figures 3.9a and 3.9b display such cross-sections calculations for both $^2P_{3/2}$ and $^2P_{1/2}$ initial states of Kr^+ respectively. It is clear from these figures that the hybrid MTCSs are correctly calculated (in agreement with quantum MTCSs) when no transitions between the subspaces are allowed. One concludes from these observations that the differences between quantum and hybrid cross-sections are mainly due to allowed (or not) transitions in our code.

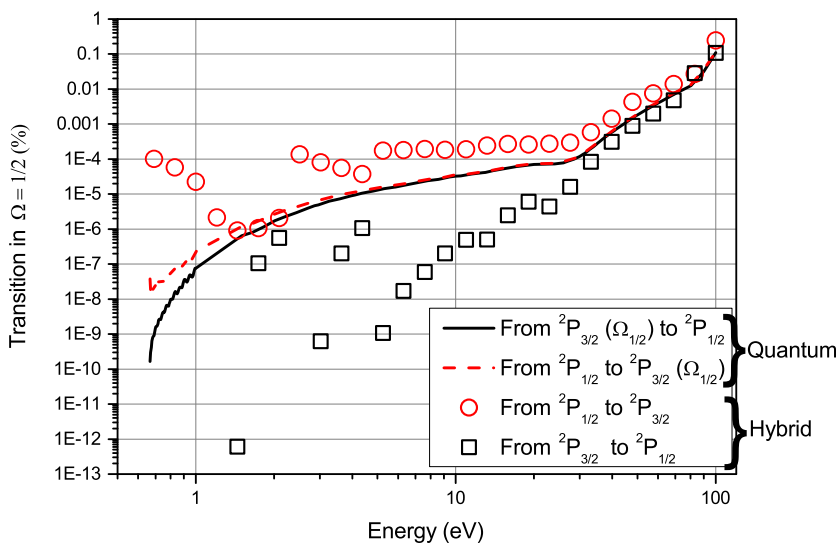

Figure 3.10: Relative (with respect to total cross-sections) transitions between $^2P_{1/2}$ and $^2P_{3/2}$ states obtained from quantum and hybrid methods.

Since the difference between quantum and hybrid method is not due to the calculations of cross-sections on single potential curve calculations, relative transitions MTCSs for hybrid method have been extracted and added to previous figure 3.6, as shown in figure 3.10. Representation of transition cross-sections contributions can help us to understand were the differences between both treatments could appeared. Unfortunately, both sets of data are not the same, for

quantum values, only transitions between $^2P_{3/2}(\Omega = 1/2)$ and $^2P_{1/2}$ states (and vice versa) are shown, while for hybrid method all transitions between $^2P_{3/2}$ and $^2P_{1/2}$ states are presented. This mean that hybrid set of data represent quantum shown transition with also transitions between $^2P_{3/2}$ ($\Omega = 3/2$) and $^2P_{1/2}$ states (and vice versa). This second type of transitions are supposed to be really low compared to the same subspace transitions (equations (3) and (4) in figure 2.4). One can see from this figure that transitions are negligible in both methods. However, hybrid method seems to overestimate $^2P_{1/2}$ to $^2P_{3/2}$ transitions and underestimate $^2P_{3/2}$ to $^2P_{1/2}$ transitions in comparison to quantum results. Even if the difference between both methods seems significant (up to a range of 6), the absolute value of transitions remains insignificant, this difference between both methods may result from $^2P_{3/2}$ inside transitions.

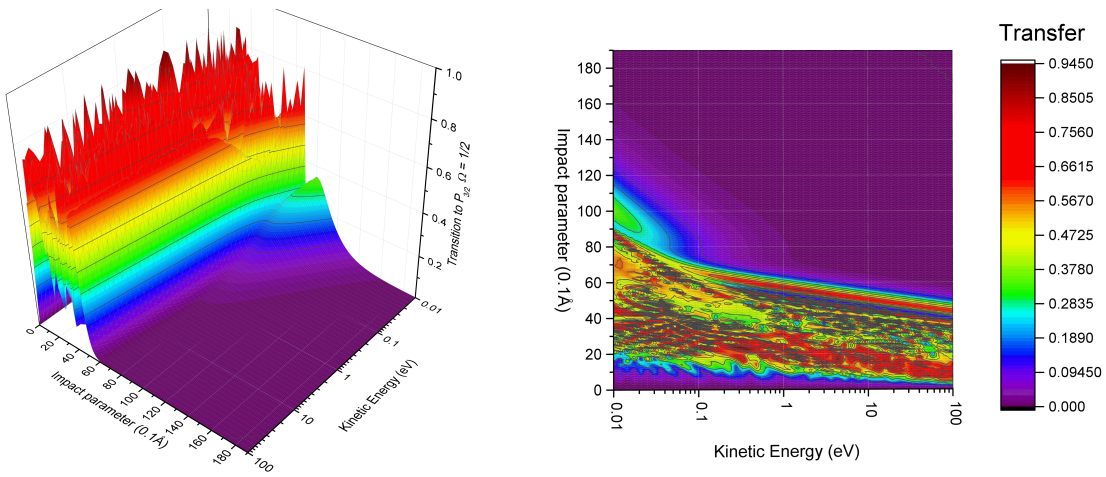

(a) Transitions in $^2P_{3/2}$ from $\Omega = 3/2$ to $1/2$

(b) flat version of figure (a)

Figure 3.11: Hypothesis verification in hybrid method to evaluate the number of transitions in $^2P_{3/2}$ states as a function of impact parameters.

To investigate this kind of transitions, all cross-sections have been compiled and normalized as function of energy and impact parameters and shown in a 3D figure, but also on the flat version of this figure as visible in figure 3.11. Note that only transitions between $^2P_{3/2}$ ($\Omega = 3/2$) and $^2P_{3/2}$ ($\Omega = 1/2$) are shown here,

since inverse transitions are the same it is not necessary to show them in this figure. For these calculations, initial state of the Kr^+ was set in $^2P_{3/2}$ (Ω = 3/2 or Ω = 1/2). Once hybrid cross-sections are obtained, all treated trajectories were investigate in order to observe possible subspace transitions during the collision. Since 504 independent trajectories have been performed for each parameter (energy and impact parameter), a normalization was done between 0 and 1. If the value is 1, this means (for this figure) that all trajectories have changed from Ω = 3/2 to Ω = 1/2. Interestingly, studied transitions appeared for the all studied kinetic energies range, but are more present for low energy where more impact parameter allowing transitions are present. One can notice (principally in the flat figure) that increasing energy leads to decrease the minimum and maximum impact parameter for the transition.

3.1.4 Mobility and diffusion coefficient

3.1.4.1 Collision energy range

Before performing all Monte Carlo calculations, a test was made to see if the range of the collision energy used for momentum transfer cross-section calculations was large enough. In figure 3.12, Kr^+ cumulative distributions of collision energy as function of collision energy are shown for different reduced electric field using MF hybrid calculation with internuclear potential model B. Cumulative distribution refers to, for each reduced electric field, the number of collisions, that are compiled with the Monte Carlo simulations, and, having energies up to a particular energy for the collision between the ion and the neutral. This cumulative distribution has been normalized with a maximum of 1 and a minimum of 0. This figure shows that for all reduced electric fields used in this thesis, the maximum colliding energy reached by the ion in the electric field is ≤ 10 eV. Concerning low reduced electric field (≤ 100 Td), some missing data are apparent for low collision energies since our energy ranges from 0.01 eV to 100 eV. This energy range was chosen in order to produce cross-section calculations within reasonable computational time. At 10 Td, 15% of considered collisions occur at

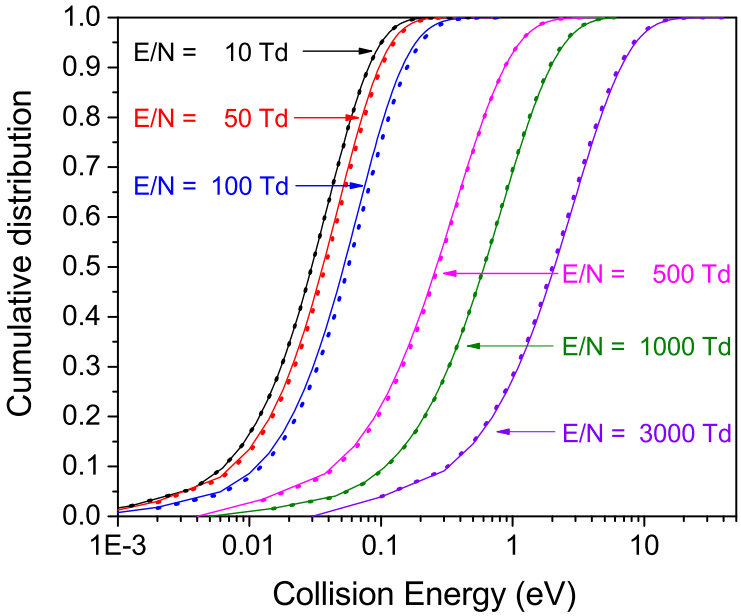

Figure 3.12: Cumulative distribution of Kr^+ collision energy for $^2P_{3/2}$ (full line) and $^2P_{1/2}$ (dotted line) states on different reduced electric field

collision energy below the chosen energy range. However, supplementary momentum transfer cross-section for lower collisions energies (0.001 - 0.01eV) were calculated and used to investigate if this data range was crucial for the calculation of mesoscopic data at low reduced electric field. The obtained cross-sections extended on this extra lower energy range shows that these missing values are not critical for transport coefficients calculations. The difference found between the two sets of mobilities are lower than the Monte Carlo statistical error (2%) and therefore the collision energy range used for hybrid and semi-classical is accurate. For quantum method, the ion energies used range from 0.001 eV to 100 eV. For this case, calculations at low collision energies were the fastest since they require a lower value of maximum angular momentum, $l_{\max}$, before reaching convergence. This figure shows that even at a high field (3000 Td), almost no ions have enough energy to be excited from $4s^24p^5$ to $4s4p^6$ level ($\approx$ 13.5 eV) [48], therefore consid-

ering only the incident Kr^+ ion in the fundamental $4s^24p^5$ level is a correct initial condition.

3.1.4.2 Mobility

Results of mobility calculations are summarized in figure 3.13 for quantum, semi-classical and hybrid methods. Since semi-classical and quantum values are almost equal, in the following, the only diffusion coefficients shown are the ones obtained from cross-sections using quantum and hybrid methods to increase the readability of figures. It is clear that if the mobility and MTCSs of quantum and semi-classical method are almost the same, the diffusion coefficients will also be really close.

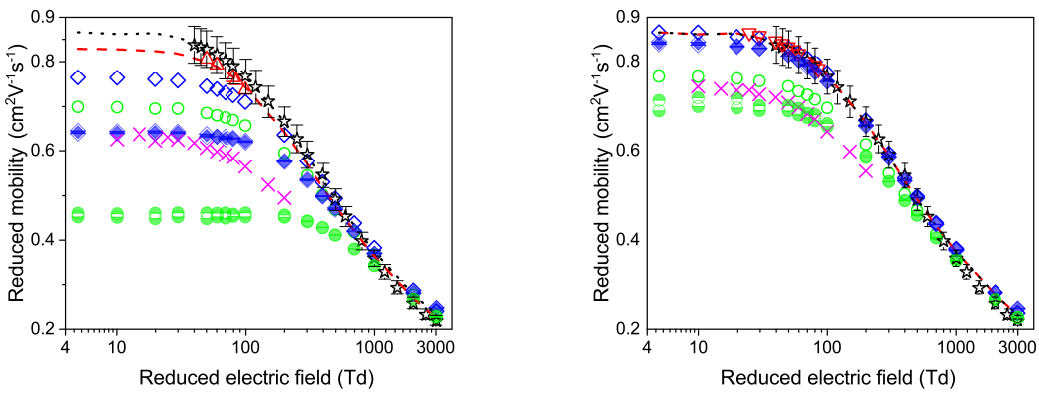

(a) Mobilities values for $^2P_{3/2}$ states for Kr^+

(b) Mobilities values for $^2P_{1/2}$ states for Kr^+

Figure 3.13: Standard reduced mobility K_0 in $cm^2V^{-1}s^{-1}$ of Kr^+ ions in $^2P_{3/2}$ and $^2P_{1/2}$ states in gaseous Kr. Experimental values: ☆ [88], △ and ▽ respectively for $^2P_{3/2}$ and $^2P_{1/2}$ states [89], dotted line corresponds to the inverse method on Ellis experimental value, dashed line on Helm experimental values. Other calculation: X [2]. This work: semi-classical method: upper half fulfilled symbol; quantum method: lower half fulfilled symbol; hybrid method: empty symbol using interaction potentials of refs [53]○ and [54] ◇.

Since the ion mobility is calculated from momentum transfer cross-section, the interaction model B gives, as expected, closer calculated Kr^+ mobility to ex-

perimental value as shown in figure 3.13. The $^2P_{1/2}$ state Kr^+ calculated mobility is close to experimental value [89] within error bars. Moreover, figure 3.13 shows a very good agreement between $^2P_{1/2}$ state Kr^+ calculated mobilities via the quantum, semi-classical and hybrid methods (with a maximum deviation of 3% between semi-classical and quantum methods). On the other hand, the $^2P_{3/2}$ state Kr^+ mobility shows a larger deviation (maximum deviation of 7% for hybrid method and 23% for semi-classical and quantum methods) from the measured one [89], than the $^2P_{1/2}$ mobility. Observed transition, as a consequence of quite strong interaction at specific distance, $I(1/2)_x \Leftrightarrow I(3/2)_x$ (not allowed in semi-classical and quantum calculation), where x refers to $gerade$ or $ungerade$ states, in the hybrid code could explain why the momentum transfer cross-section for $^2P_{3/2}$ is lower than the one obtained from quantum method and therefore higher mobility. However, for the $^2P_{1/2}$ state there is no difference for momentum transfer cross-section (and mobility) obtained from the 3 methods since this transition occurs only for the $^2P_{3/2}$ state. Results from an independent (semi-classical) calculation [1] (as reported in reference [2]) are also shown in figure 3.13. These reported data show qualitatively similar behavior to the calculated mobility in this work, but large quantitative differences, particularly in the case of mobility obtain using model B. Since no details on these alternative calculations are available, no explanation for these differences can be proposed.

3.1.4.3 Diffusion coefficient

Finally, the $^2P_{1/2}$ and $^2P_{3/2}$ states transverse and longitudinal diffusion coefficients calculated by using model B interaction potential, are displayed in figure 3.14. Values at low reduced electric field (5 Td) of these diffusion coefficients (eD_L/K_0 ≈ 25.4 meV and eD_T/K_0 ≈ 26.9 meV) are close to expected values from Nernst-Townsen-Einstein equation (25.3 meV). Moreover, as expected, very good agreement between hybrid and quantum is obtained for both states $^2P_{1/2}$ and $^2P_{3/2}$ and this is due to the fact that diffusion are less sensitive to the approximations used than the mobility data. Shown diffusion coefficients exhibit the usual behavior,

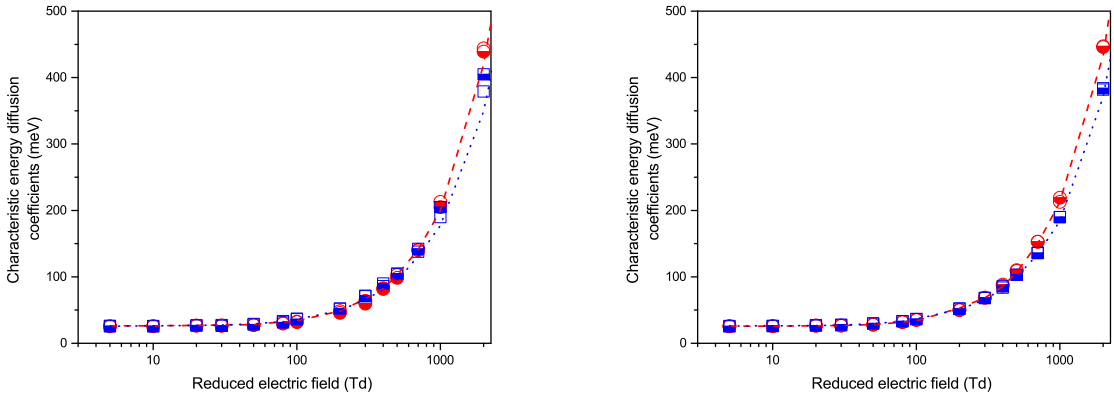

(a) $^2P_{3/2}$ state diffusion coefficients

(b) $^2P_{1/2}$ state diffusion coefficients

Figure 3.14: Simulation results of characteristic energy of longitudinal, eD_L/K_0, and transverse, eD_T/K_0, diffusion in meV for Kr^+ ions in $^2P_{1/2}$ and $^2P_{3/2}$ states in gaseous Kr using interaction potential B [54]. eD_T/K_0 □, eD_L/K_0 ○. Quantum method: lower half fulfilled symbol, hybrid method: empty symbol. Inverse method diffusion coefficient based on distinguished experimental values [89] are presented in curves: dashed for eD_T/K_0 and dotted for eD_L/K_0.

namely plateau in the low field range followed by a fast increase for higher field above nearly 100 Td. Moreover the longitudinal diffusion coefficients rise slightly faster than the transverse diffusion coefficient (maximum 5-10%).

3.1.5 Discussions

In this section, selected issues concerning the mobility of Kr^+ in Kr, the main experimental data used in this work, will be discussed.

3.1.5.1 Differences between interaction models

As follows from previous sections, interaction model B leads to results in better agreement with experimental data than model A. The momentum transfer cross-section of the Kr^+/Kr collision is larger for model A than for model B and, as a

consequence, mobilities calculated from the cross-sections obtained for model B are higher than those obtained for model A.

Since the deviations between the experimental values and the present calculations are only important at low collision energies (and/or weak electric fields), they should result mainly from inaccuracies in the long-range parts of the potentials. One can clearly see in figure 3.2b that model B potentials are always higher than model A ones in the long-distance region or, alternatively, that model B potentials converge to the Kr^+... Kr asymptote more rapidly than Model A potentials. The potentials B have thus a shorter effective range and thus should lead, at low collision energies, to smaller effective cross-sections and higher Kr^+ mobilities. This holds for potentials of group I ($I(1/2)_u$, $I(3/2)_g$, $I(1/2)_g$ and $I(3/2)_u$) as well as for those of group II ($II(1/2)_u$ and $II(1/2)_g$): the differences seen in the mobility data calculated for the $Kr^+(^2P_{3/2})$ ion are basically the same as for $Kr^+(^2P_{1/2})$ (see figure 3.13). The conclusion that the asymptotic tails of the diatomic potentials are responsible for the observed deviations is further supported by the fact that, for high collision energies, the two models lead to almost coinciding mobilities which seems to indicate that differences in the repulsive walls of the two sets of potentials are not much important. Moreover, thorough spectroscopic tests performed for the potentials in the original papers [53, 54] show their equal behavior around the minimum well. However, as seen previously, e.g., for helium [22], the mobility property is very sensitive to the global quality of the set of potentials used and even small deviations in the potential curves may result in a well observable shift in the calculated mobility.

3.1.5.2 Differences between quantum and hybrid calculations

Somewhat surprising is the high difference observed between calculations in which nuclear degrees of freedom are treated quantum mechanically (the full quantum calculation will be hereafter denoted as QUANT) and calculations based on classical treatment of nuclei (the hybrid calculation, hereafter denoted as HYB). For the heavy krypton atom, one would, on the contrary, expect that quantum

nuclear effects are negligible and that QUANT and HYB calculations should lead to quantitatively close results. Moreover, since the differences between QUANT and HYB calculations are much more pronounced for the $Kr^+(^2P_{3/2})$ ion than for $Kr^+(^2P_{1/2})$, other effects may come into play.

As a first step, we have investigated whether nuclear quantum effects are really negligible for krypton. For this, single-potential calculations (each constrained to one of the six available electronic potentials) have been run using the HYB and JWKB methods and compared to each other. Since no differences have been found for either potential, one can conclude that the nuclear quantum effects are not important in the present calculation and that the source of the difference between the HYB and QUANT approaches should be searched for elsewhere, namely in the way how electronic degrees of freedom are treated in both approaches.

As discussed in section 2.1, QUANT calculations have been done separately on two projection subspaces, $\Omega = 3/2$ and $\Omega = 1/2$, of the electronic angular momentum space. It means that for the Kr^+ ion initially in the $^2P_{3/2}$ state, no transitions are allowed between these two subspaces or, alternatively, between I(3/2) and I(1/2) states. On the other hand, in the HYB approach no such restriction is present. By inspecting selected collision trajectories started in the $^2P_{3/2}$ state of the Kr^+ ion with either $\Omega = 3/2$ or $\Omega = 1/2$ projection on the collision axis, we have found that the $\Omega = 3/2$ to $\Omega = 1/2$ transitions (and *vice versa*) occur frequently as a result of quite strong interactions of the I(3/2) and I(1/2) states at specific distances. On the other hand, for the $^2P_{1/2}$ initial state such transitions are not important since, in general, transitions to the lower family of states (I) is highly improbable. As a consequence, the difference between QUANT and HYB calculations is much smaller for the $^2P_{1/2}$ initial state than in the $^2P_{3/2}$ case.

One can thus conclude that the calculations performed on the Kr^+ ($^2P_{1/2}$) ion give a realistic estimate of the differences resulting from the use of classical approximation for treating atomic nuclei in the HYB approach while the deviations obtained for the Kr^+ ($^2P_{3/2}$) ion are also influenced by the different ways how

electronic states are treated in the HYB and QUANT methods. However, since considerably distinct pictures are seen for Model A and Model B, other effects may also contribute.

3.1.5.3 Differences between theory and experiment

As above, differences between measured and calculated mobilities will be considered here and, since interaction Model B and the hybrid method give the best agreement with the experiment, only theoretical mobility data obtained from the hybrid approach and Model B will be discussed.

The present calculations agree very well with the fine-structure state resolved experiment [89, 93] for the $\mathrm{Kr}^+(^2\mathrm{P}_{1/2})$ ion. The calculated mobility data almost coincide with the experimental data or, where the latter are not available, on their inverse method extrapolation. The situation is somewhat worse, however, if the Kr^+ ion is initially considered in the $^2\mathrm{P}_{3/2}$ state, particularly in the weak-field region. In this case, the theoretical estimate of the low-field (E/N = 5 Td) mobility of the Kr^+ ion is by about 8 per cent below the inverse method value. Several possible sources responsible for this deviation have been considered and tested in this work.

Firstly, the fact that the natural mixture of stable isotopes of krypton present in experiments is approximated, in this work, by an artificial isotope of a properly averaged mass has been justified by running parallel JWKB calculations on both this "averaged" isotope and the natural mixture of stable krypton isotopes. As discussed previously, deviations up to 2%, typically about 1%, have been obtained at low electric field, which is not enough to account for the differences between the experiment and theory in this region. Secondly, the same holds for the inclusion of quantum decoherence in the hybrid calculation which does not lead, in the weak-field region, to changes of the mobility data larger than 2% and, in addition, away from the experiment. A third possibility may be that, in our calculations, the $^2\mathrm{P}_{3/2}$ (J = 3/2) initial state of the Kr^+ ion has been modeled by randomly selected coherent (linear) combinations of four states corresponding to

$M_J = \pm 3/2$ and $M_J = \pm 1/2$ projections. To see the effect of this choice, additional hybrid calculations have been run for the $Kr^+(^2P_{3/2})$ ion with the initial state set either to $M_J = \pm 3/2$ or $M_J = \pm 1/2$ and the resulting data averaged afterwards. In this way, an incoherent mixture of the initial $M_J = \pm 3/2$ and $M_J = \pm 1/2$ projections has been considered, which may be closer to experimental conditions. However, while the $M_J = \pm 3/2$ and $M_J = \pm 1/2$ calculations have led to results considerably deviating from the original coherent calculations, points almost coinciding with the original data (deviations of about 1%) have been obtained after the two additional calculations have been averaged. As a consequence, differences well below the observed deviations between the theory and experiment have again been obtained and the way how the projections of the electronic angular momentum are mixed cannot be responsible for the latter.

Taking all this into account as well as the excellent agreement with experimental data for the $Kr^+(^2P_{1/2})$ ion, we conclude that the experimental mobility reported for the $Kr^+(^2P_{3/2})$ ion may have been contaminated. Since the $Kr^+(^2P_{3/2})$ mobilities are considerably closer to the $^2P_{1/2}$ data in the experiments than in the calculations, a contamination by signal originating from $Kr^+(^2P_{1/2})$ ions may have occurred in the experiment. Moreover reported Kr^+ mobilities by Helm were not direct measurements but they were obtained by fitting the detected double peak (which includes unresolved $^2P_{1/2}$ and $^2P_{3/2}$ states) with gaussian distributions using the diffusion coefficient as well as the mobilities as independent variables. This fitting procedure certainly introduces an error higher than the experimental error in direct mobility measurements typically estimated at 5%. This assumption may be further supported by the observation that almost perfect coincidence with the $Kr^+(^2P_{3/2})$ experimental mobility is achieved if the theoretical data calculated for $Kr^+(^2P_{3/2})$ and $Kr^+(^2P_{1/2})$ are averaged with respective weights $w_{3/2} \approx 0.3 - 0.4$ and $w_{1/2} \approx 0.6 - 0.7$.

3.2 Xenon

Present section has already been presented on conference [94] and in an article [95]. Xenon is a noble gas with an electronic configuration [Kr] $5s^2 4d^{10} 5p^6$. There are 41 known isotopes of xenon with masses ranging from ≃ 110 to ≃ 147 g.mol^{-1}. As for krypton, only stable isotopes will be taken into account and there are 9 of them:

Nuclide symbol	Z (number of proton)	N (number of neutron)	isotopic mass	nuclear spin	abundance(%)
^{124}Xe	54	70	123.9059	0	0.10
^{126}Xe	54	72	125.9043	0	0.09
^{128}Xe	54	74	127.9035	0	1.91
^{129}Xe	54	75	128.9048	1/2	26.40
^{130}Xe	54	76	129.9035	0	4.07
^{131}Xe	54	77	130.9051	3/2	21.23
^{132}Xe	54	78	131.9042	0	26.91
^{134}Xe	54	80	133.9054	0	10.44
^{136}Xe	54	82	135.9072	0	8.85

The average atomic mass assigned to xenon is 131.293 g.mol^{-1} [81].

3.2.1 Interaction potentials

Two internuclear Xe^+/Xe potentials were used for cross-section calculations. As for krypton, the denomination of internuclear potential will be Model A and Model B. Model A calculated by Paidarová *et al.* [67] provides *ab initio* values fitted with a cubic spline curve in order to obtain potential values at all internuclear distances. The second model (Model B) provided by Rupper *et al.* [96] is based on state of the art *ab initio* calculations with some adjustments made from experimental spectroscopic results. Like for krypton, the Spin-Orbit Coupling was taken into account by using the Cohen-Schneider semi empirical model [47]. For xenon, the a parameter (2/3 of the atomic splitting) is set to 0.8739 eV. Since Spin-Orbit free potentials have the same behavior as for Kr^+/Kr system, it is not

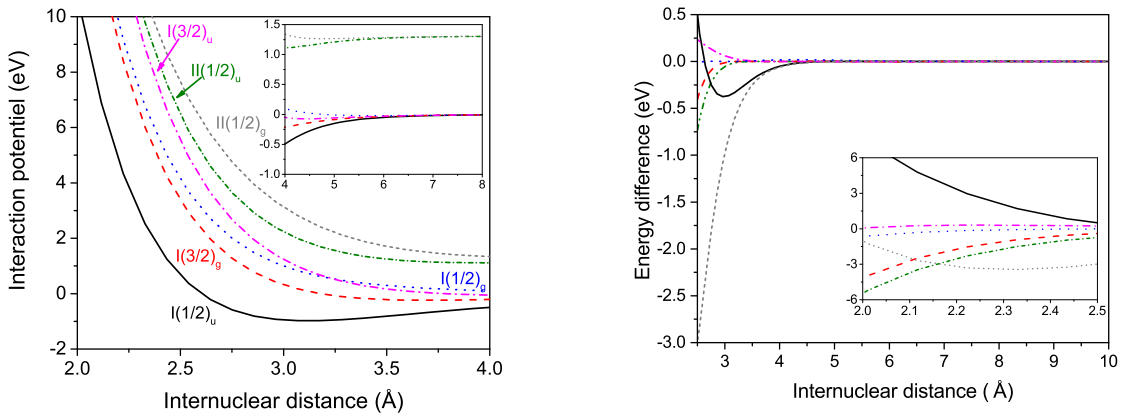

(a) Interaction potentials Model A with the inclusion of the Spin-Orbit Coupling

(b) Differences between potentials of Model A and Model B (Model B minus Model A) with the inclusion of the Spin-Orbit Coupling

Figure 3.15: Internuclear potentials with the inclusion of the Spin-Orbit Coupling and differences between them for Xe^+/Xe. Full line is $I(1/2)_u$, dashed line is $I(3/2)_g$, short dotted line is $I(1/2)_g$, dash dotted line is $I(3/2)_u$, short dash dotted line is $II(1/2)_u$, short dashed line is $II(1/2)_g$

necessary to display them once again. Internuclear potentials with the Spin-Orbit Coupling for Model A are shown in figure 3.15a and the differences between Model A and Model B internuclear potential are depicted in figure 3.15b. Differences between both models are more important than between the two models (A and B) used in the Kr^+/Kr calculations.

3.2.2 Experimental data reported in literature

Experimental values (displayed in figures 3.16) available in literature for Xe^+/Xe mobility reported by Helm *et al.* [89], Larsen *et al.* [97] and Viehland *et al.* [98] are all close to each other. All these reported data distinguish between two fine-structure states ($^2P_{3/2}$ and $^2P_{1/2}$) of the Xe^+ ion. However, Neves *et al.* experimental mobilities [2] do not distinguish between the two fine structure states. Furthermore, at low reduced electric field, the usual plateau has been replaced by a rise in the mobility which is attributed to presence of impurities, due to the

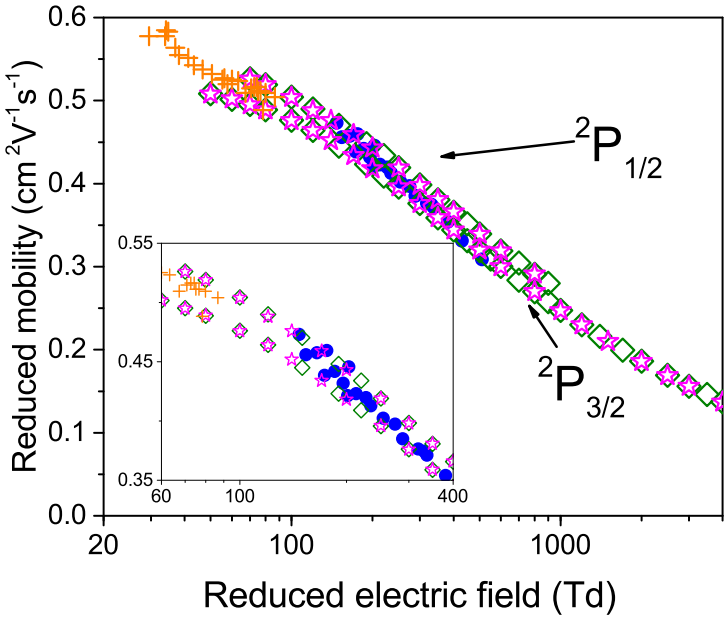

Figure 3.16: Experimental standard reduced mobility (K_0) of the Xe^+ ion in gaseous xenon. Measurements not distinguishing between the fine-structures states of the ion ($^2P_{3/2}$ and $^2P_{1/2}$): • [91] + [2]; measurements distinguishing between the fine-structures states of the ion: (☆[89] (see also reference [93]) and ◇ [97] (see also reference [98])).

non use of mass spectrometer to discriminate the detected ions. For these two reasons, Neves data will not be considered in the following discussion.

3.2.3 Cross-sections

3.2.3.1 Quantum, hybrid and semi-classical method

Momentum transfer cross-sections of Xe^+ in Xe gas calculated with the three different methods are displayed and compared to inverse method values in figure 3.17. It is clear that Model A gives larger cross-sections than Model B for all methods used. Interaction Model B provides momentum transfer cross-section closer to inverse method one far better than Model A in particular at low collision energies. Furthermore, hybrid method provides higher momentum transfer

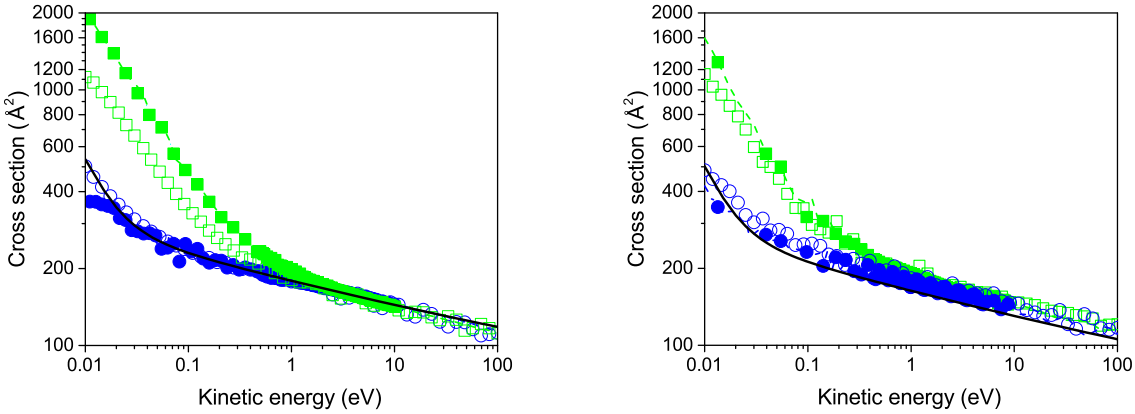

(a) MTCS values for $^2P_{3/2}$ states

(b) MTCS values for $^2P_{1/2}$ states

Figure 3.17: Momentum transfer cross-sections (MTCSs) for Xe^+/Xe collisions calculated for both $^2P_{3/2}$ (panel a) and $^2P_{1/2}$ (panel b) initial states of the colliding ion using different theoretical approaches – semi-classical method (dashed lines), quantum method (full symbols) and hybrid method (empty symbols), and interaction models – Model A [67] (□) and Model B [96] (○). Inverse method (pseudo-experimental) cross-sections obtained from fine-structure resolved experimental mobility data of references [89, 97] are also shown for comparison (thick solid curves).

cross-section than quantum or semi-classical method using Model B, while the inverse argument holds for Model A.

3.2.3.2 JWKB and isotope hypothesis verification

From figure 3.17, we notice that quantum and semi-classical cross-sections are very close one to each other. More precisely, relative deviations between cross-sections, obtained via these two methods, are displayed in figure 3.18a and are smaller than for krypton case (maximum of ≈ 4% as compared to ≈ 6% for krypton). As in krypton case, these deviations counterbalance each other and become negligible for kinetic energy above 1 eV. This is due, as verified by quantum calculation, to a negligible probability of the spin change channel (process (3) and (4) of figure 2.4).

As for krypton, to save computational time, all hybrid and quantum cross-sections calculations were performed using an artificial isotope of mass 131.293 g.mol^{-1} and nuclear spin equal to 0. To test this hypothesis, semi-classical method was used on the 45 possible collisions using the nine different stable isotopes. In figure 3.18b, is shown the relative deviation between cross-sections calculated by using the artificial isotope (131.293 g.mol^{-1}) on one hand, and the one obtained from all the weighted cross-sections associated to all isotope with their occurrence probability on the other hand. As for krypton, deviations up to 6% is observed for kinetic energy lower than 1 eV, but they are again counterbalancing each other. While for higher kinetic energies, the relative deviation is close to 0%. Interestingly, xenon has more isotopes percentage with a fermionic behavior, but even if the artificial isotope is treated as a boson, the relative deviation is not more perturbed than in the krypton case.

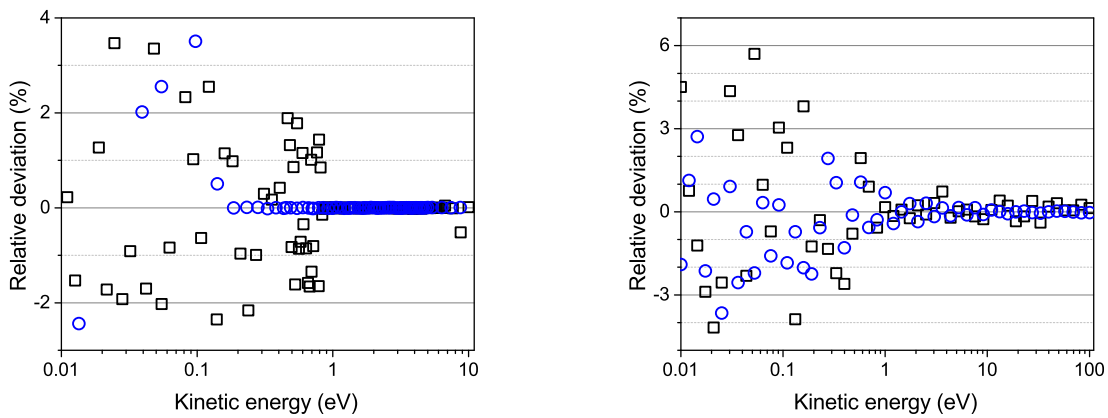

(a) JWKB approximation verification

(b) Isotope hypothesis verification

Figure 3.18: Hypothesis verification using semi-classical method and interaction potentials of ref [96]: JWKB approximation(a) and isotropic distribution (b)
□ are relative deviation for $^2P_{3/2}$ state; ○ are relative deviation for $^2P_{1/2}$ state.

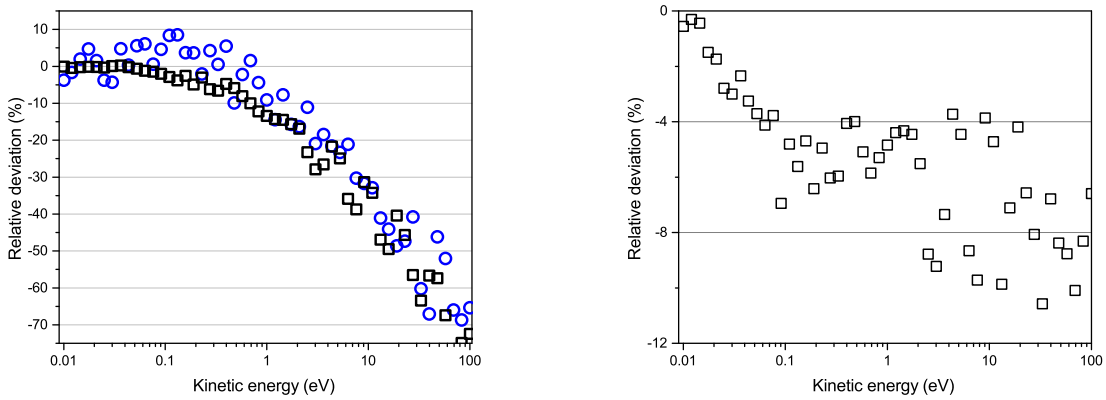

(a) Influence of quenching on cross-section

(b) Influence of subspaces separation in $^2P_{3/2}$ state

Figure 3.19: Verification of hypothesis used in hybrid method: relative deviation between quenching and non quenching cross-sections (a). Relative deviation between cross-sections obtained when the two subspaces are considered separately or simultaneously (b). Symbols, $^2P_{3/2}$ state : □ and $^2P_{3/2}$ state : ○.

3.2.3.3 Quantum decoherence

Momentum transfer cross-sections including quenching (quantum decoherence) were calculated from internuclear potential Model B by using hybrid method and compared with non quenching calculations using a relative deviation in figure 3.19a. At low energies (0.01 to 1 eV), two different kinds of behavior can be seen. Firstly, at low kinetic energies, for $^2P_{1/2}$ state, quenched cross-section values are smaller than MF ones, while for $^2P_{3/2}$ state, the quenched cross-sections are above MF values. For higher energy (more than 1 eV), the quenched cross-sections are higher than MF calculations for both states ($^2P_{3/2}$ or $^2P_{1/2}$).

3.2.3.4 Quantum-hybrid comparison

In order to verify the validity of simultaneous calculation of the substates in $^2P_{3/2}$ in hybrid method, calculations were performed by setting initial conditions to $\Omega = 1/2$ or $\Omega = 3/2$ by using Model B. Figure 3.19b shows relative variation of MTCS

with distinction in initial subspaces of $\Omega = 1/2$ and $\Omega = 3/2$ with simultaneous one. Distinguishing the subspaces leads to higher cross-sections and thus lower mobilities for the $^2P_{3/2}$ state although the variation will also remain low (less than 4%).

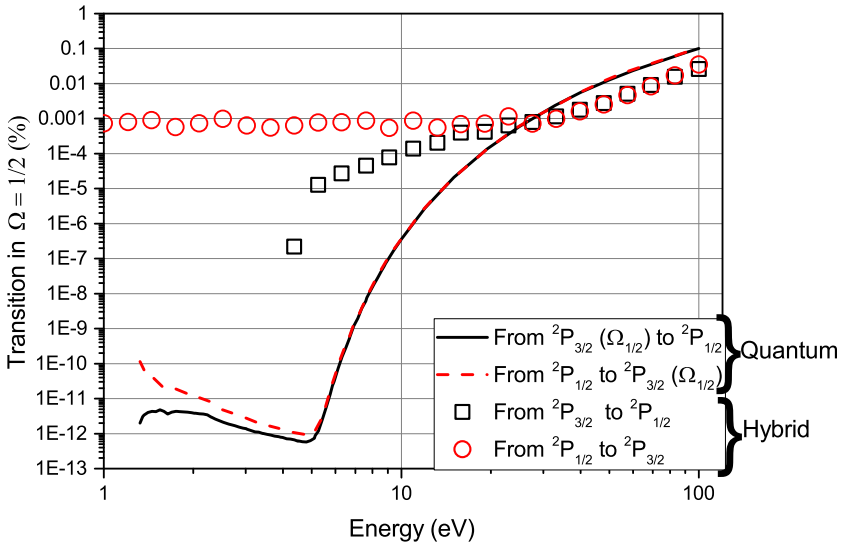

Figure 3.20: Relative (with respect to total cross-section) transitions between $^2P_{1/2}$ and $^2P_{3/2}$ states with quantum and hybrid methods.

The influence of spin change process on cross-sections calculations was studied, as for krypton, with quantum and hybrid methods based on interaction Model B. As shown in fig 3.20, the maximum relative transition cross-section with respect to subspace total collision cross-sections value at 100 eV collision energy is 0.1%. Therefore, the non consideration of spin change processes is a good approximation in the semi-classical method.

Secondly, the difference between quantum and hybrid method is not due to the calculations of cross-sections on single potential curve trajectories. Representation of transition cross-section contributions may help us to understand where the observed differences between both treatments. However, as already said in the case of krypton, both sets of data are not the same, transitions are treated dif-

ferently in both methods. Indeed, since the angular momentum projections Ω = 3/2 are treated separately in quantum method, transitions between I(1/2)$_x$ and I(3/2)$_x$ are excluded, while in hybrid method such transitions are allowed. For quantum values, only transitions between $^2P_{3/2}$ (Ω =1/2) and $^2P_{1/2}$ states (and vice versa) are shown, while for hybrid method all transitions between $^2P_{3/2}$ and $^2P_{1/2}$ states are depicted. This means that hybrid set of data represent quantum transitions in addition to transitions between $^2P_{3/2}$ (Ω = 3/2) and $^2P_{1/2}$ states (and vice versa). It is known from literature that this second type of transitions are negligible in comparison to quantum shown transitions, one can see in this figure that both methods provide negligible transitions and the order of difference between both method values are more pronounced than in the case of krypton (9 for xenon as compared to 6 for krypton). The hybrid method is overestimating transitions at kinetic energies lower than 30 eV and underestimates them at energies higher than 30 eV. Even if the difference between both methods seems significant (up to a range of 9), the absolute value of transitions remains insignificant, this between both methods may be a consequence of $^2P_{3/2}$ inside transitions.

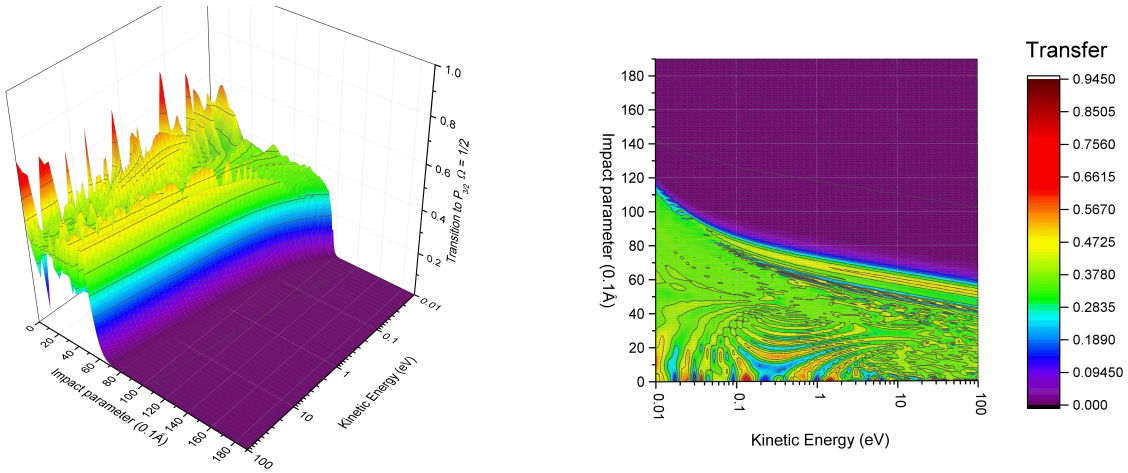

(a) Transitions in $^2P_{3/2}$ from Ω = 3/2 to 1/2

(b) flat version of figure a

Figure 3.21: Hypothesis verification in hybrid method to evaluate the number of transitions in $^2P_{3/2}$ state as a function of impact parameters and kinetic energy.

Furthermore, using hybrid method, normalized compilation of cross-sections

as function of energy and impact parameters in a 3D figure, but also on the flat version of this figure, are presented in figure 3.21. Only transitions between $^2P_{3/2}$ (Ω = 3/2) and $^2P_{3/2}$ (Ω = 1/2) are shown here, since inverse transition are the same. The transition region is larger than for krypton, but at the same time, the number of transitions is much smaller. Color legend is kept the same as for krypton case so that the reader can notice more easily differences between the two systems Kr^+/Kr (figure 3.11) and Xe^+/Xe (figure 3.21). Interestingly, while for krypton there is a minimum value for the impact parameter to allow a transition, for xenon such minimum is not present.

3.2.4 Mobility and diffusion coefficient

3.2.4.1 Collision energy range

As for krypton, in order to check the validity of the collision energy range in our calculations, cumulative distribution energy function is calculated and plotted in figure 3.22. This figure shows that low collisions energies are missing in the simulation at low reduced field (17% at 10 Townsend). The energy range was extended to lower values and new MTCS calculations were performed. No difference was observed in the mobility calculated from the new MTCS extended to the low energy range. Figure 3.22 shows also that high collisions energies ($\geq$ 12 eV) are not required for mobility calculations at reduced field of 3000 Td. Moreover this figure confirms our hypothesis of considering only the fundamental $5s^25p^5$ level of Xe^+ since even at 3000 Td the ion does not have enough energy to be excited to $5s5p^6$ level ($\approx$ 11.3 eV above the ground-state) [48].

3.2.4.2 Mobility

It is obvious from figure 3.23 that interaction Model B gives closer mobilities to experimental measures than interaction Model A as it was already expected from cross-sections results. For $^2P_{3/2}$ states, all methods are almost on the experimental data and are thus close to each other. For $^2P_{1/2}$ state, quantum and semi-classical

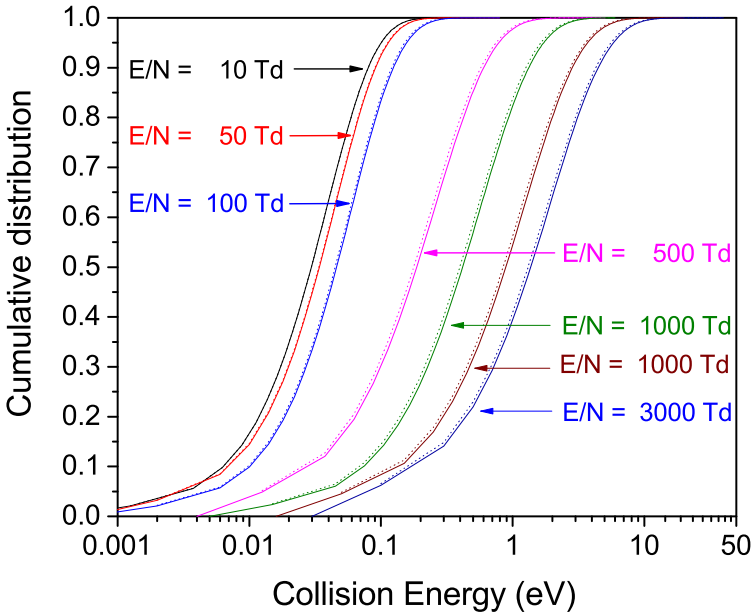

Figure 3.22: Cumulative distribution of Xe^+collision energy for different reduced electric field

mobilities are almost on the experimental data, hybrid results are not so far from the two other methods and adding quenching to Mean Filed approach improves slightly the results (not shown here because the variation is too low to be observed).

The remaining difference between calculated and measured mobility can be attributed to the applied fitting procedure [97] to extract the experimental mobilities from the two unresolved peaks curve corresponding to $^2P_{1/2}$ and $^2P_{3/2}$ xenon ion states. In reference [97], the detected ion current curve was fitted with two Gaussians associated to $^2P_{1/2}$ and $^2P_{3/2}$ states. This procedure certainly induces an error since the detected peak in mobility measurement is distorted from a Gaussian shape by ion longitudinal diffusion and this effect should be taken into account by fitting with an appropriate function which is the sum of a Gaussian function and a Gaussian error function [99, 100]. It is noteworthy that even

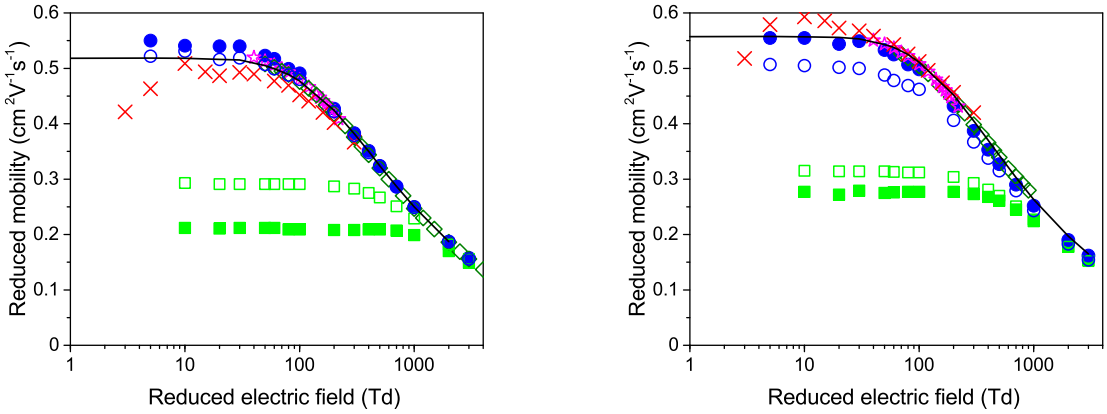

(a) Mobilities values for $^2P_{3/2}$ states

(b) Mobilities values for $^2P_{1/2}$ states

Figure 3.23: Standard reduced mobility K_0 in $cm^2V^{-1}s^{-1}$ of Xe^+ ions in $^2P_{3/2}$ and $^2P_{1/2}$ states in gaseous Xe. Experimental values: ☆[89] and ◇ [97]. Other calculation: X [2]. This work: quantum method: fulfilled symbol; hybrid method: empty symbol using interaction potentials of refs [67] □ and [96] ◯.

this latter procedure is not exempt from fitting error but certainly smaller than the error induced by fitting with a simple Gaussian function.

3.2.4.3 Diffusion coefficient

Concerning diffusion coefficient, displayed in figure 3.24, only quantum and hybrid values are shown. Here again, semi-classical and quantum mesoscopic values are too close to be shown clearly on this figure, all methods provide values close to each other. By comparing values at 5 Td with theoretical one at 0 Td (25.3 meV), quantum and hybrid methods (25.8 - 26.2 meV) provide coherent results. Same behavior can be observed as for krypton (figure 3.14) i.e. transverse diffusion coefficient is higher than longitudinal one at high fields. However, diffusion coefficients grows faster for krypton than xenon. For xenon, previous calculations done by Barata and Conde [63] allow us to compare our results. Until 300 Td our calculations are closed to them, even if isotropic collisions are more respected in

our case (eD_T/K and eD_L/K are closer). Unfortunately, higher range values are not available for comparison.

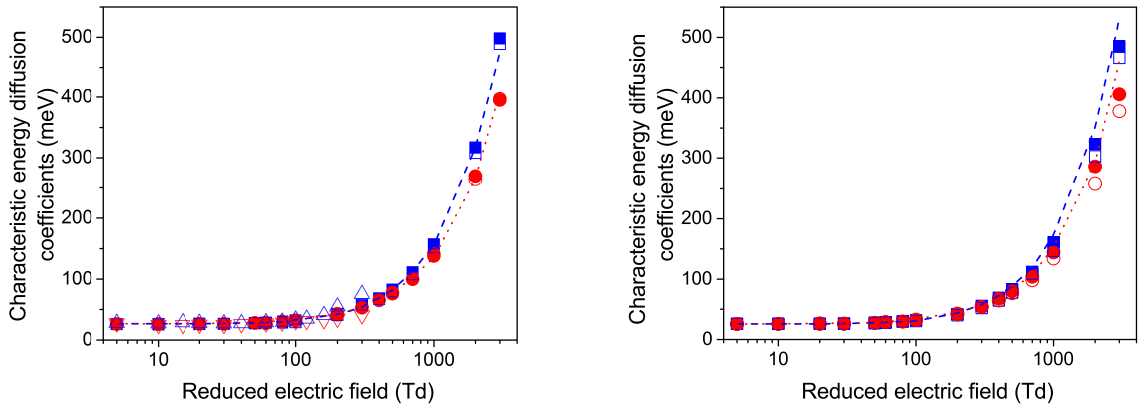

(a) $^2P_{3/2}$ state diffusion coefficients

(b) $^2P_{1/2}$ state diffusion coefficients

Figure 3.24: Characteristic longitudinal (eD_L/K, □) and transverse (eD_T/K_0, ○) energies of $Xe^+(^2P_{3/2})$ (panel a) and $Xe^+(^2P_{1/2})$ (panel b) ions in gaseous Xe calculated for interaction Model B [96] using the hybrid method (open symbols) and the quantum method (full symbols). For comparison, inverse method data are added as dashed (eD_L/K_0) and dotted (eD_T/K_0) curves, as well as data resulting from an independent calculation by Barata and Conde performed for the $Xe^+(^2P_{3/2})$ ion (see figure 4 of reference [63]), △ : (eD_L/K_0) and ▽ : (eD_T/K_0)

3.3 Conclusions

Collisions of rare-gas ions (Rg^+ = Kr^+ or Xe^+) with neutral rare-gas atoms (Rg = Kr or Xe) have been studied using three theoretical approaches, the full quantum approach [61, 101], the semi-classical (Jeffreys-Wentzel-Kramers-Brillouin approximation) method [62], and a hybrid approach [75] with electrons treated quantum mechanically and atomic nuclei described within the classical approximation. In addition, a semi empirical inverse-method approach [76, 77] has also been employed which is based on a simple isotropic potential adjusted to experimental data [89, 93] of the Rg^+ mobility in the carrier parent gas. For krypton, two state-of-the-art interaction models [53, 54] based on extensive *ab initio* calculations have been used in the three theoretical calculations. They are called Model A [53] and Model B [54, 68] throughout the paper. Within these two models, all relevant electronic states, asymptotically correlating to $4s^24p^5$ configuration of the ion, have been considered as well as the Spin-Orbit Coupling which is important in the heavy krypton ion. For xenon, two interaction models based on literature diatomic potentials have been employed to build up the electronic Hamiltonian of the $\mathrm{Xe}^+/\mathrm{Xe}$ collision complex: Model A based on *ab initio* calculations [67] and Model B derived from state-of-the-art photoelectrons spectra of the xenon dimer [96]. The Spin-Orbit Coupling, which is important in the heavy xenon ion, has been included via a semi empirical scheme [47] which was many times before proved to lead to a highly accurate representation of the Spin-Orbit Coupling in a general rare-gas dimer cation. Within these two models, all relevant electronic states, asymptotically correlating to $5s^25p^5$ configuration of the ion, have been considered as well as the Spin-Orbit Coupling which is important in the heavy xenon ion.

As a first step, effective collision cross-sections (differential, integral, and momentum transfer) have been calculated with two fine-structure states of the krypton and xenon ions, $^2P_{3/2}$ and $^2P_{1/2}$, distinguished. Then, the calculated cross-sections have been used in Monte Carlo calculations [102] of transport properties of the rare-gas ion (mobility, longitudinal and transverse diffusion coef-

ficients) in parent gas over a broad range of the reduced electric field (E/N = $5 - 3000$ Td). All the data obtained via the three theoretical approaches considered in this work have been compared to one another as well as to available experimental data (mobility) or pseudo experimental data derived from the semi empirical inverse method where experiments are not available (cross-sections, diffusion coefficients). It has been found that the cross-sections calculated from interaction Model B agree much better with the pseudo-experimental inverse-method data than cross-sections obtained from Model A. This particularly holds at low collision energies for which the Model A cross-sections significantly deviate from the inverse-method curve. Further, the full quantum treatment and the JWKB method give basically the same values of calculated cross-sections. The importance of transitions between states or subspaces during a collision was also investigated and shows that some transitions not allowed in quantum method play an important role on the mobility especially in $^2P_{3/2}$ krypton state.

A good qualitative agreement with the experiment has been obtained for all the three theoretical methods and both interaction models, which have all shown a plateau in the mobility data at low electric fields ($E/N \leq 100$ Td) followed by a drop at higher fields. A quantitative agreement has however been achieved only for the semi empirical inverse-method data and for the theoretical data obtained for higher electric fields ($E/N \geq 100 - 500$ Td). At low electric fields, quantitative differences are seen for the three purely theoretical approaches which, in general, underestimate the experiment. In general, interaction Model B leads to a better agreement with the experimental data than Model A, the quantum and semi-classical calculations provide basically the same data, and the hybrid method, if combined with interaction Model B, leads to data that are closest to the experiment. It is to note that calculated xenon mobility sets are qualitatively closer to experimental data than krypton ones.

There exist several stable isotopes of the krypton and xenon atom. Instead of considering all possible combinations of them in Rg^+ / Rg collisions, an artificial, "averaged" isotope has been considered to save the computational time. Calcula-

tion tests considering all the possible isotope combinations have been performed by using the computationally cheapest semi-classical method lead to only negligible deviations from the calculations performed with the artificial isotope.

Finally, characteristic diffusion energies (eD/K_0) have been calculated for interaction Model B and for both longitudinal and transverse diffusion coefficient. Only a slight dependence of the calculated values on the theoretical method used is seen for this transport parameter and also the difference between transverse and longitudinal diffusion is rather small. Alike, the correspondence between theoretical and pseudo-experimental inverse-method data is very good, which means that the characteristic diffusion energies are rather insensitive to the particular method used to calculate them.

To summarize, interaction Model B leads to quantitatively correct results, as compared to the experiment, and is thus preferred to be used in krypton and xenon ions scattering calculations. The hybrid method provides, despite the classical treatment of nuclei, realistic scattering data and can thus safely be used in calculations on collisions of molecular ions of rare-gas (Rg_2^+ or Rg_3^+) for which the quantum approach is very complicated. Calculations on collisions of molecular dimer (Rg_2^+) will be subject of next chapter.

Chapter 4

Ionic Dimer - Neutral Atom Collisions

This chapter is a direct continuation of Chapter 3. The only difference is that atom - atom collisions will be replaced with dimer - atom collisions here. Advantages of previous work will also be taken into account, $i.e$, using artificial isotope hypothesis, verified hybrid method and the knowledge about ion neutral interactions potentials. This chapter will cover an interesting area of collisions in plasma. Even if they are not dominant, they may be quite abundant at ambient conditions, and in order to model macroscopic plasma with high accuracy, all data calculated in this work are required. Like previous chapter, this chapter will be split in two parts, one covering krypton atoms and the other one covering xenon atoms. A final part will contain a conclusion of this chapter.

4.1 Selection of initial conditions

Compare to ionic atom, ionic dimer is more complicated to describe due to the different energy storage mechanism. While ionic atom can only store energy in different electronic levels (excited states), dimer can store energy via three different mechanisms, namely, vibrational, rotational, and electronic excitations. In this thesis both rotational and vibrational excitations will be studied. For dimer,

all the calculations were done in the lowest energy state ($I(1/2)_u$). However, different rotational-vibrational energy storage mechanisms will be studied. For two-atomic (in general, linear) molecules, only rotations around axes perpendicular to the bond axis are allowed. This gives two independent rotational degrees of freedom. In addition, there is only one vibrational mode available in a two-atomic molecule. The latter follows from a general formula providing the number of vibrational mode, $f_{vib} = 3N - 5 + A$ where N is the number of atoms in the molecule, A = -1 for a nonlinear molecule and 0 for a linear molecule. A schematic picture of vibrational states (ν) of a two-atomic molecule is given, both for harmonic approximation as well as with anharmonic corrections included, in figure 4.1.

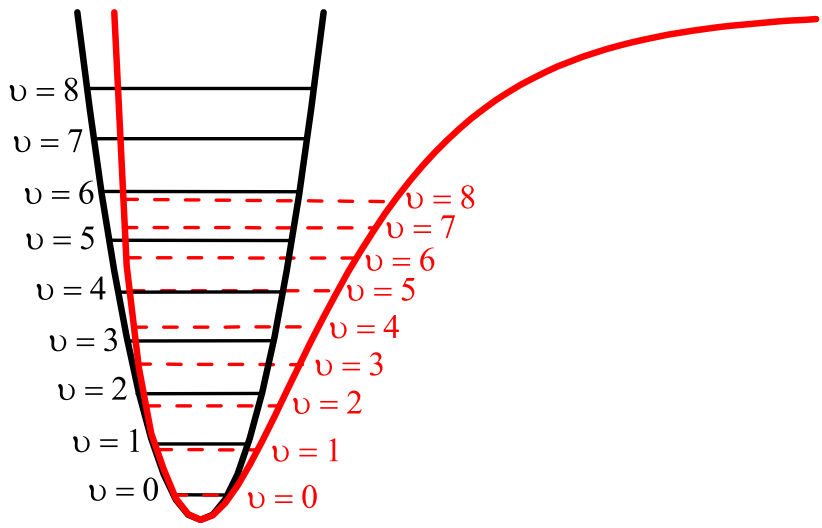

Figure 4.1: Schematic representation harmonic (black line) and anharmonic (red line) states with different vibration levels.

For an equilibrium distance, r_e, the minimum energy is reached between the two atoms. By increasing the vibrational/rotational excitation, a finite interval of distances is sampled and the maximum distance between the atoms extends as

the vibrational excitation increases. For each rotational-vibrational state an energy level is well defined, and it can be obtained, under the assumption of separability of vibrational and rotational degrees of freedom, by a sum of a vibrational contribution,

$$\mathrm{G}(\nu) = \omega_e(\nu + \frac{1}{2}) - \omega_e\chi_e(\nu + \frac{1}{2})^2, \tag{4.1}$$

where $\mathrm{G}(\nu)$ is related to the energy value for the vibrational mode, $E = hG(\nu)$, ν being the vibrational quantum number, ω_e the harmonic frequency and χ_e an anharmonicity constant, and a rotational part

$$\mathrm{F}_\nu(J) = \mathrm{B}_\nu J(J+1) - \mathrm{D}J^2(J+1)^2, \tag{4.2}$$

where $\mathrm{F}_\nu(J)$ is the rotational energy, J is the rotational quantum number, D is the centrifugal distortion constant and B_ν is the rotational constant

$$\mathrm{B}_\nu = \frac{h}{8\pi^2 c\mu r^2}. \tag{4.3}$$

By adding equations 4.1 and 4.2 we obtain:

$$E_{J\nu} = \mathrm{G}(\nu) + \mathrm{F}_\nu(J) = [\omega_e(\nu + \frac{1}{2}) + B_\nu J(J+1)] - [\omega_e\chi_e(\nu + \frac{1}{2})^2 + DJ^2(J+1)^2]. \tag{4.4}$$

The first term in square brackets on the r.h.s. of equation 4.4 can be used alone if a harmonic oscillator and rigid rotor are considered (harmonic approximation), if anharmonicity and centrifugal distortion are considered, the second bracket term has to be included. In figure 4.2, an anharmonic potential is depicted, presenting, schematically, different vibrational and rotational levels. The harmonic approximation and rigid molecule assumption may represent a good approximation for low rotation-vibrational excitation, typically under $\nu = 2$ or $J = 40$, after this the anharmonicity terms become too important for the former two approximations to provide correct internal energies of the dimer for cross-sections calculations.

The internal initial conditions of the Rg_2^+ ion are given by its rotational-vibrational state and its orientation in space. The rotational-vibrational energies and re-

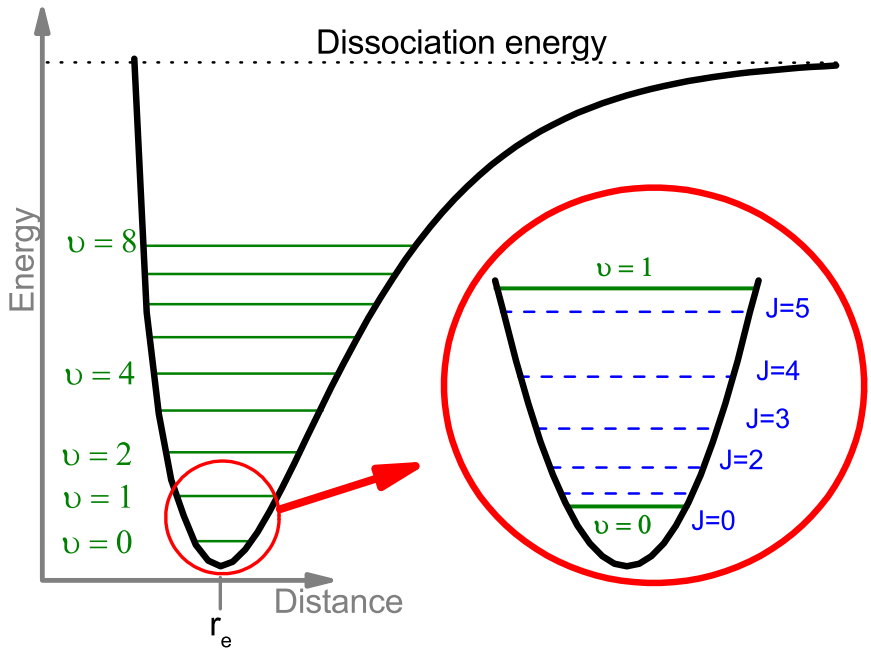

Figure 4.2: Schematic representation of different vibrational levels (green line), rotational levels (dashed blue line) and dissociation energy (dotted black line) for a ground-states dimer without harmonic approximation.

lated wave functions have been calculated by numerically solving the nuclear Schrödinger equation (see equation 2.30) on the electronic ground-state potential energy curve, $\mathrm{I}(1/2)_\mathrm{u}$,

$$-\frac{\hbar^2}{2\mu}\frac{\mathrm{d}^2\Psi_{J\nu}(r)}{\mathrm{d}r^2}+\left[V_{\mathrm{I}(1/2)_u}+\frac{\hbar^2 J(J+1)}{2\mu r^2}\right]\Psi_{J\nu}(r)=E_{J\nu}\Psi_{J\nu}(r), \tag{4.5}$$

where J and ν are rotational and vibrational quantum numbers, respectively, and $\mu = m/2$ is the effective mass of the Rg_2^+ dimer. A DVR representation of the wave function has been used with a Dirichlet boundary condition imposed, $\Psi_{J\nu}(0) = \Psi_{J\nu}(r_{\max}) = 0$ ($r_{\max} = 30$ a.u.), and with discretization step equal to $\Delta r = 0.02$ a.u.. For a particular rotational-vibrational state, the initial distances in the ion dimer have then been sampled from the square of $\Psi_{J\nu}$ and the kinetic energy have been calculated from current potential energy and the total rotational-

vibrational energy, $E_{J\nu}$. Corresponding velocities have then been added to both Rg_2^+ nuclei and oriented anti-parallelly along the dimer bond axis. After the vibrational state of the Rg_2^+ dimer has been set in this way, anti-parallel velocities perpendicular to the dimer bond axis have been added to the dimer nuclei so that the angular momentum corresponding to a specific choice of the rotational quantum number, J, is achieved. Finally, the dimer has been randomly oriented in space. In the present thesis, we denote a particular rotational-vibrational excitation of the Rg_2^+ dimer by [J=J, ν=ν]. For example, [J=0, ν=0] means that the dimer has been prepared, prior to collision, in the rotational-vibrational ground-state with $J = 0$ and $\nu = 0$.

For each particular choice of the Rg_2^+ rotational-vibrational state (J, ν), Rg_2^+ / Rg collision energy ($\mathrm{E_{coll}}$), and collision impact-parameter (b), totally 504 trajectories have been integrated for randomly oriented dimers until disintegration, either to $\mathrm{Rg}_2^+ + \mathrm{Rg}$ or $\mathrm{Rg}^+ + \mathrm{Rg} + \mathrm{Rg}$. A simple distance criterion has been used to detect the particular type of disintegration with the cut-off distance set to 20 Å. This means that about 150 000 trajectories have been used for each collision energy and Rg_2^+ rotational-vibrational excitation to calculate effective collision cross-sections.

4.2 Krypton

In this section, calculations for Kr_2^+ collisions in a krypton gas will be covered, this work has been reported in conference [103] and article [104]. Firstly, an introduction to experimental measurements will be shown, followed by a discussion about neutral potentials used in the DIM methodology. Afterwards calculated cross-sections will be presented. Following part will contain transport coefficient and dissociation rate and some calculated values (mobility) will be compared to experiments. Finally, conclusive remarks will close down this section.

4.2.1 Experimental data reported in literature

A summary of experimental reduced mobility available in literature is shown in figure 4.3. Biondi's *et al.* [92] values will be excluded from further comparison, effectively they are too much above other experimental values. By looking in following critical compilations of mobility done by Ellis *et al.* [88, 105], Biondi's *et al.* values, presented in the first edition, are replaced by Helm's *et al.* [106] one in the third edition. Varney's *et al.* [91] and Beaty's *et al.* [107] experimental mobility values cover a narrow range of reduced electric field but allow us to be confident on Helm's *et al.* measurements , at least in the electric field range covered by the two earlier measurements. For the most recent experimental values by Neves *et al.* [2], differences from previous sets of data are visible. Firstly, the absence of plateau at low field indicates that some impurities could have influence the measurements and, secondly, the evolution with the increasing reduced electric field allows us presume, that for 100-200 Td peak region, the values by Neves et al. would be considerably below previous experiments. Therefore, only Helm's *et al.* measurements will be kept for further comparison.

4.2.2 Neutral potentials

For cross-sections calculations, different interactions potentials were used as input for DIM models. Two sets of ion-neutral potentials introduced in section 3.1.1 and four different models for neutral - neutral interactions were used. For the ion-neutral potentials, the same labels will be used as in section 3.1.1 (namely Model A [53] and Model B [54]). The Kr_2 interaction potentials used will be indicated by a number added to the name of the Kr_2^+ interaction model, "1" for a semiempirical potential by Dham *et al.* [55], "2" for a *ab initio* potential by Waldrop *et al.* [56], "3" for a refit of previous *ab initio* potential done by Jäger *et al.* [57] and finally "4" for the *ab initio* potential calculated by Jäger *et al.* [57]. For example, interaction Model A1 will refer to interaction potential of Kr_2^+/Kr system using Model A for Kr_2^+ and Model 1 for Kr_2. Differences between these four neutral potentials can be observed in figure 4.4. The value of the well depth of all neu-

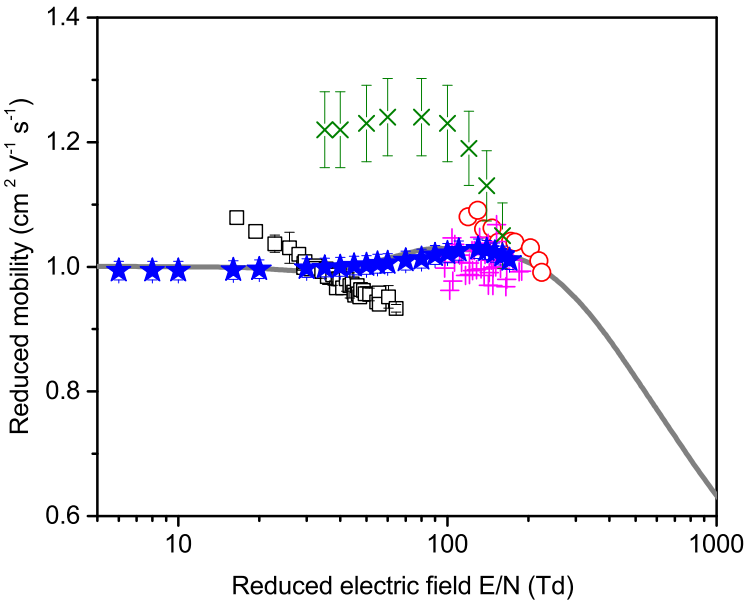

Figure 4.3: Summary of experimental data on reduced Kr_2^+/Kr mobility measured at close-to-ambient temperatures and normal pressure (P = 760 Torr): ○ Varney *et al.*[91] (T = 300 K), × Biondi & Chanin [92] as reported by Ellis *et al.* [88] (T = 300 K), + Beaty *et al.* [107] (T = 300 K), ⋆ Helm & Elford [106] (T = 295 K), □ Neves *et al.* [2] (T = 300 K). Inverse method data obtained from the experimental points by Helm & Elford [106] are also shown for comparison (straight gray line).

tral potentials are close to each other (-17.30 to -17.36 meV) and the long-distance interactions are as well very similar. However, major differences are present in the repulsive wall region (as visible in the inset of figure 4.4). Model 1 has the less repulsive part while Model 3 and Model 4 are much more repulsive at short distances. Model 2 is more repulsive than Model 1 but less repulsive than Models 3 and 4. Since Model 3 is a refit of the *ab initio* values of Model 2, one can already see that the repulsive wall is a difficult part of the interaction potential to be accurately provided from *ab initio* calculations. Model 1, being based on high-kinetic $Kr - Kr$ scattering experimental values, is considered as the most reliable at short distances and will be kept as main neutral potential in this work.

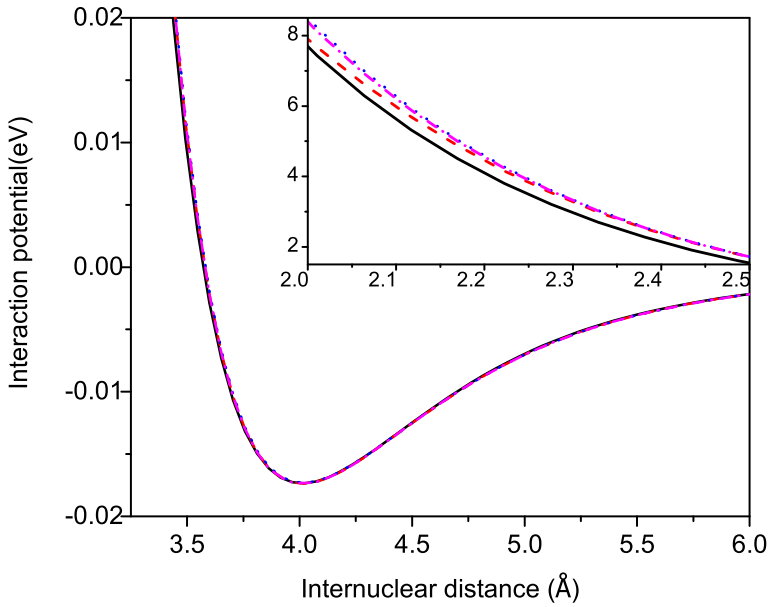

Figure 4.4: Neutral interaction potentials for the Kr_2 system: solid curve – semi-empirical potential by Dham *et al.* [55], dashed curve – *ab initio* potential by Waldrop *et al.* [56], dotted curve – *ab initio* potential by Jäger *et al.* [57], and dashed dotted curve – *ab initio* potential by Waldrop *et al.* refitted by Jäger *et al.* [57]. In the inset, a detailed view of the short-distance region is provided.

4.2.3 Cross-sections

For the Non-Reactive Scattering (NRS) channel, momentum transfer (MT) cross-sections are provided since the total cross-section diverges within the classical approximation if elastic scattering is included. This divergence can easily be removed by applying a MT approximation [101] in the cross-section calculations which, at the same time, introduces only negligible errors [64]. Following previous work on helium, neon, and argon, two MT cross-sections are considered, a usual one originally proposed for elastic scattering calculations,

$$\sigma_{\mathrm{NRS}}^{(\mathrm{MT1})} = \int_{4\pi} \left[\frac{\mathrm{d}\sigma}{\mathrm{d}\Omega}\right]_{\mathrm{NRS}} (1 - \cos\chi)\, \mathrm{d}\Omega, \tag{4.6}$$

and another previously proposed [25] for an approximate inclusion of non-elastic scattering effects due to rotation-vibrational excitations and/or desexcitations in the colliding dimer,

$$\sigma_{\mathrm{NRS}}^{(\mathrm{MT2})} = \int_{4\pi} \left[\frac{\mathrm{d}\sigma}{\mathrm{d}\Omega}\right]_{\mathrm{NRS}} \left(1 - \frac{p'}{p}\cos\chi\right) \mathrm{d}\Omega. \tag{4.7}$$

In equations 4.6 and 4.7, $[\mathrm{d}\sigma/\mathrm{d}\Omega]_{\mathrm{NRS}}$ represents the NRS differential cross-section, χ denotes the scattering angle, p' is a mean of the center-of-mass linear momentum magnitude of the Kr_2^+ dimer scattered into solid angle $\mathrm{d}\Omega$, and p is the magnitude of the Kr_2^+ momentum prior to collision. For the Collision Induced Dissociation (CID) channel, a usual total collision cross-section is used,

$$\sigma_{\mathrm{CID}}^{(\mathrm{int})} = \int_{4\pi} \left[\frac{\mathrm{d}\sigma}{\mathrm{d}\Omega}\right]_{\mathrm{CID}} \mathrm{d}\Omega, \tag{4.8}$$

since no divergence occurs within the classical theory in the case of scattering channels with a threshold.

4.2.3.1 Dependence of calculated cross-sections on ionic potentials

The performance of the DIM approach employed in the present calculations is mainly affected by the quality of the input ionic diatomic potentials. As a first step, we thus provide cross-sections calculated for the two sets of ionic potentials introduced above (Model A [53] and Model B [54]) and compare them with inverse method data (which are considered here as a substitute for missing experimental values). Results are summarized in figure 4.5. In this figure, collision cross-sections calculated for the Kr_2^+ dimer initially in the rotational-vibrational ground-state, [J=0, ν=0], are displayed. Both MT cross-sections of NRS and CID cross-sections are included, the former calculated either via equation 4.6 or using equation 4.7.

A first observation from figure 4.5 is that both methods of NRS cross-sections calculations (equations 4.6 and 4.7) give values very close to each other. This may mean that the Kr_2^+ momentum is (at least on the average) conserved during

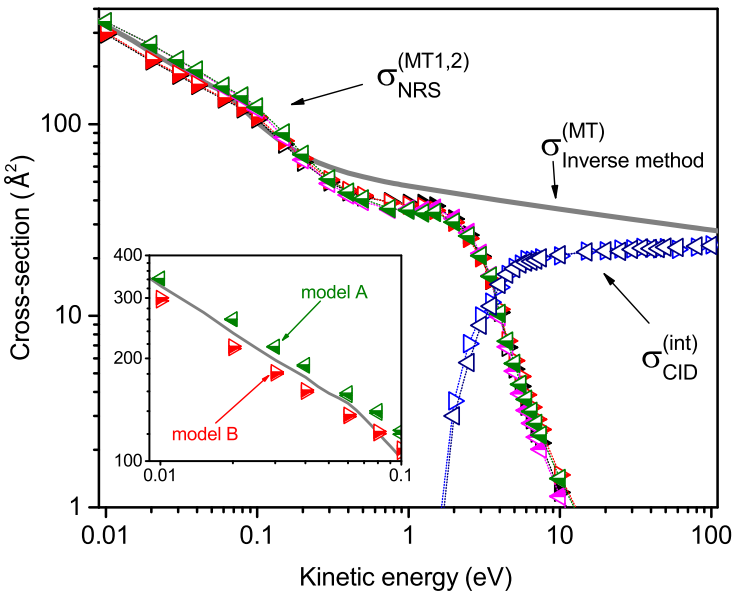

Figure 4.5: Comparison of theoretical predictions of Kr_2^+/Kr effective cross-sections calculated for the rotational-vibrational ground-state of the dimer, [J=0, ν=0]: left-oriented triangles (◁) – Model A, right-oriented triangles (▷) – Model B, half-filled symbols – momentum transfer cross-section for non-reactive scattering: upper half-filled symbols – $\sigma_{\mathrm{NRS}}^{(\mathrm{MT1})}$ (equation 4.6), lower half-filled symbols – $\sigma_{\mathrm{NRS}}^{(\mathrm{MT2})}$ (equation 4.7); empty symbols – dissociation cross-section ($\sigma_{\mathrm{CID}}^{(\mathrm{int})}$, equation 4.8), straight gray line – inverse method data based on the experiment of reference [106].

collisions with carrier gas atoms ($p = p'$), probably due to a negligible contribution of inelastic processes. Nevertheless, $\sigma_{\mathrm{NRS}}^{(\mathrm{MT2})}$ is preferred here and, if not specified otherwise, it will be used in subsequent analyses in the rest of the thesis.

Another observation related to NRS scattering is that, at low collision energies, MT cross-sections calculated for interaction Model A1 are systematically above the inverse method data, while the reverse holds for the data obtained from Model B1 (for a more detailed view see the inset of figure 4.5). Related mobilities will thus be sorted in a reverse order at low electric field and one can expect that Model A1 will underestimate, in the case of [J=0, ν=0], the mobility measurement. Moreover, as it follows from preceding calculations on neon [23]

and argon [25], increased rotational-vibrational excitation of the dimer decreases its mobility. Model A1 is thus expected to underestimate respective experiment regardless the initial rotational-vibrational state of the ion dimer. For Model B, on the other hand, considering rotational-vibrational excitations of the Kr_2^+ ion may lead to an improved agreement with the experiment. As a consequence, we can expect, in line with chapter 3.1 on Kr^+/Kr (see also reference [52]), that Model B1 describes the interactions between Kr_2^+ and Kr more accurately than Model A1 (see also subsection 4.2.4 for additional discussions).

Concerning $\sigma_{\mathrm{CID}}^{(\mathrm{int})}$, the differences between cross-sections calculated via Model A1 and Model B1 are much less pronounced than for NRS, which is particularly clear if one realizes that a log scale is used on the cross-section axis of figure 4.5. This compares well with a conclusion made with subchapter 3.1, namely that differences in the asymptotic parts of the ionic potentials are behind the observed differences in calculated mobilities (or related NRS cross-sections). Since the CID channel is prevailingly restricted to small values of the impact-parameter (the higher collision energy, the smaller impact-parameters contribute), mainly medium and short distances contribute. At these distances, however, both sets of ionic potentials are basically of the same quality and the calculated CID cross-sections are thus close to each other. Unfortunately, to our best knowledge there are no experimental cross-sections available in the literature to validate the overall accuracy of our theoretical estimates.

4.2.3.2 Dependence of calculated cross-sections on dimer rotational-vibrational excitations

Lot of rotational-vibrational states were studied in this work, only a few of them will be shown in figures. However, all of them are summarized in tables at the end of this thesis. The rotational-vibrational excitations studied, with excitations energies compared to ground-states (set at 0 meV) are summarized in table 4.1

The dependence of calculated cross-sections on the initial rotational-vibrational state of Kr_2^+ is shown in figure 4.6. Only data obtained for Model B1 are consid-

Rotational excitation (J)	Vibrational excitation (ν)	Internal energy (meV)
0	0	0
0	1	24
0	2	46
0	5	112
0	12	267
10	0	1
50	0	18
100	0	70
200	0	272

Table 4.1: Summary of rotational-vibrational excitations done on electronically ground-state dimer

ered, and two rotational and/or vibrational excitations, close in the excitation energy, are included and compared with the ground-state cross-sections ([J=0, ν=0]) of figure 4.5.

It is clear from figure 4.6 that the changes induced by the two kinds of excitations, either rotational or vibrational, are both qualitatively and even quantitatively (almost) identical, provided the energy pumped into the dimer is the same. While low excitations considered in figure 4.6 ([J=0, ν=1] and [J=50, ν=0], i.e., $\Delta\mathrm{E} \approx +20\,\mathrm{meV}$) induce, only very small changes in calculated cross-sections as compared to the ground-state, both for NRS as well as for CID, higher rotational-vibrational excitations ([J=0, ν=12] and [J=200, ν=0], $\Delta\mathrm{E} \approx +270\,\mathrm{meV}$) lead to considerably larger cross-section values. The observed enhancement of both NRS and CID cross-sections due to the rotational-vibrational excitation is rather easily understood since the (average) bond distance (geometric cross-section) of the Kr_2^+ ion growths up upon rotational-vibrational excitation due to anharmonic features in the Kr_2^+ interaction potentials. Noteworthy, the higher is the excitation, the more pronounced becomes the anharmonicity and, consequently, the larger change in the calculated cross-sections is observed. For CID, in addition, lowering of the dissociation threshold occurring in excited dimers (i.e., effectively a shift of the CID cross-section curve to lower collision energies) also contributes.

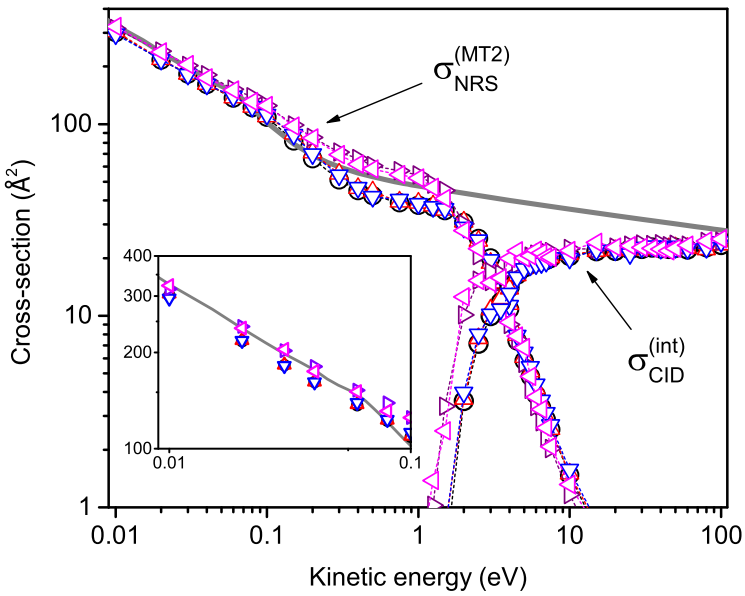

Figure 4.6: Dependence of Kr_2^+/Kr effective cross-sections on the dimer rotational-vibrational excitation (excitation energies are given in parentheses) as obtained from calculations performed for Model B1: ○ [J=0, ν=0], △ [J=0, ν=1] (+24 meV), ▷ [J=0, ν=12] (+267 meV), ▽ [J=50, ν=0] (+18 meV), ◁ [J=200, ν=0] (+272 meV). For comparison, inverse method momentum transfer cross-sections based on the experiment of reference [106] (straight gray line) are also shown.

As discussed above, the increase of the NRS cross-section induced by dimer excitation means that the mobility of excited Kr_2^+ ions will be decreased with respect to the rotational-vibrational ground-state. Since, at low collision energies, the cross-sections obtained for low and high rotational-vibrational excitations more or less bracket the inverse method cross-sections (see the inset of figure 4.6), one can expect that this will also be the case for mobilities, particularly in the low-field region. As a consequence, existence of an effective excitation can be anticipated which will lead to a good agreement between theoretical and experimental mobility data at low electric fields.

4.2.3.3 Dependence of calculated cross-sections on neutral potentials

Another ingredient that may influence the accuracy of the DIM model if applied to three-atomic, and larger ions, is the neutral - neutral potential. For a long time, semi-empirical potentials [55] adjusted to a broad range of experimental data have been used. Recently, however, a rapid progress in computational resources as well as in quantum chemistry methods has allowed delicate *ab initio* calculations employing high level correlation methods and extended basis sets which allow to treat weak van der Waals forces between neutral rare-gas atoms with an accuracy competitive to the level achieved by semi-empirical modeling. Among the most recent *ab initio* studies on the neutral krypton dimer, calculations by Waldrop *et al.* [56] and Jäger *et al.* [57] represent a benchmark. In this subsection, $\mathrm{Kr}_2^+/\mathrm{Kr}$ cross-sections calculated using these two newest *ab initio* potentials are compared with the data obtained for the semi-empirical potential by Dham *et al.* [55], otherwise exclusively used in this thesis for krypton.

Results of such comparison are shown in figure 4.7. Cross-sections obtained for the dimer initially prepared in the rotational-vibrational ground-state, [J=0, ν=0], and for a high vibrational excitation, [J=0, ν=12], are provided as calculated within Model B with four different neutral potentials considered: the semi-empirical potential [55], the two recent *ab initio* potentials [56, 57], and the potential of reference [56] refitted [57] by using the analytical representation of reference [57]. It is clear from this comparison that the four neutral potentials give basically the same CID cross-sections, but a more involved picture is seen for the NRS process and related MT cross-sections. While in the case of the ground-state dimer, [J=0, ν=0], no significant differences are seen, for the vibrationally excited dimer, [J=0, ν=12], a well pronounced difference is observed between values obtained from *ab initio* potentials on one hand and the values resulting from the semi-empirical potential on the other hand. More specifically, the use of the semi-empirical potential leads to increased values of the MT cross-section at low collision energies ($\mathrm{E_{coll}} < 1\,\mathrm{eV}$), while a bit smaller values, as compared to the data calculated from *ab initio* potentials, are obtained at higher energies

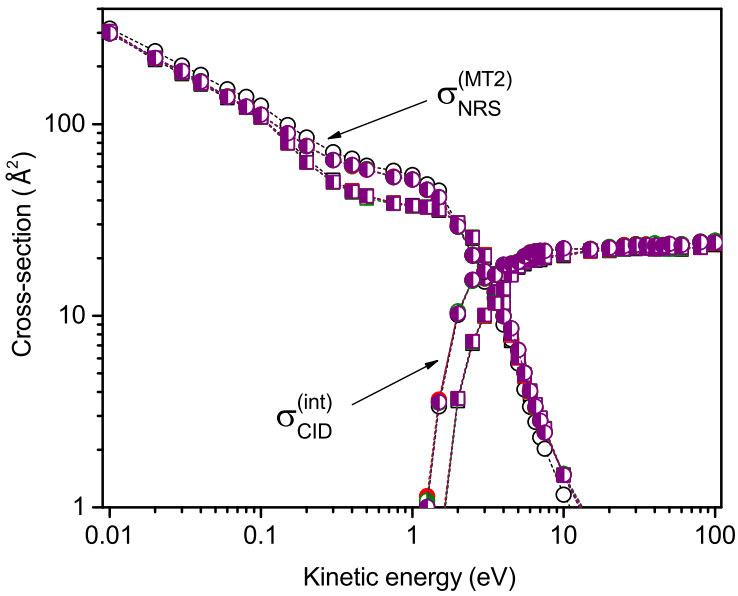

Figure 4.7: Dependence of Kr_2^+/Kr effective cross-sections on neutral potential used in the DIM model (Model B): □ – [J=0, ν=0], ○ – [J=0, ν=12]; empty symbols – semi-empirical potential by Dham *et al.* [55], upper half-filled symbols – *ab initio* potential by Waldrop *et al.* [56], right half-filled symbols – *ab initio* potential by Jäger *et al.* [57], left half-filled symbols – *ab initio* potential by Waldrop *et al.* refitted by Jäger *et al.* [57].

($E_{coll} > 5$ eV). Noteworthy, the MT cross-sections obtained for different *ab initio* potentials are more or less coincident.

The origin of the observed differences can be elucidated if one compares the four neutral potentials. In Figure 4.4, one can clearly see that the potentials are almost identical at large and intermediate internuclear distances but differ visibly at short range. In particular, the short-distance part of the semi-empirical potential is significantly less repulsive as compared to the *ab initio* potentials. Since distances in small ionic complexes of rare-gases are considerably reduced due to the attractive covalent and induction forces, it seems that the differences seen for the potentials at their short-distance parts are responsible for the observed differences in calculated cross-sections. At short distances, however, the semi-

empirical potential may be considered more reliable since a) it was fitted on state-of-the-art experimental data on high-energy Kr/Kr collisions (see reference [55] for details) and b) *ab initio*, though highly correlated calculations are known to overestimate the repulsion of closed shell rare-gas systems at short inter-atomic distances [108].

4.2.4 Mobilities

In this subsection, mobilities calculated from cross-sections reported in the preceding subsection are presented, discussed, and compared with experimental values. As argued in section 4.2.1, only the experimental measurement by Helm and Elford [106] and its inverse method extension will be considered for the comparison.

It should be also noted that, for the lowest electric fields considered, MT cross-sections are needed for $\mathrm{Kr}_2^+/\mathrm{Kr}$ collision energies which are below the values included in the dynamical calculation and reported in the preceding subsection ($\mathrm{E}_{\mathrm{coll}} \geq 0.01\,\mathrm{eV}$). To avoid expensive hybrid calculations in such a low-energy region leading to very long computational times, mainly due to a considerable fraction of long-lived orbiting trajectories, cross-sections provided in the preceding subsection have been extrapolated below $\mathrm{E}_{\mathrm{coll}} = 0.01\,\mathrm{eV}$ using a linear fit of the log-log plot performed for $\mathrm{E}_{\mathrm{coll}} = 0.01 - 0.06\,\mathrm{eV}$. No such extrapolation has been done, however, for the inverse method data which could easily be extended to any value of $\mathrm{E}_{\mathrm{coll}}$. Illustrative figure is visible in figure 4.8, one can see that the extrapolation follows the behavior of the inverse method values.

Normalized cumulative distributions as function of collision energy are shown in figure 4.9 for different reduced electric fields for Kr_2^+ in rotational-vibrational ground-state. This figure shows that dissociation of the dimer appears only from a certain energy (threshold value, 1.15 eV) and is not present for all reduced electric fields. For high reduced electric fields (< 500 Td), collision energy is high and the probability that the dimer is initially in $\mathrm{I}(3/2)_g$ or on higher electronic states is non negligible. Therefore, future calculations on $\mathrm{I}(3/2)_g$ state initial dimer elec-

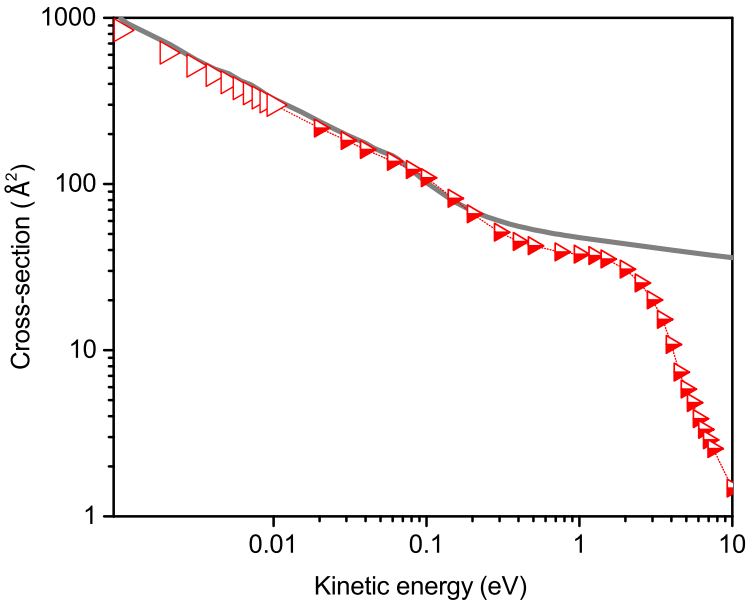

Figure 4.8: Illustrative figure of linear extension of MT cross-sections for Kr_2^+/Kr at the rotational-vibrational ground-state of the dimer, [J=0, ν=0]: lower half-filled(▷) – Model B1 $\sigma_{\mathrm{NRS}}^{(\mathrm{MT1})}$ (equation 4.6), empty ▷– Linear extension based on results of calculations, straight gray line – inverse method data based on the experiment of reference [106].

tronic state will be done to observe the influence of higher electronic states on mobility.

4.2.4.1 Dependence of calculated mobilities on ionic potentials

As for the cross-sections comparison, we start with an analysis of mobility data calculated for the two model sets of ionic potentials (Model A [53] and Model B [54]). Only the rotational-vibrational ground-state of the Kr_2^+ ion, [J=0, ν=0], is considered and the results are summarized in figure 4.10.

This figure shows a similar behavior of the dimer mobility as observed for previously studied systems, He_2^+ [21], Ne_2^+ [23], and Ar_2^+ [25], namely, a plateau in the low-field region, followed first by a maximum (at $E/N \approx 250$ Td and $E/N \approx 190$ Td for Model A1 and Model B1, respectively), and finally by a rapid drop of

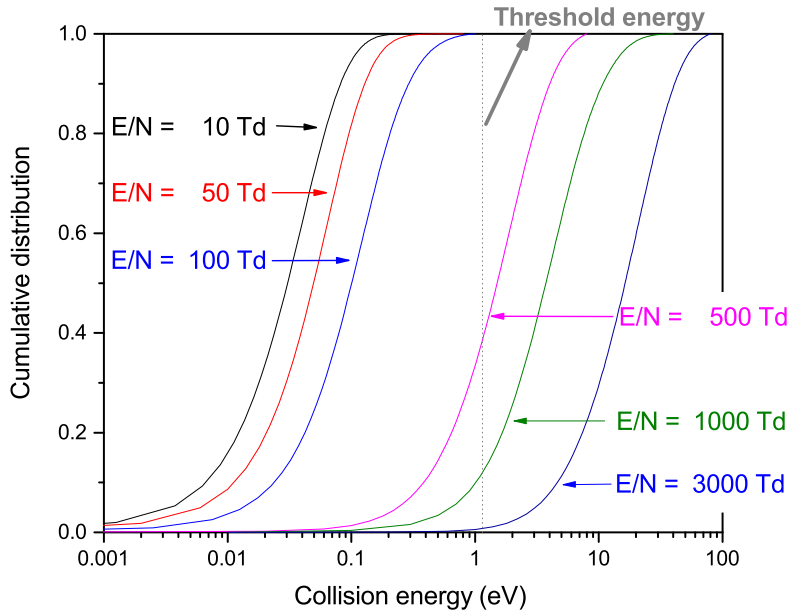

Figure 4.9: Cumulative distribution of [J=0, ν=0] Kr_2^+ collision energy for different reduced electric field.

mobility values in the high-field range. Like in previous studies, the maximum in the theoretical mobility curves is considerably shifted to stronger fields with respect to the experiment ($E/N \approx 130$ Td) with a much better estimate of the maximum position provided by Model B.

As expected from cross-section calculations, theoretical mobilities obtained for Model B1 overestimate the experiment in the plateau region ($E/N \leq 100$ Td) while the estimated calculated with Model A1 systematically lie here below the experimental points. Though the differences between respective mobility calculations based on $\sigma_{\mathrm{NRS}}^{(\mathrm{MT1})}$ and $\sigma_{\mathrm{NRS}}^{(\mathrm{MT2})}$ MT cross-sections are better pronounced than for cross-sections themselves, they do not change this general picture. If $\sigma_{\mathrm{NRS}}^{(\mathrm{MT2})}$ data are considered, the deviations from the experimental points (and/or from the inverse method curve which nicely reproduces them) are about -8% and 4% for Model A1 and B1, respectively.

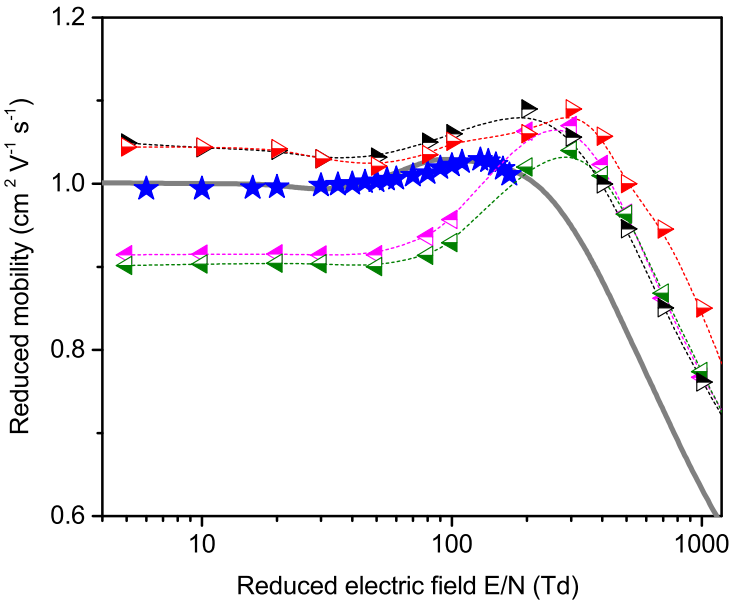

Figure 4.10: Comparison of theoretical predictions of Kr_2^+/Kr mobility calculated for the rotational-vibrational ground-state of the dimer, [J=0, ν=0]: left-oriented triangles (◁) – Model A, right-oriented triangles (▷) – Model B, upper half-filled symbols – mobilities calculated from $\sigma_{\mathrm{NRS}}^{(\mathrm{MT1})}$ (equation 4.6), lower half-filled symbols – mobilities calculated from $\sigma_{\mathrm{NRS}}^{(\mathrm{MT2})}$ (equation 4.7), ⋆ experimental data by Helm & Elford [106], straight gray line – inverse method data based on the experiment of reference [106].

Considering the results of our previous calculations on Ne_2^+ and Ar_2^+, we expect that the Kr_2^+ mobility will decrease with increasing rotational-vibrational excitations in the Kr_2^+ dimer. This means that mobilities obtained via Model B1 will move, in contrast to Model A1 data, towards the experiment as the Kr_2^+ excitation is increased. For this reason, we assume that, in agreement with the procedure adopted for the Kr^+/Kr system in section 3.3 (see also reference [52]), Model B1 may provide a better description of interactions in the Kr_2^+/Kr collision complex and, as a consequence, only mobility data calculated via Model B1 will hereafter be considered for further discussions.

4.2.4.2 Dependence of calculated mobilities on dimer rotational-vibrational excitations

Mobilities obtained from cross-sections calculated for rotationally-vibrationally excited Kr_2^+ dimers are shown in figure 4.11. Clearly, the observations resulting from this figure basically follow the conclusions made for underlying cross-sections.

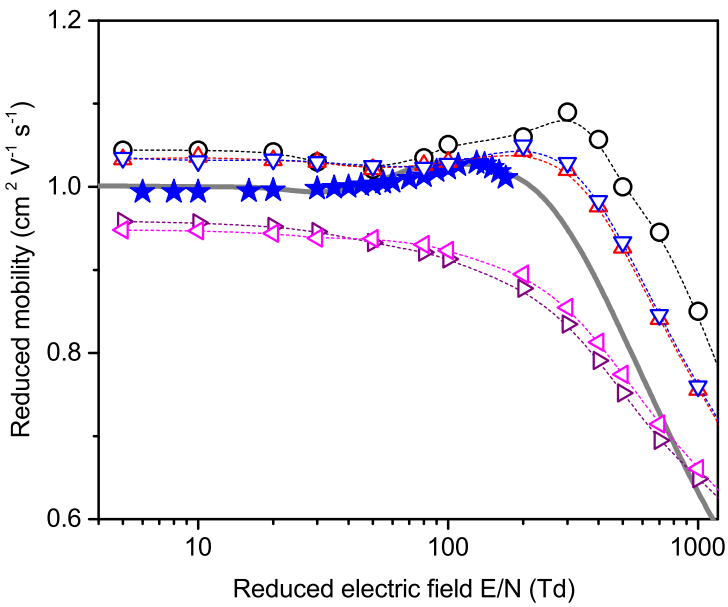

Figure 4.11: Dependence of the Kr_2^+/Kr mobility on the dimer rotational-vibrational excitation (excitation energies are given in parentheses) as obtained from calculations performed for Model B1 and using $\sigma_{\mathrm{NRS}}^{(\mathrm{MT2})}$ (equation 4.7): ○ [J=0, ν=0], △ [J=0, ν=1] (+24 meV), ▷ [J=0, ν=12] (+267 meV), ▽ [J=50, ν=0] (+18 meV), ◁ [J=200, ν=0] (+272 meV). For comparison, experimental data of reference [106] (⋆), and corresponding inverse method data (straight gray line) are also shown.

Firstly, the mobility seems to depend on the total excitation energy only and is rather insensitive to its distribution between dimer rotation and vibration degrees of freedom. More specifically, almost identical mobility values are obtained for excitations for which the extra energy stored in the vibrational and/or rotational

degrees of freedom of the Kr_2^+ dimer are close to each other (here, either [J=0, ν=1] and [J=50, ν=0], or [J=0, ν=12] and [J=200, ν=0]).

Secondly, small rotational-vibrational excitations ([J=0, ν=1] and [J=50, ν=0]) lead to data which are very close to the values obtained for the rotational-vibrational ground-state ([J=0, ν=0]) and, in the plateau region ($E/N \leq 100$ Td), and related calculations overestimate, like the ground-state calculations, the experimental mobility. Higher excitations ([J=0, ν=12] and [J=200, ν=0]), on the other hand, lead, in this region, to mobility values lying below the experiment. As a consequence, the low-excitation and high-excitation mobility data bracket the experiment.

This bracketing can be used to roughly estimate the (average) excitation in the experimental dimer population. If the mobility data obtained for the lowest electric field ($E/N = 5$ Td) are specifically considered, we obtain, by a linear interpolation, an average excitation energy of $\Delta\mathrm{E} \approx 142$ meV needed to reproduce the experimental point. If, in addition, equipartition of this energy is presumed between rotational and vibrational degrees of freedom, the following average excitations are predicted for experimental dimers: $\bar{v} \approx 3$ and $\bar{j} \approx 100 - 120$. Since, under ambient conditions ($T = 300$ K), these average values should read $\bar{v} \approx 0.7$ and $\bar{j} \approx 54$, the experimental population of Kr_2^+ seems to be overheated ($T_{\mathrm{Kr}_2^+} \approx 650 - 700$ K). Many effects may contribute. First of all, the ionic dimers may be formed in highly excited states, maybe even electronically excited states either through an associative ionization reaction called Hornbeck-Molnar process [109, 110],

$$\mathrm{Kr}^* + \mathrm{Kr} \rightarrow \mathrm{Kr}_2^+ + \mathrm{e}^-, \tag{4.9}$$

where asterisk denotes a (high) electronic excitation in the (neutral) krypton atom, or by a *three-body associative reaction*,

$$\mathrm{Kr}^+ + \mathrm{Kr} + \mathrm{Kr} \rightarrow \mathrm{Kr}_2^+ + \mathrm{Kr}. \tag{4.10}$$

And, secondly, some heating may also result from ions acceleration via the ap-

plied external field. Moreover, the experimental dimer population needs not be fully thermalized.

4.2.4.3 Dependence of calculated mobilities on neutral potentials

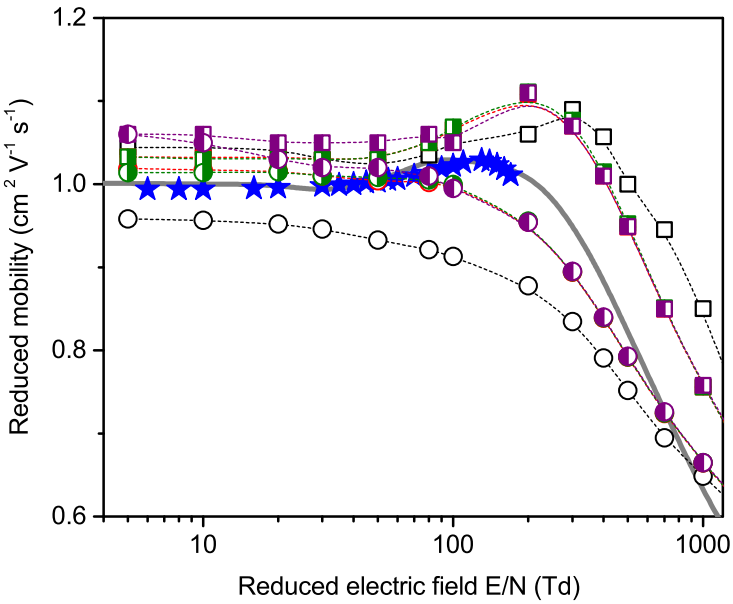

Figure 4.12: Dependence of the Kr_2^+/Kr mobility calculated from $\sigma_{NRS}^{(MT2)}$ (equation 4.7) on neutral potential used in the DIM model (Model B): squares – [J=0, ν=0], circles – [J=0, ν=12]; empty symbols – semi-empirical potential by Dham *et al.* [55], upper half-filled symbols – *ab initio* potential by Waldrop *et al.* [56], right half-filled symbols – *ab initio* potential by Jäger *et al.* [57], left half-filled symbols – *ab initio* potential by Waldrop *et al.* refitted by Jäger *et al.* [57]. For comparison, experimental data of reference [106] ($\star$) and corresponding inverse method data (straight gray line) are also shown.

Mobilities of Kr_2^+ calculated from cross-sections obtained for different neutral potentials employed in the DIM model are shown in figure 4.12. As expected from related cross-section data (see figure 4.7), a replacement of the semi-empirical neutral potential [55] with one of the *ab initio* potentials [56, 57] induces changes in calculated mobility only for high rotational-vibrational excitations of the Kr_2^+ dimer (here, [J=0, ν=12]). Indeed, we see from figure 4.12 that the

mobilities calculated using different neutral potentials lie on one another for the rotational-vibrational ground-state while significant deviations are observed between the *ab initio* potentials on one hand and the semi-empirical potential on the other hand for excited dimer (with different *ab initio* neutral potentials yielding almost identical data). The situation fully complies with what has been observed for cross-sections, just the differences are magnified. Interestingly, the *ab initio* potentials lead, in the low-field region, to considerably higher Kr_2^+ mobility estimates for the excited dimer ([J=0, ν=12]) than the semi-empirical potential and they even overestimate the experimental data. As a consequence, much higher excitations would have to be presumed to reproduce the experiment. This means that an even higher overheating of the experimental population of Kr_2^+ dimers is predicted for the *ab initio* potentials than for the semi-empirical one.

4.2.5 Diffusion coefficients

Longitudinal, eD_{L}/K_0, and transverse, eD_{T}/K_0, characteristic diffusion energies have also been calculated since they represent an important ingredient of macroscopic plasmas modelings. They are summarized, as obtained for models B1 and B4, in figure 4.13. For clarity, only data calculated for [J=0, ν=0], and for a Kr_2^+ excited state, [J=0, ν=12] are considered.

Quite surprisingly, we notice from this figure that, in contrast to the Kr_2^+ mobility, both characteristic diffusion energies are almost insensitive to the neutral potential used. The other observations, however, remain basically the same as those made for the mobility data. In particular, increased rotational-vibrational energy leads to a well seen decrease in the characteristic diffusion energies, and the (pseudo experimental) inverse method curves, both longitudinal and transversal, are better reproduced by excited hybrid data, [J=0, ν=12], then by the ground-state ones, [J=0, ν=0].

We further notice that the longitudinal diffusion energy increases faster for the ground-state, [J=0, ν=0], then for vibrationally excited dimer, [J=0, ν=12]. This enhanced growth is seen up to $E/N \approx 500\,\mathrm{Td}$ (the mean CMS collision en-

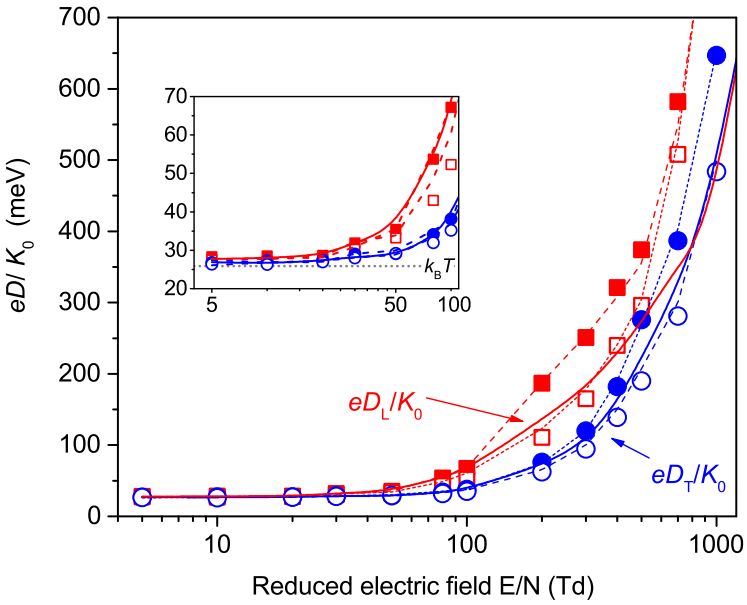

Figure 4.13: Longitudinal (□) and transverse (○) characteristic diffusion energies of the Kr_2^+ ion in krypton gas calculated for interaction Model B1, the semi-empirical potential for neutral - neutral interactions [55], and $\sigma_{\mathrm{NRS}}^{(\mathrm{MT2})}$: filled symbols – [$J$=0, ν=0], empty symbols – [J=0, ν=12]. Dashed lines close to respective symbols represent data obtained for Model B4. For comparison, inverse method data (solid lines) based on experimental mobilities of reference [106] are also shown. In the inset, a magnified view of the low-filed region is provided.

ergy of the $\mathrm{Kr}_2^+/\mathrm{Kr}$ complex corresponding to this field strength is about $\mathrm{E}_{\mathrm{coll}} \approx 2\,\mathrm{eV}$), then both longitudinal diffusion curves become more or less coincident at higher fields. This can be related to the threshold energy of the Kr_2^+ dissociation ($D_0 \approx 1.17\,\mathrm{eV}$ for the ground-state, $\mathrm{I}(1/2)_{\mathrm{u}}$ potential) which dominates at higher collision energies.

As expected, longitudinal and transverse characteristic diffusion energies coincide in the low-field region ($E/N \leq 30\,\mathrm{Td}$) when they form a typical plateau ($eD_{\mathrm{L}}/K_0 \approx eD_{\mathrm{T}}/K_0 \approx 27\,\mathrm{meV}$). This observation compares well with a value following from the Nernst-Townsend-Einstein equation, $eD/K_0 \rightarrow k_{\mathrm{B}}T$ as $E/N \rightarrow 0\,\mathrm{Td}$ ($k_{\mathrm{B}}T = 25.3\,\mathrm{meV}$ for $T = 300\,\mathrm{K}$). The longitudinal characteristic diffusion en-

ergy then becomes higher than the value obtained for transverse diffusion as the field strength is increased ($E/N \geq 30$ Td), which is an expected effect of the extra force acting on the dimer ion via the applied electric field.

4.2.6 Dissociation rate constants

Finally, theoretical estimates of the rate constant, k_{CID}, of the collision induced dissociation (CID) of the Kr_2^+ ion (equation 2.24) are presented and discussed. Data calculated for the ground-state dimer, [J=0, ν=0], as well as for selected excited states (either vibrationally [J=0, ν=12] or rotationally [J=200, ν=0]) are displayed in figure 4.14. All the data have been calculated using the ionic potentials of Model B and, like above, two representative neutral potentials have been considered for comparison, the semi-empirical potential [55] and the most recent *ab initio* potential [57]. Since, to our best knowledge, no experimental data exist on the $\mathrm{Kr}_2^+/\mathrm{Kr}$ dissociation, no comparison with experiment can be provided.

Like for the diffusion characteristic energies, the values of the dissociation rate constant are only marginally influenced by the neutral potential used, both neutral potentials considered here yield almost identical values over the whole range of the reduced electric field. Moreover, even the rotational and vibrational excitations affect the dissociation of Kr_2^+ only marginally and at rather high reduced electric fields ($E/N \geq 1000$ Td). In this range of the electric field, the Kr_2^+ disintegration is slightly enhanced for excited dimers, the enhancement being, in line with previous observations, independent of whether the excitation energy has been pumped into vibrational or rotational degrees of freedom.

We also notice in the inset of figure 4.14 that the threshold electric field of the CID of the Kr_2^+ ion is around $E/N \approx 150$ Td (depending on the internal excitation of the colliding dimer). At this field, the corresponding mean collision energy is around $\mathrm{E_{coll}} \approx 0.3$ eV which is significantly below the Kr_2^+ binding energy provided for its electronic ground-state by Model B1 ($D_0 \approx 1.17$ eV). However, the distribution of $\mathrm{Kr}_2^+/\mathrm{Kr}$ collision energies becomes rather broad as the strength of the electric field grows. For example, while at $E/N = 100$ Td almost all collisions

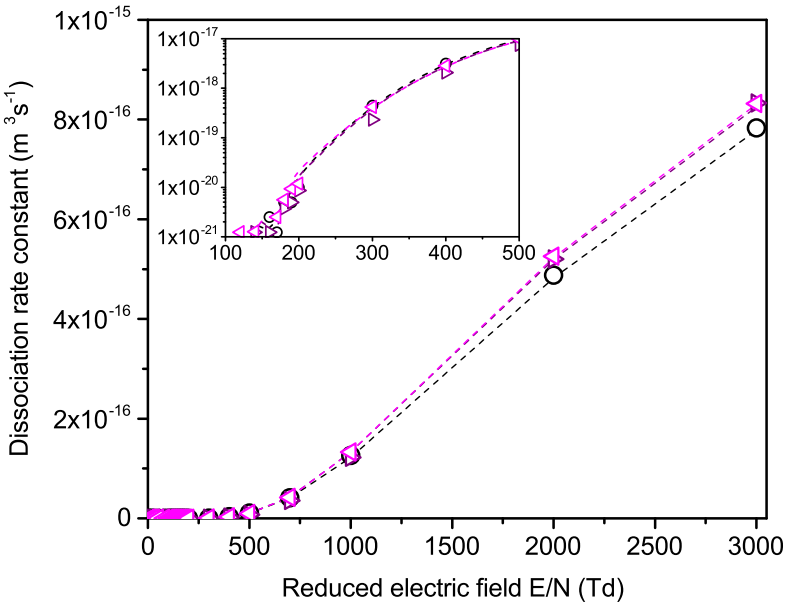

Figure 4.14: Rate constant of the Kr_2^+ collision-induced dissociation calculated for interaction Model B1, the semi-empirical potential for neutral - neutral interactions [55], and $\sigma_{\mathrm{NRS}}^{(\mathrm{MT2})}$: ◯ [$J$=0, ν=0], ▷ [J=0, ν=12], ◁ [J=200, ν=0]. Dashed lines close to respective symbols represent data obtained for Model B4. In the inset, a magnified view of the CID threshold region is provided (note that a logarithmic scale is used on the vertical axis in the inset).

run at energies which are lower that the theoretical dissociation threshold (D_0), almost 10% of them have enough energy to disintegrate even the rotationally-vibrationally ground-state dimer at E/N = 200 Td.

4.3 Xenon

This sub-chapter will follow the layout of the previous one on Kr_2^+. This means that first experimental data available in literature will be presented, then the neutral potentials for Xe_2 will be discussed and finally calculated cross-sections, mobilities and diffusion coefficients derived from this cross-sections will be presented and analyzed. This work has already been presented in a conference [111]

4.3.1 Experimental data reported in literature

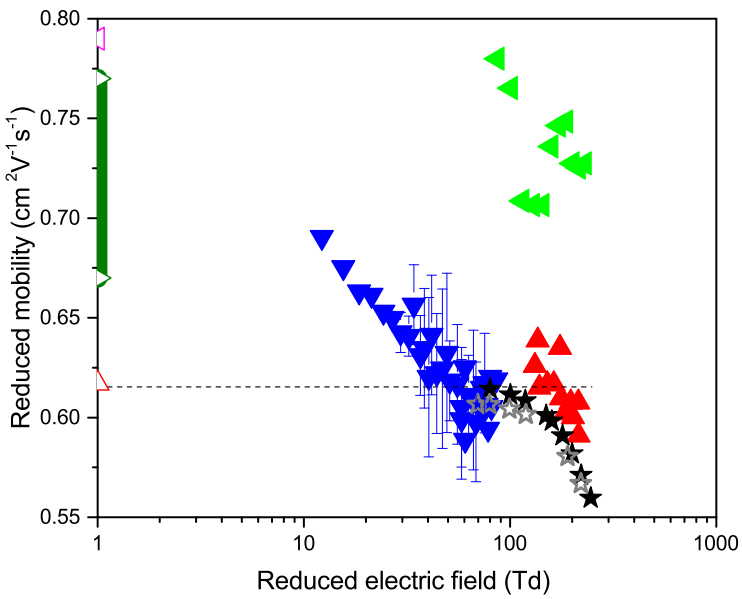

Figure 4.15: Summary of experimental data on reduced Xe_2^+/Xe mobility: fulfilled △ Varney *et al.* [91], fulfilled ▽ Neves *et al.* [2], fulfilled ☆ Helm [110], empty ☆ Larsen *et al.* [97]. Predicted values at E/N= 0 Td done by Neves *et al.* [112] on experimental values: Interval between empty ▷ [91], empty ◁ [92], empty △ [110]. Short dotted line represents an artificial plateau set at K_0 = 0.615 cm^{2}V^{-1}s^{-1}.

Multiple experimental data sets of mobility are available in literature for Xe_2^+/Xe system, all of them are depicted in figure 4.15. The oldest set, provided by Var-

ney *et al.* [91] in 1952 represents reduced mobility for a short range of reduced electric field [E/N = 130 - 210 Td] with a predicted value in the range K_0 = 0.67-0.77 cm^{2}V^{-1}s^{-1} at E/N = 0 Td [112]. Helm [110] and Larsen *et al.* [97] reported measurements for a broader range of the reduced electric field than Varney [E/N = 70 - 200 Td]. Interestingly, while the results of references [110] and [97] are almost identical to each other, they deviate rather significantly from the older measurement of Varney *et al.* A decreasing part is observed on both sets of values. Furthermore, value extrapolated to E/N = 0 Td was provided by Neves *et al.* [112]. Since a typical behavior of reduced mobility consists of a plateau at low fields followed by a peak at intermediate fields and a fast decreasing region at high fields, one can extend the measurements reported by Helm *et al.* [110] to the zero field mobility predicted by Neves [112]. Biondi's *et al.* measurements [92] are well above all the other reported values and are therefore excluded for further comparison. Most recent measurements reported by Neves *et al.* [2] [E/N = 12- 85 Td] present a strange behavior at low fields. Effectively, Neves data shows an increase in the mobility instead of the expected plateau. This can be due to a contamination by Xe_3^+ trimers which can't be discriminated due to the absence of mass spectrometer in their experimental setup. Presence of Xe_3^+ in xenon plasma have already been evidenced in references [110] and [113]. The following monomer accretion processes have been proposed to be responsible for their creation,

$$\begin{aligned} \mathrm{Xe}^+ + \mathrm{Xe} + \mathrm{Xe} &\rightarrow \mathrm{Xe}_2^+ + \mathrm{Xe} \\ \mathrm{Xe}_2^+ + \mathrm{Xe} + \mathrm{Xe} &\rightarrow \mathrm{Xe}_3^+ + \mathrm{Xe}. \end{aligned} \tag{4.11}$$

Moreover, ion drift velocity experiment [112] shows that it is difficult to distinguish between the mobility values of Xe_2^+ and Xe_3^+ ions without mass spectrometer. If we only look on highest values of the electric field considered by Neves [E/N = 36 - 85 Td] and Varney's values, an average value can be extracted at K_0 = 0.615 cm^{2}V^{-1}s^{-1}. This value will be kept as the value of the plateau, making a hypothesis that Neves values have been corrupted at low field and that the plateau is not as high as their data may indicate. For further considerations, only Helm's

and Larsen's values will be considered together with the estimated plateau. Like for krypton, the inverse method is used to extrapolated measured values outside the experimental range of the reduced electric field. Based on the discussion of the quality of available experimental data, only Helm's and Varney's values have been considered for the inverse method treatment.

4.3.2 Neutral potentials

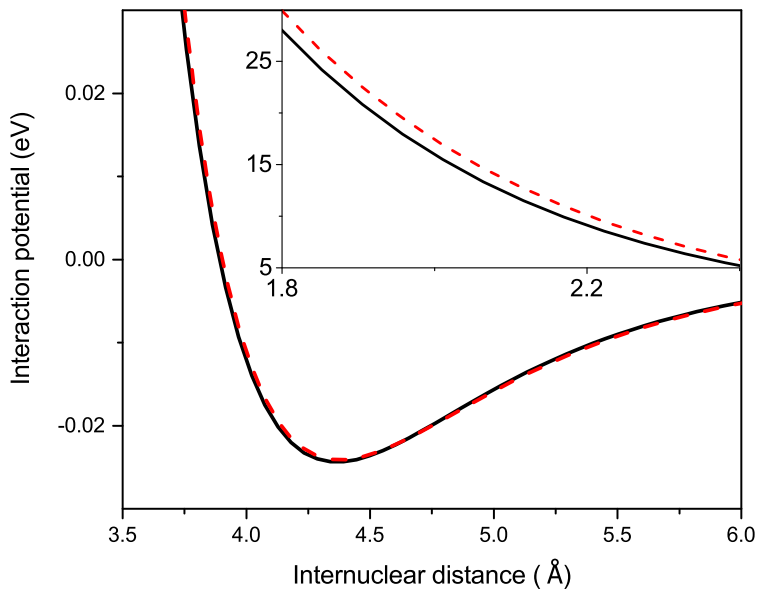

Figure 4.16: Neutral interactions models used for Xe_2 system. Black full curve : Model 1 [114], red dashed curve : Model 2 [69].

Two different neutral potentials were tested for Xe_2 interactions. The same denomination will be used as for krypton, a letter will be used to denominate the interaction potentials for Xe_2^+ ("A" for potentials taken from reference [67] and "B" for potentials of reference [96]) and a digit will be used to denominate the Xe_2 interaction potential. For xenon, only two highly accurate neutral potentials were found in literature and used as input for DIM models. The first one, denoted as

neutral Model 1, is provided by Aziz *et al.* [114]. This model is based on a broad range of experimental data covering all relevant parts of interatomic distances. The other neutral potential used in our calculations (Model 2) was reported by Hellmann *et al.* [69]. This semi-empirical model is based on accurate *ab initio* calculations. Both models are shown in figure 4.16. For both models, the well depths are well defined and close to each other in values (respectively -24.33 meV and -24.12 meV). Alike, long part interactions are similar for both models. The repulsive walls, in contrast, are not the same for both models. Model 1 has a less repulsive wall than Model 2. However, Model 1 may be considered more reliable in this range of atomic distance since a) it was fitted on state-of-the-art experimental data on high-energy Xe/Xe collisions (see reference [55] for details) and b) *ab initio*, though highly correlated calculations are known to overestimate the repulsion of closed shell rare-gas systems at short inter-atomic distances [108].

4.3.3 Cross-sections

4.3.3.1 Dependence of calculated cross-sections on ionic potentials

Differences in MT cross-sections calculated using the two ionic models (Model A and Model B) and neutral Model 1 are clear from in figure 4.17, most visible difference is seen between 0.2 eV and 2 eV where Model A1 provides larger MT cross-sections than Model B1. Concerning the dissociation cross-sections, both interaction models provide the same values. Due to small variations between both sets of cross-sections, resulting mobilities behavior should be close to each other. As in the krypton case, $\sigma_{\mathrm{NRS}}^{(\mathrm{MT1})}$ is close to $\sigma_{\mathrm{NRS}}^{(\mathrm{MT2})}$. This may mean that the Xe_2^+ momentum is (at least on the average) conserved during collisions with carrier gas atoms ($p = p'$), probably due to a negligible contribution of inelastic processes. Nevertheless, as for krypton, $\sigma_{\mathrm{NRS}}^{(\mathrm{MT2})}$ is preferred here and, if not specified otherwise, it will be used in subsequent analyses.

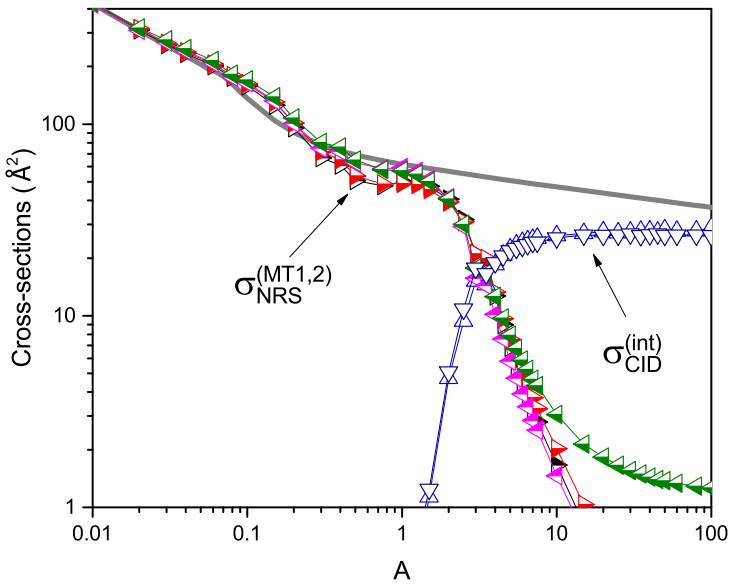

Figure 4.17: Comparison of theoretical predictions of Xe_2^+/Xe effective cross-sections calculated for the rotation-vibrational ground-state of the dimer, [J=0, ν=0]: left-oriented triangles (◁) – Model A1, right-oriented triangles (▷) – Model B1, half-filled symbols – momentum transfer cross-section for non-reactive scattering: upper half-filled symbols – $\sigma_{\mathrm{NRS}}^{(\mathrm{MT1})}$ (equation 4.6), lower half-filled symbols – $\sigma_{\mathrm{NRS}}^{(\mathrm{MT2})}$ (equation 4.7); empty symbols – dissociation cross-section ($\sigma_{\mathrm{CID}}^{(\mathrm{int})}$, equation 4.8), thick grey line – inverse method data based on the experiment of references [97, 110].

4.3.3.2 Dependence of calculated cross-sections on dimer rotational-vibrational excitation

Lot of rotational-vibrational states were studied in this work, only a few of them will be shown in figures. However, all of them are summarized in tables at the end of this thesis. The rotational-vibrational excitations studied, with excitations energies compared to ground-states (set at 0 meV) are summarized in table 4.2

Figure 4.18 depicts the variation of cross-sections depending on the internal rotation-vibrational excitation. Only selected excitations, 2 vibrational excitations ([J=0, ν=2] and [J=0, ν=12]) and 2 rotational ones ([J=60, ν=0] and [J=200, ν=0]),

Rotational excitation (J)	Vibrational excitation (ν)	Internal energy (meV)
0	0	0
0	1	15.1
0	2	30.1
0	4	59.8
0	8	117.8
0	12	173.8
60	0	12.6
70	0	17.1
90	0	28.2
100	0	34.8
100	1	49.7
200	0	137.5

Table 4.2: Summary of rotational-vibrational excitations done on electronically ground-state dimer

are shown to preserve readability of the figure. Two different type of behavior are visible depending on the way used to store the internal energy. If the vibrational level increases, the cross-section $\sigma_{\mathrm{NRS}}^{(\mathrm{MT2})}$ remains mostly the same while the $\sigma_{\mathrm{CID}}^{(\mathrm{int})}$will increase significantly. For rotational excitations, $\sigma_{\mathrm{CID}}^{(\mathrm{int})}$will increase slightly while $\sigma_{\mathrm{NRS}}^{(\mathrm{MT2})}$ decreases for low energy (< 0.15 eV) and remains mostly constant after.

The enhancement of dissociation cross-section is due to two different mechanisms. Firstly, internal excitation of a dimer will diminish the gap between Xe_2^+ and the dissociate state, as is visible especially for rotational excitation. Secondly, this excitation will lead to an increased linear size of the dimer and, with longer internuclear distance, the dissociation is facilitated. Interestingly, the behavior observed for rotational excitation at low kinetic energy is not the same as for krypton. Here rotation seems to decrease the resulting cross-sections. This will lead to a significant difference from previous calculation on krypton. For xenon, the internal energy storage mechanism, either rotational or vibrational, leads to qualitatively different behavior patterns. In particular, rotational excitations of the xenon dimer, in contrast to krypton and other rare-gases, decreases the MT

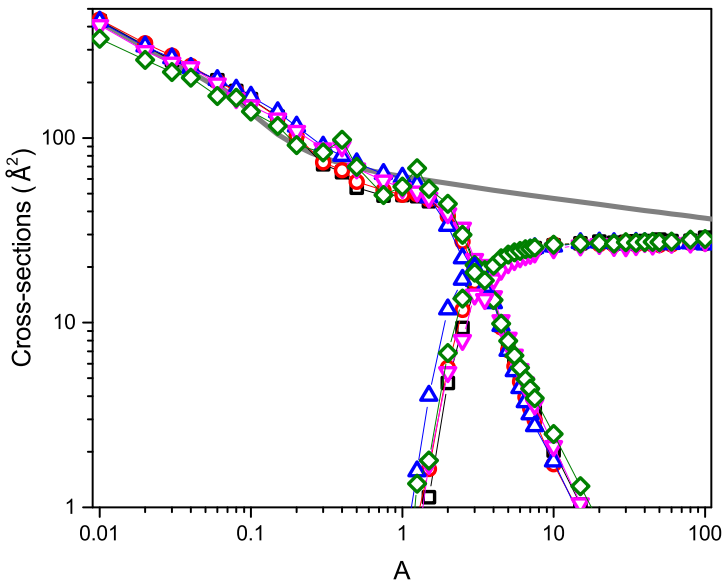

Figure 4.18: Dependence of Xe_2^+/Xe effective cross-sections on the dimer rotation-vibrational excitation (excitation energies are given in parentheses) as obtained from calculations performed for Model B1: □ [J=0, ν=0], ◯ [J=0, ν=2] (+30.1 meV), △ [J=0, ν=12] (+173.8 meV), ▽ [J=60, ν=0] (+12.6 meV), ◇ [J=200, ν=0] (+137.5 meV). For comparison, inverse method momentum transfer cross-sections based on the experiment of references [97, 110] (thick gray line) are also shown.

cross-section and, as a consequence, will increase xenon dimer mobility.

4.3.3.3 Dependence of calculated cross-sections on neutral potentials

The exchange of the neutral potential in the DIM model leads to variations for high excited states only, as already visible in the case of Kr_2^+/Kr system. As visible in figure 4.19, where only rotational-vibrational ground-state and the highest vibrational and rotational states considered in this work are shown, $\sigma_{\mathrm{CID}}^{(\mathrm{int})}$is slightly changed upon employing the *ab initio* neutral potential for all three rotation-vibrational states of Xe_2^+ considered. Concerning $\sigma_{\mathrm{NRS}}^{(\mathrm{MT2})}$, a swap of neutral potential from Model 1 [114] to Model 2 [69] will decrease MTCSs for excited states

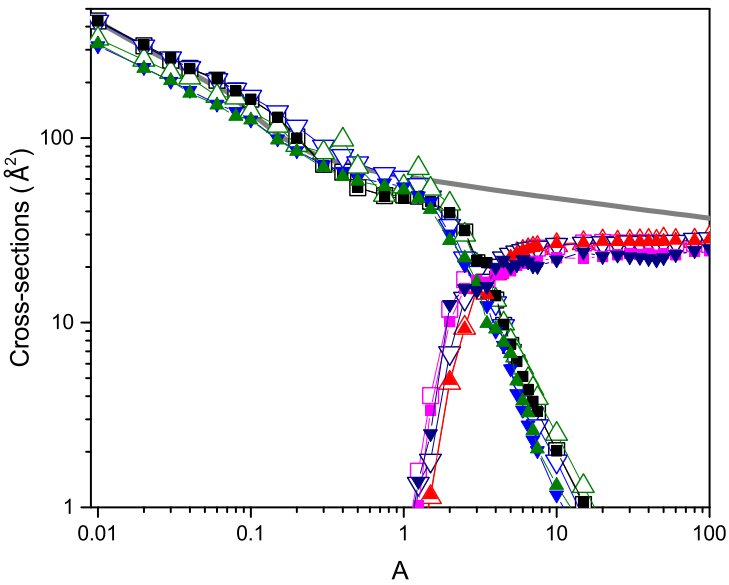

Figure 4.19: Dependence of Xe_2^+/Xe effective cross-sections on neutral potential used in the DIM model (Model B): □ [J=0, ν=0], △ [J=200, ν=0] (+137.5 meV), ▽ [J=0, ν=12] (+173.8 meV); empty symbols – Model 1 [114], filled symbols – Model 2 [69]. For comparison, inverse method momentum transfer cross-sections based on the experiment of references [97, 110] (thick gray line) are also shown.

only. Interestingly, using this second neutral potential, MTCSs of [J=0, ν=12] are almost on the same values as MTCS of [J=200, ν=0] even if their intern energies are not the same. However, a difference between both is more visible on the $\sigma_{\mathrm{CID}}^{(\mathrm{int})}$ where vibration induce dissociation cross-sections at lower energies, but rotation induce higher values once the $\sigma_{\mathrm{NRS}}^{(\mathrm{MT2})}$ are near zero. One can say that all model used in this DIM methodology are highly accurate and provide close results.

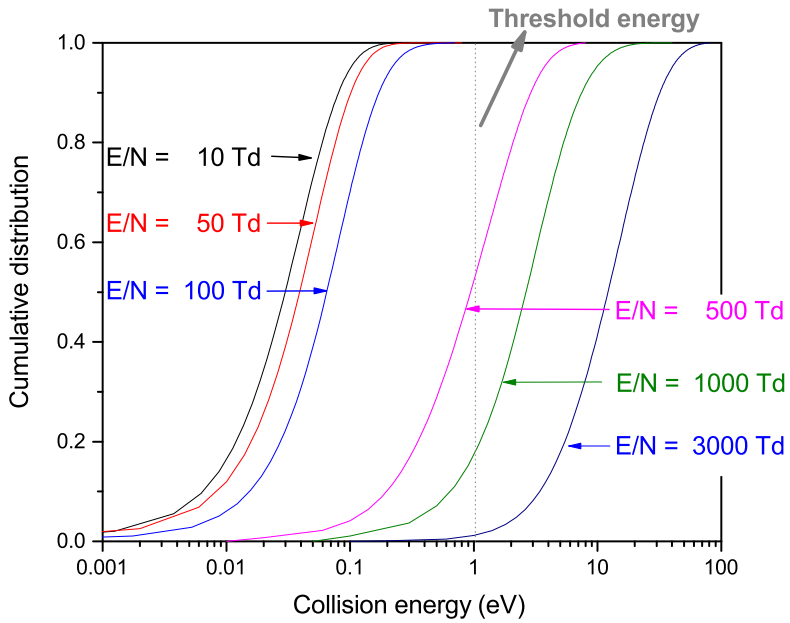

Figure 4.20: Cumulative distribution of [J=0, ν=0] Xe_2^+ collision energy for different reduced electric fields.

4.3.4 Mobilities

4.3.4.1 Dependence of calculated mobilities on ionic potentials

Normalized cumulative distributions as function of collision energy are shown in figure 4.20 for different reduced electric fields for Xe_2^+ in rotational-vibrational ground-state. This figure shows that dissociation of the dimer appears only from a certain energy (threshold value, 1.03 eV) and is not present for all reduced electric fields. Compared to krypton, the threshold energy is lower and therefore the dissociation channel will be more influent than krypton one in the same energy range.

Comparison between Model A1 and Model B1 shows a proximity of the two sets of results if one look to the mobilities. In figure 4.21, it is visible that the plateau for Model B1 is slightly above the one obtained for Model A1 but both plateau remain close to each other ($\approx$ 4%). However, the maximum of the mo-

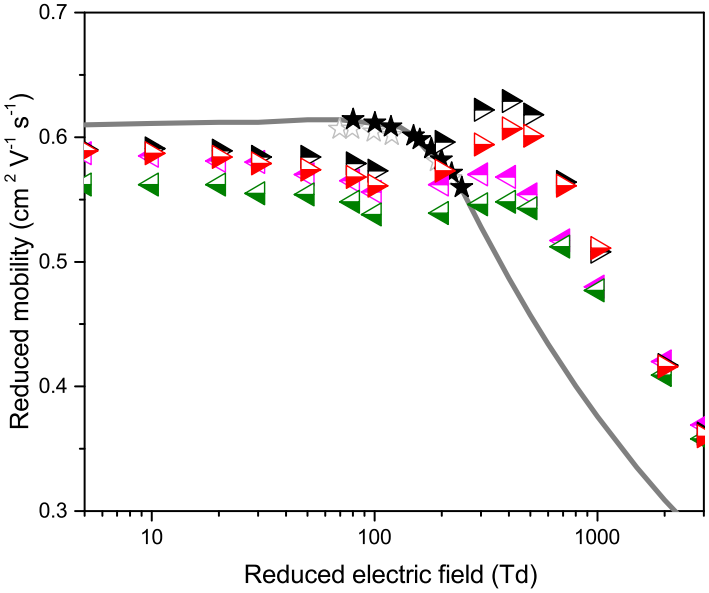

Figure 4.21: Comparison of theoretical predictions of Xe_2^+/Xe mobility calculated for the rotation-vibration ground-state of the dimer, [J=0, ν=0]: left-oriented triangles (◁) – Model A1, right-oriented triangles (▷) – Model B1, upper half-filled symbols – mobilities calculated from $\sigma_{\mathrm{NRS}}^{(\mathrm{MT1})}$ (equation 4.6), lower half-filled symbols – mobilities calculated from $\sigma_{\mathrm{NRS}}^{(\mathrm{MT2})}$ (equation 4.7), fulfilled ☆ Helm's *et al.* experimental data [110], empty ☆ Larsen *et al.* experimental data [97], thick grey line – inverse method data based on the experiment of references [97, 110].

bility profile shows a bigger difference. Model B1 provides a higher peak and thus closer mobility to Varney's one. This has led us to use Model B in further calculations reported later in this section. However, new experiments around the peak or in the decreasing region may be needed to justify our choice.

The harmonic approximation approach to sample initial configurations of the xenon in Xe_2^+/Xe collision was, as in the case of krypton, used and compared to non-approximate sampling method based on the vibrational wave function obtained from a numerical solution of nuclear Schrödinger equation considering the anharmonic dimer ground-state potential. Even through the difference between both calculations should be close to zero at low vibrational excitations and differ-

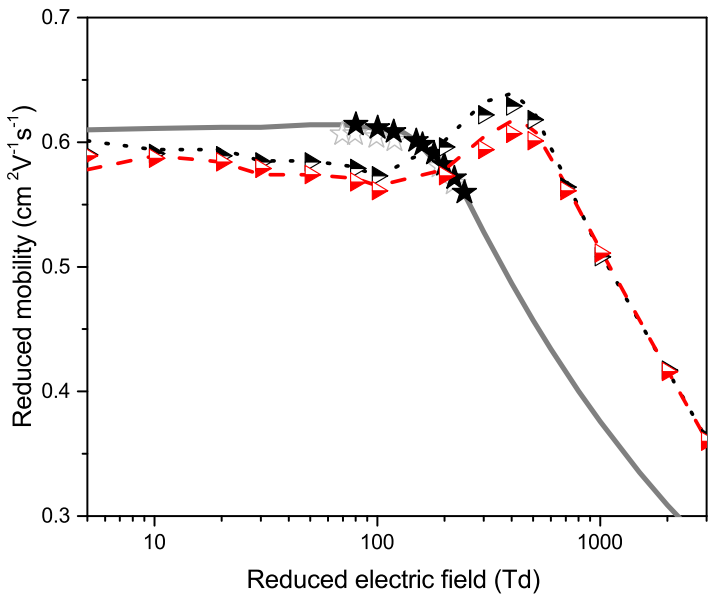

Figure 4.22: Comparison of harmonic approximation and non-approximate energy values for Xe_2^+/Xe mobility calculated for the rotation-vibrational ground-state of the dimer, [J=0, ν=0]: right-oriented triangles (▷) – Model B1 without approximation, upper half-filled symbols – mobilities calculated from $\sigma_{\mathrm{NRS}}^{(\mathrm{MT1})}$ (equation 4.6), lower half-filled symbols – mobilities calculated from $\sigma_{\mathrm{NRS}}^{(\mathrm{MT2})}$ (equation 4.7), Harmonic approximate on Model B1, dotted curve – mobilities calculated from $\sigma_{\mathrm{NRS}}^{(\mathrm{MT1})}$ (equation 4.6), dashed curve – mobilities calculated from $\sigma_{\mathrm{NRS}}^{(\mathrm{MT2})}$ (equation 4.7), fulfilled ☆ Helm's *et al.* experimental data [110], empty ☆ Larsen *et al.* experimental data [97], thick grey line – inverse method data based on the experiment of references [97, 110].

ences should only appear at higher excitations, it is always a good point to verify approximate calculations. In figure 4.22, it is well seen that the values obtained within the harmonic approximation and the anharmonic ones are close to each other.

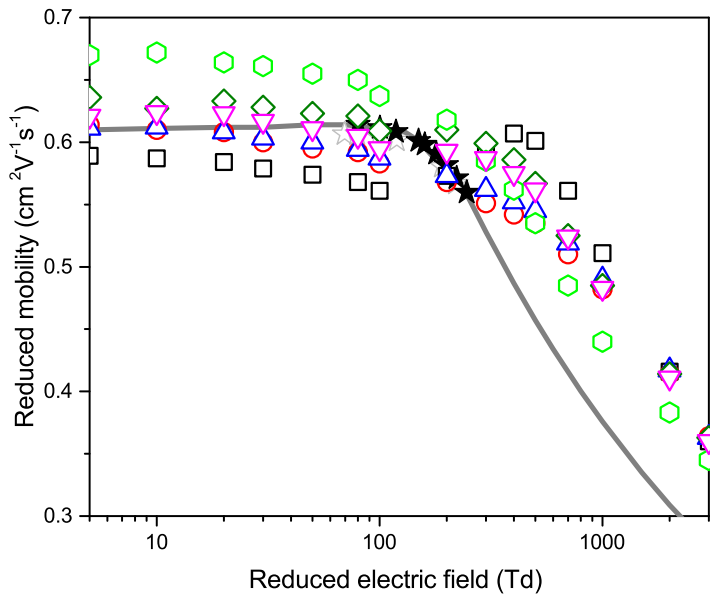

Figure 4.23: Dependence of the Xe_2^+/Xe mobility on the dimer rotational excitation (excitation energies are given in parentheses) as obtained from calculations performed for Model B1 and using $\sigma_{\mathrm{NRS}}^{(\mathrm{MT2})}$ (equation 4.7): □ [J=0, ν=0] ○ [J=60, ν=0] (+12.6 meV), △ [J=70, ν=0] (+17.1 meV), ▽ [J=90, ν=0] (+28.2 meV), ◇ [J=100, ν=0] (+34.8 meV), ⬡ [J=200, ν=0] (+137.5 meV). fulfilled ☆ Helm's *et al.* experimental data [110], empty ☆ Larsen *et al.* experimental data [97], thick grey line – inverse method data based on the experiment of references [97, 110].

4.3.4.2 Dependence of calculated mobilities on dimer rotational-vibrational excitation

Raising up dimer rotational excitation will enhance mobilities as is visible in figure 4.23. For low excitations (< 18 meV) the peak of mobility decreases and the plateau moves up. With higher rotational excitation, the mobility plateau continues to raise up and its further enhancement of the plateau leads to a disappearance of the peak. Interestingly, contrary to the krypton case, with a particular value of rotational excitation, +34.8 meV [J=100, ν=0] for example, resulting mobilities are on the experimental values.

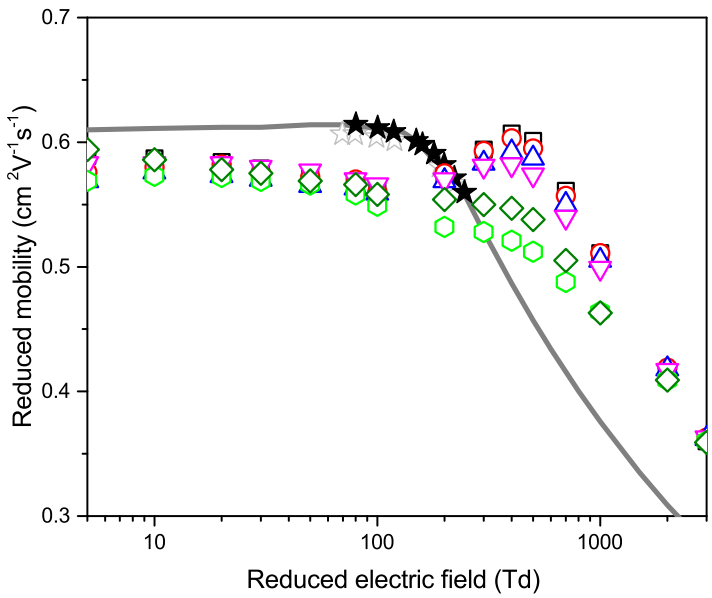

Figure 4.24: Dependence of the Xe_2^+/Xe mobility on the dimer vibrational excitation (excitation energies are given in parentheses) as obtained from calculations performed for Model B1 and using $\sigma_{\mathrm{NRS}}^{(\mathrm{MT2})}$ (equation 4.7): □ [J=0, ν=0] ○ [J=0, ν=1] (+15.1 meV), △ [J=0, ν=2] (+30.1 meV), ▽ [J=0, ν=4] (+59.8 meV), ◇ [J=0, ν=8] (+117.8 meV), ⬡ [J=0, ν=12] (+173.8 meV). For comparison, fulfilled ☆ representing Helm's *et al.* experimental data [110], empty ☆ for Larsen *et al.* experimental data [97] and thick grey line depicting inverse method data based on the two experiments of references [97, 110].

The influence of xenon dimer vibrational excitation on its mobility is illustrated in figure 4.24. As is visible in this figure, vibrational excitation in the ionic xenon dimer does not seem to have a huge influence on the value of the plateau. The position of the plateau is more or less stable as the vibrational excitation of the xenon dimer increases. The peak, however, like for the rotational excitations, decreases with enhancement of internal vibrational energy.

A detailed view of how the the Xe_2^+ mobility is influenced by selected vibrational excitations is given in figure 4.25. First, vibrational excitations are analyzed for non-rotating dimers ($J = 0$). Three of the four presented variations have the same enhancement of excitation energy (≈ +15 meV) distributed in the dimer vi-

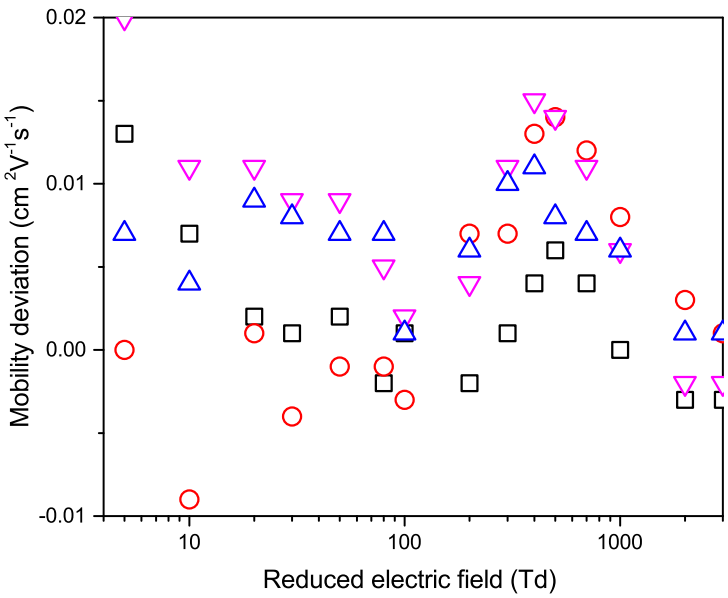

Figure 4.25: Dependence of the Xe_2^+/Xe mobility on the dimer vibrational excitation between different rotational-vibrational levels (excitation energies are given in parentheses) as obtained from calculations performed for Model B1 and using $\sigma_{\mathrm{NRS}}^{(\mathrm{MT2})}$ (equation 4.7): □ [J=0, ν=0] $\longmapsto$ [J=0, ν=1] (+15.1 meV), ○ [J=100, ν=0] $\longmapsto$ [J=100, ν=1] (+15 meV), △ [J=0, ν=1] $\longmapsto$ [J=0, ν=2] (+15 meV), ▽ [J=0, ν=0] $\longmapsto$ [J=0, ν=2] (+30.1 meV). Values presented here are obtained as mobility calculated for initial state minus values obtained for final state.

brational mode and the last one ([J=0, ν=0] $\longmapsto$ [J=0, ν=2]) has a gap twice more energetic than the others. By looking at reduced electric fields below E/N = 100 Td, the enhancement of the vibrational energy leads to a sight decrease of the mobility (particularly visible at E/N = 5 Td). However, if rotationally excited dimer is considered (J = 100 in figure 4.25), the vibration enhancement does not play major role in th low field region. Concerning higher reduced electric field, the change of the mobility peak value depends on the dimer internal energy more visibly. It is interesting to see that increasing of vibrational excitation (with a similar energy gap) leads to similar peak variations more or less independent of the initial state.

4.3.4.3 Dependence of calculated mobilities on neutral potentials

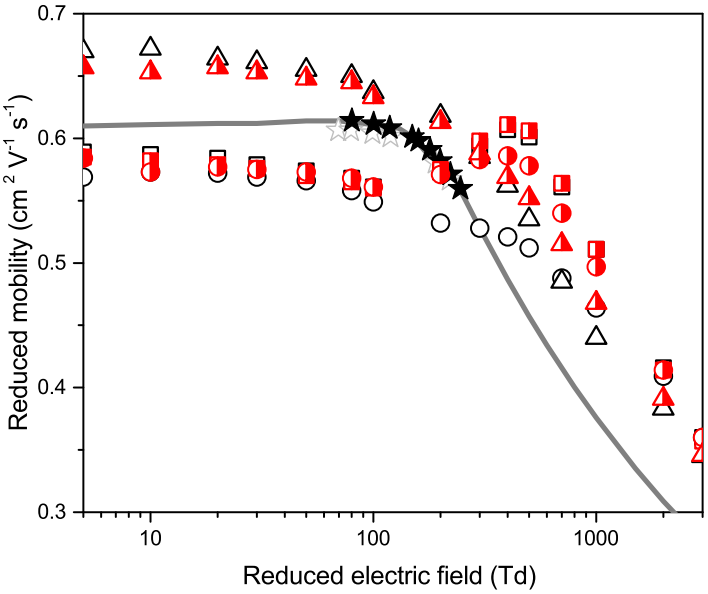

Figure 4.26: Dependence of the Xe_2^+/Xe mobility calculated from $\sigma_{NRS}^{(MT2)}$ (equation 4.7) on the neutral potential used in the DIM model (Model B): □ – [J=0, ν=0], ○ – [J=0, ν=12], △ – [J=0, ν=200]; empty symbols – Neutral Model 1 [114], red right half-filled symbols – Neutral Model 2 [69]; fulfilled ☆ Helm's *et al.* experimental data [110], empty ☆ Larsen *et al.* experimental data [97], thick grey line – inverse method data based on the experiments of references [97, 110].

Exchange of neutral potentials in the DIM model yields interesting results as is visible in figure 4.26. For clarity, only ground-state ([J=0, ν=0]) and highly excited dimers ([J=200, ν=0] and [J=0, ν=12]) are considered in figure 4.26. Clearly, the difference in the repulsive wall of the neutral interaction potentials has a major role concerning mobility values. While the plateau region is more or less the same independently of the neutral potential used, significant differences are seen between the two neutral interaction models in the high-field region region where high-energy collisions are expected during which repulsive, high energy parts of the neutral interaction potentials are sampled. For rotational excitation or for

small vibrational excitation, the peak and the decreasing part of the mobility profile are similar for the two neutral models. However, for higher vibrational states, the *ab initio* neutral model (Model 2 [69]) yields a well pronounced peak in the mobility profile while no peak is seen in the semi-empirical Model 1 data.

4.3.5 Diffusion coefficients

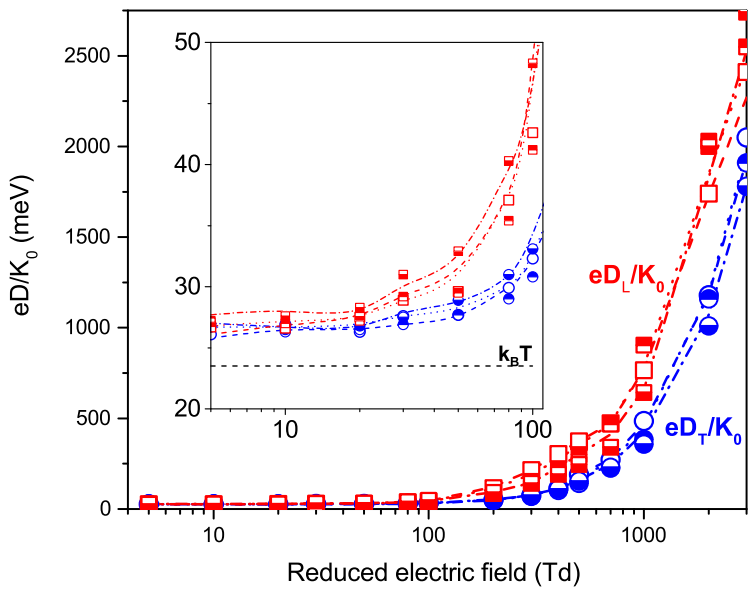

Figure 4.27: Longitudinal (◯) and transverse (□) characteristic diffusion energies of the Xe_2^+ ion in xenon gas calculated for interaction Model B1, $\sigma_{\mathrm{NRS}}^{(\mathrm{MT2})}$: empty symbols – [$J$=0, ν=0], upper half-filled symbols – [J=0, ν=12], lower half-filled symbols – [J=200, ν=0]. (lines for Model B2: dashed – [J=0, ν=0], dotted – [J=0, ν=12], dashed dotted – [J=200, ν=0])

Calculated values of drift (transverse and longitudinal diffusion) coefficients are presented in figure 4.27. At low field (5 Td) both coefficients are in good correlation with the value predicted for $E/N = 0$ Td one from Nernst-Townsend-Einstein equation ($eD_T \approx$ 26.1 meV, $eD_L \approx$ 26.7 meV as compared with the value of 25.3 meV obtained for $T = 300$ K). This comparison allows us to be confident in

our calculations. Choice of neutral interaction potential does not play a big role for these parameters, as is visible in figure 4.27. Variation of both drift coefficients due to internal excitation of the dimer is not important. However it is more visible for the transverse coefficient than for the longitudinal coefficient. Like in the krypton case or for neon [23], the values of the longitudinal diffusion coefficient (eD_L) is above transverse ones.

4.3.6 Dissociation rate constants

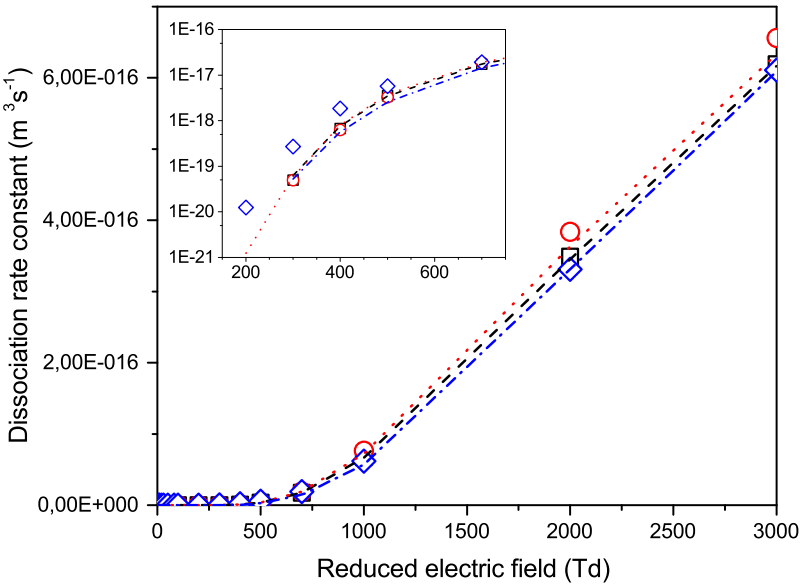

Figure 4.28: Rate constant of the Xe_2^+ collision-induced dissociation calculated for interaction Model B1 (semi-empirical neutral potential [114]) and$\sigma_{\mathrm{NRS}}^{(\mathrm{MT2})}$: □ [$J$=0, ν=0], ○ [J=0, ν=12], ◇ [J=200, ν=0]. Dashed, dotted and dashed dotted lines close to respective symbols represent data obtained for Model B2 (*ab initio* neutral potential [69]). In the inset, a magnified view of the dissociation threshold region is provided (note that a logarithmic scale is used on the vertical axis).

Collision induced dissociation rate constants calculated for interaction Models B1 and B2 and for selected rotational-vibrational states of the colliding Xe_2^+

dimer are summarized in figure 4.28. Since basically similar features are seen in this figure as discussed before for krypton, only brief comments are attached here. At medium field, the dissociation rate constant calculated using Model B1 is dependent on the dimer vibrational excitation while the rotational level does not seem important, as is visible in figure 4.28. Only for the vibration excitation level considered in figure 4.28, the choice of neutral potential influences calculated dissociation rates at low field. Interestingly, the values of dissociation rate constant is not highly dependent on the choice of the neutral potential.

4.4 Conclusions

A computational study is presented here extending a previous chapter on collisions of atomic rare-gas ions, Rg^+, to collisions of ionic diatoms, Rg_2^+. Collisions of diatomic ions of krypton (Kr_2^+) and xenon (Xe_2^+) with atoms of respective carrier gas have been studied numerically using a semi-emprical interaction method based on the *Diatomics In Molecules* approach and hybrid dynamical approach (classical description of nuclei and quantum treatment of electrons). Subsequently, Monte Carlo simulations have been applied to convert calculated dynamical data to mesoscopic transport properties of krypton and xenon diatomic ions such as their mobility, diffusion coefficients, and dissociation rate constants.

Within the *Diatomics In Molecules* approach [50] applied to rare-gas ions [49, 51], the effective electronic Hamiltonian is constructed from diatomic interaction energies of both the diatomic ion, Rg_2^+ (Rg = Kr and Xe), and the diatomic neutral, Rg_2. Two model sets of ionic potentials have been tested, Model A ([53] for krypton and [63] for xenon) and Model B ([54] for krypton and [96] for xenon). In addition, several neutral diatomic potentials have been considered, including benchmark semi-empirical potential ([55] for krypton and [114] for xenon) and recent *ab initio* potentials ([56, 57] for krypton and [69] for xenon) among which the semi-empirical potentials still seem to represent a best choice.

Using the advantage of being able to process electrons using quantum formalism and nuclei classically, the hybrid method makes it possible to obtain different cross-sections (Non Reactive Scattering and Collision-Induced Dissociation) in a precise manner with different possible rotational-vibrational levels. Effective cross-sections have been calculated for collisions of the ionic diatom with krypton and xenon atoms. Specifically, momentum transfer cross-sections have been calculated for non-reactive collisions, $\mathrm{Rg}_2^+ + \mathrm{Rg} \rightarrow \mathrm{Rg}_2^+ + \mathrm{Rg}$, and total cross-sections for the collision-induced dissociation of the ionic dimer, $\mathrm{Rg}_2^+ + \mathrm{Rg} \rightarrow \mathrm{Rg}^+ + \mathrm{Rg} + \mathrm{Rg}$. Momentum transfer approximation was used to avoid divergence of cross-sections for low impact parameters in calculations. Thousands of trajectories have been integrated in this way for each particular collision energy to get converged cross-sections. A broad range of collision energies has been considered ($\mathrm{E}_{\mathrm{coll}} = 0.01 - 100\,\mathrm{eV}$).

Calculated cross-sections have further been used in Monte Carlo simulations [102] of transport properties of the Rg_2^+ ion in Rg gas at ambient conditions, mobility, effective diffusion energies, and the reaction rate constant for the collision-induced dissociation of the ionic Rg_2^+ dimer. Generally, a qualitative agreement has been found between our and experimental mobility data for both models, Model A1 and Model B1, only the latter, however, leads, both for krypton as well as for xenon, to a quantitative agreement with the experimental measurement.

An interesting conclusion, concerning krypton case, is that rotationally - vibrationally excited dimers (with their effective temperature exceeding the room temperature by about 300 K) have to be presumed in the calculations so that the experimental data can be quantitatively reproduced, while for xenon, an assumption that the experimental populations of ions have an effective temperature is a good approximation.

Furthermore, we used an inverse method based on JWKB approximation [76, 77] to calculate a global momentum transfer collision cross-section without considering inelastic processes like dissociation. The associated transport coefficients, like mobility, are also in a good coherence with experimental data, par-

ticularly at low E/N. This is expected since inverse method is principally used to extrapolate mobilities and at low fields inelastic process are not present.

The present chapter extends preceding calculations on helium [21, 64], neon [23], and argon [25, 64] dimers into the realm of heavy rare-gases for which relativistic effects (the Spin-Orbit Coupling, in particular) are important. Additional calculations on krypton and xenon dimers (including electronically excited species) are running to see further development.

Chapter 5

Conclusions and Perspectives

As a general conclusion for this thesis, one can conclude that every interaction model from the literature used in this work provides qualitatively coherent results with measurements, while Model B provide, for monomer (Rg^+) and dimer (Rg_2^+) ion collisions with neutral atoms (Rg = Kr or Xe), quantitatively better mobility agreement with experiments. Furthermore, the accuracy of the $\mathrm{Rg}^+/\mathrm{Rg}$ interaction potential in the *Diatomics In Molecules* (DIM) is very important for ionic trimers (Rg_3^+) interaction system. On the other hand, neutral interaction potentials (Rg/Rg) are less crucial (for considered atoms in this thesis) for low initial rotational-vibrational excited dimer, even if the accuracy of the repulsive wall (and thus the neutral potential) is important in the case of higher excited states.

Firstly in chapter 3, semi-classical and hybrid methods are compared to quantum method in order to check the validity of these approximations in the case of ionic atom - neutral atom collision ($\mathrm{Rg}^+/\mathrm{Rg}$). Using the fact that JWKB approximation, of semi-classical method, is validated on artificial isotope, with average mass and bosonic behavior, new runs of calculations using this method are performed considering all possible collisions in order to validate the isotropic mass distribution hypothesis. Classical treatment of nuclei, with or without quantum decoherence in the hybrid method, provides also coherent results with quantum method or experimental values. Both approximated methods (hybrid and semi-classical) allow us a time saving while providing coherent results compared to

quantum method.

Good quantitative agreement between calculated values and measurements are obtained only for one state ($^2P_{1/2}$ for krypton and $^2P_{3/2}$ for xenon) but the calculations diverge little bit more from experiments for the other state ($^2P_{3/2}$ for krypton and $^2P_{1/2}$ for xenon). This can be attributed to imperfection in Model B interaction potentials or to a detection of impurities in experiments. This small difference between calculated and measured mobility can also be attributed to the applied fitting procedure [97] to extract the experimental mobilities from the two unresolved peaks curve corresponding to $^2P_{1/2}$ and $^2P_{3/2}$ rare-gas ion states.

Moreover, there is also an error in the Monte Carlo mobility calculations, estimated to 2% in previous calculations [22], which arises from the use of momentum transfer cross-section instead of differential cross-section in Monte Carlo transport coefficients calculations. Finally, Monte Carlo simulations allow to calculate transport coefficients (mobility and diffusion coefficients) of Rg^+ in gaseous Rg over a wide range of reduced electric fields (5 Td to 3000 Td). This allows us to add or complete missing data in literature.

Secondly in chapter 4, hybrid method is the more appropriate method to study dimer-atoms collisions and therefore was used to calculate all cross-sections needed for Monte Carlo simulations. The ionic dimer (Rg_2^+), in this thesis work, is considered before collision only in electronic ground state ($\mathrm{I}(1/2)_\mathrm{u}$), however different rotational-vibrational states are considered in order to improve the correlation between mobility calculations and measurements (0 to 200 meV). At intermediate reduced electric fields, Rg_2^+ mobility decreases with enhancement of internal energy for both considered ionic dimer (Kr_2^+ and Xe_2^+). While at low reduced electric field, for Kr_2^+ ion initial internal energy leads to a mobility decrease independently of the way the internal energy is stored (rotational or vibrational), for the Xe_2^+ ion mobility increases only if initial energy is stored in the rotational mode.

Different neutral potentials are tested in the DIM methodology and their influence is effective only at high rotational-vibrational excitations.

Rg_2^+ transport coefficients (mobility and diffusion coefficients) and dissociation rate constants in their parent gas are calculated over a wide range of reduced electric fields [5 Td to 3000 Td] and the mobility is in general in a good qualitative agreement with the measurements available on a limited range, the observed quantitative deviation can be attributed to the contamination of the impurity measurements.

In future work, it would be interesting to persevere calculations with electronically excited dimer and also trimers which may play an important role at high pressure. As a second step, it is also interesting to study collisions between the rare-gas ions and air after plasma jet dilution. All this data are devoted to be used as input in macroscopic chemical hydrodynamic model of low temperature plasmas generated at atmospheric pressure in the near future.

Appendices

A Tables of transport coefficients for $\mathrm{Kr}^+/\mathrm{Kr}$ collisions

Reduced electric field (Td)	(a)	(b)	(c)	(d)	(e)	(f)	(g)	(h)	(i)
5	0.866	0.840	0.884	0.460	0.714	0.639	0.840	0.668	0.887
10	0.862	0.843	0.881	0.459	0.720	0.639	0.838	0.665	0.879
20	0.864	0.838	0.881	0.460	0.718	0.640	0.834	0.663	0.864
30	0.854	0.830	0.869	0.461	0.702	0.639	0.830	0.656	0.857
50	0.835	0.814	0.850	0.461	0.702	0.631	0.813	0.649	0.838
60	0.820	0.802	0.835	0.460	0.696	0.632	0.801	0.645	0.824
80	0.797	0.773	0.804	0.458	0.682	0.627	0.776	0.635	0.795
100	0.771	0.753	0.783	0.461	0.662	0.619	0.756	0.629	0.776
200	0.665	0.645	0.667	0.456	0.589	0.575	0.656	0.580	0.666
300	0.589	0.571	0.588	0.443	0.533	0.533	0.586	0.538	0.591
400	0.534	0.518	0.536	0.428	0.490	0.497	0.534	0.501	0.537
500	0.492	0.479	0.493	0.411	0.457	0.468	0.495	0.471	0.496
700	0.432	0.420	0.433	0.380	0.405	0.420	0.435	0.422	0.437
1000	0.374	0.364	0.375	0.343	0.355	0.370	0.377	0.372	0.378
2000	0.279	0.271	0.279	0.269	0.268	0.282	0.283	0.282	0.283
3000	0.234	0.227	0.234	0.228	0.226	0.249	0.248	0.238	0.237

Table 5.1: Mobility values in $cm^2V^{-1}s^{-1}$ from inverse method and semi-classical calculations. (a) mobility from inverse method using experimental mobility provided by Ellis [88], (b) mobility from inverse method using experimental mobility for fine-structure $^2P_{3/2}$ provided by Helm [89], (c) mobility from inverse method using experimental mobility for fine-structure $^2P_{1/2}$ provided by Helm [89], (d) mobility obtained using momentum transfer cross-section calculated from semi-classical method based on interaction Model A for $^2P_{3/2}$ state, (e) mobility obtained using momentum transfer cross-section calculated from semi-classical method based on interaction Model A for $^2P_{1/2}$ state, (f) mobility obtained using momentum transfer cross-section calculated from semi-classical method based on interaction Model B for $^2P_{3/2}$ state, (g) mobility obtained using momentum transfer cross-section calculated from semi-classical method based on interaction Model B for $^2P_{1/2}$ state, (h) mobility obtained using momentum transfer cross-section calculated from semi-classical method based on interaction Model B for $^2P_{3/2}$ state using the 45 possible collisions, (i) mobility obtained using momentum transfer cross-section calculated from semi-classical method based on interaction Model B for $^2P_{1/2}$ state using the 45 possible collisions.

Reduced electric field (Td)	(a)	(b)	(c)	(d)	(e)	(f)	(g)	(h)
5	0.699	0.767	0.685	0.758	0.734	0.810	0.698	0.810
10	0.698	0.767	0.684	0.757	0.735	0.809	0.698	0.806
20	0.695	0.763	0.682	0.753	0.733	0.808	0.697	0.802
30	0.695	0.757	0.678	0.750	0.731	0.801	0.692	0.796
50	0.685	0.745	0.672	0.738	0.725	0.784	0.684	0.779
60	0.680	0.734	0.668	0.728	0.718	0.773	0.673	0.761
80	0.669	0.716	0.656	0.709	0.704	0.753	0.660	0.742
100	0.657	0.697	0.644	0.690	0.691	0.729	0.648	0.723
200	0.595	0.615	0.584	0.606	0.623	0.636	0.584	0.635
300	0.544	0.551	0.534	0.544	0.566	0.568	0.531	0.568
400	0.501	0.504	0.494	0.512	0.522	0.521	0.489	0.517
500	0.468	0.467	0.461	0.462	0.487	0.483	0.456	0.479
700	0.418	0.413	0.411	0.410	0.433	0.426	0.405	0.420
1000	0.367	0.359	0.362	0.358	0.381	0.373	0.352	0.363
2000	0.278	0.270	0.273	0.270	0.289	0.281	0.262	0.266
3000	0.234	0.227	0.230	0.227	0.244	0.237	0.217	0.220

Table 5.2: Mobility values in $cm^2V^{-1}s^{-1}$ from hybrid calculations using internuclear potential Model A. (a) mobility obtained using momentum transfer cross-section calculated from with hybrid method for $^2P_{3/2}$ state, (b) mobility obtained using momentum transfer cross-section calculated from hybrid method for $^2P_{1/2}$ state, (c) mobility obtained using momentum transfer cross-section calculated from hybrid method for $^2P_{3/2}$ state on isotope ^{86}Kr, (d) mobility obtained using momentum transfer cross-section calculated from hybrid method for $^2P_{1/2}$ state on isotope ^{86}Kr, (e) mobility obtained using momentum transfer cross-section calculated from hybrid method for $^2P_{3/2}$ state on isotope ^{78}Kr, (f) mobility obtained using momentum transfer cross-section calculated from hybrid method for $^2P_{1/2}$ state on isotope ^{78}Kr, (g) mobility obtained using momentum transfer cross-section calculated from hybrid method with quantum decoherence for $^2P_{3/2}$ state, (h) mobility obtained using momentum transfer cross-section calculated from hybrid method with quantum decoherence for $^2P_{1/2}$ state.

Reduced electric field (Td)	(a)	(b)	(c)	(d)	(e)	(f)	(g)	(h)	(i)	(j)
5	0.765	0.866	0.864	0.748	0.878	0.771	0.452	0.690	0.645	0.845
10	0.764	0.866	0.863	0.747	0.876	0.770	0.451	0.700	0.644	0.844
20	0.761	0.856	0.855	0.745	0.867	0.768	0.448	0.697	0.645	0.836
30	0.758	0.853	0.850	0.738	0.858	0.764	0.452	0.691	0.643	0.831
50	0.745	0.831	0.832	0.728	0.841	0.751	0.448	0.690	0.638	0.813
60	0.739	0.820	0.819	0.721	0.828	0.744	0.452	0.681	0.632	0.802
80	0.725	0.798	0.796	0.706	0.804	0.727	0.453	0.668	0.629	0.778
100	0.710	0.773	0.773	0.691	0.779	0.709	0.452	0.655	0.623	0.756
200	0.636	0.669	0.667	0.615	0.669	0.631	0.451	0.587	0.577	0.658
300	0.577	0.594	0.593	0.554	0.591	0.570	0.441	0.532	0.536	0.587
400	0.530	0.540	0.539	0.506	0.533	0.522	0.428	0.489	0.499	0.534
500	0.493	0.499	0.497	0.468	0.489	0.486	0.412	0.456	0.472	0.495
700	0.438	0.439	0.437	0.413	0.426	0.431	0.380	0.406	0.420	0.436
1000	0.383	0.381	0.38	0.357	0.365	0.376	0.343	0.355	0.370	0.379
2000	0.288	0.284	0.283	0.263	0.267	0.283	0.269	0.268	0.282	0.283
3000	0.242	0.238	0.238	0.218	0.220	0.238	0.228	0.226	0.249	0.248

Table 5.3: Mobility values in $cm^2V^{-1}s^{-1}$ from hybrid method using interaction Model B only and quantum method calculations. (a) mobility obtained using momentum transfer cross-section calculated from hybrid method for $^2P_{3/2}$ state, (b) mobility obtained using momentum transfer cross-section calculated from hybrid method for $^2P_{1/2}$ state, (c) mobility obtained using momentum transfer cross-section calculated from hybrid method for $^2P_{1/2}$ state with the extension of collision energies to 0.001 eV, (d)mobility obtained using momentum transfer cross-section calculated from hybrid method with quantum decoherence for $^2P_{3/2}$ state, (e) mobility obtained using momentum transfer cross-section calculated from hybrid method with quantum decoherence for $^2P_{1/2}$ state, (f) mobility obtained using momentum transfer cross-section calculated from hybrid method for $^2P_{1/2}$ state with distinct calculation for $\Omega = 1/2$ and $\Omega = 3/2$, (g) mobility obtained using momentum transfer cross-section calculated from quantum method for $^2P_{3/2}$ state using interaction Model A, (h) mobility obtained using momentum transfer cross-section calculated from quantum method for $^2P_{1/2}$ state using interaction Model A, (i) mobility obtained using momentum transfer cross-section calculated from quantum method for $^2P_{3/2}$ state using interaction Model B, (j) mobility obtained using momentum transfer cross-section calculated from quantum method for $^2P_{1/2}$ state using interaction Model B.

Reduced electric field (Td)	(a)	(b)	(c)	(d)	(e)	(f)	(g)	(h)
5	25.9	26.1	26.0	26.1	25.5	25.5	26.2	26.1
10	26.3	26.2	26.0	25.8	25.5	26.3	26.0	25.9
20	27.0	26.6	26.4	27.2	26.8	26.7	27.0	27.2
30	27.5	27.6	27.2	27.2	26.4	27.9	27.4	27.3
50	29.5	29.5	28.5	29.5	28.4	30.0	29.2	29.4
80	32.3	32.8	31.7	33.5	31.4	33.2	33.4	33.4
100	36.1	36.9	35.9	36.1	36.3	36.6	37.2	36.5
200	49.3	51.1	54.0	51.4	52.3	52.2	51.9	52.5
300	66.2	65.7	71.8	67.7	71.7	68.4	70.7	67.9
400	80.2	82.7	91.2	84.4	89.9	85.7	86.2	83.8
500	94.2	99.9	111	102	105	103	104	103
700	131	134	142	140	142	136	138	136
1000	177	184	205	190	205	190	190	190
2000	349	371	405	384	405	384	379	382

Table 5.4: Longitudinal coefficient (eD_L/K_0) in meV from different method using internuclear potential Model B. (a) longitudinal coefficient obtained using inverse method on experimental $^2P_{3/2}$ state values provided by Helm [89], (b) longitudinal coefficient obtained using inverse method on experimental $^2P_{1/2}$ state values provided by Helm [89], (c) longitudinal coefficient obtained using momentum transfer cross-section calculated from semi-classical method for $^2P_{3/2}$ state, (d) longitudinal coefficient obtained using momentum transfer cross-section calculated from semi-classical method for $^2P_{1/2}$ state, (e) longitudinal coefficient obtained using momentum transfer cross-section calculated from quantum method for $^2P_{3/2}$ state, (f) longitudinal coefficient obtained using momentum transfer cross-section calculated from quantum method for $^2P_{1/2}$ state, (g) longitudinal coefficient obtained using momentum transfer cross-section calculated from hybrid method for $^2P_{3/2}$ state, (h) longitudinal coefficient obtained using momentum transfer cross-section calculated from hybrid method for $^2P_{1/2}$ state.

Reduced electric field (Td)	(a)	(b)	(c)	(d)	(e)	(f)	(g)	(h)
5	26.3	25.9	25.9	26.2	25.7	25.5	25.5	26.1
10	26.2	25.9	25.9	25.6	25.7	26.3	25.7	26.0
20	26.8	26.4	26.7	26.4	26.5	26.7	26.6	27.0
30	27.4	26.5	26.2	26.6	26.4	27.9	26.9	26.7
50	28.1	28.2	27.0	28.4	27.4	30.0	27.4	28.4
80	31.9	31.9	29.1	31.5	29.7	33.2	30.8	31.9
100	33.9	34.1	30.6	34.2	32.1	36.6	32.7	35.5
200	48.3	52.9	45.0	51.2	45.8	52.2	48.3	50.7
300	67.2	68.4	61.8	69.0	59.6	68.4	63.9	68.6
400	82.2	85.4	78.2	88.1	81.9	85.7	83.0	86.7
500	103	107	98.9	108	98.6	103	103	109
700	141	150	140	152	140	136	141	153
1000	200	213	213	219	213	190	205	213
2000	420	433	439	447	439	384	444	446

Table 5.5: Transversal coefficient (eD_T/K_0) in meV from different method using inter-nuclear potential Model B. (a) transversal coefficient obtained using inverse method on experimental $^2P_{3/2}$ state values provided by Helm [89], (b) transversal coefficient obtained using inverse method on experimental $^2P_{1/2}$ state values provided by Helm [89], (c) transversal coefficient obtained using momentum transfer cross-section calculated from semi-classical method for $^2P_{3/2}$ state, (d) transversal coefficient obtained using momentum transfer cross-section calculated from semi-classical method for $^2P_{1/2}$ state, (e) transversal coefficient obtained using momentum transfer cross-section calculated from quantum method for $^2P_{3/2}$ state, (f) transversal coefficient obtained using momentum transfer cross-section calculated from quantum method for $^2P_{1/2}$ state, (g) transversal coefficient obtained using momentum transfer cross-section calculated from hybrid method for $^2P_{3/2}$ state, (h) transversal coefficient obtained using momentum transfer cross-section calculated from hybrid method for $^2P_{1/2}$ state.

B Tables of transport coefficients for $\mathrm{Xe}^+/\mathrm{Xe}$ collisions

Reduced electric field (Td)	(a)	(b)	(c)	(d)	(e)	(f)	(g)	(h)
5	0.518	0.557	0.195	0.275	0.558	0.555	0.551	0.549
10	0.518	0.557	0.196	0.275	0.553	0.552	0.554	0.553
20	0.516	0.556	0.193	0.274	0.546	0.549	0.545	0.545
30	0.515	0.553	0.197	0.275	0.546	0.545	0.540	0.540
50	0.505	0.543	0.195	0.277	0.532	0.534	0.528	0.530
60	0.499	0.538	0.195	0.277	0.521	0.520	0.519	0.519
80	0.489	0.525	0.196	0.277	0.506	0.506	0.503	0.505
100	0.477	0.511	0.195	0.278	0.493	0.496	0.492	0.494
200	0.424	0.452	0.199	0.277	0.430	0.431	0.428	0.428
300	0.382	0.405	0.202	0.272	0.384	0.387	0.384	0.384
400	0.350	0.370	0.204	0.266	0.350	0.353	0.349	0.352
500	0.324	0.343	0.206	0.259	0.325	0.328	0.324	0.327
700	0.287	0.303	0.204	0.243	0.287	0.290	0.287	0.289
1000	0.250	0.263	0.197	0.223	0.249	0.253	0.250	0.252
2000	0.187	0.197	0.169	0.178	0.187	0.190	0.187	0.190
3000	0.159	0.162	0.148	0.152	0.157	0.160	0.157	0.160

Table 5.6: Mobility values in $cm^2V^{-1}s^{-1}$ from inverse method and semi-classical calculations based on internuclear potential Model A and B. (a) mobility obtained using inverse method momentum transfer cross-section calculated from $^2P_{3/2}$ mobility state experimental value from [89, 97], (b) mobility obtained using inverse method momentum transfer cross-section calculated from $^2P_{1/2}$ mobility state experimental value from [89, 97], (c) mobility obtained using momentum transfer cross-section calculated from semi-classical method for $^2P_{3/2}$ state based on Model A interaction potential, (d) mobility obtained using momentum transfer cross-section calculated from semi-classical method for $^2P_{1/2}$ state based on Model A interaction potential, (e) mobility obtained using momentum transfer cross-section calculated from semi-classical method for $^2P_{3/2}$ state based on Model B interaction potential, (f) mobility obtained using momentum transfer cross-section calculated from semi-classical method for $^2P_{1/2}$ state based on Model B interaction potential, (g) mobility obtained using average momentum transfer cross-section calculated from semi-classical method for $^2P_{3/2}$ state based on Model B interaction potential from all 45 possible collisions, (h) mobility obtained using average momentum transfer cross-section calculated from semi-classical method for $^2P_{1/2}$ state based on Model B interaction potential from all 45 possible collisions.

Reduced electric field (Td)	(a)	(b)	(c)	(d)	(e)	(f)	(g)	(h)	(i)	(j)
5	0.211	0.275	0.550	0.555	0.293	0.315	0.522	0.507	0.513	0.513
10	0.212	0.277	0.541	0.555	0.293	0.315	0.531	0.505	0.514	0.513
20	0.211	0.272	0.540	0.544	0.291	0.314	0.516	0.502	0.515	0.512
30	0.212	0.279	0.540	0.549	0.291	0.314	0.519	0.500	0.509	0.500
50	0.212	0.275	0.523	0.533	0.291	0.314	0.507	0.488	0.499	0.476
60	0.212	0.276	0.517	0.525	0.291	0.313	0.499	0.478	0.492	0.481
80	0.209	0.277	0.499	0.507	0.291	0.312	0.488	0.469	0.479	0.472
100	0.209	0.277	0.491	0.498	0.291	0.312	0.480	0.462	0.470	0.414
200	0.208	0.277	0.427	0.432	0.287	0.304	0.422	0.406	0.413	0.372
300	0.208	0.273	0.383	0.387	0.283	0.293	0.379	0.367	0.372	0.339
400	0.209	0.268	0.351	0.353	0.275	0.281	0.348	0.338	0.339	0.314
500	0.209	0.261	0.324	0.327	0.267	0.270	0.323	0.315	0.315	0.277
700	0.207	0.245	0.287	0.290	0.251	0.251	0.286	0.279	0.282	0.240
1000	0.199	0.224	0.250	0.252	0.229	0.227	0.249	0.243	0.240	0.177
2000	0.170	0.178	0.187	0.190	0.182	0.178	0.187	0.183	0.177	0.147
3000	0.149	0.154	0.158	0.162	0.156	0.152	0.156	0.154	0.147	0.147

Table 5.7: Mobility values in $cm^2V^{-1}s^{-1}$ from quantum and hybrid method based on interaction Model A and B. (a) mobility obtained using momentum transfer cross-section calculated from quantum method for $^2P_{3/2}$ state based on Model A interaction potential, (b) mobility obtained using momentum transfer cross-section calculated from quantum method for $^2P_{1/2}$ state based on Model A interaction potential, (c) mobility obtained using momentum transfer cross-section calculated from quantum method for $^2P_{3/2}$ state based on Model B interaction potential, (d) mobility obtained using momentum transfer cross-section calculated from quantum method for $^2P_{1/2}$ state based on Model B interaction potential, (e) mobility obtained using momentum transfer cross-section calculated from hybrid method for $^2P_{3/2}$ state based on Model A interaction potential, (f) mobility obtained using momentum transfer cross-section calculated from hybrid method for $^2P_{1/2}$ state based on Model A interaction potential, (g) mobility obtained using momentum transfer cross-section calculated from hybrid method for $^2P_{3/2}$ state based on Model B interaction potential, (h) mobility obtained using momentum transfer cross-section calculated from hybrid method for $^2P_{1/2}$ state based on Model B interaction potential, (i) mobility obtained using momentum transfer cross-section calculated from hybrid method with quantum decoherence for $^2P_{3/2}$ state based on Model B interaction potential, (j) mobility obtained using momentum transfer cross-section calculated from hybrid method with quantum decoherence for $^2P_{1/2}$ state based on Model B interaction potential.

Reduced electric field (Td)	(a)	(b)	(c)	(d)	(e)	(f)	(g)	(h)
5	26.2	25.5	25.4	25.8	26.1	25.9	25.4	25.6
10	25.8	25.8	25.6	25.9	26.3	26.0	25.6	25.7
20	26.4	26.7	27.1	27.4	26.2	26.3	26.7	25.9
30	27.0	27.1	26.5	26.1	26.5	26.6	26.6	26.6
50	27.8	27.9	27.4	27.6	27.8	27.9	27.5	26.9
60	29.1	29.4	28.4	28.6	28.4	28.5	28.2	27.7
80	31.3	31.5	30.7	30.2	30.1	29.9	28.7	29.7
100	33.1	33.8	32.9	32.0	32.2	31.7	29.3	30.6
200	42.3	45.3	42.7	42.6	42.5	42.0	41.1	40.2
300	52.3	56.4	53.8	54.0	56.2	55.6	58.1	52.0
400	65.0	70.2	65.9	64.9	68.2	69.2	67.1	64.4
500	77.2	83.6	76.5	79.5	82.5	82.9	79.7	77.6
700	103	107	104	103	111	112	108	109
1000	136	153	136	143	157	161	152	147
2000	267	293	271	286	317	323	308	303
3000	440	461	455	455	498	485	489	466

Table 5.8: Longitudinal coefficient (eD_L/K_0) in meV from different method based on internuclear potential Model B. (a) longitudinal coefficient obtained using inverse method on experimental $^2P_{3/2}$ state values provided by Helm [89] and Larsen [97], (b) longitudinal coefficient obtained using inverse method on experimental $^2P_{1/2}$ state values provided by Helm [89] and Larsen [97], (c) longitudinal coefficient obtained using momentum transfer cross-section calculated from semi-classical method for $^2P_{3/2}$ state, (d) longitudinal coefficient obtained using momentum transfer cross-section calculated from semi-classical method for $^2P_{1/2}$ state, (e) longitudinal coefficient obtained using momentum transfer cross-section calculated from quantum method for $^2P_{3/2}$ state, (f) longitudinal coefficient obtained using momentum transfer cross-section calculated from quantum method for $^2P_{1/2}$ state, (g) longitudinal coefficient obtained using momentum transfer cross-section calculated from hybrid method for $^2P_{3/2}$ state, (h) longitudinal coefficient obtained using momentum transfer cross-section calculated from hybrid method for $^2P_{1/2}$ state.

Reduced electric field (Td)	(a)	(b)	(c)	(d)	(e)	(f)	(g)	(h)
5	26.2	25.8	25.7	26.0	26.0	25.8	25.7	25.8
10	26.1	25.7	25.8	26.1	26.1	25.9	25.8	25.8
20	26.0	25.8	26.9	27.4	26.5	26.9	26.6	25.8
30	26.8	26.6	26.7	26.7	26.6	25.8	26.4	26.5
50	27.4	27.7	27.3	27.5	27.9	27.4	27.6	27.8
60	28.5	28.6	29.0	28.4	28.2	28.5	27.3	28.8
80	29.7	29.7	30.0	30.4	29.6	29.8	30.2	29.7
100	32.6	30.9	30.7	31.4	31.8	33.0	32.4	32.3
200	41.3	43.6	41.9	42.2	41.4	42.9	43.0	41.5
300	53.8	58.0	54.0	55.7	53.0	53.8	53.0	54.1
400	69.0	72.3	69.3	70.2	65.5	67.5	64.9	64.4
500	82.2	88.5	82.8	85.4	76.0	80.0	77.4	76.7
700	113	119	108	110	99.5	104	99.9	98.0
1000	157	173	155	161	138	144	141	134
2000	318	351	320	324	270	286	264	258
3000	475	531	490	508	395	406	397	378

Table 5.9: Transversal coefficient (eD_T/K_0) in meV from different method based on inter-nuclear potential Model B. (a) transverse coefficient obtained using inverse method on experimental $^2P_{3/2}$ state values provided by Helm [89] and Larsen [97], (b) transverse coefficient obtained using inverse method on experimental $^2P_{1/2}$ state values provided by Helm [89] and Larsen [97], (c) transverse coefficient obtained using momentum transfer cross-section calculated from semi-classical method for $^2P_{3/2}$ state, (d) transverse coefficient obtained using momentum transfer cross-section calculated from semi-classical method for $^2P_{1/2}$ state, (e) transverse coefficient obtained using momentum transfer cross-section calculated from quantum method for $^2P_{3/2}$ state, (f) transverse coefficient obtained using momentum transfer cross-section calculated from quantum method for $^2P_{1/2}$ state, (g) transverse coefficient obtained using momentum transfer cross-section calculated from hybrid method for $^2P_{3/2}$ state, (h) transverse coefficient obtained using momentum transfer cross-section calculated from hybrid method for $^2P_{1/2}$ state.

C Tables of transport coefficients and dissociation rate constant for $\mathrm{Kr}_2^+/\mathrm{Kr}$ collisions

Reduced electric field (Td)	(a)	(b)	(c)	(d)	(e)	(f)	(g)	(h)	(i)	(j)
5	0.915	0.902	1.044	1.070	1.060	1.033	1.044	1.070	1.050	1.033
10	0.915	0.903	1.040	1.080	1.080	1.032	1.044	1.080	1.080	1.030
20	0.915	0.904	1.042	1.070	1.070	1.033	1.042	1.070	1.070	1.031
30	0.914	0.904	1.030	1.060	1.060	1.030	1.030	1.060	1.060	1.030
50	0.915	0.900	1.021	1.050	1.060	1.030	1.021	1.050	1.060	1.030
80	0.936	0.914	1.035	1.060	1.080	1.050	1.035	1.060	1.090	1.050
100	0.957	0.929	1.050	1.040	1.080	1.066	1.051	1.040	1.080	1.069
200	1.063	1.020	1.060	1.070	1.140	1.108	1.060	1.070	1.150	1.111
300	1.070	1.040	1.090	1.030	1.090	1.070	1.090	1.030	1.090	1.077
400	1.023	1.010	1.057	0.971	1.010	1.010	1.057	0.971	1.020	1.015
500	0.964	0.963	1.000	0.917	0.944	0.948	1.000	0.917	0.950	0.953
700	0.862	0.868	0.946	0.826	0.842	0.849	0.946	0.826	0.843	0.851
1000	0.767	0.774	0.850	0.748	0.748	0.756	0.850	0.748	0.750	0.756
2000	0.611	0.591	0.606	0.607	0.602	0.600	0.606	0.607	0.602	0.600
3000	0.519	0.517	0.515	0.517	0.515	0.511	0.515	0.517	0.514	0.511

Table 5.10: Mobility values in $cm^2V^{-1}s^{-1}$ from hybrid calculations using different interactions models and $\sigma_{\mathrm{NRS}}^{(\mathrm{MT1})}$ and $\sigma_{\mathrm{NRS}}^{(\mathrm{MT2})}$ for a initial dimer [J=0, ν=0]. (a) Model A1 $\sigma_{\mathrm{NRS}}^{(\mathrm{MT1})}$, (b) Model A1 $\sigma_{\mathrm{NRS}}^{(\mathrm{MT2})}$, (c) Model B1 $\sigma_{\mathrm{NRS}}^{(\mathrm{MT1})}$, (d) Model B1 $\sigma_{\mathrm{NRS}}^{(\mathrm{MT2})}$, (e) Model B2 $\sigma_{\mathrm{NRS}}^{(\mathrm{MT1})}$, (f) Model B2 $\sigma_{\mathrm{NRS}}^{(\mathrm{MT2})}$, (g) Model B3 $\sigma_{\mathrm{NRS}}^{(\mathrm{MT1})}$, (h) Model B3 $\sigma_{\mathrm{NRS}}^{(\mathrm{MT2})}$, (i) Model B4 $\sigma_{\mathrm{NRS}}^{(\mathrm{MT1})}$, (j) Model B4 $\sigma_{\mathrm{NRS}}^{(\mathrm{MT2})}$.

Reduced electric field (Td)	(a)	(b)	(c)	(d)	(e)	(f)	(g)	(h)
5	1.070	1.033	1.070	1.080	1.020	0.984	0.951	0.958
10	1.080	1.036	1.070	1.070	0.998	0.991	0.960	0.957
20	1.070	1.032	1.070	1.060	0.999	0.983	0.955	0.952
30	1.060	1.030	1.060	1.060	0.982	0.972	0.945	0.946
50	1.050	1.021	1.050	1.050	0.977	0.964	0.938	0.933
80	1.060	1.026	1.050	1.050	0.968	0.951	0.928	0.921
100	1.040	1.030	1.040	1.040	0.951	0.938	0.915	0.913
200	1.070	1.043	1.070	1.070	0.958	0.950	0.893	0.878
300	1.030	1.020	1.030	1.030	0.926	0.931	0.859	0.835
400	0.971	0.976	0.974	0.975	0.880	0.896	0.819	0.791
500	0.917	0.927	0.914	0.915	0.832	0.851	0.782	0.752
700	0.826	0.841	0.824	0.839	0.760	0.780	0.721	0.695
1000	0.748	0.756	0.744	0.755	0.699	0.713	0.668	0.648
2000	0.607	0.604	0.607	0.607	0.590	0.589	0.567	0.564
3000	0.517	0.513	0.519	0.516	0.510	0.507	0.494	0.494

Table 5.11: Mobility values in $cm^2V^{-1}s^{-1}$ from hybrid calculations using Model B1 and $\sigma_{\mathrm{NRS}}^{(\mathrm{MT1})}$ and $\sigma_{\mathrm{NRS}}^{(\mathrm{MT2})}$ for different initial rotational-vibrational dimer values. (a) $\sigma_{\mathrm{NRS}}^{(\mathrm{MT1})}$ [J=0, ν=1], (b) $\sigma_{\mathrm{NRS}}^{(\mathrm{MT2})}$ [J=0, ν=1], (c) $\sigma_{\mathrm{NRS}}^{(\mathrm{MT1})}$ [J=0, ν=2], (d) $\sigma_{\mathrm{NRS}}^{(\mathrm{MT2})}$ [J=0, ν=2], (e) $\sigma_{\mathrm{NRS}}^{(\mathrm{MT1})}$ [J=0, ν=5], (f) $\sigma_{\mathrm{NRS}}^{(\mathrm{MT2})}$ [J=0, ν=5], (g) $\sigma_{\mathrm{NRS}}^{(\mathrm{MT1})}$ [J=0, ν=12], (h) $\sigma_{\mathrm{NRS}}^{(\mathrm{MT1})}$ [J=0, ν=12].

Reduced electric field (Td)	(a)	(b)	(c)	(d)	(e)	(f)	(g)	(h)
5	1.080	1.070	1.080	1.035	1.090	1.070	0.963	0.948
10	1.070	1.060	1.080	1.031	1.090	1.070	0.963	0.947
20	1.070	1.060	1.070	1.033	1.090	1.060	0.960	0.944
30	1.060	1.050	1.060	1.030	1.080	1.060	0.950	0.938
50	1.060	1.040	1.060	1.025	1.080	1.050	0.942	0.937
80	1.060	1.030	1.060	1.023	1.080	1.050	0.930	0.931
100	1.040	1.020	1.040	1.028	1.060	1.040	0.913	0.923
200	1.090	1.060	1.080	1.050	1.060	1.050	0.875	0.895
300	1.060	1.040	1.040	1.029	1.000	1.000	0.830	0.855
400	0.997	0.996	0.984	0.983	0.934	0.945	0.787	0.813
500	0.940	0.945	0.924	0.933	0.875	0.892	0.745	0.774
700	0.843	0.856	0.832	0.846	0.789	0.808	0.686	0.714
1000	0.760	0.768	0.753	0.760	0.719	0.733	0.641	0.661
2000	0.612	0.612	0.611	0.607	0.598	0.597	0.565	0.564
3000	0.521	0.520	0.521	0.516	0.514	0.513	0.496	0.491

Table 5.12: Mobility values in $cm^2V^{-1}s^{-1}$ from hybrid calculations using Model B1 and $\sigma_{\mathrm{NRS}}^{(\mathrm{MT1})}$ and $\sigma_{\mathrm{NRS}}^{(\mathrm{MT2})}$ for different initial rotational-vibrational dimer values. (a) $\sigma_{\mathrm{NRS}}^{(\mathrm{MT1})}$ [J=10, ν=0], (b) $\sigma_{\mathrm{NRS}}^{(\mathrm{MT2})}$ [J=10, ν=0], (c) $\sigma_{\mathrm{NRS}}^{(\mathrm{MT1})}$ [J=50, ν=0], (d) $\sigma_{\mathrm{NRS}}^{(\mathrm{MT2})}$ [J=50, ν=0], (e) $\sigma_{\mathrm{NRS}}^{(\mathrm{MT1})}$ [J=100, ν=0], (f) $\sigma_{\mathrm{NRS}}^{(\mathrm{MT2})}$ [J=100, ν=0], (g) $\sigma_{\mathrm{NRS}}^{(\mathrm{MT1})}$ [J=200, ν=0], (h) $\sigma_{\mathrm{NRS}}^{(\mathrm{MT1})}$ [J=200, ν=0].

Reduced electric field (Td)	(a)	(b)	(c)	(d)	(e)	(f)	(g)	(h)	(i)	(j)
5	1.090	1.080	1.080	1.070	1.060	1.060	1.020	1.019	1.040	1.040
10	1.090	1.060	1.090	1.070	1.070	1.050	1.040	1.017	1.030	1.040
20	1.080	1.060	1.080	1.070	1.060	1.040	1.030	1.016	1.030	1.040
30	1.070	1.050	1.080	1.060	1.050	1.040	1.030	1.010	1.020	1.030
50	1.070	1.050	1.070	1.050	1.050	1.030	1.010	1.004	1.010	1.010
80	1.090	1.060	1.100	1.070	1.050	1.040	0.999	1.002	1.000	1.010
100	1.080	1.050	1.090	1.060	1.040	1.020	0.989	0.998	0.986	0.991
200	1.110	1.090	1.120	1.100	1.030	1.030	0.939	0.955	0.939	0.954
300	1.060	1.050	1.060	1.060	0.973	0.974	0.872	0.894	0.872	0.894
400	0.992	0.991	0.989	0.996	0.906	0.921	0.813	0.839	0.813	0.840
500	0.924	0.935	0.922	0.933	0.850	0.869	0.765	0.792	0.765	0.793
700	0.826	0.841	0.827	0.838	0.767	0.786	0.698	0.724	0.691	0.719
1000	0.742	0.753	0.741	0.751	0.697	0.711	0.648	0.665	0.641	0.660
2000	0.602	0.600	0.601	0.601	0.584	0.584	0.563	0.561	0.561	0.562
3000	0.514	0.512	0.514	0.512	0.506	0.503	0.494	0.489	0.493	0.490

Table 5.13: Mobility values in $cm^2V^{-1}s^{-1}$ from hybrid calculations using Model B2 and $\sigma_{\mathrm{NRS}}^{(\mathrm{MT1})}$ and $\sigma_{\mathrm{NRS}}^{(\mathrm{MT2})}$ for different initial rotational-vibrational dimer values. (a) $\sigma_{\mathrm{NRS}}^{(\mathrm{MT1})}$ [J=0, ν=1], (b) $\sigma_{\mathrm{NRS}}^{(\mathrm{MT2})}$ [J=0, ν=1], (c) $\sigma_{\mathrm{NRS}}^{(\mathrm{MT1})}$ [J=0, ν=2], (d) $\sigma_{\mathrm{NRS}}^{(\mathrm{MT2})}$ [J=0, ν=2], (e) $\sigma_{\mathrm{NRS}}^{(\mathrm{MT1})}$ [J=0, ν=5], (f) $\sigma_{\mathrm{NRS}}^{(\mathrm{MT2})}$ [J=0, ν=5], (g) $\sigma_{\mathrm{NRS}}^{(\mathrm{MT1})}$ [J=0, ν=12], (h) $\sigma_{\mathrm{NRS}}^{(\mathrm{MT1})}$ [J=0, ν=12], (i) $\sigma_{\mathrm{NRS}}^{(\mathrm{MT1})}$ [J=200, ν=0], (j) $\sigma_{\mathrm{NRS}}^{(\mathrm{MT2})}$ [J=200, ν=0].

Reduced electric field (Td)	(a)	(b)	(c)	(d)	(e)	(f)	(g)	(h)	(i)	(j)
5	1.100	1.080	1.100	1.090	1.070	1.060	1.040	1.060	1.050	1.050
10	1.090	1.060	1.100	1.070	1.070	1.050	1.040	1.050	1.040	1.050
20	1.090	1.070	1.090	1.060	1.070	1.050	1.030	1.030	1.030	1.040
30	1.080	1.060	1.090	1.060	1.070	1.050	1.030	1.020	1.020	1.030
50	1.080	1.060	1.090	1.060	1.060	1.050	1.010	1.020	1.010	1.020
80	1.090	1.070	1.100	1.070	1.060	1.040	1.000	1.010	1.000	1.010
100	1.070	1.050	1.090	1.060	1.050	1.030	0.985	0.995	0.985	0.995
200	1.120	1.090	1.130	1.110	1.030	1.030	0.940	0.954	0.937	0.956
300	1.060	1.050	1.070	1.060	0.970	0.979	0.873	0.895	0.870	0.895
400	0.990	0.995	0.993	0.997	0.903	0.922	0.814	0.840	0.808	0.834
500	0.927	0.935	0.927	0.937	0.850	0.869	0.765	0.793	0.760	0.787
700	0.829	0.842	0.828	0.842	0.769	0.787	0.699	0.726	0.691	0.719
1000	0.743	0.752	0.742	0.753	0.698	0.713	0.649	0.665	0.641	0.660
2000	0.600	0.601	0.601	0.602	0.584	0.584	0.564	0.564	0.561	0.563
3000	0.513	0.512	0.514	0.512	0.506	0.504	0.493	0.491	0.492	0.490

Table 5.14: Mobility values in $cm^2V^{-1}s^{-1}$ from hybrid calculations using Model B3 and $\sigma_{\mathrm{NRS}}^{(\mathrm{MT1})}$ and $\sigma_{\mathrm{NRS}}^{(\mathrm{MT2})}$ for different initial rotational-vibrational dimer values. (a) $\sigma_{\mathrm{NRS}}^{(\mathrm{MT1})}$ [J=0, ν=1], (b) $\sigma_{\mathrm{NRS}}^{(\mathrm{MT2})}$ [J=0, ν=1], (c) $\sigma_{\mathrm{NRS}}^{(\mathrm{MT1})}$ [J=0, ν=2], (d) $\sigma_{\mathrm{NRS}}^{(\mathrm{MT2})}$ [J=0, ν=2], (e) $\sigma_{\mathrm{NRS}}^{(\mathrm{MT1})}$ [J=0, ν=5], (f) $\sigma_{\mathrm{NRS}}^{(\mathrm{MT2})}$ [J=0, ν=5], (g) $\sigma_{\mathrm{NRS}}^{(\mathrm{MT1})}$ [J=0, ν=12], (h) $\sigma_{\mathrm{NRS}}^{(\mathrm{MT1})}$ [J=0, ν=12], (i) $\sigma_{\mathrm{NRS}}^{(\mathrm{MT1})}$ [J=200, ν=0], (j) $\sigma_{\mathrm{NRS}}^{(\mathrm{MT2})}$ [J=200, ν=0].

Reduced electric field (Td)	(a)	(b)	(c)	(d)	(e)	(f)	(g)	(h)	(i)	(j)
5	1.100	1.080	1.090	1.080	1.070	1.060	1.040	1.014	1.040	1.050
10	1.090	1.070	1.090	1.070	1.070	1.050	1.040	1.014	1.040	1.040
20	1.080	1.060	1.080	1.080	1.060	1.050	1.030	1.015	1.030	1.030
30	1.070	1.050	1.080	1.070	1.050	1.040	1.020	1.010	1.020	1.020
50	1.070	1.050	1.080	1.070	1.050	1.040	1.010	1.008	1.010	1.020
80	1.090	1.060	1.100	1.070	1.050	1.040	1.010	1.005	1.000	1.010
100	1.080	1.050	1.090	1.060	1.040	1.030	0.987	1.000	0.987	0.996
200	1.110	1.090	1.130	1.100	1.030	1.030	0.940	0.956	0.938	0.955
300	1.060	1.050	1.060	1.060	0.970	0.978	0.876	0.895	0.871	0.894
400	0.986	0.990	0.992	0.997	0.905	0.925	0.815	0.839	0.810	0.837
500	0.922	0.932	0.926	0.937	0.849	0.868	0.766	0.792	0.761	0.790
700	0.826	0.840	0.827	0.842	0.767	0.785	0.699	0.725	0.693	0.718
1000	0.741	0.750	0.742	0.751	0.698	0.711	0.649	0.665	0.642	0.661
2000	0.600	0.600	0.601	0.601	0.584	0.583	0.562	0.561	0.561	0.561
3000	0.514	0.512	0.515	0.512	0.505	0.503	0.493	0.449	0.492	0.489

Table 5.15: Mobility values in $cm^2V^{-1}s^{-1}$ from hybrid calculations using Model B4 and $\sigma_{\mathrm{NRS}}^{(\mathrm{MT1})}$ and $\sigma_{\mathrm{NRS}}^{(\mathrm{MT2})}$ for different initial rotational-vibrational dimer values. (a) $\sigma_{\mathrm{NRS}}^{(\mathrm{MT1})}$ [J=0, ν=1], (b) $\sigma_{\mathrm{NRS}}^{(\mathrm{MT2})}$ [J=0, ν=1], (c) $\sigma_{\mathrm{NRS}}^{(\mathrm{MT1})}$ [J=0, ν=2], (d) $\sigma_{\mathrm{NRS}}^{(\mathrm{MT2})}$ [J=0, ν=2], (e) $\sigma_{\mathrm{NRS}}^{(\mathrm{MT1})}$ [J=0, ν=5], (f) $\sigma_{\mathrm{NRS}}^{(\mathrm{MT2})}$ [J=0, ν=5], (g) $\sigma_{\mathrm{NRS}}^{(\mathrm{MT1})}$ [J=0, ν=12], (h) $\sigma_{\mathrm{NRS}}^{(\mathrm{MT1})}$ [J=0, ν=12], (i) $\sigma_{\mathrm{NRS}}^{(\mathrm{MT1})}$ [J=200, ν=0], (j) $\sigma_{\mathrm{NRS}}^{(\mathrm{MT2})}$ [J=200, ν=0].

Reduced electric field (Td)	(a)	(b)	(c)	(d)	(e)	(f)	(g)	(h)
5	27.4	26.8	27.4	26.9	26.7	26.9	27.7	26.1
10	27.0	27.3	27.0	26.9	27.3	27.2	27.1	26.8
20	27.2	27.5	27.1	26.6	26.6	27.7	27.3	27.0
30	28.9	29.0	28.4	28.8	28.6	28.8	29.2	29.1
50	29.7	29.1	29.7	29.8	29.2	29.4	29.5	29.9
80	34.9	34.1	35.7	34.9	35.2	35.3	36.3	35.2
100	38.1	38.1	38.7	36.6	37.2	39.7	39.3	37.6
200	76.7	76.1	78.7	74.5	79.1	76.6	77.8	74.3
300	122	120	122	119	126	119	129	120
400	181	182	193	186	184	180	190	191
500	265	276	275	274	276	272	271	269
700	387	387	390	397	382	403	385	403
1000	642	647	633	655	621	643	646	652
2000	1630	1660	1600	159	1550	1570	150	1620
3000	2630	2660	2590	2610	2650	2560	2520	2620

Table 5.16: Transverse coefficient (eD_T/K_0) in meV from hybrid calculations using different interactions models and $\sigma_{\mathrm{NRS}}^{(\mathrm{MT1})}$ and $\sigma_{\mathrm{NRS}}^{(\mathrm{MT2})}$ for a initial dimer [J=0, ν=0]. (a) Model B1 $\sigma_{\mathrm{NRS}}^{(\mathrm{MT1})}$, (b) Model B1 $\sigma_{\mathrm{NRS}}^{(\mathrm{MT2})}$, (c) Model B2 $\sigma_{\mathrm{NRS}}^{(\mathrm{MT1})}$, (d) Model B2 $\sigma_{\mathrm{NRS}}^{(\mathrm{MT2})}$, (e) Model B3 $\sigma_{\mathrm{NRS}}^{(\mathrm{MT1})}$, (f) Model B3 $\sigma_{\mathrm{NRS}}^{(\mathrm{MT2})}$, (g) Model B4 $\sigma_{\mathrm{NRS}}^{(\mathrm{MT1})}$, (h) Model B4 $\sigma_{\mathrm{NRS}}^{(\mathrm{MT2})}$.

Reduced electric field (Td)	(a)	(b)	(c)	(d)	(e)	(f)	(g)	(h)
5	27.1	26.9	27.3	27.0	26.4	26.6	26.9	26.4
10	26.8	26.6	27.3	26.7	26.9	26.7	26.6	26.3
20	28.0	27.3	27.3	27.2	27.2	27.2	26.9	27.0
30	29.1	28.5	29.3	27.8	27.7	28.2	28.4	28.0
50	29.4	30.0	29.5	29.1	28.7	29.3	29.1	29.2
80	34.5	34.7	35.2	35.3	34.0	33.7	32.9	32.0
100	38.1	36.9	38.8	39.6	36.0	34.3	35.5	35.2
200	74.6	71.0	73.8	73.5	66.4	65.1	63.2	62.6
300	115	116	119	110	104	104	97.0	94.5
400	180	174	173	175	159	159	144	139
500	262	262	263	256	217	229	203	190
700	375	380	381	379	325	347	303	281
1000	637	641	625	652	555	581	520	484
2000	1580	1570	1620	1610	1510	1520	1390	1400
3000	2670	2640	2670	2640	2570	2440	2440	2450

Table 5.17: Transverse coefficient (eD_T/K_0) in meV from hybrid calculations using Model B1 and $\sigma_{\mathrm{NRS}}^{(\mathrm{MT1})}$ and $\sigma_{\mathrm{NRS}}^{(\mathrm{MT2})}$ for different initial rotational-vibrational dimer values. (a) $\sigma_{\mathrm{NRS}}^{(\mathrm{MT1})}$ [J=0, ν=1], (b) $\sigma_{\mathrm{NRS}}^{(\mathrm{MT2})}$ [J=0, ν=1], (c) $\sigma_{\mathrm{NRS}}^{(\mathrm{MT1})}$ [J=0, ν=2], (d) $\sigma_{\mathrm{NRS}}^{(\mathrm{MT2})}$ [J=0, ν=2], (e) $\sigma_{\mathrm{NRS}}^{(\mathrm{MT1})}$ [J=0, ν=5], (f) $\sigma_{\mathrm{NRS}}^{(\mathrm{MT2})}$ [J=0, ν=5], (g) $\sigma_{\mathrm{NRS}}^{(\mathrm{MT1})}$ [J=0, ν=12], (h) $\sigma_{\mathrm{NRS}}^{(\mathrm{MT1})}$ [J=0, ν=12].

Reduced electric field (Td)	(a)	(b)	(c)	(d)	(e)	(f)	(g)	(h)
5	26.9	26.5	26.9	26.5	27.0	26.8	26.8	26.1
10	27.3	27.3	26.8	27.1	26.9	26.6	26.6	26.3
20	27.3	27.7	27.4	27.5	27.4	27.8	27.8	26.8
30	28.6	28.8	28.6	28.1	29.4	28.1	28.2	28.5
50	29.2	29.6	29.6	29.4	29.9	29.5	28.9	29.1
80	33.9	34.4	34.3	34.4	34.5	34.4	32.8	33.4
100	37.0	37.5	36.4	38.9	38.4	37.5	36.9	36.7
200	77.0	74.0	74.9	73.1	71.6	71.6	62.4	62.2
300	117	114	119	115	115	114	93.1	96.7
400	177	175	179	172	168	165	135	136
500	266	275	263	262	246	248	187	200
700	391	388	373	395	353	355	275	266
1000	649	668	609	677	609	587	481	481
2000	1670	1640	1640	1620	1570	1600	1390	1410
3000	2690	2660	2660	2630	2610	2590	2420	2440

Table 5.18: Transverse coefficient (eD_T/K_0) in meV from hybrid calculations using Model B1 and $\sigma_{\mathrm{NRS}}^{(\mathrm{MT1})}$ and $\sigma_{\mathrm{NRS}}^{(\mathrm{MT2})}$ for different initial rotational-vibrational dimer values. (a) $\sigma_{\mathrm{NRS}}^{(\mathrm{MT1})}$ [J=10, ν=0], (b) $\sigma_{\mathrm{NRS}}^{(\mathrm{MT2})}$ [J=10, ν=0], (c) $\sigma_{\mathrm{NRS}}^{(\mathrm{MT1})}$ [J=50, ν=0], (d) $\sigma_{\mathrm{NRS}}^{(\mathrm{MT2})}$ [J=50, ν=0], (e) $\sigma_{\mathrm{NRS}}^{(\mathrm{MT1})}$ [J=100, ν=0], (f) $\sigma_{\mathrm{NRS}}^{(\mathrm{MT2})}$ [J=100, ν=0], (g) $\sigma_{\mathrm{NRS}}^{(\mathrm{MT1})}$ [J=200, ν=0], (h) $\sigma_{\mathrm{NRS}}^{(\mathrm{MT1})}$ [J=200, ν=0].

Reduced electric field (Td)	(a)	(b)	(c)	(d)	(e)	(f)	(g)	(h)	(i)	(j)
5	26.9	27.2	27.7	27.3	27.2	26.8	26.9	26.4	26.9	27.1
10	27.3	27.1	27.2	27.1	26.8	26.8	26.6	26.8	26.9	26.8
20	27.6	27.3	27.6	27.7	27.6	27.2	27.4	27.3	27.2	26.9
30	28.8	29.0	28.9	28.6	29.1	28.2	28.5	28.3	28.7	28.2
50	30.0	29.8	30.3	29.4	29.8	29.7	28.9	29.6	29.6	29.8
80	35.0	34.8	35.1	34.5	34.6	34.9	33.3	33.4	33.7	33.4
100	37.3	37.6	37.8	37.9	38.4	39.1	36.6	37.7	36.2	37.7
200	76.5	74.0	76.5	77.2	72.2	70.5	65.7	67.4	65.8	69.2
300	121	117	124	121	112	112	100	103	102	103
400	184	173	185	181	160	163	142	145	143	146
500	264	261	262	261	232	232	196	209	191	206
700	368	385	376	389	341	350	288	301	282	299
1000	631	648	631	564	551	570	482	500	472	501
2000	1550	1530	1530	1570	1510	1440	1350	1370	1390	1390
3000	2600	2610	2570	2560	2520	2480	2400	2390	2290	2270

Table 5.19: Transverse coefficient (eD_T/K_0) in meV from hybrid calculations using Model B2 and $\sigma_{\mathrm{NRS}}^{(\mathrm{MT1})}$ and $\sigma_{\mathrm{NRS}}^{(\mathrm{MT2})}$ for different initial rotational-vibrational dimer values. (a) $\sigma_{\mathrm{NRS}}^{(\mathrm{MT1})}$ [J=0, ν=1], (b) $\sigma_{\mathrm{NRS}}^{(\mathrm{MT2})}$ [J=0, ν=1], (c) $\sigma_{\mathrm{NRS}}^{(\mathrm{MT1})}$ [J=0, ν=2], (d) $\sigma_{\mathrm{NRS}}^{(\mathrm{MT2})}$ [J=0, ν=2], (e) $\sigma_{\mathrm{NRS}}^{(\mathrm{MT1})}$ [J=0, ν=5], (f) $\sigma_{\mathrm{NRS}}^{(\mathrm{MT2})}$ [J=0, ν=5], (g) $\sigma_{\mathrm{NRS}}^{(\mathrm{MT1})}$ [J=0, ν=12], (h) $\sigma_{\mathrm{NRS}}^{(\mathrm{MT1})}$ [J=0, ν=12], (i) $\sigma_{\mathrm{NRS}}^{(\mathrm{MT1})}$ [J=200, ν=0], (j) $\sigma_{\mathrm{NRS}}^{(\mathrm{MT2})}$ [J=200, ν=0].

Reduced electric field (Td)	(a)	(b)	(c)	(d)	(e)	(f)	(g)	(h)	(i)	(j)
5	26.6	26.5	26.6	26.4	27.1	26.8	26.6	27.1	27.1	27.0
10	27.0	27.1	27.2	27.2	27.2	26.9	26.9	26.6	27.2	27.0
20	27.6	26.8	27.2	27.6	27.4	26.6	27.1	26.8	27.4	27.5
30	28.6	28.6	28.9	28.6	29.2	27.9	28.5	29.5	28.4	28.2
50	30.1	29.5	30.4	29.5	29.7	28.6	29.1	29.2	29.5	29.3
80	34.3	34.4	35.5	35.2	34.5	35.0	33.3	32.6	33.9	33.8
100	38.5	37.8	39.6	38.3	38.2	37.5	37.8	36.2	36.6	36.1
200	78.6	77.0	78.1	76.6	72.1	69.6	66.4	67.4	66.5	64.6
300	120	117	121	117	110	109	97.2	105	98.5	104
400	182	181	180	186	164	164	138	147	142	144
500	269	265	259	264	228	244	195	204	194	206
700	371	384	382	402	340	337	287	315	291	291
1000	630	640	627	622	558	575	481	498	470	498
2000	1570	1540	1550	1590	1470	1520	1390	1330	1310	1380
3000	2540	2550	2620	2520	2490	2410	2410	2360	2330	2380

Table 5.20: Transverse coefficient (eD_T/K_0) in meV from hybrid calculations using Model B3 and $\sigma_{\mathrm{NRS}}^{(\mathrm{MT1})}$ and $\sigma_{\mathrm{NRS}}^{(\mathrm{MT2})}$ for different initial rotational-vibrational dimer values. (a) $\sigma_{\mathrm{NRS}}^{(\mathrm{MT1})}$ [J=0, ν=1], (b) $\sigma_{\mathrm{NRS}}^{(\mathrm{MT2})}$ [J=0, ν=1], (c) $\sigma_{\mathrm{NRS}}^{(\mathrm{MT1})}$ [J=0, ν=2], (d) $\sigma_{\mathrm{NRS}}^{(\mathrm{MT2})}$ [J=0, ν=2], (e) $\sigma_{\mathrm{NRS}}^{(\mathrm{MT1})}$ [J=0, ν=5], (f) $\sigma_{\mathrm{NRS}}^{(\mathrm{MT2})}$ [J=0, ν=5], (g) $\sigma_{\mathrm{NRS}}^{(\mathrm{MT1})}$ [J=0, ν=12], (h) $\sigma_{\mathrm{NRS}}^{(\mathrm{MT1})}$ [J=0, ν=12], (i) $\sigma_{\mathrm{NRS}}^{(\mathrm{MT1})}$ [J=200, ν=0], (j) $\sigma_{\mathrm{NRS}}^{(\mathrm{MT2})}$ [J=200, ν=0].

Reduced electric field (Td)	(a)	(b)	(c)	(d)	(e)	(f)	(g)	(h)	(i)	(j)
5	26.7	26.5	27.1	26.9	26.8	26.3	26.5	27.4	26.5	27.1
10	27.0	26.9	27.5	26.8	26.9	26.8	27.0	26.8	26.8	27.4
20	27.1	27.4	27.0	27.0	27.0	27.0	27.0	27.3	27.1	27.9
30	29.2	28.3	28.9	28.5	28.4	28.1	28.3	28.1	28.7	28.2
50	29.3	29.2	30.2	28.3	30.1	29.8	29.5	28.8	29.8	29.5
80	34.9	34.7	35.8	35.2	34.4	34.4	33.9	33.4	34.2	33.4
100	38.6	38.1	37.9	38.2	38.1	39.1	35.4	36.9	38.8	37.2
200	77.7	75.1	77.2	76.6	73.2	70.6	66.4	65.4	66.1	64.4
300	118	118	123	120	111	106	101	100	101	102
400	181	182	183	179	162	162	141	150	141	146
500	256	256	261	273	231	235	200	207	190	203
700	385	388	378	386	353	349	284	300	280	293
1000	615	636	628	637	543	596	493	499	478	513
2000	1590	1550	1620	1580	1500	1480	1380	1390	1380	1360
3000	2650	2610	2650	2590	2510	2430	2360	2330	2490	2390

Table 5.21: Transverse coefficient (eD_T/K_0) in meV from hybrid calculations using Model B4 and $\sigma_{\mathrm{NRS}}^{(\mathrm{MT1})}$ and $\sigma_{\mathrm{NRS}}^{(\mathrm{MT2})}$ for different initial rotational-vibrational dimer values. (a) $\sigma_{\mathrm{NRS}}^{(\mathrm{MT1})}$ [J=0, ν=1], (b) $\sigma_{\mathrm{NRS}}^{(\mathrm{MT2})}$ [J=0, ν=1], (c) $\sigma_{\mathrm{NRS}}^{(\mathrm{MT1})}$ [J=0, ν=2], (d) $\sigma_{\mathrm{NRS}}^{(\mathrm{MT2})}$ [J=0, ν=2], (e) $\sigma_{\mathrm{NRS}}^{(\mathrm{MT1})}$ [J=0, ν=5], (f) $\sigma_{\mathrm{NRS}}^{(\mathrm{MT2})}$ [J=0, ν=5], (g) $\sigma_{\mathrm{NRS}}^{(\mathrm{MT1})}$ [J=0, ν=12], (h) $\sigma_{\mathrm{NRS}}^{(\mathrm{MT1})}$ [J=0, ν=12], (i) $\sigma_{\mathrm{NRS}}^{(\mathrm{MT1})}$ [J=200, ν=0], (j) $\sigma_{\mathrm{NRS}}^{(\mathrm{MT2})}$ [J=200, ν=0].

Reduced electric field (Td)	(a)	(b)	(c)	(d)	(e)	(f)	(g)	(h)
5	28.0	28.3	28.3	27.7	26.9	28.1	28.9	27.6
10	28.3	28.5	27.9	27.7	28.2	28.1	28.1	27.8
20	29.0	28.7	28.3	28.7	29.8	29.3	29.1	28.1
30	33.3	31.9	31.3	31.9	32.8	31.7	32.6	30.9
50	36.8	35.4	37.7	35.9	35.7	35.7	35.6	35.6
80	55.6	53.7	60.1	55.7	57.9	58.3	61.5	56.1
100	72.2	67.2	70.2	65.5	70.5	66.9	74.2	68.1
200	175	187	186	181	182	186	189	188
300	228	251	241	256	242	246	234	254
400	284	321	289	313	280	310	287	308
500	345	374	339	373	340	354	350	355
700	546	582	532	557	527	546	548	549
1000	1050	988	949	961	986	960	975	930
2000	2080	2010	1980	1980	2060	1960	2100	2010
3000	2680	2540	2570	2570	2650	2660	2720	2550

Table 5.22: Longitudinal coefficient (eD_L/K_0) in meV from hybrid calculations using different interactions models and $\sigma_{\mathrm{NRS}}^{(\mathrm{MT1})}$ and $\sigma_{\mathrm{NRS}}^{(\mathrm{MT2})}$ for a initial dimer [J=0, ν=0]. (a) Model B1 $\sigma_{\mathrm{NRS}}^{(\mathrm{MT1})}$, (b) Model B1 $\sigma_{\mathrm{NRS}}^{(\mathrm{MT2})}$, (c) Model B2 $\sigma_{\mathrm{NRS}}^{(\mathrm{MT1})}$, (d) Model B2 $\sigma_{\mathrm{NRS}}^{(\mathrm{MT2})}$, (e) Model B3 $\sigma_{\mathrm{NRS}}^{(\mathrm{MT1})}$, (f) Model B3 $\sigma_{\mathrm{NRS}}^{(\mathrm{MT2})}$, (g) Model B4 $\sigma_{\mathrm{NRS}}^{(\mathrm{MT1})}$, (h) Model B4 $\sigma_{\mathrm{NRS}}^{(\mathrm{MT2})}$.

Reduced electric field (Td)	(a)	(b)	(c)	(d)	(e)	(f)	(g)	(h)
5	28.1	27.8	28.1	28.3	27.3	27.6	27.3	27.5
10	28.3	27.8	28.2	27.9	28.2	27.3	27.0	27.1
20	28.7	28.2	28.5	29.2	28.6	27.3	27.8	27.8
30	32.2	32.3	31.7	32.3	31.9	30.4	31.0	30.3
50	35.7	33.9	35.6	34.8	34.1	32.7	33.3	33.2
80	54.5	50.1	53.7	53.5	45.4	46.4	42.8	43.0
100	65.2	62.1	63.0	67.3	57.4	55.4	53.0	52.3
200	170	170	173	173	146	147	122	111
300	228	249	238	240	214	223	194	165
400	289	326	282	295	273	292	253	240
500	372	375	358	348	338	362	327	296
700	568	611	560	583	580	578	531	508
1000	1040	995	1040	1020	1030	1030	1020	1060
2000	2080	2030	2150	2090	2160	2090	2160	2320
3000	2570	2610	2650	2640	2750	2700	2840	2750

Table 5.23: Longitudinal coefficient (eD_L/K_0)in meV from hybrid calculations using Model B1 and $\sigma_{\mathrm{NRS}}^{(\mathrm{MT1})}$ and $\sigma_{\mathrm{NRS}}^{(\mathrm{MT2})}$ for different initial rotational-vibrational dimer values. (a) $\sigma_{\mathrm{NRS}}^{(\mathrm{MT1})}$ [J=0, ν=1], (b) $\sigma_{\mathrm{NRS}}^{(\mathrm{MT2})}$ [J=0, ν=1], (c) $\sigma_{\mathrm{NRS}}^{(\mathrm{MT1})}$ [J=0, ν=2], (d) $\sigma_{\mathrm{NRS}}^{(\mathrm{MT2})}$ [J=0, ν=2], (e) $\sigma_{\mathrm{NRS}}^{(\mathrm{MT1})}$ [J=0, ν=5], (f) $\sigma_{\mathrm{NRS}}^{(\mathrm{MT2})}$ [J=0, ν=5], (g) $\sigma_{\mathrm{NRS}}^{(\mathrm{MT1})}$ [J=0, ν=12], (h) $\sigma_{\mathrm{NRS}}^{(\mathrm{MT1})}$ [J=0, ν=12].

Reduced electric field (Td)	(a)	(b)	(c)	(d)	(e)	(f)	(g)	(h)
5	28.0	27.4	27.6	26.8	28.0	28.0	27.4	26.9
10	28.1	27.8	28.1	28.0	27.9	27.8	27.8	26.9
20	28.6	28.7	29.1	29.6	28.8	28.9	27.1	27.6
30	31.7	33.2	32.4	32.1	33.3	31.5	29.7	30.5
50	34.8	34.1	35.0	35.3	35.9	36.1	33.3	34.1
80	55.0	51.8	52.3	49.5	54.5	52.4	42.8	43.8
100	66.3	64.2	63.8	62.2	64.9	64.9	52.6	52.7
200	174	184	173	183	154	157	113	120
300	248	257	242	251	213	223	173	191
400	312	339	298	320	262	290	225	244
500	353	384	358	386	330	366	296	314
700	598	610	576	622	573	575	518	533
1000	1020	1020	1040	1010	1060	980	1030	987
2000	2050	1980	2130	2020	2280	2110	2400	2190
3000	2670	2650	2750	2580	2740	2570	2840	2700

Table 5.24: Longitudinal coefficient (eD_L/K_0) in meV from hybrid calculations using Model B1 and $\sigma_{\mathrm{NRS}}^{(\mathrm{MT1})}$ and $\sigma_{\mathrm{NRS}}^{(\mathrm{MT2})}$ for different initial rotational-vibrational dimer values. (a) $\sigma_{\mathrm{NRS}}^{(\mathrm{MT1})}$ [J=10, ν=0], (b) $\sigma_{\mathrm{NRS}}^{(\mathrm{MT2})}$ [J=10, ν=0], (c) $\sigma_{\mathrm{NRS}}^{(\mathrm{MT1})}$ [J=50, ν=0], (d) $\sigma_{\mathrm{NRS}}^{(\mathrm{MT2})}$ [J=50, ν=0], (e) $\sigma_{\mathrm{NRS}}^{(\mathrm{MT1})}$ [J=100, ν=0], (f) $\sigma_{\mathrm{NRS}}^{(\mathrm{MT2})}$ [J=100, ν=0], (g) $\sigma_{\mathrm{NRS}}^{(\mathrm{MT1})}$ [J=200, ν=0], (h) $\sigma_{\mathrm{NRS}}^{(\mathrm{MT1})}$ [J=200, ν=0].

Reduced electric field (Td)	(a)	(b)	(c)	(d)	(e)	(f)	(g)	(h)	(i)	(j)
5	27.6	27.8	28.5	27.9	27.7	27.3	27.9	27.3	27.8	27.8
10	28.0	27.8	28.4	27.7	27.9	27.8	27.4	27.7	27.8	27.3
20	29.2	29.4	29.4	28.8	29.0	28.8	28.0	28.4	29.5	28.0
30	31.5	32.2	32.1	32.0	32.0	32.2	31.9	31.2	31.9	31.5
50	36.2	35.5	36.8	36.2	35.3	36.7	34.3	34.5	34.2	35.0
80	56.8	55.9	58.6	56.6	50.3	52.5	47.9	48.5	46.8	46.3
100	66.6	66.5	70.8	68.8	63.6	65.4	55.6	56.6	54.7	56.4
200	175	183	171	176	142	144	119	125	117	120
300	232	240	219	233	195	209	164	175	159	178
400	297	299	280	300	242	263	210	230	223	232
500	335	360	322	358	320	343	285	304	305	303
700	540	584	557	541	519	549	520	501	503	495
1000	1050	966	980	971	1040	969	980	991	973	965
2000	2100	1900	2080	2030	2220	209	2280	2190	2330	219
3000	2580	2670	2580	2610	2820	2690	2870	2810	2790	2710

Table 5.25: Longitudinal coefficient (eD_L/K_0) in meV from hybrid calculations using Model B2 and $\sigma_{\mathrm{NRS}}^{(\mathrm{MT1})}$ and $\sigma_{\mathrm{NRS}}^{(\mathrm{MT2})}$ for different initial rotational-vibrational dimer values. (a) $\sigma_{\mathrm{NRS}}^{(\mathrm{MT1})}$ [J=0, ν=1], (b) $\sigma_{\mathrm{NRS}}^{(\mathrm{MT2})}$ [J=0, ν=1], (c) $\sigma_{\mathrm{NRS}}^{(\mathrm{MT1})}$ [J=0, ν=2], (d) $\sigma_{\mathrm{NRS}}^{(\mathrm{MT2})}$ [J=0, ν=2], (e) $\sigma_{\mathrm{NRS}}^{(\mathrm{MT1})}$ [J=0, ν=5], (f) $\sigma_{\mathrm{NRS}}^{(\mathrm{MT2})}$ [J=0, ν=5], (g) $\sigma_{\mathrm{NRS}}^{(\mathrm{MT1})}$ [J=0, ν=12], (h) $\sigma_{\mathrm{NRS}}^{(\mathrm{MT1})}$ [J=0, ν=12], (i) $\sigma_{\mathrm{NRS}}^{(\mathrm{MT1})}$ [J=200, ν=0], (j) $\sigma_{\mathrm{NRS}}^{(\mathrm{MT2})}$ [J=200, ν=0].

Reduced electric field (Td)	(a)	(b)	(c)	(d)	(e)	(f)	(g)	(h)	(i)	(j)
5	27.7	26.8	27.5	27.5	27.6	27.6	27.1	27.9	27.5	28.5
10	28.1	28.1	27.5	28.0	28.1	28.0	28.0	27.3	27.4	27.6
20	28.3	29.2	29.5	28.8	29.4	28.7	28.6	28.3	28.7	28.6
30	31.9	31.7	32.8	31.2	31.8	32.6	31.4	31.2	31.9	31.3
50	36.8	36.0	36.4	36.7	35.2	34.6	33.7	34.3	33.5	34.2
80	58.0	56.4	59.8	56.4	53.8	51.1	46.9	47.8	48.2	48.8
100	67.2	66.9	76.5	69.4	65.0	64.0	53.5	56.5	54.7	59.2
200	172	178	181	180	143	146	115	122	114	122
300	227	243	223	233	193	210	159	165	157	172
400	285	296	279	304	247	280	214	236	222	225
500	331	364	340	343	326	357	287	322	274	309
700	568	589	524	569	523	548	517	532	479	497
1000	990	948	971	971	978	950	1010	963	1030	978
2000	2060	1950	2100	2000	2180	2060	2320	2180	2320	2220
3000	2640	2480	2680	2580	2710	2710	2770	2810	2810	2690

Table 5.26: Longitudinal coefficient (eD_L/K_0) in meV from hybrid calculations using Model B3 and $\sigma_{\mathrm{NRS}}^{(\mathrm{MT1})}$ and $\sigma_{\mathrm{NRS}}^{(\mathrm{MT2})}$ for different initial rotational-vibrational dimer values. (a) $\sigma_{\mathrm{NRS}}^{(\mathrm{MT1})}$ [J=0, ν=1], (b) $\sigma_{\mathrm{NRS}}^{(\mathrm{MT2})}$ [J=0, ν=1], (c) $\sigma_{\mathrm{NRS}}^{(\mathrm{MT1})}$ [J=0, ν=2], (d) $\sigma_{\mathrm{NRS}}^{(\mathrm{MT2})}$ [J=0, ν=2], (e) $\sigma_{\mathrm{NRS}}^{(\mathrm{MT1})}$ [J=0, ν=5], (f) $\sigma_{\mathrm{NRS}}^{(\mathrm{MT2})}$ [J=0, ν=5], (g) $\sigma_{\mathrm{NRS}}^{(\mathrm{MT1})}$ [J=0, ν=12], (h) $\sigma_{\mathrm{NRS}}^{(\mathrm{MT1})}$ [J=0, ν=12], (i) $\sigma_{\mathrm{NRS}}^{(\mathrm{MT1})}$ [J=200, ν=0], (j) $\sigma_{\mathrm{NRS}}^{(\mathrm{MT2})}$ [J=200, ν=0].

Reduced electric field (Td)	(a)	(b)	(c)	(d)	(e)	(f)	(g)	(h)	(i)	(j)
5	27.6	27.4	28.0	27.4	27.4	27.4	27.6	27.8	27.6	27.3
10	28.1	27.9	28.2	28.0	28.0	27.7	28.1	27.8	27.5	27.5
20	28.9	29.2	29.4	28.5	28.5	28.5	28.7	28.5	28.7	29.2
30	32.9	32.5	32.8	32.2	32.2	31.7	31.8	32.2	31.0	31.3
50	35.6	35.3	36.2	35.7	35.9	34.0	34.3	33.9	33.8	34.6
80	57.3	52.8	59.6	57.1	52.0	50.9	46.6	48.6	46.8	47.0
100	71.4	66.2	72.0	68.5	60.3	65.4	55.6	60.6	57.2	58.0
200	173	178	169	177	143	148	117	123	114	122
300	222	239	221	239	198	204	164	178	159	171
400	282	304	272	302	259	272	219	241	224	234
500	334	357	337	363	331	348	291	304	278	308
700	545	579	541	559	535	544	507	526	471	503
1000	980	958	998	966	1000	991	1010	952	988	946
2000	2040	2000	2080	2000	2190	214	2180	2190	2330	2230
3000	2690	2680	2670	2580	2740	2630	2840	2780	2870	2760

Table 5.27: Longitudinal coefficient (eD_L/K_0) in meV from hybrid calculations using Model B4 and $\sigma_{\mathrm{NRS}}^{(\mathrm{MT1})}$ and $\sigma_{\mathrm{NRS}}^{(\mathrm{MT2})}$ for different initial rotational-vibrational dimer values. (a) $\sigma_{\mathrm{NRS}}^{(\mathrm{MT1})}$ [J=0, ν=1], (b) $\sigma_{\mathrm{NRS}}^{(\mathrm{MT2})}$ [J=0, ν=1], (c) $\sigma_{\mathrm{NRS}}^{(\mathrm{MT1})}$ [J=0, ν=2], (d) $\sigma_{\mathrm{NRS}}^{(\mathrm{MT2})}$ [J=0, ν=2], (e) $\sigma_{\mathrm{NRS}}^{(\mathrm{MT1})}$ [J=0, ν=5], (f) $\sigma_{\mathrm{NRS}}^{(\mathrm{MT2})}$ [J=0, ν=5], (g) $\sigma_{\mathrm{NRS}}^{(\mathrm{MT1})}$ [J=0, ν=12], (h) $\sigma_{\mathrm{NRS}}^{(\mathrm{MT1})}$ [J=0, ν=12], (i) $\sigma_{\mathrm{NRS}}^{(\mathrm{MT1})}$ [J=200, ν=0], (j) $\sigma_{\mathrm{NRS}}^{(\mathrm{MT2})}$ [J=200, ν=0].

Reduced electric field (Td)	(a)	(b)	(c)	(d)	(e)	(f)	(g)	(h)	(i)	(j)
150	/	/	/	/	/	/	/	/	/	/
160	/	/	/	2.49E-21	/	/	/	/	/	1.24E-21
170	/	/	/	1.24E-21	/	/	/	/	/	2.49E-21
180	/	/	/	4.96E-21	/	/	/	/	/	4.96E-21
190	/	/	/	4.96E-21	/	/	/	/	/	8.06E-21
200	1.05E-20	1.43E-20	1.74E-20	9.92E-21	3.09E-20	8.68E-21	1.49E-20	2.05E-20	1.80E-20	1.98E-20
300	3.87E-19	4.59E-19	4.22E-19	4.49E-19	4.56E-19	5.14E-19	4.19E-19	4.89E-19	4.47E-19	5.25E-19
400	2.91E-18	3.05E-18	2.91E-18	3.14E-18	3.06E-18	3.33E-18	3.09E-18	3.37E-18	3.08E-18	3.40E-18
500	9.41E-18	1.04E-17	9.41E-18	1.06E-17	9.67E-18	1.07E-17	9.72E-18	1.08E-17	9.76E-18	1.05E-17
700	1.73E-17	1.75E-17	3.85E-17	4.13E-17	3.83E-17	4.12E-17	3.82E-17	4.11E-17	3.83E-17	4.08E-17
1000	7.04E-17	7.09E-17	1.21E-16	1.26E-16	1.18E-16	1.23E-16	1.17E-16	1.23E-16	1.18E-16	1.22E-16
2000	4.19E-16	4.18E-16	4.90E-16	4.88E-16	4.83E-16	4.82E-16	4.83E-16	4.82E-16	4.82E-16	4.82E-16
3000	7.72E-16	7.59E-16	7.89E-16	7.83E-16	7.87E-16	7.79E-16	7.85E-16	7.80E-16	7.85E-16	7.79E-16

Table 5.28: Dissociation rate constant in m^3s^{-1} from hybrid calculations using different interactions models and $\sigma_{\mathrm{NRS}}^{(\mathrm{MT1})}$ and $\sigma_{\mathrm{NRS}}^{(\mathrm{MT2})}$ for a initial dimer [J=0, ν=0]. (a) Model A1 $\sigma_{\mathrm{NRS}}^{(\mathrm{MT1})}$, (b) Model A1 $\sigma_{\mathrm{NRS}}^{(\mathrm{MT2})}$, (c) Model B1 $\sigma_{\mathrm{NRS}}^{(\mathrm{MT1})}$, (d) Model B1 $\sigma_{\mathrm{NRS}}^{(\mathrm{MT2})}$, (e) Model B2 $\sigma_{\mathrm{NRS}}^{(\mathrm{MT1})}$, (f) Model B2 $\sigma_{\mathrm{NRS}}^{(\mathrm{MT2})}$, (g) Model B3 $\sigma_{\mathrm{NRS}}^{(\mathrm{MT1})}$, (h) Model B3 $\sigma_{\mathrm{NRS}}^{(\mathrm{MT2})}$, (i) Model B4 $\sigma_{\mathrm{NRS}}^{(\mathrm{MT1})}$, (j) Model B4 $\sigma_{\mathrm{NRS}}^{(\mathrm{MT2})}$.

Reduced electric field (Td)	(a)	(b)	(c)	(d)	(e)	(f)	(g)	(h)
150	/	1.23E-21	/	/	/	/	/	/
160	/	1.25E-21	/	/	/	/	/	1.24E-21
170	/	1.22E-21	/	/	/	/	/	/
180	/	4.95E-21	/	/	/	/	/	3.71E-21
190	/	9.96E-21	/	/	/	/	/	4.94E-21
200	1.24E-20	1.61E-20	1.49E-20	1.99E-20	3.71E-21	2.45E-21	1.24E-20	8.64E-21
300	3.77E-19	4.44E-19	4.19E-19	4.05E-19	2.48E-19	3.86E-19	3.73E-19	2.32E-19
400	2.88E-18	3.21E-18	3.04E-18	3.05E-18	2.23E-18	2.79E-18	2.85E-18	2.06E-18
500	9.37E-18	1.05E-17	9.82E-18	9.98E-18	7.80E-18	9.68E-18	9.87E-18	7.53E-18
700	3.85E-17	4.22E-17	4.05E-17	4.38E-17	3.54E-17	3.97E-17	4.18E-17	3.59E-17
1000	1.22E-16	1.26E-16	1.25E-16	1.30E-16	1.18E-16	1.25E-16	1.34E-16	1.22E-16
2000	4.92E-16	4.89E-16	4.96E-16	4.95E-16	4.97E-16	4.95E-16	5.21E-16	5.2E-16
3000	7.90E-16	7.85E-16	7.94E-16	7.90E-16	8.01E-16	7.96E-16	8.26E-16	8.33E-16

Table 5.29: Dissociation rate constant in m^3s^{-1} from hybrid calculations using Model B1 and $\sigma_{\mathrm{NRS}}^{(\mathrm{MT1})}$ and $\sigma_{\mathrm{NRS}}^{(\mathrm{MT2})}$ for different initial rotational-vibrational dimer values. (a) $\sigma_{\mathrm{NRS}}^{(\mathrm{MT1})}$ [J=0, ν=1], (b) $\sigma_{\mathrm{NRS}}^{(\mathrm{MT2})}$ [J=0, ν=1], (c) $\sigma_{\mathrm{NRS}}^{(\mathrm{MT1})}$ [J=0, ν=2], (d) $\sigma_{\mathrm{NRS}}^{(\mathrm{MT2})}$ [J=0, ν=2], (e) $\sigma_{\mathrm{NRS}}^{(\mathrm{MT1})}$ [J=0, ν=5], (f) $\sigma_{\mathrm{NRS}}^{(\mathrm{MT2})}$ [J=0, ν=5], (g) $\sigma_{\mathrm{NRS}}^{(\mathrm{MT1})}$ [J=0, ν=12], (h) $\sigma_{\mathrm{NRS}}^{(\mathrm{MT1})}$ [J=0, ν=12].

Reduced electric field (Td)	(a)	(b)	(c)	(d)	(e)	(f)	(g)	(h)
150	/	/	/	1.22E-21	/	/	/	/
160	/	/	/	/	/	/	/	/
170	/	/	/	1.87E-21	/	/	/	2.49E-21
180	/	/	/	6.22E-21	/	/	/	5.59E-21
190	/	/	/	3.74E-21	/	/	/	9.26E-21
200	1.86E-20	8.64E-21	9.89E-21	1.42E-20	6.18E-21	9.88E-21	1.11E-20	1.18E-20
300	3.70E-19	4.29E-19	4.20E-19	4.68E-19	3.35E-19	4.16E-19	2.64E-19	4.17E-19
400	2.69E-18	3.27E-18	3.03E-18	3.43E-18	2.55E-18	3.13E-18	2.10E-18	2.85E-18
500	9.62E-18	1.06E-17	9.80E-18	1.09E-17	8.69E-18	1.03E-17	7.44E-18	9.84E-18
700	3.90E-17	4.20E-17	3.92E-17	4.33E-17	3.69E-17	4.09E-17	3.52E-17	4.20E-17
1000	1.22E-16	1.26E-16	1.23E-16	1.27E-16	1.20E-16	1.26E-16	1.22E-16	1.33E-16
2000	4.87E-16	4.84E-16	4.87E-16	4.84E-16	4.95E-16	4.93E-16	5.24E-16	5.26E-16
3000	7.85E-16	7.80E-16	7.81E-16	7.75E-16	7.99E-16	7.92E-16	8.39E-16	8.32E-16

Table 5.30: Dissociation rate constant in m^3s^{-1} from hybrid calculations using Model B1 and $\sigma_{\mathrm{NRS}}^{(\mathrm{MT1})}$ and $\sigma_{\mathrm{NRS}}^{(\mathrm{MT2})}$ for different initial rotational-vibrational dimer values. (a) $\sigma_{\mathrm{NRS}}^{(\mathrm{MT1})}$ [J=10, ν=0], (b) $\sigma_{\mathrm{NRS}}^{(\mathrm{MT2})}$ [J=10, ν=0], (c) $\sigma_{\mathrm{NRS}}^{(\mathrm{MT1})}$ [J=50, ν=0], (d) $\sigma_{\mathrm{NRS}}^{(\mathrm{MT2})}$ [J=50, ν=0], (e) $\sigma_{\mathrm{NRS}}^{(\mathrm{MT1})}$ [J=100, ν=0], (f) $\sigma_{\mathrm{NRS}}^{(\mathrm{MT2})}$ [J=100, ν=0], (g) $\sigma_{\mathrm{NRS}}^{(\mathrm{MT1})}$ [J=200, ν=0], (h) $\sigma_{\mathrm{NRS}}^{(\mathrm{MT1})}$ [J=200, ν=0].

Reduced electric field (Td)	(a)	(b)	(c)	(d)	(e)	(f)	(g)	(h)	(i)	(j)
200	1.93E-20	1.86E-20	2.30E-20	2.60E-20	6.19E-21	1.05E-20	1.18E-20	1.37E-20	6.19E-21	1.99E-20
300	4.68E-19	5.55E-19	4.21E-19	5.36E-19	3.39E-19	3.66E-19	2.76E-19	3.96E-19	2.65E-19	4.02E-19
400	3.20E-18	3.51E-18	3.26E-18	3.82E-18	2.36E-18	2.94E-18	2.16E-18	3.10E-18	2.25E-18	2.99E-18
500	1.01E-17	1.13E-17	1.03E-17	1.17E-17	8.34E-18	1.01E-17	7.98E-18	1.04E-17	7.93E-18	1.01E-17
700	3.92E-17	4.30E-17	4.09E-17	4.42E-17	3.52E-17	4.04E-17	3.65E-17	4.23E-17	3.51E-17	4.21E-17
1000	1.21E-16	1.27E-16	1.25E-16	1.29E-16	1.17E-16	1.23E-16	1.23E-16	1.33E-16	1.22E-16	1.33E-16
2000	4.87E-16	4.84E-16	4.92E-16	4.92E-16	4.94E-16	4.92E-16	5.17E-16	5.19E-16	5.22E-16	5.24E-16
3000	7.84E-16	7.79E-16	7.93E-16	7.87E-16	8.00E-16	7.93E-16	8.32E-16	8.23E-16	8.39E-16	8.33E-16

Table 5.31: Dissociation rate constant in m^3s^{-1} from hybrid calculations using Model B2 and $\sigma_{\mathrm{NRS}}^{(\mathrm{MT1})}$ and $\sigma_{\mathrm{NRS}}^{(\mathrm{MT2})}$ for different initial rotational-vibrational dimer values. (a) $\sigma_{\mathrm{NRS}}^{(\mathrm{MT1})}$ [J=0, ν=1], (b) $\sigma_{\mathrm{NRS}}^{(\mathrm{MT2})}$ [J=0, ν=1], (c) $\sigma_{\mathrm{NRS}}^{(\mathrm{MT1})}$ [J=0, ν=2], (d) $\sigma_{\mathrm{NRS}}^{(\mathrm{MT2})}$ [J=0, ν=2], (e) $\sigma_{\mathrm{NRS}}^{(\mathrm{MT1})}$ [J=0, ν=5], (f) $\sigma_{\mathrm{NRS}}^{(\mathrm{MT2})}$ [J=0, ν=5], (g) $\sigma_{\mathrm{NRS}}^{(\mathrm{MT1})}$ [J=0, ν=12], (h) $\sigma_{\mathrm{NRS}}^{(\mathrm{MT1})}$ [J=0, ν=12], (i) $\sigma_{\mathrm{NRS}}^{(\mathrm{MT1})}$ [J=200, ν=0], (j) $\sigma_{\mathrm{NRS}}^{(\mathrm{MT2})}$ [J=200, ν=0].

Reduced electric field (Td)	(a)	(b)	(c)	(d)	(e)	(f)	(g)	(h)	(i)	(j)
200	1.36E-20	1.24E-20	1.43E-20	1.98E-20	5.57E-21	9.92E-21	4.92E-21	1.74E-20	8.07E-21	1.49E-20
300	4.71E-19	5.12E-19	5.08E-19	5.68E-19	3.12E-19	4.07E-19	3.01E-19	4.19E-19	2.47E-19	4.51E-19
400	3.08E-18	3.38E-18	3.29E-18	3.69E-18	2.33E-18	3.14E-18	2.22E-18	3.00E-18	2.09E-18	3.01E-18
500	1.00E-17	1.11E-17	1.05E-17	1.19E-17	8.08E-18	1.00E-17	7.78E-18	1.01E-17	7.70E-18	1.01E-17
700	3.92E-17	4.27E-17	4.15E-17	4.49E-17	3.60E-17	4.01E-17	3.67E-17	4.30E-17	3.52E-17	4.24E-17
1000	1.20E-16	1.25E-16	1.25E-16	1.30E-16	1.16E-16	1.24E-16	1.23E-16	1.32E-16	1.21E-16	1.32E-16
2000	4.85E-16	4.85E-16	4.91E-16	4.93E-16	4.89E-16	4.91E-16	5.19E-16	5.19E-16	5.20E-16	5.23E-16
3000	7.85E-16	7.82E-16	7.92E-16	7.86E-16	7.99E-16	7.92E-16	8.30E-16	8.24E-16	8.34E-16	8.32E-16

Table 5.32: Dissociation rate constant in m^3s^{-1} from hybrid calculations using Model B3 and $\sigma_{\mathrm{NRS}}^{(\mathrm{MT1})}$ and $\sigma_{\mathrm{NRS}}^{(\mathrm{MT2})}$ for different initial rotational-vibrational dimer values. (a) $\sigma_{\mathrm{NRS}}^{(\mathrm{MT1})}$ [J=0, ν=1], (b) $\sigma_{\mathrm{NRS}}^{(\mathrm{MT2})}$ [J=0, ν=1], (c) $\sigma_{\mathrm{NRS}}^{(\mathrm{MT1})}$ [J=0, ν=2], (d) $\sigma_{\mathrm{NRS}}^{(\mathrm{MT2})}$ [J=0, ν=2], (e) $\sigma_{\mathrm{NRS}}^{(\mathrm{MT1})}$ [J=0, ν=5], (f) $\sigma_{\mathrm{NRS}}^{(\mathrm{MT2})}$ [J=0, ν=5], (g) $\sigma_{\mathrm{NRS}}^{(\mathrm{MT1})}$ [J=0, ν=12], (h) $\sigma_{\mathrm{NRS}}^{(\mathrm{MT1})}$ [J=0, ν=12], (i) $\sigma_{\mathrm{NRS}}^{(\mathrm{MT1})}$ [J=200, ν=0], (j) $\sigma_{\mathrm{NRS}}^{(\mathrm{MT2})}$ [J=200, ν=0].

Reduced electric field (Td)	(a)	(b)	(c)	(d)	(e)	(f)	(g)	(h)	(i)	(j)
150	/	/	/	/	/	/	/	/	/	2.46E-21
160	/	1.24E-21	/	2.47E-21	/	/	/	/	/	1.25E-21
170	/	2.49E-21	/	1.23E-21	/	/	/	/	/	1.24E-21
180	/	4.96E-21	/	8.03E-21	/	/	/	/	/	/
190	/	8.06E-21	/	6.22E-21	/	/	/	/	/	1.12E-20
200	1.80E-20	1.98E-20	1.55E-20	1.55E-20	2.11E-20	2.04E-20	8.01E-21	1.73E-20	1.61E-20	1.79E-20
300	4.47E-19	5.25E-19	4.85E-19	5.13E-19	5.16E-19	5.30E-19	2.77E-19	3.93E-19	3.35E-19	4.82E-19
400	3.08E-18	3.40E-18	3.02E-18	3.39E-18	3.32E-18	3.69E-18	2.34E-18	2.96E-18	2.34E-18	3.09E-18
500	9.76E-18	1.05E-17	9.82E-18	1.08E-17	1.05E-17	1.19E-17	8.09E-18	1.00E-17	8.10E-18	1.02E-17
700	3.83E-17	4.08E-17	3.84E-17	4.21E-17	4.12E-17	4.49E-17	3.57E-17	4.00E-17	3.62E-17	4.23E-17
1000	1.18E-16	1.22E-16	1.19E-16	1.24E-16	1.24E-16	1.30E-16	1.16E-16	1.24E-16	1.24E-16	1.33E-16
2000	4.82E-16	4.82E-16	4.84E-16	4.82E-16	4.93E-16	4.92E-16	4.92E-16	4.91E-16	5.18E-16	5.19E-16
3000	7.85E-16	7.79E-16	7.88E-16	7.80E-16	7.95E-16	7.88E-16	7.98E-16	7.93E-16	8.31E-16	8.25E-16

Table 5.33: Dissociation rate constant in m^3s^{-1} from hybrid calculations using Model B4 and $\sigma_{\mathrm{NRS}}^{(\mathrm{MT1})}$ and $\sigma_{\mathrm{NRS}}^{(\mathrm{MT2})}$ for different initial rotational-vibrational dimer values. (a) $\sigma_{\mathrm{NRS}}^{(\mathrm{MT1})}$ [J=0, ν=1], (b) $\sigma_{\mathrm{NRS}}^{(\mathrm{MT2})}$ [J=0, ν=1], (c) $\sigma_{\mathrm{NRS}}^{(\mathrm{MT1})}$ [J=0, ν=2], (d) $\sigma_{\mathrm{NRS}}^{(\mathrm{MT2})}$ [J=0, ν=2], (e) $\sigma_{\mathrm{NRS}}^{(\mathrm{MT1})}$ [J=0, ν=5], (f) $\sigma_{\mathrm{NRS}}^{(\mathrm{MT2})}$ [J=0, ν=5], (g) $\sigma_{\mathrm{NRS}}^{(\mathrm{MT1})}$ [J=0, ν=12], (h) $\sigma_{\mathrm{NRS}}^{(\mathrm{MT1})}$ [J=0, ν=12], (i) $\sigma_{\mathrm{NRS}}^{(\mathrm{MT1})}$ [J=200, ν=0], (j) $\sigma_{\mathrm{NRS}}^{(\mathrm{MT2})}$ [J=200, ν=0].

D Tables of transport coefficients and dissociation rate constant for $\mathrm{Xe}_2^+/\mathrm{Xe}$ collisions

Reduced electric field (Td)	(a)	(b)	(c)	(d)	(e)	(f)
5	0.587	0.562	0.590	0.589	0.586	0.585
10	0.585	0.562	0.591	0.587	0.587	0.582
20	0.581	0.562	0.589	0.584	0.586	0.579
30	0.58	0.555	0.584	0.579	0.582	0.576
50	0.570	0.554	0.584	0.574	0.581	0.570
80	0.565	0.548	0.579	0.568	0.578	0.565
100	0.556	0.538	0.573	0.561	0.572	0.560
200	0.562	0.539	0.596	0.573	0.598	0.575
300	0.570	0.546	0.622	0.594	0.628	0.598
400	0.568	0.548	0.629	0.607	0.632	0.611
500	0.554	0.543	0.618	0.601	0.623	0.606
700	0.517	0.512	0.564	0.561	0.569	0.564
1000	0.480	0.477	0.508	0.511	0.510	0.511
2000	0.420	0.409	0.417	0.416	0.414	0.414
3000	0.369	0.358	0.362	0.360	0.359	0.357

Table 5.34: Mobility values in $cm^2V^{-1}s^{-1}$ from hybrid calculations using different interactions models and $\sigma_{\mathrm{NRS}}^{(\mathrm{MT1})}$ and $\sigma_{\mathrm{NRS}}^{(\mathrm{MT2})}$ for a initial dimer [J=0, ν=0]. (a) Model A1 $\sigma_{\mathrm{NRS}}^{(\mathrm{MT1})}$, (b) Model A1 $\sigma_{\mathrm{NRS}}^{(\mathrm{MT2})}$, (c) Model B1 $\sigma_{\mathrm{NRS}}^{(\mathrm{MT1})}$, (d) Model B1 $\sigma_{\mathrm{NRS}}^{(\mathrm{MT2})}$, (e) Model B2 $\sigma_{\mathrm{NRS}}^{(\mathrm{MT1})}$, (f) Model B2 $\sigma_{\mathrm{NRS}}^{(\mathrm{MT2})}$.

Reduced electric field (Td)	(a)	(b)	(c)	(d)	(e)	(f)	(g)	(h)
5	0.589	0.576	0.595	0.569	0.591	0.583	0.587	0.594
10	0.591	0.580	0.588	0.576	0.592	0.583	0.587	0.586
20	0.590	0.582	0.586	0.573	0.593	0.583	0.586	0.578
30	0.585	0.576	0.580	0.570	0.589	0.580	0.580	0.575
50	0.583	0.572	0.577	0.565	0.585	0.577	0.576	0.569
80	0.578	0.570	0.573	0.563	0.581	0.570	0.569	0.566
100	0.571	0.560	0.568	0.559	0.574	0.566	0.561	0.558
200	0.592	0.575	0.584	0.569	0.584	0.570	0.557	0.554
300	0.613	0.593	0.601	0.583	0.591	0.581	0.553	0.550
400	0.617	0.603	0.603	0.592	0.589	0.582	0.543	0.547
500	0.606	0.595	0.593	0.587	0.576	0.574	0.531	0.538
700	0.557	0.557	0.548	0.550	0.534	0.540	0.495	0.505
1000	0.507	0.511	0.501	0.505	0.492	0.499	0.464	0.463
2000	0.419	0.419	0.418	0.418	0.417	0.417	0.409	0.409
3000	0.364	0.363	0.364	0.362	0.364	0.363	0.362	0.359

Table 5.35: Mobility values in $cm^2V^{-1}s^{-1}$ from hybrid calculations using Model B1 and $\sigma_{\mathrm{NRS}}^{(\mathrm{MT1})}$ and $\sigma_{\mathrm{NRS}}^{(\mathrm{MT2})}$ for different initial rotational-vibrational dimer values. (a) $\sigma_{\mathrm{NRS}}^{(\mathrm{MT1})}$ [J=0, ν=1], (b) $\sigma_{\mathrm{NRS}}^{(\mathrm{MT2})}$ [J=0, ν=1], (c) $\sigma_{\mathrm{NRS}}^{(\mathrm{MT1})}$ [J=0, ν=2], (d) $\sigma_{\mathrm{NRS}}^{(\mathrm{MT2})}$ [J=0, ν=2], (e) $\sigma_{\mathrm{NRS}}^{(\mathrm{MT1})}$ [J=0, ν=4], (f) $\sigma_{\mathrm{NRS}}^{(\mathrm{MT2})}$ [J=0, ν=4], (g) $\sigma_{\mathrm{NRS}}^{(\mathrm{MT1})}$ [J=0, ν=8], (h) $\sigma_{\mathrm{NRS}}^{(\mathrm{MT2})}$ [J=0, ν=8].

Reduced electric field (Td)	(a)	(b)	(c)	(d)	(e)	(f)	(g)	(h)
5	0.582	0.569	0.595	0.612	0.614	0.615	0.611	0.627
10	0.575	0.573	0.588	0.613	0.610	0.615	0.612	0.628
20	0.568	0.572	0.586	0.615	0.608	0.616	0.608	0.626
30	0.565	0.569	0.580	0.608	0.600	0.610	0.603	0.617
50	0.564	0.566	0.577	0.604	0.595	0.608	0.600	0.614
80	0.556	0.558	0.573	0.603	0.592	0.605	0.594	0.612
100	0.549	0.549	0.568	0.593	0.583	0.596	0.587	0.604
200	0.531	0.532	0.584	0.583	0.568	0.588	0.573	0.610
300	0.519	0.528	0.601	0.567	0.551	0.579	0.562	0.606
400	0.512	0.521	0.603	0.559	0.542	0.568	0.552	0.592
500	0.500	0.512	0.593	0.547	0.535	0.558	0.545	0.573
700	0.473	0.488	0.548	0.515	0.510	0.527	0.519	0.527
1000	0.452	0.464	0.501	0.481	0.482	0.489	0.490	0.484
2000	0.408	0.409	0.418	0.416	0.414	0.418	0.417	0.412
3000	0.363	0.36	0.364	0.366	0.364	0.367	0.363	0.363

Table 5.36: Mobility values in $cm^2V^{-1}s^{-1}$ from hybrid calculations using Model B1 and $\sigma_{\mathrm{NRS}}^{(\mathrm{MT1})}$ and $\sigma_{\mathrm{NRS}}^{(\mathrm{MT2})}$ for different initial rotational-vibrational dimer values. (a) $\sigma_{\mathrm{NRS}}^{(\mathrm{MT1})}$ [J=0, ν=12], (b) $\sigma_{\mathrm{NRS}}^{(\mathrm{MT2})}$ [J=0, ν=12], (c) $\sigma_{\mathrm{NRS}}^{(\mathrm{MT1})}$ [J=60, ν=0], (d) $\sigma_{\mathrm{NRS}}^{(\mathrm{MT2})}$ [J=60, ν=0], (e) $\sigma_{\mathrm{NRS}}^{(\mathrm{MT1})}$ [J=70, ν=0], (f) $\sigma_{\mathrm{NRS}}^{(\mathrm{MT2})}$ [J=70, ν=0], (g) $\sigma_{\mathrm{NRS}}^{(\mathrm{MT1})}$ [J=90, ν=0], (h) $\sigma_{\mathrm{NRS}}^{(\mathrm{MT2})}$ [J=90, ν=0].

Reduced electric field (Td)	(a)	(b)	(c)	(d)	(e)	(f)
5	0.632	0.636	0.636	0.670	0.631	0.636
10	0.637	0.627	0.636	0.672	0.635	0.636
20	0.634	0.633	0.628	0.664	0.632	0.632
30	0.631	0.628	0.628	0.661	0.630	0.628
50	0.626	0.623	0.628	0.655	0.627	0.624
80	0.623	0.621	0.626	0.650	0.625	0.622
100	0.614	0.609	0.623	0.637	0.616	0.612
200	0.627	0.610	0.605	0.618	0.617	0.603
300	0.617	0.599	0.585	0.585	0.603	0.592
400	0.600	0.586	0.563	0.562	0.583	0.573
500	0.576	0.567	0.538	0.535	0.559	0.553
700	0.530	0.525	0.484	0.485	0.515	0.513
1000	0.487	0.485	0.435	0.440	0.475	0.477
2000	0.417	0.414	0.382	0.383	0.413	0.411
3000	0.366	0.363	0.347	0.345	0.365	0.362

Table 5.37: Mobility values in $cm^2V^{-1}s^{-1}$ from hybrid calculations using Model B1 and $\sigma_{\mathrm{NRS}}^{(\mathrm{MT1})}$ and $\sigma_{\mathrm{NRS}}^{(\mathrm{MT2})}$ for different initial rotational-vibrational dimer values. (a) $\sigma_{\mathrm{NRS}}^{(\mathrm{MT1})}$ [J=100, ν=0], (b) $\sigma_{\mathrm{NRS}}^{(\mathrm{MT2})}$ [J=100, ν=0], (c) $\sigma_{\mathrm{NRS}}^{(\mathrm{MT1})}$ [J=200, ν=0], (d) $\sigma_{\mathrm{NRS}}^{(\mathrm{MT2})}$ [J=200, ν=0], (e) $\sigma_{\mathrm{NRS}}^{(\mathrm{MT1})}$ [J=100, ν=1], (f) $\sigma_{\mathrm{NRS}}^{(\mathrm{MT2})}$ [J=100, ν=1].

Reduced electric field (Td)	(a)	(b)	(c)	(d)	(e)	(f)	(g)	(h)	(i)	(j)
5	0.589	0.576	0.586	0.578	0.570	0.574	0.622	0.606	0.581	0.584
10	0.578	0.575	0.583	0.573	0.571	0.577	0.620	0.603	0.585	0.575
20	0.584	0.576	0.579	0.574	0.570	0.571	0.611	0.606	0.585	0.577
30	0.580	0.572	0.576	0.571	0.565	0.567	0.608	0.598	0.580	0.573
50	0.575	0.568	0.573	0.566	0.561	0.563	0.605	0.595	0.583	0.573
80	0.574	0.566	0.573	0.562	0.556	0.554	0.601	0.590	0.578	0.568
100	0.568	0.557	0.566	0.555	0.547	0.548	0.592	0.584	0.572	0.561
200	0.597	0.577	0.588	0.572	0.531	0.535	0.581	0.566	0.585	0.571
300	0.621	0.602	0.610	0.592	0.525	0.530	0.567	0.550	0.593	0.583
400	0.628	0.611	0.613	0.602	0.515	0.524	0.556	0.542	0.591	0.586
500	0.613	0.603	0.597	0.593	0.502	0.515	0.543	0.532	0.578	0.578
700	0.564	0.561	0.551	0.554	0.473	0.489	0.512	0.508	0.535	0.540
1000	0.507	0.509	0.500	0.506	0.451	0.462	0.478	0.478	0.491	0.497
2000	0.416	0.415	0.415	0.415	0.406	0.405	0.411	0.410	0.414	0.414
3000	0.361	0.361	0.362	0.360	0.360	0.358	0.362	0.361	0.362	0.360

Table 5.38: Mobility values in $cm^2V^{-1}s^{-1}$ from hybrid calculations using Model B2 and $\sigma_{\mathrm{NRS}}^{(\mathrm{MT1})}$ and $\sigma_{\mathrm{NRS}}^{(\mathrm{MT2})}$ for different initial vibrational dimer values. (a) $\sigma_{\mathrm{NRS}}^{(\mathrm{MT1})}$ [J=0, ν=1], (b) $\sigma_{\mathrm{NRS}}^{(\mathrm{MT2})}$ [J=0, ν=1], (c) $\sigma_{\mathrm{NRS}}^{(\mathrm{MT1})}$ [J=0, ν=2], (d) $\sigma_{\mathrm{NRS}}^{(\mathrm{MT2})}$ [J=0, ν=2], (e) $\sigma_{\mathrm{NRS}}^{(\mathrm{MT1})}$ [J=0, ν=4], (f) $\sigma_{\mathrm{NRS}}^{(\mathrm{MT2})}$ [J=0, ν=4], (g) $\sigma_{\mathrm{NRS}}^{(\mathrm{MT1})}$ [J=0, ν=8], (h) $\sigma_{\mathrm{NRS}}^{(\mathrm{MT1})}$ [J=0, ν=8], (i) $\sigma_{\mathrm{NRS}}^{(\mathrm{MT1})}$ [J=0, ν=12], (j) $\sigma_{\mathrm{NRS}}^{(\mathrm{MT2})}$ [J=0, ν=12].

Reduced electric field (Td)	(a)	(b)	(c)	(d)	(e)	(f)	(g)	(h)	(i)	(j)
5	0.577	0.578	0.613	0.612	0.612	0.623	0.632	0.630	0.628	0.657
10	0.581	0.584	0.613	0.609	0.615	0.624	0.627	0.624	0.630	0.653
20	0.578	0.580	0.612	0.611	0.619	0.614	0.626	0.627	0.629	0.657
30	0.576	0.575	0.608	0.606	0.615	0.612	0.621	0.623	0.624	0.643
50	0.574	0.570	0.606	0.599	0.610	0.609	0.618	0.617	0.624	0.648
80	0.567	0.563	0.603	0.593	0.608	0.601	0.617	0.613	0.619	0.645
100	0.560	0.557	0.597	0.588	0.600	0.592	0.609	0.606	0.611	0.633
200	0.559	0.554	0.588	0.572	0.608	0.592	0.623	0.609	0.602	0.613
300	0.556	0.554	0.577	0.562	0.604	0.588	0.621	0.603	0.587	0.588
400	0.548	0.551	0.569	0.554	0.594	0.577	0.605	0.590	0.573	0.569
500	0.533	0.542	0.558	0.545	0.572	0.560	0.581	0.571	0.559	0.552
700	0.497	0.508	0.525	0.517	0.527	0.522	0.531	0.526	0.516	0.515
1000	0.464	0.474	0.487	0.486	0.483	0.483	0.486	0.484	0.468	0.468
2000	0.406	0.406	0.415	0.414	0.410	0.407	0.413	0.410	393	0.391
3000	0.359	0.358	0.363	0.361	0.360	0.358	0.364	0.360	0.348	0.346

Table 5.39: Mobility values in $cm^2V^{-1}s^{-1}$ from hybrid calculations using Model B2 and $\sigma_{\mathrm{NRS}}^{(\mathrm{MT1})}$ and $\sigma_{\mathrm{NRS}}^{(\mathrm{MT2})}$ for different initial rotational dimer values. (a) $\sigma_{\mathrm{NRS}}^{(\mathrm{MT1})}$ [J=60, ν=0], (b) $\sigma_{\mathrm{NRS}}^{(\mathrm{MT2})}$ [J=60, ν=0], (c) $\sigma_{\mathrm{NRS}}^{(\mathrm{MT1})}$ [J=70, ν=0], (d) $\sigma_{\mathrm{NRS}}^{(\mathrm{MT2})}$ [J=70, ν=0], (e) $\sigma_{\mathrm{NRS}}^{(\mathrm{MT1})}$ [J=90, ν=0], (f) $\sigma_{\mathrm{NRS}}^{(\mathrm{MT2})}$ [J=90, ν=0], (g) $\sigma_{\mathrm{NRS}}^{(\mathrm{MT1})}$ [J=100, ν=0], (h) $\sigma_{\mathrm{NRS}}^{(\mathrm{MT1})}$ [J=100, ν=0], (i) $\sigma_{\mathrm{NRS}}^{(\mathrm{MT1})}$ [J=200, ν=0], (j) $\sigma_{\mathrm{NRS}}^{(\mathrm{MT2})}$ [J=200, ν=0].

Reduced electric field (Td)	(a)	(b)	(c)	(d)	(e)	(f)
5	26.8	27.0	26.9	26.1	26.5	25.8
10	27.0	27.0	27.2	26.9	26.4	26.6
20	26.6	26.8	27.6	27.1	26.7	26.4
30	28.1	28.3	28.1	27.6	27.3	27.0
50	30.6	29.5	28.0	27.7	28.3	27.2
80	36.2	35.7	29.2	29.9	30.2	30.0
100	42.4	41.5	31.0	32.3	31.4	31.1
200	106	96.4	51.0	50.7	51.8	49.0
300	184	177	79.4	75.2	77.3	77.8
400	249	244	120	113	119	114
500	315	324	189	190	195	185
700	448	478	280	272	283	277
1000	896	846	472	485	467	472
2000	2110	190	1240	1180	1170	1180
3000	2550	2460	1990	2050	1980	1930

Table 5.40: Transverse coefficient (eD_T/K_0) in meV from hybrid calculations using different interactions models and $\sigma_{\mathrm{NRS}}^{(\mathrm{MT1})}$ and $\sigma_{\mathrm{NRS}}^{(\mathrm{MT2})}$ for a initial dimer [J=0, ν=0]. (a) Model A1 $\sigma_{\mathrm{NRS}}^{(\mathrm{MT1})}$, (b) Model A1 $\sigma_{\mathrm{NRS}}^{(\mathrm{MT2})}$, (c) Model B1 $\sigma_{\mathrm{NRS}}^{(\mathrm{MT1})}$, (d) Model B1 $\sigma_{\mathrm{NRS}}^{(\mathrm{MT2})}$, (e) Model B2 $\sigma_{\mathrm{NRS}}^{(\mathrm{MT1})}$, (f) Model B2 $\sigma_{\mathrm{NRS}}^{(\mathrm{MT2})}$.

Reduced electric field (Td)	(a)	(b)	(c)	(d)	(e)	(f)	(g)	(h)
5	26.5	26.6	26.4	27.0	26.5	25.7	26.3	25.7
10	26.5	26.2	26.4	27.2	26.9	26.4	26.4	25.8
20	27.0	27.0	27.1	27.0	26.9	27.2	26.5	26.0
30	27.6	27.6	27.4	27.1	27.5	28.0	27.4	27.1
50	27.4	27.6	26.9	28.0	27.8	28.1	27.9	27.9
80	29.9	29.7	30.8	29.4	30.2	29.8	29.1	30.2
100	32.4	30.8	32.1	31.7	32.0	31.1	31.6	31.1
200	52.0	50.9	50.4	49.2	50.1	48.4	48.7	46.1
300	74.8	75.6	76.6	70.3	76.7	75.1	72.4	69.6
400	119	113	117	112	119	112	103	105
500	178	180	178	175	169	171	151	155
700	267	269	261	266	255	251	225	232
1000	463	469	459	460	449	468	408	426
2000	1200	1230	1210	1190	1190	1190	1150	1130
3000	2030	2010	2040	2020	1990	1980	1930	2000

Table 5.41: Transverse coefficient (eD_T/K_0) in meV from hybrid calculations using Model B1 and $\sigma_{\mathrm{NRS}}^{(\mathrm{MT1})}$ and $\sigma_{\mathrm{NRS}}^{(\mathrm{MT2})}$ for different initial rotational-vibrational dimer values. (a) $\sigma_{\mathrm{NRS}}^{(\mathrm{MT1})}$ [J=0, ν=1], (b) $\sigma_{\mathrm{NRS}}^{(\mathrm{MT2})}$ [J=0, ν=1], (c) $\sigma_{\mathrm{NRS}}^{(\mathrm{MT1})}$ [J=0, ν=2], (d) $\sigma_{\mathrm{NRS}}^{(\mathrm{MT2})}$ [J=0, ν=2], (e) $\sigma_{\mathrm{NRS}}^{(\mathrm{MT1})}$ [J=0, ν=4], (f) $\sigma_{\mathrm{NRS}}^{(\mathrm{MT2})}$ [J=0, ν=4], (g) $\sigma_{\mathrm{NRS}}^{(\mathrm{MT1})}$ [J=0, ν=8], (h) $\sigma_{\mathrm{NRS}}^{(\mathrm{MT2})}$ [J=0, ν=8].

Reduced electric field (Td)	(a)	(b)	(c)	(d)	(e)	(f)	(g)	(h)
5	26.3	26.7	26.7	26.2	26.5	26.5	26.6	26.7
10	26.8	26.3	26.5	26.3	26.8	26.4	26.5	26.9
20	27.5	26.5	26.5	25.9	26.5	27.1	27.0	26.9
30	27.3	26.9	27.8	28.0	27.6	28.3	27.8	27.7
50	27.6	27.7	28.7	28.2	28.2	28.3	28.2	28.1
80	30.5	29.0	28.9	30.4	29.9	30.3	30.4	30.4
100	31.4	30.8	32.7	32.1	32.2	32.3	32.4	33.0
200	46.7	46.8	51.1	50.0	50.9	48.9	52.6	50.3
300	66.4	70.2	76.3	71.3	73.2	72.6	78.7	75.9
400	96.2	102	107	104	108	107	115	111
500	139	142	159	155	171	157	165	169
700	218	225	246	253	244	251	248	244
1000	375	384	446	435	435	428	448	419
2000	1140	1160	1190	1220	1220	1180	1170	1150
3000	2020	1910	2070	2010	2100	2030	2040	1980

Table 5.42: Transverse coefficient (eD_T/K_0) in meV from hybrid calculations using Model B1 and $\sigma_{\mathrm{NRS}}^{(\mathrm{MT1})}$ and $\sigma_{\mathrm{NRS}}^{(\mathrm{MT2})}$ for different initial rotational-vibrational dimer values. (a) $\sigma_{\mathrm{NRS}}^{(\mathrm{MT1})}$ [J=0, ν=12], (b) $\sigma_{\mathrm{NRS}}^{(\mathrm{MT2})}$ [J=0, ν=12], (c) $\sigma_{\mathrm{NRS}}^{(\mathrm{MT1})}$ [J=60, ν=0], (d) $\sigma_{\mathrm{NRS}}^{(\mathrm{MT2})}$ [J=60, ν=0], (e) $\sigma_{\mathrm{NRS}}^{(\mathrm{MT1})}$ [J=70, ν=0], (f) $\sigma_{\mathrm{NRS}}^{(\mathrm{MT2})}$ [J=70, ν=0], (g) $\sigma_{\mathrm{NRS}}^{(\mathrm{MT1})}$ [J=90, ν=0], (h) $\sigma_{\mathrm{NRS}}^{(\mathrm{MT2})}$ [J=90, ν=0].

Reduced electric field (Td)	(a)	(b)	(c)	(d)	(e)	(f)
5	26.6	26.8	26.8	26.8	26.7	26.7
10	26.7	27.1	26.9	26.5	26.5	26.4
20	26.7	27.0	27.5	26.8	26.7	27.3
30	27.9	27.8	28.0	27.5	27.5	28.4
50	27.6	27.9	28.5	28.9	27.9	28.2
80	30.5	30.3	29.5	31.0	31.3	30.9
100	33.3	32.7	31.4	33.1	34.7	32.4
200	52.0	53.4	51.0	52.4	54.3	49.8
300	78.7	77.8	75.9	76.5	79.9	73.9
400	118	113	109	111	114	111
500	173	169	155	154	173	162
700	243	248	218	231	238	245
1000	444	433	357	358	439	415
2000	1200	1160	1020	1010	1150	1150
3000	2060	2050	1840	1780	2050	2030

Table 5.43: Transverse coefficient (eD_T/K_0) in meV from hybrid calculations using Model B1 and $\sigma_{\mathrm{NRS}}^{(\mathrm{MT1})}$ and $\sigma_{\mathrm{NRS}}^{(\mathrm{MT2})}$ for different initial rotational-vibrational dimer values. (a) $\sigma_{\mathrm{NRS}}^{(\mathrm{MT1})}$ [J=100, ν=0], (b) $\sigma_{\mathrm{NRS}}^{(\mathrm{MT2})}$ [J=100, ν=0], (c) $\sigma_{\mathrm{NRS}}^{(\mathrm{MT1})}$ [J=200, ν=0], (d) $\sigma_{\mathrm{NRS}}^{(\mathrm{MT2})}$ [J=200, ν=0], (e) $\sigma_{\mathrm{NRS}}^{(\mathrm{MT1})}$ [J=100, ν=1], (f) $\sigma_{\mathrm{NRS}}^{(\mathrm{MT2})}$ [J=100, ν=1].

Reduced electric field (Td)	(a)	(b)	(c)	(d)	(e)	(f)	(g)	(h)	(i)	(j)
5	26.3	25.9	26.1	26.5	26.6	26.4	26.3	26.7	26.7	26.7
10	26.8	26.2	26.6	26.5	26.5	26.2	26.3	26.9	26.9	26.5
20	26.2	26.4	27.1	26.2	26.6	26.2	27.2	26.6	26.6	27.1
30	27.7	27.8	28.6	27.2	27.0	27.1	27.5	27.8	27.8	27.3
50	28.0	28.0	27.7	27.4	27.2	27.7	27.8	27.5	27.5	27.5
80	30.5	29.4	29.3	30.0	29.3	28.6	30.1	30.2	30.2	30.0
100	31.6	32.8	32.2	33.5	30.2	31.7	32.4	32.0	32.0	30.4
200	51.5	50.6	48.8	48.6	46.3	46.5	50.8	48.0	48.0	51.8
300	77.9	73.1	75.4	74.9	67.8	68.2	75.0	71.5	71.5	74.5
400	123	121	117	114	99.0	97.2	108	104	104	113
500	186	187	181	179	139	144	154	154	154	171
700	273	273	266	268	208	220	249	237	237	264
1000	465	473	469	466	372	416	423	421	421	442
2000	1200	1180	1170	1190	1110	1170	1190	1170	1170	1170
3000	1950	1960	1960	2000	1950	1980	2010	2010	2010	2000

Table 5.44: Transverse coefficient (eD_T/K_0) in meV from hybrid calculations using Model B2 and $\sigma_{\mathrm{NRS}}^{(\mathrm{MT1})}$ and $\sigma_{\mathrm{NRS}}^{(\mathrm{MT2})}$ for different initial rotational-vibrational dimer values. (a) $\sigma_{\mathrm{NRS}}^{(\mathrm{MT1})}$ [J=0, ν=1], (b) $\sigma_{\mathrm{NRS}}^{(\mathrm{MT2})}$ [J=0, ν=1], (c) $\sigma_{\mathrm{NRS}}^{(\mathrm{MT1})}$ [J=0, ν=2], (d) $\sigma_{\mathrm{NRS}}^{(\mathrm{MT2})}$ [J=0, ν=2], (e) $\sigma_{\mathrm{NRS}}^{(\mathrm{MT1})}$ [J=0, ν=4], (f) $\sigma_{\mathrm{NRS}}^{(\mathrm{MT2})}$ [J=0, ν=4], (g) $\sigma_{\mathrm{NRS}}^{(\mathrm{MT1})}$ [J=0, ν=8], (h) $\sigma_{\mathrm{NRS}}^{(\mathrm{MT1})}$ [J=0, ν=8], (i) $\sigma_{\mathrm{NRS}}^{(\mathrm{MT1})}$ [J=0, ν=12], (j) $\sigma_{\mathrm{NRS}}^{(\mathrm{MT2})}$ [J=0, ν=12].

Reduced electric field (Td)	(a)	(b)	(c)	(d)	(e)	(f)	(g)	(h)	(i)	(j)
5	26.6	26.2	27.0	26.6	27.2	26.6	26.7	26.5	27.1	27
10	26.3	26.2	26.8	26.6	26.1	26.4	26.6	26.7	26.8	26.7
20	26.9	26.5	27.0	26.4	26.4	26.9	27.1	26.7	27.1	26.4
30	27.2	27.3	28.4	27.6	28.1	27.8	27.9	27.8	28.0	28.1
50	28.0	28.1	28.0	28.3	28.3	28.0	27.9	27.7	28.2	28.5
80	29.9	29.7	30.7	30.0	31.0	30.4	30.8	31.3	30.6	30.5
100	32.9	32.5	32.8	33.9	32.2	33.6	31.8	32.3	33.4	33.4
200	48.6	48.0	49.6	47.9	50.1	51.1	55.2	51.1	51.3	52.7
300	71.6	70.5	74.0	73.4	78.9	71.5	78.3	77.7	76.2	74.1
400	108	103	109	103	116	112	116	111	107	113
500	156	156	164	159	166	169	176	169	165	161
700	234	238	249	248	248	261	250	246	242	247
1000	403	409	437	436	440	430	450	435	398	420
2000	1100	1120	1200	1200	1170	1150	1200	1160	1070	1070
3000	1940	1880	2000	2060	2040	1950	2030	2020	1860	1780

Table 5.45: Transverse coefficient (eD_T/K_0) in meV from hybrid calculations using Model B2 and $\sigma_{\mathrm{NRS}}^{(\mathrm{MT1})}$ and $\sigma_{\mathrm{NRS}}^{(\mathrm{MT2})}$ for different initial rotational-vibrational dimer values. (a) $\sigma_{\mathrm{NRS}}^{(\mathrm{MT1})}$ [J=60, ν=0], (b) $\sigma_{\mathrm{NRS}}^{(\mathrm{MT2})}$ [J=60, ν=0], (c) $\sigma_{\mathrm{NRS}}^{(\mathrm{MT1})}$ [J=70, ν=0], (d) $\sigma_{\mathrm{NRS}}^{(\mathrm{MT2})}$ [J=70, ν=0], (e) $\sigma_{\mathrm{NRS}}^{(\mathrm{MT1})}$ [J=90, ν=0], (f) $\sigma_{\mathrm{NRS}}^{(\mathrm{MT2})}$ [J=90, ν=0], (g) $\sigma_{\mathrm{NRS}}^{(\mathrm{MT1})}$ [J=100, ν=0], (h) $\sigma_{\mathrm{NRS}}^{(\mathrm{MT1})}$ [J=100, ν=0], (i) $\sigma_{\mathrm{NRS}}^{(\mathrm{MT1})}$ [J=200, ν=0], (j) $\sigma_{\mathrm{NRS}}^{(\mathrm{MT2})}$ [J=200, ν=0].

Reduced electric field (Td)	(a)	(b)	(c)	(d)	(e)	(f)
5	26.3	26.3	27.0	26.7	26.8	26.1
10	26.0	26.2	27.3	26.6	26.5	26.9
20	26.4	26.1	29.2	27.5	28.1	27.3
30	27.1	26.6	28.5	28.9	29.7	29.5
50	28.3	28.1	30.7	29.6	30.1	30.6
80	29.7	29.4	37.0	37.1	37.8	37.1
100	33.1	32.5	42.8	42.6	43.6	43.2
200	49.1	47.7	127	115	135	123
300	75.2	69.2	226	214	233	215
400	110	104	285	303	294	307
500	166	159	337	373	347	375
700	247	245	439	473	435	472
1000	419	429	718	765	706	771
2000	1220	1170	1800	1740	1740	1730
3000	2090	1970	2430	2410	2440	2270

Table 5.46: Longitudinal coefficient (eD_L/K_0) in meV from hybrid calculations using different interactions models and $\sigma_{\mathrm{NRS}}^{(\mathrm{MT1})}$ and $\sigma_{\mathrm{NRS}}^{(\mathrm{MT2})}$ for a initial dimer [J=0, ν=0]. (a) Model A1 $\sigma_{\mathrm{NRS}}^{(\mathrm{MT1})}$, (b) Model A1 $\sigma_{\mathrm{NRS}}^{(\mathrm{MT2})}$, (c) Model B1 $\sigma_{\mathrm{NRS}}^{(\mathrm{MT1})}$, (d) Model B1 $\sigma_{\mathrm{NRS}}^{(\mathrm{MT2})}$, (e) Model B2 $\sigma_{\mathrm{NRS}}^{(\mathrm{MT1})}$, (f) Model B2 $\sigma_{\mathrm{NRS}}^{(\mathrm{MT2})}$.

Reduced electric field (Td)	(a)	(b)	(c)	(d)	(e)	(f)	(g)	(h)
5	27.3	27.1	26.1	27.0	27.5	26.9	26.8	26.1
10	27.0	26.8	26.6	27.2	27.4	27.5	27.0	26.4
20	27.0	27.6	27.4	26.6	26.7	26.7	27.1	26.7
30	29.1	29.3	28.8	29.9	29.8	28.8	28.5	28.8
50	30.6	30.6	30.5	29.8	29.8	30.8	30.3	30.0
80	36.5	35.1	37.4	37.4	37.0	35.7	35.4	35.6
100	44.7	41.8	44.5	40.2	44.3	41.8	41.9	41.0
200	116	119	116	115	115	104	95.8	99.4
300	203	209	200	196	188	184	157	164
400	277	289	275	280	257	258	213	228
500	337	364	332	358	315	340	297	314
700	437	486	456	487	447	489	424	454
1000	746	801	797	809	812	852	856	833
2000	1880	1790	1930	1850	1970	1870	2070	1950
3000	2510	2470	2420	2480	2490	2450	2500	2500

Table 5.47: Longitudinal coefficient (eD_L/K_0) in meV from hybrid calculations using Model B1 and $\sigma_{\mathrm{NRS}}^{(\mathrm{MT1})}$ and $\sigma_{\mathrm{NRS}}^{(\mathrm{MT2})}$ for different initial rotational-vibrational dimer values. (a) $\sigma_{\mathrm{NRS}}^{(\mathrm{MT1})}$ [J=0, ν=1], (b) $\sigma_{\mathrm{NRS}}^{(\mathrm{MT2})}$ [J=0, ν=1], (c) $\sigma_{\mathrm{NRS}}^{(\mathrm{MT1})}$ [J=0, ν=2], (d) $\sigma_{\mathrm{NRS}}^{(\mathrm{MT2})}$ [J=0, ν=2], (e) $\sigma_{\mathrm{NRS}}^{(\mathrm{MT1})}$ [J=0, ν=4], (f) $\sigma_{\mathrm{NRS}}^{(\mathrm{MT2})}$ [J=0, ν=4], (g) $\sigma_{\mathrm{NRS}}^{(\mathrm{MT1})}$ [J=0, ν=8], (h) $\sigma_{\mathrm{NRS}}^{(\mathrm{MT2})}$ [J=0, ν=8].

Reduced electric field (Td)	(a)	(b)	(c)	(d)	(e)	(f)	(g)	(h)
5	26.5	27.2	27.5	26.3	27.4	26.9	27.2	27.4
10	26.9	27.0	27.0	26.6	27.2	27.2	27.2	27.5
20	27.2	27.2	27.5	27.7	27.8	27.3	28.6	27.1
30	28.9	29.2	29.5	30.2	29.9	29.4	28.9	29.8
50	30.4	29.5	30.5	30.6	31.6	31.2	30.9	30.5
80	36.0	35.4	39.3	36.7	38.7	36.5	38.7	37.3
100	40.5	41.2	43.8	42.3	45.1	42.2	43.7	46.0
200	84.5	85.8	93.4	86.8	95.3	92.5	110	98.7
300	141	153	148	147	157	163	175	173
400	197	222	238	233	240	240	227	221
500	288	300	313	319	327	348	300	316
700	445	469	479	485	467	507	425	468
1000	938	904	865	885	857	879	810	812
2000	2160	2030	2040	1950	1970	1900	2000	1890
3000	2570	2550	1650	2530	2510	2510	2570	2540

Table 5.48: Longitudinal coefficient (eD_L/K_0) in meV from hybrid calculations using Model B1 and $\sigma_{\mathrm{NRS}}^{(\mathrm{MT1})}$ and $\sigma_{\mathrm{NRS}}^{(\mathrm{MT2})}$ for different initial rotational-vibrational dimer values. (a) $\sigma_{\mathrm{NRS}}^{(\mathrm{MT1})}$ [J=0, ν=12], (b) $\sigma_{\mathrm{NRS}}^{(\mathrm{MT2})}$ [J=0, ν=12], (c) $\sigma_{\mathrm{NRS}}^{(\mathrm{MT1})}$ [J=60, ν=0], (d) $\sigma_{\mathrm{NRS}}^{(\mathrm{MT2})}$ [J=60, ν=0], (e) $\sigma_{\mathrm{NRS}}^{(\mathrm{MT1})}$ [J=70, ν=0], (f) $\sigma_{\mathrm{NRS}}^{(\mathrm{MT2})}$ [J=70, ν=0], (g) $\sigma_{\mathrm{NRS}}^{(\mathrm{MT1})}$ [J=90, ν=0], (h) $\sigma_{\mathrm{NRS}}^{(\mathrm{MT2})}$ [J=90, ν=0].

Reduced electric field (Td)	(a)	(b)	(c)	(d)	(e)	(f)
5	27.7	27.2	27.9	27.1	27.6	27.6
10	27.5	27.6	27.4	27.6	27.9	27.2
20	28.3	28.4	29.0	28.3	28.1	28.4
30	29.5	30.1	30.6	31.0	30.1	30.0
50	31.2	31.8	30.9	32.9	31.1	31.1
80	39.8	39.5	39.3	40.3	38.7	38.7
100	44.9	46.3	46.4	48.3	45.9	45.8
200	112	105	92.5	91.7	106	105
300	174	174	153	141	157	154
400	224	218	209	192	204	214
500	297	312	228	246	277	283
700	427	457	303	341	427	455
1000	843	822	665	643	858	833
2000	2030	1970	2160	2000	2030	1980
3000	2550	2610	2830	2740	2700	2580

Table 5.49: Longitudinal coefficient (eD_L/K_0) in meV from hybrid calculations using Model B2 and $\sigma_{\mathrm{NRS}}^{(\mathrm{MT1})}$ and $\sigma_{\mathrm{NRS}}^{(\mathrm{MT2})}$ for different initial rotational-vibrational dimer values. (a) $\sigma_{\mathrm{NRS}}^{(\mathrm{MT1})}$ [J=100, ν=0], (b) $\sigma_{\mathrm{NRS}}^{(\mathrm{MT2})}$ [J=100, ν=0], (c) $\sigma_{\mathrm{NRS}}^{(\mathrm{MT1})}$ [J=200, ν=0], (d) $\sigma_{\mathrm{NRS}}^{(\mathrm{MT2})}$ [J=200, ν=0], (e) $\sigma_{\mathrm{NRS}}^{(\mathrm{MT1})}$ [J=100, ν=1], (f) $\sigma_{\mathrm{NRS}}^{(\mathrm{MT2})}$ [J=100, ν=1].

Reduced electric field (Td)	(a)	(b)	(c)	(d)	(e)	(f)	(g)	(h)	(i)	(j)
5	27.0	26.5	26.9	26.3	27.3	26.5	27.1	27.4	27.3	26.8
10	26.9	27.4	27.6	26.9	26.7	26.8	27.1	26.8	27.2	27.2
20	27.0	27.4	26.5	27.0	27.4	27.2	27.4	28.2	27.7	27.3
30	29.0	30.0	28.9	29.6	28.9	28.7	29.5	29.7	28.6	29.0
50	30.5	30.3	31.0	30.1	30.1	29.4	31.5	31.6	30.0	30.0
80	35.8	37.0	38.4	36.5	36.0	34.6	36.4	38.1	37.0	37.4
100	42.4	43.7	43.3	44.3	40.1	37.0	45.1	46.6	43.0	41.4
200	128	120	126	118	84.5	85.4	89.7	85.4	109	112
300	228	206	199	209	139	155	157	152	183	192
400	276	292	267	285	206	218	240	231	248	274
500	335	368	326	347	272	280	317	333	316	353
700	430	462	446	485	436	465	466	481	447	468
1000	754	763	763	791	918	885	859	872	803	786
2000	1830	1710	1840	1730	2130	1990	2030	1910	1920	1850
3000	2470	2450	2500	2460	2620	2540	2610	2660	2590	2450

Table 5.50: Longitudinal coefficient (eD_L/K_0) in meV from hybrid calculations using Model B2 and $\sigma_{\mathrm{NRS}}^{(\mathrm{MT1})}$ and $\sigma_{\mathrm{NRS}}^{(\mathrm{MT2})}$ for different initial rotational-vibrational dimer values. (a) $\sigma_{\mathrm{NRS}}^{(\mathrm{MT1})}$ [J=0, ν=1], (b) $\sigma_{\mathrm{NRS}}^{(\mathrm{MT2})}$ [J=0, ν=1], (c) $\sigma_{\mathrm{NRS}}^{(\mathrm{MT1})}$ [J=0, ν=2], (d) $\sigma_{\mathrm{NRS}}^{(\mathrm{MT2})}$ [J=0, ν=2], (e) $\sigma_{\mathrm{NRS}}^{(\mathrm{MT1})}$ [J=0, ν=4], (f) $\sigma_{\mathrm{NRS}}^{(\mathrm{MT2})}$ [J=0, ν=4], (g) $\sigma_{\mathrm{NRS}}^{(\mathrm{MT1})}$ [J=0, ν=8], (h) $\sigma_{\mathrm{NRS}}^{(\mathrm{MT1})}$ [J=0, ν=8], (i) $\sigma_{\mathrm{NRS}}^{(\mathrm{MT1})}$ [J=0, ν=12], (j) $\sigma_{\mathrm{NRS}}^{(\mathrm{MT2})}$ [J=0, ν=12].

Reduced electric field (Td)	(a)	(b)	(c)	(d)	(e)	(f)	(g)	(h)	(i)	(j)
5	27.3	26.7	27.1	27.1	27.7	27.3	27.1	26.6	27.6	27.7
10	27.4	26.9	27.4	27.8	27.5	27.3	27.4	27.7	27.6	28.2
20	28.2	26.7	28.4	28.0	27.4	27.3	28.0	28.1	28.1	27.4
30	29.1	29.2	30.0	30.8	30.0	29.7	29.3	30.4	29.7	30.5
50	29.9	30.0	31.0	30.9	31.3	30.7	31.0	30.7	31.3	31.3
80	37.1	36.7	38.1	36.5	39.5	37.0	39.5	38.3	37.3	39.8
100	42.5	41.0	45.5	44.5	48.0	43.2	44.8	44.6	45.3	43.1
200	94.8	101	104	91.6	110	105	119	113	98.4	93.6
300	160	163	172	160	175	160	178	168	157	145
400	222	239	247	227	233	235	234	231	235	231
500	296	309	324	340	303	310	295	295	310	300
700	418	454	465	494	432	460	419	422	399	412
1000	852	823	837	842	787	788	805	820	651	662
2000	2040	1850	1920	1870	1920	1870	1990	1940	1830	1830
3000	2550	2540	2550	2530	2550	2480	2590	2600	2530	2530

Table 5.51: Longitudinal coefficient (eD_L/K_0) in meV from hybrid calculations using Model B2 and $\sigma_{\mathrm{NRS}}^{(\mathrm{MT1})}$ and $\sigma_{\mathrm{NRS}}^{(\mathrm{MT2})}$ for different initial rotational-vibrational dimer values. (a) $\sigma_{\mathrm{NRS}}^{(\mathrm{MT1})}$ [J=60, ν=0], (b) $\sigma_{\mathrm{NRS}}^{(\mathrm{MT2})}$ [J=60, ν=0], (c) $\sigma_{\mathrm{NRS}}^{(\mathrm{MT1})}$ [J=70, ν=0], (d) $\sigma_{\mathrm{NRS}}^{(\mathrm{MT2})}$ [J=70, ν=0], (e) $\sigma_{\mathrm{NRS}}^{(\mathrm{MT1})}$ [J=90, ν=0], (f) $\sigma_{\mathrm{NRS}}^{(\mathrm{MT2})}$ [J=90, ν=0], (g) $\sigma_{\mathrm{NRS}}^{(\mathrm{MT1})}$ [J=100, ν=0], (h) $\sigma_{\mathrm{NRS}}^{(\mathrm{MT1})}$ [J=100, ν=0], (i) $\sigma_{\mathrm{NRS}}^{(\mathrm{MT1})}$ [J=200, ν=0], (j) $\sigma_{\mathrm{NRS}}^{(\mathrm{MT2})}$ [J=200, ν=0].

Reduced electric field (Td)	(a)	(b)	(c)	(d)	(e)	(f)
200	/	1.24E-21	2.47E-21	/	5.01E-21	/
300	3.26E-20	1.63E-20	6.74E-20	4.97E-20	7.53E-20	6.27E-20
400	3.90E-19	3.39E-19	7.49E-19	6.74E-19	8.00E-19	7.68E-19
500	2.11E-18	2.06E-18	3.40E-18	3.52E-18	3.55E-18	3.47E-18
700	1.31E-17	1.27E-17	1.67E-17	1.73E-17	1.72E-17	1.75E-17
1000	6.17E-17	5.93E-17	6.47E-17	6.73E-17	6.48E-17	6.66E-17
2000	3.66E-16	3.41E-16	3.50E-16	3.49E-16	3.46E-16	3.45E-16
3000	6.45E-16	6.09E-16	6.26E-16	6.19E-16	6.22E-16	6.17E-16

Table 5.52: Dissociation rate constant in m^3s^{-1} from hybrid calculations using different interactions models and $\sigma_{\mathrm{NRS}}^{(\mathrm{MT1})}$ and $\sigma_{\mathrm{NRS}}^{(\mathrm{MT2})}$ for a initial dimer [J=0, ν=0]. (a) Model A1 $\sigma_{\mathrm{NRS}}^{(\mathrm{MT1})}$, (b) Model A1 $\sigma_{\mathrm{NRS}}^{(\mathrm{MT2})}$, (c) Model B1 $\sigma_{\mathrm{NRS}}^{(\mathrm{MT1})}$, (d) Model B1 $\sigma_{\mathrm{NRS}}^{(\mathrm{MT2})}$, (e) Model B2 $\sigma_{\mathrm{NRS}}^{(\mathrm{MT1})}$, (f) Model B2 $\sigma_{\mathrm{NRS}}^{(\mathrm{MT2})}$.

Reduced electric field (Td)	(a)	(b)	(c)	(d)	(e)	(f)	(g)	(h)
200	/	1.23E-21	/	/	2.48E-21	/	/	4.35E-21
300	7.37E-20	4.80E-20	6.27E-20	6.98E-20	5.64E-20	6.27E-20	3.42E-20	4.50E-20
400	7.94E-19	8.16E-19	7.02E-19	7.94E-19	6.67E-19	7.03E-19	4.77E-19	6.18E-19
500	3.62E-18	3.70E-18	3.59E-18	3.88E-18	3.2E-18	3.49E-18	2.73E-18	3.29E-18
700	1.72E-17	1.83E-17	1.79E-17	1.94E-17	1.71E-17	1.90E-17	1.56E-17	1.75E-17
1000	6.81E-17	7.09E-17	6.98E-17	7.23E-17	6.89E-17	7.27E-17	6.79E-17	7.19E-17
2000	3.59E-16	3.58E-16	3.65E-16	3.61E-16	3.67E-16	3.67E-16	3.76E-16	3.73E-16
3000	6.36E-16	6.31E-16	6.39E-16	6.33E-16	6.45E-16	6.38E-16	6.55E-16	6.47E-16

Table 5.53: Dissociation rate constant in m^3s^{-1} from hybrid calculations using Model B1 and $\sigma_{\mathrm{NRS}}^{(\mathrm{MT1})}$ and $\sigma_{\mathrm{NRS}}^{(\mathrm{MT2})}$ for different initial (a) $\sigma_{\mathrm{NRS}}^{(\mathrm{MT1})}$ [J=0, ν=1], (b) $\sigma_{\mathrm{NRS}}^{(\mathrm{MT2})}$ [J=0, ν=1], (c) $\sigma_{\mathrm{NRS}}^{(\mathrm{MT1})}$ [J=0, ν=2], (d) $\sigma_{\mathrm{NRS}}^{(\mathrm{MT2})}$ [J=0, ν=2], (e) $\sigma_{\mathrm{NRS}}^{(\mathrm{MT1})}$ [J=0, ν=4], (f) $\sigma_{\mathrm{NRS}}^{(\mathrm{MT2})}$ [J=0, ν=4], (g) $\sigma_{\mathrm{NRS}}^{(\mathrm{MT1})}$ [J=0, ν=8], (h) $\sigma_{\mathrm{NRS}}^{(\mathrm{MT2})}$ [J=0, ν=8].

Reduced electric field (Td)	(a)	(b)	(c)	(d)	(e)	(f)	(g)	(h)
200	/	/	1.25E-21	1.25E-21	/	6.19E-22	1.25E-21	/
300	2.10E-20	4.95E-20	2.16E-20	3.10E-20	4.11E-20	2.41E-20	3.25E-20	4.02E-20
400	5.50E-19	6.26E-19	4.13E-19	4.03E-19	4.30E-19	4.16E-19	5.10E-19	5.18E-19
500	2.68E-18	3.27E-18	2.03E-18	2.14E-18	2.41E-18	2.43E-18	2.48E-18	2.60E-18
700	1.63E-17	1.90E-17	1.25E-17	1.26E-17	1.39E-17	1.39E-17	1.40E-7	1.43E-17
1000	7.07E-17	7.63E-17	5.52E-17	5.63E-17	5.92E-17	5.97E-17	5.93E-17	5.94E-17
2000	3.85E-16	3.84E-16	3.34E-16	3.30E-16	3.39E-16	3.36E-16	3.41E-16	3.36E-16
3000	6.63E-16	6.56E-16	6.07E-16	6.00E-16	6.13E-16	6.03E-16	6.14E-16	6.05E-16

Table 5.54: Dissociation rate constant in m^3s^{-1} from hybrid calculations using Model B1 and $\sigma_{\mathrm{NRS}}^{(\mathrm{MT1})}$ and $\sigma_{\mathrm{NRS}}^{(\mathrm{MT2})}$ for different initial rotational-vibrational dimer values. (a) $\sigma_{\mathrm{NRS}}^{(\mathrm{MT1})}$ [J=0, ν=12], (b) $\sigma_{\mathrm{NRS}}^{(\mathrm{MT2})}$ [J=0, ν=12], (c) $\sigma_{\mathrm{NRS}}^{(\mathrm{MT1})}$ [J=60, ν=0], (d) $\sigma_{\mathrm{NRS}}^{(\mathrm{MT2})}$ [J=60, ν=0], (e) $\sigma_{\mathrm{NRS}}^{(\mathrm{MT1})}$ [J=70, ν=0], (f) $\sigma_{\mathrm{NRS}}^{(\mathrm{MT2})}$ [J=70, ν=0], (g) $\sigma_{\mathrm{NRS}}^{(\mathrm{MT1})}$ [J=90, ν=0], (h) $\sigma_{\mathrm{NRS}}^{(\mathrm{MT2})}$ [J=90, ν=0].

Reduced electric field (Td)	(a)	(b)	(c)	(d)	(e)	(f)
200	/	2.50E-21	1.24E-20	1.25E-20	/	/
300	4.03E-20	3.41E-20	2.98E-19	2.72E-19	3.50E-20	4.19E-20
400	5.18E-19	4.88E-19	1.86E-18	1.86E-18	4.27E-19	4.43E-19
500	2.67E-18	2.56E-18	5.52E-18	5.67E-18	2.27E-18	2.25E-18
700	1.45E-17	1.44E-17	1.82E-17	1.92E-17	1.35E-17	1.35E-17
1000	6.05E-17	6.00E-17	5.85E-17	6.17E-17	5.89E-17	5.98E-17
2000	3.42E-16	3.37E-16	3.31E-16	3.31E-16	3.45E-16	3.39E-16
3000	6.12E-16	6.03E-16	6.16E-16	6.11E-16	6.18E-16	6.09E-16

Table 5.55: Dissociation rate constant in m^3s^{-1} from hybrid calculations using Model B2 and $\sigma_{\mathrm{NRS}}^{(\mathrm{MT1})}$ and $\sigma_{\mathrm{NRS}}^{(\mathrm{MT2})}$ for different initial rotational-vibrational dimer values. (a) $\sigma_{\mathrm{NRS}}^{(\mathrm{MT1})}$ [J=100, ν=0], (b) $\sigma_{\mathrm{NRS}}^{(\mathrm{MT2})}$ [J=100, ν=0], (c) $\sigma_{\mathrm{NRS}}^{(\mathrm{MT1})}$ [J=200, ν=0], (d) $\sigma_{\mathrm{NRS}}^{(\mathrm{MT2})}$ [J=200, ν=0], (e) $\sigma_{\mathrm{NRS}}^{(\mathrm{MT1})}$ [J=100, ν=1], (f) $\sigma_{\mathrm{NRS}}^{(\mathrm{MT2})}$ [J=100, ν=1].

Reduced electric field (Td)	(a)	(b)	(c)	(d)	(e)	(f)	(g)	(h)	(i)	(j)
200	1.25E-21	/	1.23E-21	1.23E-21	/	/	1.24E-21	/	1.24E-21	1.24E-21
300	8.98E-20	8.23E-20	7.68E-20	7.35E-20	4.64E-20	6.81E-20	3.09E-20	2.62E-20	8.29E-20	5.90E-20
400	8.56E-19	8.54E-19	8.87E-19	8.74E-19	5.37E-19	7.08E-19	4.27E-19	3.90E-19	7.56E-19	8.00E-19
500	3.90E-18	4.08E-18	3.82E-18	4.25E-18	2.59E-18	3.29E-18	2.06E-18	2.01E-18	3.38E-18	3.75E-18
700	1.83E-17	1.90E-17	1.87E-17	2.01E-17	1.63E-17	1.90E-17	1.21E-17	1.24E-17	1.72E-17	1.90E-17
1000	6.84E-17	6.96E-17	6.95E-17	7.33E-17	7.05E-17	7.60E-17	5.37E-17	5.41E-17	6.84E-17	7.22E-17
2000	3.54E-16	3.52E-16	3.60E-16	3.59E-16	3.84E-16	3.82E-16	3.26E-16	3.23E-16	3.64E-16	3.63E-16
3000	6.32E-16	6.28E-16	6.38E-16	6.33E-16	6.62E-16	6.54E-16	6.01E-16	5.95E-16	6.40E-16	6.33E-16

Table 5.56: Dissociation rate constant in m^3s^{-1} from hybrid calculations using Model B2 and $\sigma_{\mathrm{NRS}}^{(\mathrm{MT1})}$ and $\sigma_{\mathrm{NRS}}^{(\mathrm{MT2})}$ for different initial rotational-vibrational dimer values. (a) $\sigma_{\mathrm{NRS}}^{(\mathrm{MT1})}$ [J=0, ν=1], (b) $\sigma_{\mathrm{NRS}}^{(\mathrm{MT2})}$ [J=0, ν=1], (c) $\sigma_{\mathrm{NRS}}^{(\mathrm{MT1})}$ [J=0, ν=2], (d) $\sigma_{\mathrm{NRS}}^{(\mathrm{MT2})}$ [J=0, ν=2], (e) $\sigma_{\mathrm{NRS}}^{(\mathrm{MT1})}$ [J=0, ν=4], (f) $\sigma_{\mathrm{NRS}}^{(\mathrm{MT2})}$ [J=0, ν=4], (g) $\sigma_{\mathrm{NRS}}^{(\mathrm{MT1})}$ [J=0, ν=8], (h) $\sigma_{\mathrm{NRS}}^{(\mathrm{MT1})}$ [J=0, ν=8], (i) $\sigma_{\mathrm{NRS}}^{(\mathrm{MT1})}$ [J=0, ν=12], (j) $\sigma_{\mathrm{NRS}}^{(\mathrm{MT2})}$ [J=0, ν=12].

Reduced electric field (Td)	(a)	(b)	(c)	(d)	(e)	(f)	(g)	(h)	(i)	(j)
200	/	2.49E-21	1.24E-21	1.25E-21	1.26E-21	/	2.48E-21	2.48E-21	2.48E-21	/
300	3.87E-20	6.20E-20	3.57E-20	3.40E-20	3.56E-20	3.42E-20	3.33E-20	2.33E-20	5.89E-20	5.27E-20
400	5.72E-19	6.74E-19	4.91E-19	4.29E-19	5.38E-19	5.67E-19	5.81E-19	5.33E-19	5.66E-19	5.64E-19
500	2.62E-18	3.27E-18	2.45E-18	2.36E-18	2.55E-18	2.44E-18	2.70E-18	2.51E-18	2.64E-18	2.58E-18
700	1.58E-17	1.78E-17	1.37E-17	1.34E-17	1.42E-17	1.43E-17	1.43E-17	1.40E-17	1.37E-17	1.43E-17
1000	6.65E-17	7.25E-17	5.73E-17	5.77E-17	5.87E-17	5.93E-17	5.94E-17	5.89E-17	5.65E-17	5.71E-17
2000	3.70E-16	3.68E-16	3.33E-16	3.29E-16	3.36E-16	3.31E-16	3.36E-16	3.31E-16 3.35E-16	3.31E-16	
3000	6.52E-16	6.44E-16	6.04E-16	5.97E-16	6.11E-16	6.03E-16	6.08E-16	5.96E-16	6.15E-16	6.09E-16

Table 5.57: Dissociation rate constant in m^3s^{-1} from hybrid calculations using Model B2 and $\sigma_{\mathrm{NRS}}^{(\mathrm{MT1})}$ and $\sigma_{\mathrm{NRS}}^{(\mathrm{MT2})}$ for different initial rotational-vibrational dimer values. (a) $\sigma_{\mathrm{NRS}}^{(\mathrm{MT1})}$ [J=60, ν=0], (b) $\sigma_{\mathrm{NRS}}^{(\mathrm{MT2})}$ [J=60, ν=0], (c) $\sigma_{\mathrm{NRS}}^{(\mathrm{MT1})}$ [J=70, ν=0], (d) $\sigma_{\mathrm{NRS}}^{(\mathrm{MT2})}$ [J=70, ν=0], (e) $\sigma_{\mathrm{NRS}}^{(\mathrm{MT1})}$ [J=90, ν=0], (f) $\sigma_{\mathrm{NRS}}^{(\mathrm{MT2})}$ [J=90, ν=0], (g) $\sigma_{\mathrm{NRS}}^{(\mathrm{MT1})}$ [J=100, ν=0], (h) $\sigma_{\mathrm{NRS}}^{(\mathrm{MT1})}$ [J=100, ν=0], (i) $\sigma_{\mathrm{NRS}}^{(\mathrm{MT1})}$ [J=200, ν=0], (j) $\sigma_{\mathrm{NRS}}^{(\mathrm{MT2})}$ [J=200, ν=0].

Bibliography

[1] J. A. S. Barata, PhD thesis, Departamento de Física, Universidade da Beira Interior, **2006**.

[2] P. N. B. Neves, C. A. N. Conde, L. M. N. Távora, *J. Chem. Phys.* **2010**, *133*, 124316.

[3] A. Fridman, G. Friedman, *Plasma medicine*, John Wiley and Sons, Ltd. Drexel University, Philadelphia, USA, **2013**.

[4] L. Auvray, J.-M. Berroir, N. Billy, L. Daudet, C. Fabre, K. Laval, R. Madariaga, G. Megie, J.-Y. Ollitrault, J.-L. Oudar, G. Pietrik, F. Ravetta, L. Rezeau, J.-P.Uzan, C. Vigny, *Panorama de la Physique*, Belin, **2007**.

[5] J. C. F. Televisions, D'impréssionantes aurores boréales tournées en très haute résolution, [Online; accessed October 1, 2018], **2014**.

[6] A. Fridman, *Plasma chemistry*, Cambridge University Press, New York, **2008**.

[7] F. Judéé, PhD thesis, Université Toulouse 3 Paul Sabatier, ED GEET : Ingénieurie des PLASMAS, **2016**.

[8] S. Kanazawa, M. Kogoma, T. Moriwaki, S. Okazaki, *J. Phys. Appl. Phys.* **1988**, *21*, 838.

[9] U. Kogelschatz, *Pure Appl. Chem* **1990**, *62*, 1667.

[10] F. Massines, A. Rabehi, P. Decomps, R. B. Gadri, P. Ségur, C. Mayoux, *J. of Appl. Phys.* **1998**, *83*, 2950.

[11] M. Yousfi, N. Merbahi, J. P. Sarrette, O. Eichwald, A. Ricard, J. Gardou, O. Ducasse, M. Benhenni in *Biomedical Engineering*, (Ed.: R. Fazel-Rezai), IntechOpen, Rijeka, **2011**, Chapter 5.

[12] J. G Eden., S.-J. Park, N. P. Ostrom, S. T. McCain, C. J. Wagner, B. A. Vojak, J. Chen, C. Liu, P. von Allmen, F. Zenhausern, D. J. Sadler, C. Jensen, D. L. Wilcox, J. J. Ewing, *J. Phys. Appl. Phys.* **2003**, *36*, 2869.

[13] A. El-Habachi, K. H. Schoenbach, *Appl. Phys. Lett.* **1998**, *72*, 22.

[14] M. Laroussi, *IEEE. Trans. Plasma Sci.* **2002**, *30*, 1049.

[15] Analytica-wolrd.com, Selecting your ICP-OES analyzer's plasma interface: axial-view, radial-view, dual-view or new MultiView?, [Online; accessed October 1, 2018], **2018**.

[16] J. J. Shi, M. G. Mode, *IEEE Trans. Plasma Sci.* **2005**, *33*, 624.

[17] J. Chauvin, PhD thesis, Université Toulouse 3 Paul Sabatier, ED GEET : Ingénieurie des PLASMAS, **2018**.

[18] M. Laroussi, T. Akan, *Plasma Process. Polym* **2007**, *4*, 777.

[19] M. Laroussi, *IEEE Trans. Plasma Sci.* **2009**, *37*, 714.

[20] Q. Li, X.-M Zhu, J.-T. Li, Y.-K. Pu, *J. Appl. Phys.* **2010**, *107*, 043304.

[21] A. Chicheportiche, M. Benhenni, M. Yousfi, B. Lepetit, R. Kalus, F. X. Gadéa, *Phys. Rev. E* **2013**, *88*, 043104.

[22] A. Chicheportiche, B. Lepetit, M. Benhenni, F. X. Gadéa, M. Yousfi, *J. Phys. B: At. Mol. Opt. Phys.* **2013**, *46*, 065201.

[23] M. Benhenni, M. Stachoň, F. X. Gadéa, M. Yousfi, R. Kalus, *J. Phys. B: At. Mol. Opt. Phys.* **2016**, *49*, 175205.

[24] A. Chicheportiche, B. Lepetit, F. X. Gadéa, M. Benhenni, M. Yousfi, R. Kalus, *Phys. Rev. E* **2014**, *89*, 063102.

[25] A. Chicheportiche, M. Stachoň, M. Benhenni, F. X. Gadéa, R. Kalus, M. Yousfi, *J. Chem. Phys.* **2014**, *141*, 134302.

[26] M. Yousfi, N. Merbahi, A. Pathak, O. Eichwald, *Fundam Clin Pharmacol.* **2014**, *28*, 123.

[27] J. Chauvin, F. Judée, M. Yousfi, P. Vicendo, N. Merbahi, *Scientific reports* **2017**, *7*, 4562.

[28] F. Girard, PhD thesis, Université de Pau et des Pays de l'Adour, ED 211 Sciences Exactes et leurs Applications, **2017**.

[29] M. Bafoil, A. Jemmat, Y. M. ans N. Merbahi, O. Eichwald, C. Dunand, M. Yousfi, *PLoS ONE* **2018**, *13*, 4.

[30] D. V. Schitz, M. I. Lomaev, V. S. Skakun, V. F. Tarasenko, *Proc. SPIE* **2009**, *720119*, VII.

[31] N. Merbahi, N. Sewraj, F. Marchal, J.-P. Gardou, *Eur. Phys.J. Appl. Phys.* **2010**, *49*, 13103.

[32] N. Merbahi, G. Ledru, N. Sewraj, F. Marchal, *J. of Appl. Phys.* **2007**, *101*, 123309.

[33] M. I. Lomaev, E. A. Sosnin, V. F. Tarasenko, D. V. Shits, V. S. Shakun, M. V. Erofeev, *Instruments and experimental techniques* **2006**, *49*, 595.

[34] T. Oppenländer, *J. of Env. Eng.* **2007**, *6*, 253.

[35] G. Matafonova, V. Batoev, *Chemosphere* **2012**, *89*, 637.

[36] K. Kollner, M. B. Wimmershoff, C. Hints, M. Landthaler, U. Hohenleutner, *British Journal of Dermatology* **2005**, *152*, 750.

[37] G. Matafonova, V. B. Batoev, S. A. M. Gó, N. Christofi, *Letters in Applied Microbiology* **2008**, *47*, 508.

[38] P. Muranyi, J. Wunderlich, M. Heise, *J. Appl. Microbiol.* **2007**, *103*, 1535.

[39] E. A. Sosnin, T. Oppenländer, F. V. Tarasenko, *J. Photochem. Photobiol C* **2006**, *7*, 145.

[40] N. Aeronotics, S. Administration, Solar Electric Propulsion, [Online; accessed October 1, 2018], **2018**.

[41] A. I. Bugrova, A. M. Bishaev, A. V. Desyatskov, M. V. Kozintseva, A. S. Lipatov, M. Dudeck, *Int. J. of Aero. Eng.* **2013**, *2013*, ID 686132.

[42] G. Saccoccia, J. G. del Amo, D. Estublier, Ion engine gets SMART-1 to the Moon, `http://www.esa.int/Our_Activities/Space_Science/SMART-1/Ion_engine_gets_SMART-1_to_the_Moon`.

[43] NASA, Dawn Launch, `https://www.jpl.nasa.gov/news/press_kits/dawn-launch.pdf`.

[44] S. Mazouffre, *Plasma Sources Science and Technology* **2016**, *25*, 033002.

[45] D. Liu, R. E. Huffman, R. D. Branam, W. A. H. Jr, *IEEE transactions on Plasma science* **2011**, *39*, 2926.

[46] E. A. Mason, E. W. McDaniel, *TRANSPORT PROPERTIES OF IONS IN GASES*, John Wiley and Sons, Toronto, **1988**, p. 398.

[47] J. S. Cohen, B. I. Schneider, *J. Chem. Phys.* **1974**, *61*, 3230.

[48] A. Kramida, Y. andJ. Reader, and NIST ASD Team, NIST Atomic Spectra Database(ver. 5.3), [Online]. Available:`http://physics.nist.gov/asd` [2017, September 22].National Institute of Standards and Technology,Gaithersburg, MD. **2015**.

[49] M. Amarouche, G. Durand, J. P. Malrieu, *J. Chem. Phys.* **1988**, *88*, 1010.

[50] F. O. Ellison, *J. Am. Chem. Soc.* **1963**, *85*, 3540.

[51] P. J. Kuntz, J. Valldorf, *Z. Phys. D* **1988**, *8*, 195.

[52] C. Van de Steen, M. Benhenni, R. Kalus, B. Lepetit, F. X. Gadea, M. Yousfi, *Plasma Sources Sci. Tecnol.* **2018**, *27*, 065005.

[53] R. Kalus, I. Paidarová, D. Hrivňák, P. Paška, F. X. Gadéa, *J. Chem. Phys* **2003**, *294*, 141.

[54] T.-K. Ha, P. Rupper, A. Wüest, F. Merkt, *Mol. Phys.* **2003**, *101*, 827.

[55] A. K. Dham, A. R. Allnatt, W. J. Meath, R. A. Aziz, *Mol. Phys.* **1989**, *67*, 1291.

[56] J. M. Waldrop, B. Song, K. Patkowski, X. Wang, *J. Chem. Phys.* **2015**, *142*, 204307.

[57] B. Jäger, R. Hellmann, E. Bich, E. Vogel, *J. Chem. Phys.* **2016**, *144*, 114304.

[58] A. Nicklass, M. Dolg, H. Stoll, H. Preuss, *J. Chem. Phys.* **1995**, *102*, 8942.

[59] J. Sugar, A. Musgrove, *J. Phys. Chem. Ref. Data* **1991**, *20*, 859.

[60] M. Child, *Molecular Collision Theory*, Mineola, NY, **1996**.

[61] T. Wu, T Ohmura, *Quantum Theory of Scattering*, Englewood Cliffs, NJ, **1962**, p. 34.

[62] L. Landau, E. M. Lifshitz in, Pergamon Press, Oxford, **1965**, Chapter VII.

[63] J. A. S. Barata, C. A. N. Conde, *IEEE Trans. Nucl. Sci.* **2005**, *52*, 2889.

[64] A. Chicheportiche, PhD thesis, Université Toulouse 3 Paul Sabatier, ED GEET : Ingénieurie des PLASMAS, **2014**.

[65] P. Ehrenfest, *Z. Phys.* **1927**, *45*, 455.

[66] M. Amarouche, F. X. Gadéa, J. Durup, *Chem. Phys.* **1989**, *130*, 145.

[67] I. Paidarová, F. X. Gadéa, *J. Chem. Phys* **2001**, *274*, 1.

[68] D. Bonhommeau, T. Bouissou, N. Halberstadt, A. Viel, *J. Chem. Phys* **2006**, *124*, 164308.

[69] R. Hellmann, B. Jäger, E. Bich, *The J. of Chem. Phys.* **2017**, *147*, 034304.

[70] I. Janeček, S. Cintavá, D. Hrivňák, R. Kalus, M. Fárník, F. X. Gadéa, *J. Chem. Phys.* **2009**, *131*, 114306.

[71] As expected, the cross-section of the collision-induced dissociation of the dimer ion has always been converged at considerably smaller values of $b_{\max}$ than the non-reactive momentum-transfer cross-sections.

[72] Let us remind that the initial electronic state of the dimer ion has been always set to the ground state. As a consequence, the internal state of the ion is given by its rotation and vibration quantum numbers, J and ν, respectively. Hereafter, we will denote a particular rotational-vibrational state of the dimer ion by [J=J,ν=ν]; e.g., [J=0,ν=0] denotes the rotational-vibrational ground state, [J=0,ν=1] the first excited vibrational state etc.

[73] Note that only classically accessible region of the rotational-vibrational wave function has been sampled in this way so that the remaining vibrational kinetic energy be non-negative. Outside this region, the wave function has been set to zero.

[74] E. Vitásek in, SNTL, Praha, **1987**, p. 144.

[75] I. Janeček, D. Hrivňák, R. Kalus, F. X. Gadéa, *J. Chem. Phys.* **2006**, *125*, 104315.

[76] E. A. Mason, H. O'Hara, F. J. Smith, *J. Phys. B.* **1972**, *5*, 169.

[77] E. A. Mason, E. W. McDaniel, *Transport Properties of ions in gas*, Wiley-VCH, Weinheim, **2005**.

[78] J. Hammerslay, D. Handscomb, *Monte Carlo Methods*, Methuen and Co, London, **1964**.

[79] INRIA, Le jeu de go et la revolution de Monte Carlo, `https://interstices.info/jcms/c_43860/le-jeu-de-go-et-la-revolution-de-monte-carlo`.

[80] ICPIG XXXIII, Estoril, Portugal, **2017**.

[81] J. Meija, T. Coplen, M. Berglund, al., *Pure Appl. Chem.* **2016**, *688*, 265.

[82] B. Roos, *Chem. Phys. Lett.* **1972**, *15*, 153.

[83] S. R. Langhoff, E. R. Davidson, *Int. J. Quant. Chem.* **1974**, *8*, 61.

[84] P.-O. Widmark, P.-A. Malmqvist, B. O. Roos, *Theor. Chim. Acta* **1990**, *77*, 291.

[85] P.-O. Widmark, B. Joakim, B. J. Persson, B. O. Roos, *Theor. Chim. Acta* **1990**, *77*, 291.

[86] R. Signorell, U. Hollenstein, F. Merkt, *J. Chem. Phys.* **2001**, *114*, 9840.

[87] R. I. Hall, Y. Lu, Y. Morioka, T.Matsui, H. Yoshii, T. Hayaishi, K.Ito, *J. Phys. B: At. molec. opt. Phys.* **1995**, *28*, 2435.

[88] H. W. Ellis, R. Y. Pai, E. W. M. Daniel, E. A. Mason, L. A. Viehland, *At. Data Nucl. Data Tables* **1976**, *17*, 177.

[89] H. Helm, *J. Phys. B* **1976**, *9*, 2931.

[90] E. A. Mason, E. W. McDaniel in *Transport Properties of Ions in Gases*, Wiley-VCH Verlag GmbH et Co. KGaA, **2005**, pp. 137–193.

[91] R. N. Varney, *Phys. Rev.* **1952**, *88*, 362.

[92] M. A. Biondi, L. M. Chanin, *Phys. Rev.* **1954**, *94*, 910.

[93] H. W. Ellis, D. L. Albritton, L. A. Viehland, S. L. Lin, E. A. Mason, *At. Data Nucl. Data Tables* **1978**, *22*, 179.

[94] ISPC XXIII, Montréal, Canada, **2017**.

[95] C. Van de Steen, M. Benhenni, R. Kalus, B. Lepetit, F. X. Gadea, M. Yousfi, *J. Phys. B: At. Mol. Opt. Phys.* **2018**, *51*, 185204.

[96] P. Rupper, O. Zehnder, F. Merkt, *J. Chem. Phys* **2004**, *121*, 8279.

[97] P. H. Larsen, M. T. Elford, *J. Phys. B* **1986**, *19*, 449.

[98] L. A. Viehland, E. A. Mason, *At. Data Nucl. Data Tables* **1995**, *60*, 37.

[99] J. Brambring, *Z. Physik* **1964**, *179*, 352.

[100] J. L. Hernandez-Avila, E. Basurto, J. D. Urquijo, *J. Phys. D : Appl. Phys.* **2002**, *35*, 2264.

[101] M. Child, *Molecular Collision Theory*, Mineola, NY, **1996**.

[102] M. Yousfi, A. Hennad, O. Eichwald, *J. of Appl. Phys.* **1998**, *84*, 107.

[103] ESCAMMPIG XXIV, Glasgow, Scotland, **2018**.

[104] C. Van de Steen, M. Benhenni, R. Kalus, R. Ćosić, S. Illésová, F. X. Gadea, M. Yousfi, *Plasma Sources Sci. Tecnol.* **2018**, *Under publication*, ?

[105] H. W. Ellis, M. G. Thackston, E. W. McDaniel, E. A. Mason, *At. Data Nucl. Data Tables* **1984**, *31*, 113.

[106] H. Helm, M. T. Elford, *J. Phys. B* **1978**, *11*, 3939.

[107] E. C. Beaty, *Phys. Rev.* **1956**, *104*, 17.

[108] P. Slavíček, R. Kalus, P. Paška, I. Odvárková, P. Hobza, A. Malijevsk'y, *J. Chem. Phys.* **2003**, *119*, 2102.

[109] C. Praxmarer, A. Hansel, A. Jordan, H. Kraus, W. Lindinger, *Int. J. Mass Spec. Ion. Proc.* **1993**, *129*, 121.

[110] H. Helm, *Phys. Rev. A* **1976**, *14*, 680.

[111] Gaseous Electronic Meeting XX, Magnetic Island, Australia, **2018**.

[112] P. Neves, C. Conde, L. Távora, *Nucl. Inst. and Methods in Phys. Res. S. A: Accelerators Spectrometers Detectors and Associated Equipment* **2007**, *580*, 66.

[113] A. P. Vitols, H. J. Oskam, *Phys. Rev. A* **1973**, *8*, 1860.

[114] R. A. Aziz, M. J. Slaman, *Mol. Phys.* **1986**, *57*, 825.